P R O C E E D I N G S MPA/P13

APRIL 2002

P R O C E E D I N G S

of the 11th Workshop on

"Nuclear Astrophysics"

Ringberg Castle, Tegernsee, Germany

February 11 - 16, 2002

Wolfgang Hillebrandt and Ewald Müller (Eds.)
Max-Planck-Institut für Astrophysik
Karl-Schwarzschild-Strasse 1
85740 Garching b. München

Preface

From February 11 through 15, 2002, again a Workshop on Nuclear Astrophysics was held at the Ringberg Castle near Munich. This workshop was the 11th in a series which began in May 1981. As on all previous occasions, nuclear physicists, astrophysicists, and astronomers met for one week at the spectacular Ringberg Castle to discuss problems and projects of common interest.

This year's workshop was attended by 51 scientists from 11 countries many of whom had participated in previous workshops. For the first time in the history of the workshop series many more colleagues wanted to come than the Castle could accommodate and, therefore, several of the applications had to be rejected.

Continuing a good tradition of the series, again several students had an opportunity to present, for the fist time, their work to an international audience in a benevolently and friendly atmosphere. The workshop programme consisted of 44 talks often stimulating intensive discussions. As during all previous meetings the relaxed atmosphere of the Castle, ample time for discussions between the sessions, and the good weather provided nearly perfect conditions for a successful workshop.

The topics discussed in the talks covered most aspects of nuclear astrophysics including abundance determinations, reaction rate measurements, modeling specific nucleosynthetic processes and stellar evolutionary phases, simulating stellar explosions, and discussing cosmic chemical evolution. It was amazing to see the enormous progress that has been achieved since the earlier workshops: Fully 3-dimensional simulations of stellar explosions have become feasible, some important nuclear reaction rate have been measured with astonishing accuracy, and abundance determinations in stars as well as in meteorites have reached a level of quality that was not foreseen when we started these workshops.

In these Proceedings extended abstracts of most of the contributions are included. An electronic (color) version is available via the MPA homepage (`http://www.mpa-garching.mpg.de/english/greenreports.html`).

The success of the workshop, of course, also depended on financial support by the Max–Planck–Gesellschaft and, needless to say, on the enormous efficiency and friendliness of Mr. Hörmann and his crew.

Garching, April 2002

Wolfgang Hillebrandt Ewald Müller

List of Participants	**Institute**
Carlos Abia	Universidad de Granada, E
Marialuisa Aliotta	Univ. of Edinburgh, UK
Dominik Argast	Universität Basel, CH
Sergei Blinnikov	ITEP, Moscow, RUS
Maurizio Busso	Univ. of Perugia, I
Ramon Canal	Univ. Barcelona, E
Alessandro Chieffi	Instituto di Astrofisica Spaziale, I
John Cowan	Univ. of Oklahoma, Norman, USA
Roland Diehl	MPI fr Extraterrestrische Physik
Inma Dominguez	Universidad de Granada, E
Abouazza Elmhamdi	SISSA, Trieste, I
Jacob Fisker	Universitt Basel, CH
Alba Formicola	Ruhr-Universität Bochum, D
Cris Fryer	Los Alamos National Laboratory, USA
Roberto Gallino	Univ. Torino, I
Joachim Görres	University of Notre Dame, Indiana, USA
Wolfgang Hammer	Universität Stuttgart, D
Dieter Hartmann	Clemson University, USA
Alexander Heger	University of Chicago, USA
Margarita Hernanz	Catalonia Space Studies, Barcelona, E
Wolfgang Hillebrandt	MPI für Astrophysik, Garching, D
Gianluca Imbriani	INFN, Napoli, I
Jordi Isern	Catalonia Space Studies, Barcelona, E
Yuhri Ishimaru	Institut d'Astrophysique, Paris, F
Anatoli Iyudin	MPI für extraterrestrische Physik,
Hans-Thomas Janka	MPI für Astrophysik, Garching, D
Franz Käppeler	Forschungszentrum Karlsruhe, D
K.-L. Kratz	Universität Mainz, D
Matthias Liebendörfer	Oak Ridge Natl. Lab., USA
Ewald Müller	MPI für Astrophysik, Garching, D

List of Participants	**Institute**
Jens Niemeyer	MPI für Astrophysik, Garching, D
Roland Oechslin	Universität Basel, CH
Alexander Ostrowski	University of Edinburgh, U.K.
Luciano Piersanti	Osservatorio Astronomico di Teramo, I
Markus Rampp	MPI für Astrophysik, Garching, D
Rene Reifarth	Forschungszentrum Karlsruhe, D
Martin Reinecke	MPI für Astrophysik, Garching, D
Friedrich Röpke	MPI für Astrophysik, Garching, D
Jorge Miguel Sampaio	Aarhus University, DK
Daniel Sauer	MPI für Astrophysik, Garching, D
Daniel Schürmann	Ruhr-Universität Bochum, D
Olivier Sorlin	Institut de Physique Nucleaire, Orsay, F
Elena Sorokina	Sternberg Astr. Inst. Moscow
Oscar Straniero	Osservatorio Astronomico di Teramo, I
Claudia Travaglio	MPI für Astrophysik, Garching, D
Jim Truran	University of Chicago, USA
Hideyuki Umeda	University of Tokyo, Japan
Victor Utrobin	ITEP, Moscow, Russia
Rainer Wehrse	Universität Heidelberg, D,
Andreas Woehr	University of Maryland, USA
Sung-chul Yoon	Utrecht University, NL

Contents

The Beginning of Stellar Nucleosynthesis

A. Heger[1], *S.E. Woosley*[2]

[1] *Department of Astronomy and Astrophysics, Enrico Fermi Institute, The University of Chicago, 5640 S. Ellis Ave, Chicago, IL 60637, U.S.A.*
[2] *Department of Astronomy and Astrophysics, University of California, 1156 High St, Santa Cruz, CA 95064, U.S.A.*

The first stars to form in the universe were essentially devoid of any metals. This lack of metals affected not only their formation but their evolution and nucleosynthesis. Recent calculations suggest that the the first generation might have contained many very massive members, stars of over 100 solar masses [1, 2, 3, 4]. In addition, stability analysis shows that stars with no metals may be much more impervious to mass loss than their modern counterparts. Thus they may not only have been born big, they died big. [5, 6] (see Figure 1):

After central helium depletion, stars over about 100 solar masses encounter the electron-positron pair creation instability which leads to explosive burning of oxygen and, later, silicon [7]. For stars from 100 to 140 solar masses the instability results in several violent pulsations accompanied by supernova-like outbursts. From $\sim 140 - 260\,\mathrm{M}_\odot$ complete disruption of the star results (pair SN). Explosion energies up to 100 times that of typical core collapse supernovae are developed and up to 50 solar masses nickel are expelled [8]. Besides the implications for nucleosynthesis (50 solar masses can provide the iron for 500 million solar masses of material with metallicity [Z] = -4) the radioactively helps to make these explosions very bright. For more massive (non-rotating) stars, photo-disintegration leads to collapse into a black hole instead of disruption. From about 40 to 140 solar masses, with the lower value somewhat uncertain, one also expects direct black hole formation [10] where no shock is launched to eject the nucleosynthesis products in the core of the star. Thus the pair instability supernovae are bounded above and below by stars that may contribute little to nucleosynthesis (Figure 1), the pair SNe are a source of nucleosynthesis that is not polluted by contributions from lower or higher masses. Also, no nucleosynthetic contributions from metal-free supermassive stars are to be expected [12].

In Figure 2 we give the production factor for the ejecta of these stars, assuming different power law slopes for the initial mass function (IMF). We find an overproduction of elements with even charge number relative to those with odd charge number by about a factor hundred. The largest overproductions are those of silicon, sulfur, calcium and argon. The production of the iron group, including the observationally interesting oxygen to iron ratio, strongly depends on the initial mass function in this regime, and if it were strongly peaked at the upper or lower end of the pair SNe regime, it could vary by orders of magnitude.

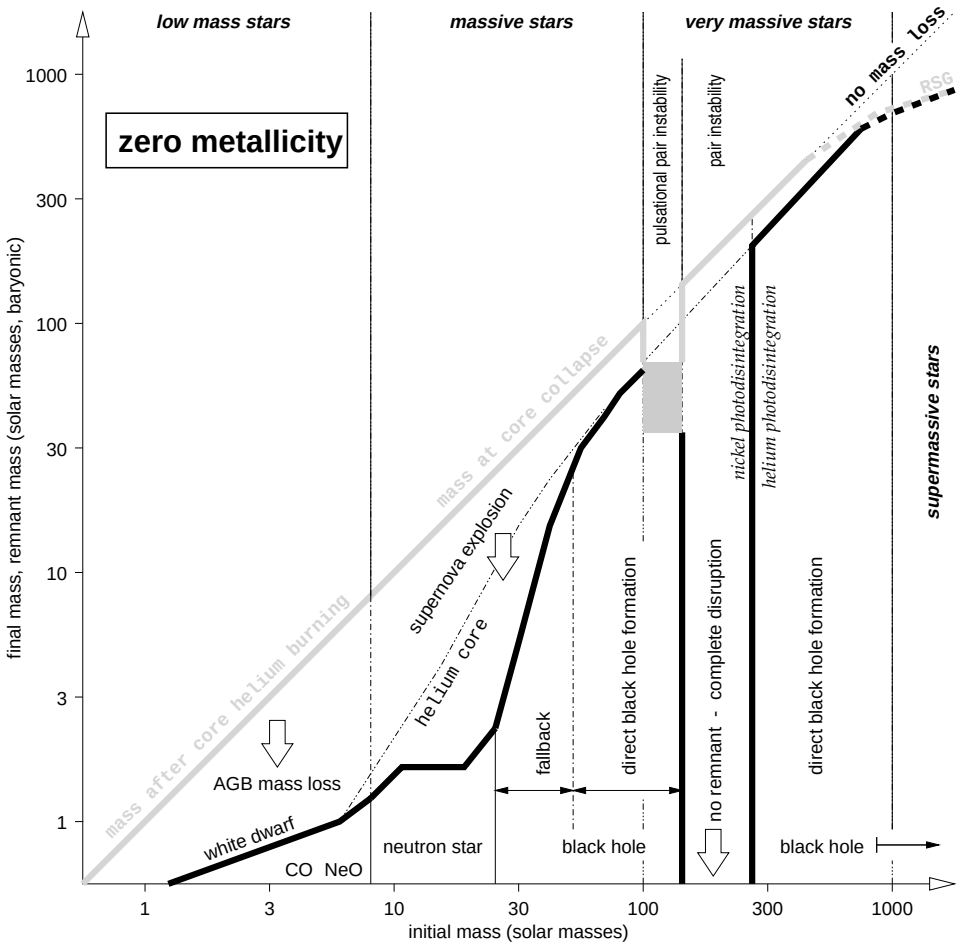

Figure 1: Initial-final mass function of non-rotating primordial stars ($Z = 0$). The *x-axis* gives the initial stellar mass. The *y-axis* gives both the final mass of the collapsed remnant (*thick black curve*) and the mass of the star when the event begins that produces that remnant (*thick gray curve*). We distinguish four regimes of initial mass: *low mass stars* below $\sim 10\,\mathrm{M}_\odot$ that end as white dwarfs; *massive stars* between $\sim 10\,\mathrm{M}_\odot$ and $\sim 100\,\mathrm{M}_\odot$; *very massive stars* between $\sim 100\,\mathrm{M}_\odot$ and $\sim 1000\,\mathrm{M}_\odot$; and *supermassive stars* (arbitrarily) above several $1000\,\mathrm{M}_\odot$. Since no mass loss is expected for $Z = 0$ stars before the final stage, the grey curve is approximately the same as the line of no mass loss (*dotted*). Exceptions are $\sim 100 - 140\,\mathrm{M}_\odot$ where the pulsational pair-instability ejects the outer layers of the star up to several thousand years before it collapses, and above $\sim 500\,\mathrm{M}_\odot$ where pulsational instabilities in red supergiants may lead to significant mass loss [6]. For more details please refer to [8, 9].

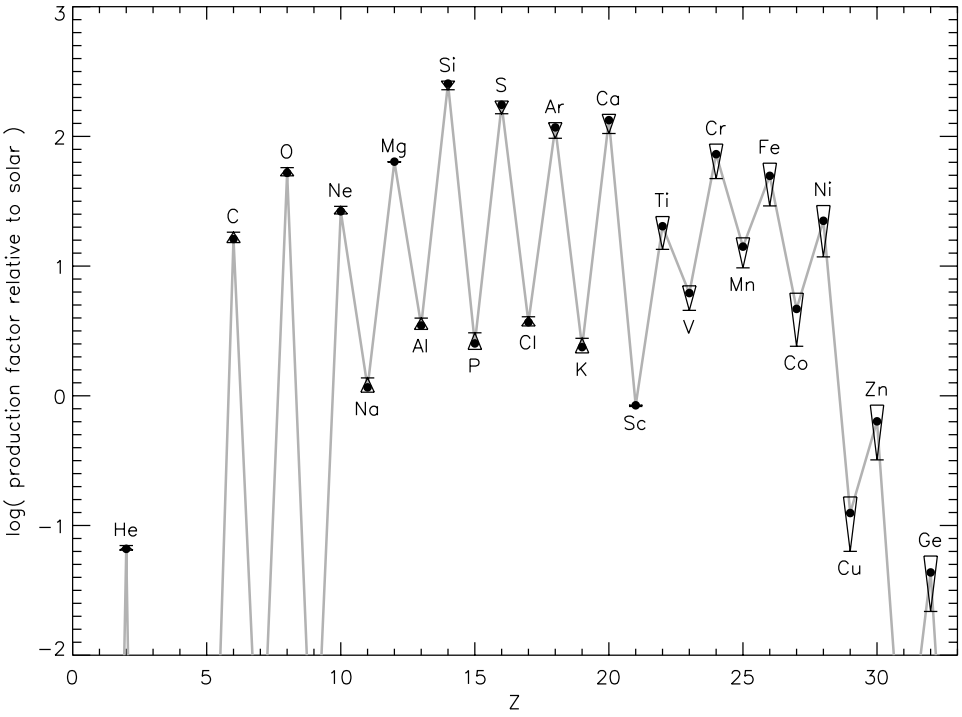

Figure 2: Production factors for very massive stars (helium cores of $65 - 130\,\mathrm{M}_\odot$, corresponding to initial masses of $\sim 140 - 260\,\mathrm{M}_\odot$) integrated over an IMF and compared to solar abundances as a function of element charge number, Z (note that here Z is not the metallicity). The integration assumed a Salpeter-like IMF with three different exponents: -0.5 (*thick end of triangle*), -1.5 (*solid dot*), and -3.5 (*thin end of triangle*).

Since no initial metal seeds are present, no *s*-process occurs in any of the primordial stars, i.e., nothing heaver than Zn is produced during the hydrostatic burning phases. The collapse (and explosion) of the pair SNe occurs on a dynamic time-scale, reaching only moderate peak densities ($\sim 10^7\,\mathrm{g\,cm^{-3}}$) and no compact remnant is formed, so that these objects do not contribute to the *r*-process either. Core collapse supernovae that do not directly form a black hole ($M < 40\,\mathrm{M}_\odot$), however, may contribute to the *r*-process.

In Figure 3 we present the production factors for massive metal-free stars (*dotted line*; not including a possible *r*-process contribution) and the combination of the massive star yields ($11\,\mathrm{M}_\odot < M < 40\,\mathrm{M}_\odot$) and very massive star yields ($140\,\mathrm{M}_\odot < M < 260\,\mathrm{M}_\odot$) using a common IMF with

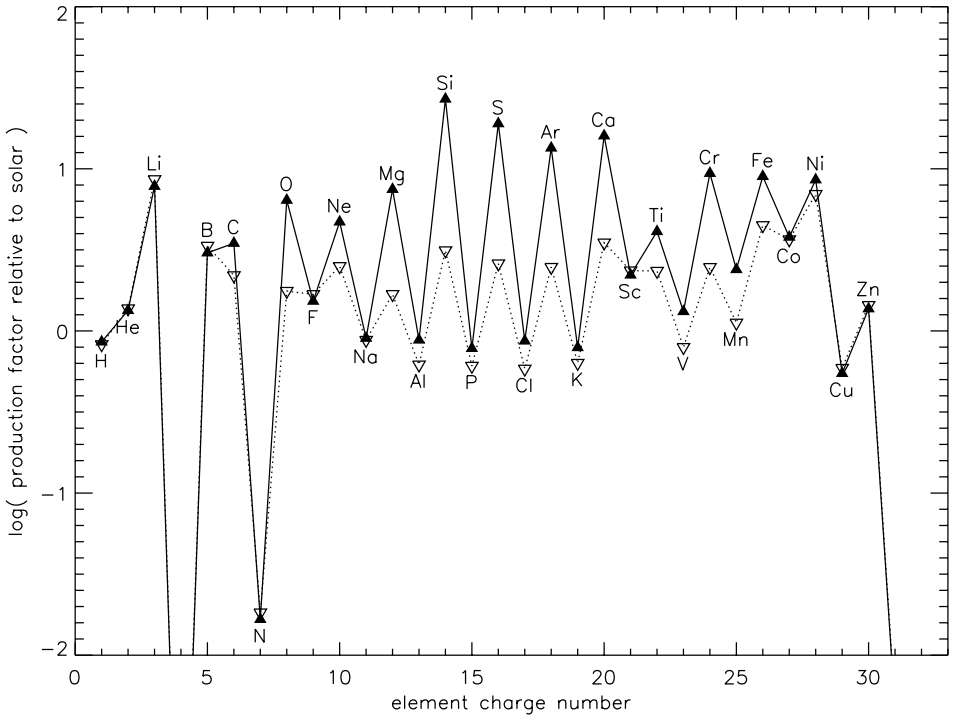

Figure 3: Production factors for massive stars ($12-40\,\mathrm{M}_\odot$; *dotted line* and *open triangles*) integrated over IMF and compared with solar abundances as a function of element charge number. The yields are taken from [11] and in this plot we use the low explosion energy primordial models of the "A" series, Z12A, Z15A, ... The *solid line* and *filled triangles*) give the same integration but also including exploding very massive stars ($\sim 140-260\,\mathrm{M}_\odot$). In the mass range $40-100\,\mathrm{M}_\odot$ essentially the whole helium core falls into a black hole, ejecting only the unprocessed envelope. In the mass range $100-140\,\mathrm{M}_\odot$ some of the outer layers of the helium core may be ejected, adding to the carbon and oxygen yields and maybe a little to the neon and magnesium yields, but not to the heavier elements. The IMF is assumed Salpeter-like with an exponent of -1.5.

slope -1.5. Stars in the range ($40\ldots140\,\mathrm{M}_\odot$) are not expected to contribute to the nucleosynthesis of heavy elements. Also the combined yield still shows a strong odd-even effect which is strongest in the Si—Ca region, about one order of magnitude. The Si—Ca even charge elements are overproduce with respect to the iron group, while they are slightly underproduced if only the massive star yields are considered. The overproduction of Ni and the

underproduction of Cr relative to Fe disappear when the contribution from the very massive stars is added.

Finally we have to caution that the IMF in the first generation of stars is still very uncertain. It may have been very different from an Salpeter IMF assumed here, strongly affecting the population yields of Figures 2 and 3. For example, if the population of very massive stars had a steep cutoff at high masses, the production of then iron peak elements could be strongly suppressed. In case the IMF were peaked around $250\,M_\odot$ the production factor of Fe cold become even larger than that of Si. The overproduction of Si relative to O on the other hand seems very robust, provided very massive stars had a significant contribution to the beginning of stellar nucleosynthesis. However, one must keep in mind that very metal deficient stars might sample only a few – or even only one – of these giant element factories. Quite non-solar abundances could be possible for metallicity $[Z] < -3$.

If a subsequent generation of stars has formed solely form the debris of a very massive metal poor star, at the present, it is also not clear where in the Galaxy such stars may be found today. Ultra metal-poor halo stars currently under investigation might be the result of a later epoch where other source have already contributed.

Acknowledgments

We are grateful to Chris Fryer for discussions about Figure 1. This research was supported by the Scientific Discovery through Advanced Computing (SciDAC) Program of the DOE. DOE Grant No DE-FC02-01ER41176, the DOE ASCI/Alliances FLASH Center at the University of Chicago (B341495) and the Alexander von Humboldt-Stiftung (FLF-1065004).

References

[1] R.B. Larson, to be published in the ESA Special Publications Series (SP-445), edited by F. Favata, A. A. Kaas, and A. Wilson, astro-ph/9912539.

[2] T.G. Abel, G.L. Bryan, M.L. Norman, ApJ **540** (2000) 39

[3] K. Omukai, F. Palla, ApJL **561** (2001) L55.

[4] F. Nakamura, M. Umemura, ApJ **548** (2000) 19.

[5] R.-P. Kudritzki, Proceedings of the MPA/ESO Workshop on "The First Stars", eds. A. Weiss, T. G. Abel, V. Hill, Springer (2000) p. 127

[6] I. Baraffe, A. Heger, S.E. Woosley, ApJ **550** (2001) 890.

[7] J.R. Bond, W.D. Arnett, B.J. Carr, ApJ **280** (1984) 825.

[8] A. Heger, S.E. Woosley, ApJ **567** (2002) 532.

[9] A. Heger, S.E. Woosley, I. Baraffe, T. Abel, to appear in Proc. Lighthouses in the Universe, "ESO Astrophysics Symposia", Springer-Verlag (2002); astro-ph/0112059.

[10] C.L. Fryer, ApJ **522** (1999) 413.

[11] S.E. Woosley, T.A. Weaver, ApJS **101** 181 (1995).

[12] G.M. Fuller, S.E. Woosley, T.A. Weaver, ApJ **307** 675 (1986)

The chemical composition of the ultra metal poor stars

A. Chieffi[1], *M. Limongi*[2]

[1] *Istituto di Astrofisica Spaziale e Fisica Cosmica (CNR), Via Fosso del Cavaliere, I-00133, Roma, Italy; achieffi@ias.rm.cnr.it*
[2] *Istituto Nazionale di AstroFisica - Osservatorio Astronomico di Roma, Via Frascati 33, I-00040, Monteporzio Catone, Italy; marco@mporzio.astro.it*

Extended Abstract

The stars of very low iron abundance ($[Fe/H] < -3$) that we observe today very probably formed in clouds enriched in metals by just the first stellar generation and hence they have preserved up to the present time the fingerprints of the ejecta of the first generation of stars which formed after the Big Bang. The most recent database of surface chemical abundances of ultra metal poor stars is the one published by [1]. Five stars are included in this database, namely CD -38^o245 ([Fe/H]=- 3.98), CS 22172-002 ([Fe/H]=-3.61), CS 22885-096 ([Fe/H]=-3.66), CD -24^o17504 ([Fe/H]=-3.37) and CS 22949-037 ([Fe/H]=- 3.79); abundances have been determined in these five stars for the following elements: C, Mg, Al, Si, Ca, Sc, Ti, Cr, Mn, Co and Ni. This rather wide set of elements include elements produced in many different nucleosynthetic environments: i.e., hydrostatic burnings (C, Mg and Al), explosive O burning and incomplete explosive Si burning (Si and Ca), incomplete explosive Si burning (Cr and Mn) and complete explosive Si burning (Sc, Ti, Co and Ni). Therefore a simultaneous fit of the elemental abundances we observe in these stars would largely improve our knowledge about either the stars which firstly populated the universe at early times (e.g. their mass function) and, more in general, the physics of the explosion of the core collapse supernovae (e.g. the location of the mass cut, the time delay between the collapse and the rejuvenation of the shock front, the degree of α rich freeze-out).

A comparison among the elemental abundances derived for these five stars shows that at least three of them have very similar [X/Fe], so that it is meaningful to define an average (AVG) star which is a sort of "template" star representing all three of them; the abundances of this AVG star are shown in Figure 1. The other two stars (CD -24^o17504 and CS 22949-037)

have some distinctive differences with respect to the other three and hence have not been taken into account in the definition of the AVG star.

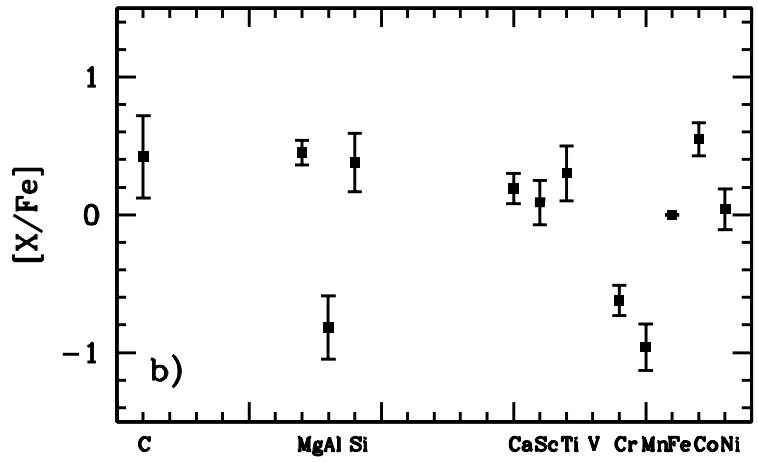

Figure 1: Chemical pattern of the AVG star; see text.

To fit the observed chemical composition of this AVG star we have computed new explosive yields; unfortunately the explosive yields produced by the core collapse supernovae strongly depend on the adopted $^{12}C(\alpha,\gamma)^{16}O$ reaction rate, as shown by, e.g., [2] and [3]. In order to bracket the range of possible values for this rate we computed a first set of models with the rate quoted by [4] and a second one with the rate quoted by [5] - but see also the contribution by Hammer in these proceedings. Each set of models consists of six masses (15, 20, 25, 35, 50 and 80 $M_{\odot}$): the evolution up to the core collapse has been followed with the FRANEC (Frascati RAphson Newton Evolutionary Code - rel. 4.84) with the same choices adopted in [6] while the passage of the shock wave through the mantle of the stars has been mimicked with the radiation dominated shock approximation.

We have also assumed, in all these fits, that these ultra metal poor stars formed in clouds polluted by just one core collapse supernova, as suggested e.g. by [7]: in this case their chemical composition would reflect the ejecta of one supernova and not an average of a more or less complex mass function.

The main results of this rather extended analysis are the following:

a) the fit to [Si/Fe] and [Ca/Fe] of these very metal poor stars favors a rather low $^{12}C(\alpha,\gamma)^{16}O$ reaction rate (if the border of the convective core is strictly determined by the Schwarzschild criterion);

b) a high $^{12}C(\alpha,\gamma)^{16}O$ rate would imply a low [Al/Mg] (< -1.2 dex)

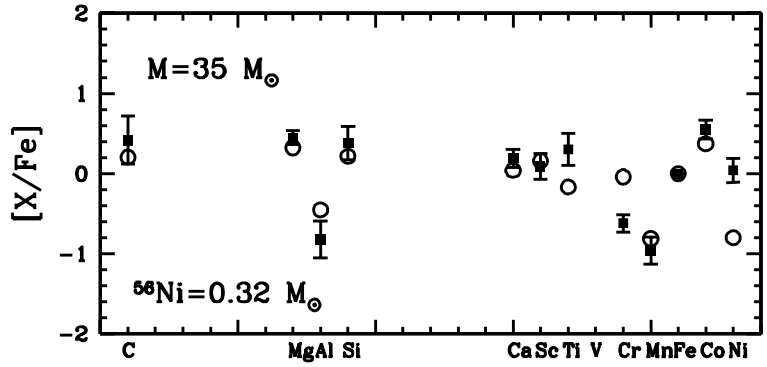

Figure 2: Comparison between the AVG star (*filled squares*) and the ejecta of the $35M_{\odot}$ (*open circles*) computed with the $^{12}C(\alpha,\gamma)^{16}O$ reaction rate quoted by [4]. The amount of ^{56}Ni ejected is also shown.

independently on the initial mass of the exploding star while a low rate would produce a low [Al/Mg] only for the most massive stellar model;

c) at variance with current beliefs that it is difficult to interpret the observed overabundance of [Co/Fe], we find that a rather low $^{12}C(\alpha,\gamma)^{16}O$ reaction rate would easily allow a good fit to the observed [Co/Fe];

d) our yields allow a reasonable fit to 8 out of the 11 available elemental abundances for a mass of the order of $35M_{\odot}$ as shown in Figure 2;

e) within the present grid of models it is not possible to find a good match of the remaining three elements, Ti, Cr and Ni (even for an arbitrary choice of the mass cut);

f) the adoption of other yields available in the literature does not improve the fit;

g) since no mass in our grid provides a satisfactory fit to these three elements, even an arbitrary choice of the initial mass function would not improve their fit.

The quest for the ultra metal poor stars is very active and we expect to increase shortly the number of stars for which a wide number of elemental abundances are determined. On the theoretical side we are already preparing a new set of much more refined models which we will present quite soon. Keep in touch....

References

[1] J.E. Norris, S.G. Ryan and T.C. Beers, Ap.J. 2001, **561** 1034

[2] T.A. Weaver and S.E. Woosley, Phys. Rep. 1993, **227** 65

[3] G. Imbriani, M. Limongi, L. Gialanella, F. Terrasi, O. Straniero and A. Chieffi, Ap.J. 2001, **558** 903

[4] G.R. Caughlan and W.A. Fowler, A.D.N.D.T. 1988, **40**, 283

[5] G.R. Caughlan, W.A. Fowler, M.J. Harris and B.A. Zimmerman, A.D.N.D.T. 1985, **32** 197

[6] M. Limongi, O. Straniero and A. Chieffi, ApJ.Supp. 2000, **129** 625

[7] J. Audouze and J. Silk, Ap.J. 1995, **451** L49

Implications of Cool Bottom Processes in Thermally Pulsing Phases of AGB Stars

M. Busso[1], *K.M. Nollett*[2], *G.J. Wasserburg*[3]

[1] *Department of Physics, University of Perugia, via Pascoli - Perugia (Italy)*
[2] *MC130-33, California Institute of Technology, Pasadena, CA91125 USA*
[3] *The Lunatic Asylum, Division of Geological and Planetary Sciences, California Institute of Technology, Pasadena, CA91125 USA*

Low mass stars populating the upper part of the Red Giant Branch (RGB) show several isotopic abundances of low and intermediate mass elements that deviate from the predictions of canonical stellar models. The best studied example is a ubiquitous enhancement of ^{13}C, occurring in stars below $M = 2M_{\odot}$ [1]; standard mixing induced by the downward expansion of envelope convection after core H burning, known as the *first dredge up*, is insufficient to account for the low observed ^{12}C/^{13}C ratios. A similar case occurs with the reduction in ^{18}O/^{16}O, both in stars [2] and in oxide grains of circumstellar origin [3],[4]. It is also reasonable to believe that the same processes involved in creating such abundance anomalies may help in reducing the yield of ^{3}He from Red Giants, so that it can become compatible with the moderate Galactic enhancement of this isotope [5].

Penetration of envelope material through regions in which the energy transport is radiative, occurring on long time scales, has been invoked to explain the above phenomena. This has been modeled either as a true mixing process, often ascribed to rotational shear [6] or, in a more general approach, as a low-efficiency circulation of matter reaching zones of relatively high temperature, not necessarily involving chemical mixing [7]. The first group of models is often referred to as "extra mixing", the second one as "cool bottom processing" (or CBP). Should these phenomena occur also later in the evolution, during the Asymptotic Giant Branch (AGB) phases, they would meet radiative regions characterized by temperatures remarkably higher than on the RGB, and this might permit proton captures to reach the Mg-Al nuclei, possibly contributing to the ^{26}Al synthesis in a more efficient way than otherwise achievable. It is also to be remembered that, when an AGB star reaches the thermally pulsing phase, the mixing mechanism known as *third dredge-up* (TDU) carries to the envelope newly produced carbon,

which fact ultimately induces the formation of a carbon star. Therefore, CBP at this time may also help to explain the isotopic shifts observed in circumstellar carbide grains: see e.g. [8].

In order to explore the above possibility, we constructed a model of CBP during the final phases (about 1 million years) of the star's lifetime, using stellar structures computed by [9], which model the evo1ving envelope composition of a $1.5 M_{\odot}$ star with solar initial composition. We then developed a "conveyor belt" model [10] in which material taken from the outer envelope circulates down through the thin radiative zone which separates the envelope from the H-burning shel1. It can thus reach a relatively high temperature, before returning to the envelope with a composition changed by nuclear reactions occurring along its path. In the approximation of no chemical mixing along the belt, the results of this model can be simply expressed as a function of two parameters: $\dot{M}$, the rate of mass transport through the radiative zone, and T_P, the maximum temperature to which the material is exposed. In this way we computed the resulting envelope composition as a function of time, finding that CBP can induce remarkable changes in the isotopic composition of elements up to Al. Here we present only a brief summary of those results; more extended discussion is to be found in [10].

Starting with oxygen isotopes, when CBP operates their ratios depend primarily on the amount of mass that has circulated and not on T_P, as long as *Log* T_P exceeds 7.6. Their final ratios will therefore be a function of the product of $\dot{M}$ and the time for which CBP is active, and this last is limited by the interpulse durations characterizing the TP-AGB phase. As ^{18}O is always destroyed, for $\dot{M}$ values in excess of 10^{-5} $M_{\odot}$/yr, ^{18}O/^{16}O may drop to 10^{-3} of its initial value. In contrast, for ^{17}O one has to determine the balance between production and destruction, and this translates into an equi1ibrium value determined solely by reaction rates and T_P. Depending on uncertainties in measured reaction rates and on when exactly in the stellar evolution CBP occurs, this equilibrium value falls in a range around 0.0011, with an uncertainty width of about 30%. For low circulation rates, CBP has litt1e effect on ^{17}O, whereas high $\dot{M}$ eventually brings the envelope to the H-burning equilibrium abundance. As a consequence of the above discussion, the oxygen isotopic mix induced by CBP tends to lie on a mixing line connecting the equilibrium H-burning ratios (point B in Figure 1) to the initial composition. In the figure, line a) shows the case of our 1.5 $M_{\odot}$ star, in which the initial envelope composition from which CBP starts is the one expected after the RGB phase; see e.g. [7], from which the figure is partly adapted. Occurrence of CBP in a more massive star would give rise (approximately) to a mixing line starting from a composition more evolved

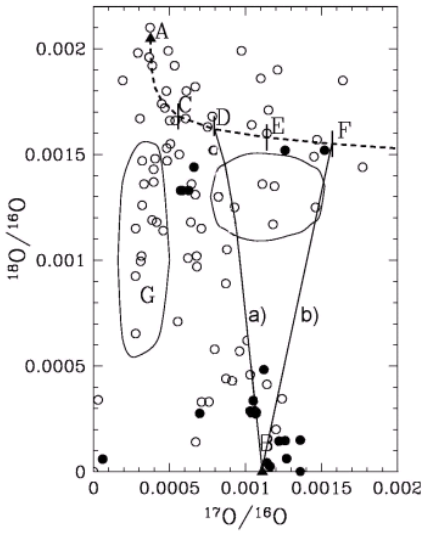

Figure 1: Permitted values of the oxygen isotopic mix in the stellar envelope, after CBP has occurred for a long time at temperatures in excess of $Log\, T_P = 7.44$, tend to be aligned along mixing lines connecting the RGB composition (D: 1.5 $M_\odot$ star – F: 1.8 $M_\odot$ star) to the end point B, having equilibrium H-burning abundances. The envelope composition after first dredge up is represented by the curve from C to F for different masses between 1.35 and 1.8 $M_\odot$. For illustration purposes CBP was computed here through a simplified semi-analytic approximation. The figure is adapted from [7]. Superimposed data points are from [4], and filled symbols refer to grains with $^{26}Al/^{27}Al$ ratios larger than 10^{-3}.

along the curve A-F, like e.g. line b) in the figure. This behavior also tells that the plot area that can be accounted for by CBP compositions has a limiting border on its left, made by a mixing line connecting the solar composition A to B. Hence, region G cannot be reached by CBP in a solar metallicity star, and at least some of the grains in that zone may reflect supernova nucleosynthesis or previous phases of Galactic evolution [11].

CBP can also produce much more ^{26}Al (orders of magnitude) than in standard stel1ar models. Contrary to the case of oxygen isotopes, the amount of Al production is independent of $\dot{M}$, and is only a function of the maximum temperature at which CBP operates. Levels of $^{26}Al/^{27}Al$ up

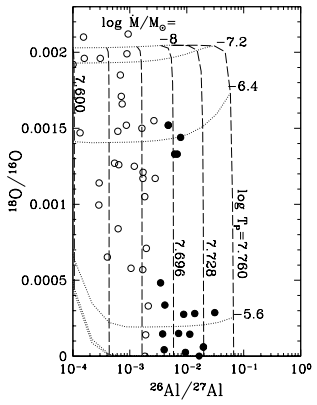

Figure 2: Final envelope compositions in oxygen and Al isotopes after CBP, as computed for different constant values of $\dot{M}$ (dotted lines) and of *Log* T_P (dashed lines). $\dot{M}$ varies between 10^{-8} and 10^{-4} $M_\odot$/yr, *Log* T_P varies between 7.60 and 7.76 in equal steps. The same semi-analytic model and the same reference for data points as in Figure 1 were used.

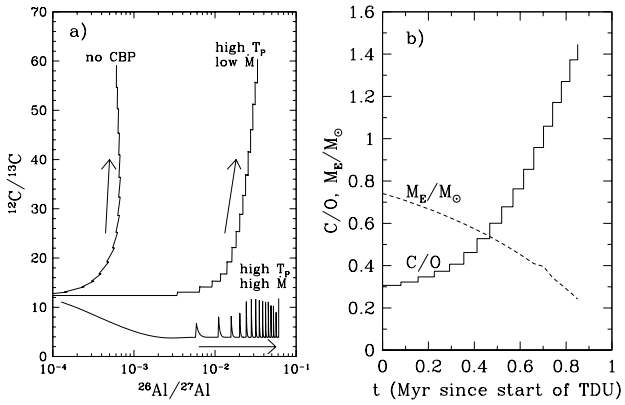

Figure 3: Envelope enrichment in carbon and aluminum isotopes, computed through a full numerical CBP code. Panel a) shows three results, obtained for TDU only (no CBP), for $\dot{M} = 6.3{\times}10^{-8}$ $M_\odot$/yr and *Log* $T_P = 7.744$ (case high T_P, low $\dot{M}$), and for $\dot{M} = 10^{-4}$ $M_\odot$/yr and *Log* $T_P = 7.744$ (case high T_P, high $\dot{M}$). The last case shows how for high circulation rates C-star formation is prevented. The sudden jumps in abundances are due to TDU episodes. Panel b) shows the general evolution of the C/O ratio and of the envelope mass with time, when CBP is not present.

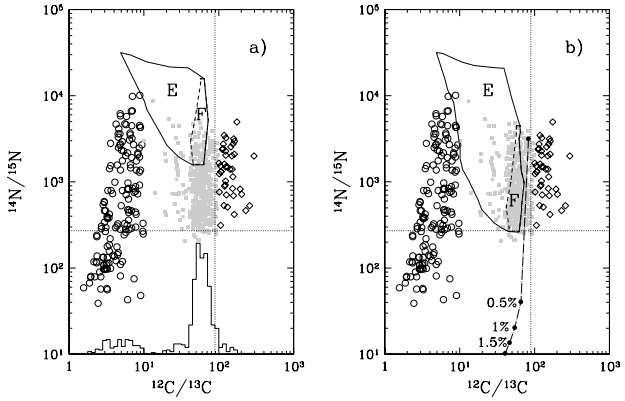

Figure 4: Carbon and nitrogen isotopic compositions of SiC grains, as compiled by [8] (grey symbols: mainstream grains, circles: A+B grains; rhombs: Y grains). Panel a) assumes solar nitrogen abundances at stellar birth. Here region E covers the whole area of possible CBP compositions, while region F is restricted to $^{26}Al/^{27}Al$ ratios larger than 10^{-3}. Panel b) shows a case in which the initial $^{14}N/^{15}N$ ratio is 70, so that a nearly solar ratio (270) is reached only at the AGB stage. The dash-dotted line shows compositions reached after mixing with given percentages of nova material, rich in ^{15}N.

to 0.1, covering the whole range found in circumstellar grains, can thus be explained, for a range of *Log* T_P of 7.6 – 7.76 (see Figure 2). The different ways in which ^{26}Al production and the shifts in the O iotopic mix are achieved lead us to predict the absence of a correlation between the two phenomena.

During the last Ma of stellar evolution, while the $^{26}Al/^{27}Al$ ratio increases due to CBP, the star also experiences He shell flashes and subsequent episodes of dredge-up ("third dredge-up"), which bring to the surface newly synthesized ^{12}C. In the absence of CBP, this results in the ratio C/O reaching values ≥ 1. A carbon star is formed, and its circumstellar environment becomes rich in carbide grains. TDU alone would also drive up $^{12}C/^{13}C$ in the envelope, from 12-15 after the RGB phase, up to about 60 (in a 1.5 $M_\odot$ star). The effect of CBP is to lower both C/O and $^{12}C/^{13}C$, as it produces (and destroys) ^{13}C via $^{12}C(p,\gamma)^{13}N(\beta^+\nu)^{13}C(p,\gamma)^{14}N$.

The degree of the above processing depends on both T_P and $\dot{M}$. In particular, extensive mass circulation implies efficient destruction of ^{12}C (and production of ^{13}C), and would prevent formation of a carbon star. If T_P is sufficiently high, we can in this way obtain O-rich envelopes, rich in ^{26}Al and

^{13}C. In them also ^{14}N would be enhanced (up to a factor of 10), thus contributing to the explanation of the high nitrogen enhancement observed in certain classes of planetary nebulae [12]. If, on the contrary, mass circulation is small, ^{12}C can be only marginally affected, and ^{26}Al-rich C stars can be formed (see Figure 3). This also leads us to suggest that many SiC grains of circumstellar origin, rich in ^{26}Al and belonging to the mainstream group (see e.g. [8]) may derive from low mass carbon stars, having experienced CBP not only along their RGB, but also during the subsequent AGB stages. The observed range of their ^{14}N/^{15}N ratios then introduces new constraints (see Figure 4). In particular, observations of ^{14}N/^{15}N values below 10^3 can be made compatible with CBP in advanced evolutionary phases (and with first dredge-up) only if the mainstream grains originated in stars with a spread of subsolar initial ^{14}N/^{15}N. The direction of the Galactic evolution of this ratio is unclear, but observations of the interstellar medium of our Galaxy and of the Magellanic Clouds [13, 14] give some support to an increase with metallicity. As figure 4 shows, there is instead no way to explain A or B grains through CBP in AGB stars. Even admixture of nova material rich in ^{15}N does not help in this purpose.

Acknowledgements

We thank O. Straniero, A. Chieffi and M. Limongi for use of unpublished details of models run by [8]. Work supported by NASA grant NAG5-10293, Caltech Division Contrib. 8781-1092, MURST contract cofin2000.

References

[1] Gilroy, K.K. & Brown, J.A. Ap.J. **371** (1991), 578.

[2] Kahane et al., A.&A. **256** (1992), 235.

[3] Nittler, L.R. et al. Ap.J. **483** (1997), 475.

[4] Choi, B.-G. et al. Science **282** (1999), 1284.

[5] Gloeckler, J. & Gleiss, G. Space Sci. Rev. **84** (1998), 239.

[6] Charbonnel, C. Ap.J. **453** (1995), L41.

[7] Wasserburg, G.J., et al. Ap.J. **447** (1995), L37.

[8] Amari, S. et al. ApJ **546** (2001), 248.

[9] Straniero et al. ApJ **478** (1997), 332.

[10] Nollett, K.M. et al. ApJ (submitted)

[11] Nittler, L.R., & Cowsik, R., Met. & planet. Sci. **31** (1996), A100.

[12] Péquinot et al. A&A **361** (2000), L1.

[13] Chin, Y.-N. et al. ApJ **512** (1999), L143.

[14] Wilson, T.L. & Rood, R.T. Ann Rev. Astron. Astrophys. **32** (1994), 191.

The Effect of Rotation on the Evolution of CO WDs Accreting CO-rich Matter

L. Piersanti[1,2], *S. Gagliardi*[2,3] & *A. Tornambé*[2]

[1] *Università degli Studi di Napoli "Federico II"*
[2] *I.N.A.F. - Osservatorio Astronomico di Teramo*
[3] *Università degli Studi de L'Aquila*

The Double Degenerate (DD) scenario has been regarded as not promising as SNe Ia progenitor for two reasons: 1) the observational search of DD systems with the right orbital parameters has provided negative results (see [1], [2], but also [3] for a positive signature); 2) on the theoretical point of view, if a DD system suitable as SN Ia progenitor does exist, the less massive component of the binary system disrupts in an accretion disk around the more massive one; therefore it can be argued that the effective accretion rate is expected to be very high (see [4], [5], [6]), giving rise to an off-center C-burning ignition before the accreting WD could attain the Chandrasekhar mass limit (M_{Ch} - see [7], [8], [9]). This result is a direct consequence of the fact that the accreted matter delivers accretional energy on the surface of the CO WD more rapidly than it could be transferred inward via thermal diffusion so that the physical conditions suitable for C-burning ignition are attained in the accreted layers.

It is important to remark that the extant numerical analysis has been performed by neglecting at all the lifting effect of rotation in the evolution of accreting models. In general this is a good assumption since the observational evidence suggests that stars are very slow rotators ($10^{-6} < \omega < 10^{-3}$ rad/s), but it is no longer valid for WDs in close binary systems because, in this case, the synchronization of the orbits occurs on a time scale very small compared to the evolution of the system itself; this means that at the merging time the angular velocity of each WD is very high (~ 0.1 rad/s) so that rotation has to be accounted for in modeling the thermal evolution of CO WDs accreting CO-rich matter directly.

As it is well known, rotating structures are cooler and less dense with respect to non-rotating ones: this implies that for a fixed value of the accretion rate the thermal diffusion time scale of the accreting structure decreases increasing the angular velocity, so that a huger thermal energy excess is localized in the accreted layers (see left panel in Fig. 1). As a consequence rotating models have to expand to higher dimensions with respect to the

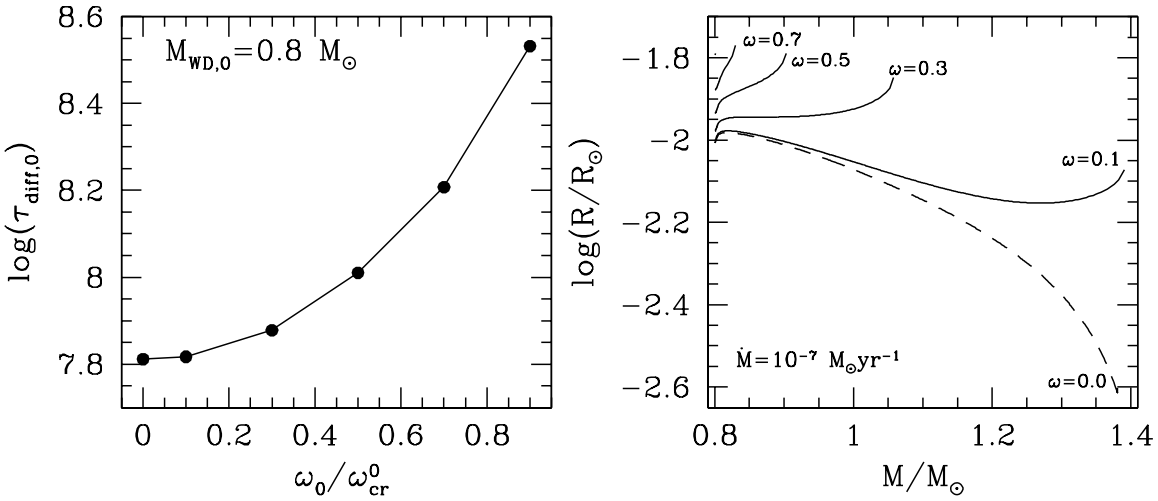

Figure 1: Left Panel: Initial value of the thermal diffusion time scale (τ_{diff} - in yr) as a function of the initial angular velocity (in units of $\omega^0_{cr} = 0.625$ rad/s). Right panel: Evolution of the surface radius for models rotating with different initial angular velocities as labeled (in units of ω^0_{cr}) and with accretion rate $10^{-7} M_\odot yr^{-1}$. For comparison, the corresponding standard model is also shown (dashed line).

standard case in the attempt to dissipate the extra-energy injected by the accreted matter (see right panel in Fig. 1). Such an expansion induces the decrease of the surface value of the critical angular velocity so that the accreting structure can become gravitationally unbound. We find that models with high values of both accretion rate and initial angular velocity undergo the Roche instability when a small amount of mass has been accreted ($\Delta M_{acc} \sim 0.1 M_\odot$), while models with low values of both $\dot{M}$ and ω_0 become gravitationally unbound when the total mass is approaching $\sim 1.4 M_\odot$.

In particular, for what concerns the latter models (low values of both $\dot{M}$ and ω_0), we find that when the Roche instability occurs the rotational energy of the WD is one tenth of the gravitational energy and in addition the angular velocity is of the order of 1 rad/s: the first occurrence determines the deformation of the WD into an elliptical configuration and gravitational wave radiation (GWR) is emitted (see [10]), whereas the second occurrence ensures that the intensity of GWR is high enough to produce the reduction of rotational energy and angular momentum, playing an important role in the evolution of the accreting WD (see [11]). The lose of rotational en-

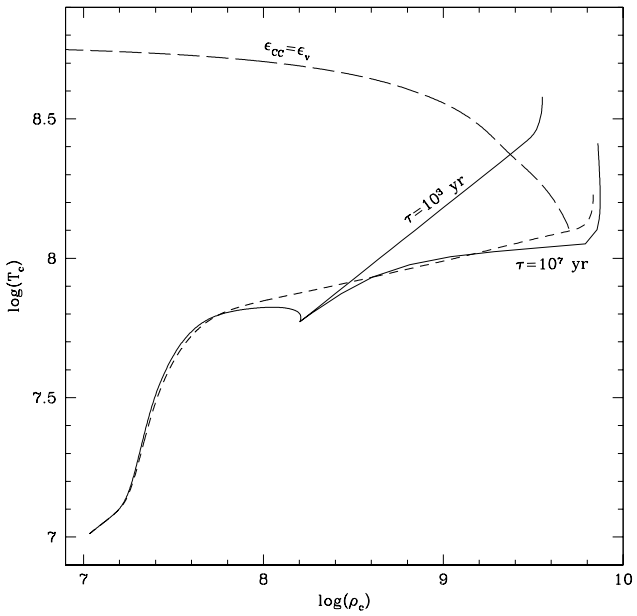

Figure 2: Evolution in the $\rho - T$ plane of the center of a CO WD accreting CO-rich matter directly at $\dot{M} = 10^{-8} M_\odot yr^{-1}$ and with initial angular velocity $\omega_0 = 0.07$ rad/s. The evolution during the braking phase is also shown for two different values of the braking time scale, as labeled. For comparison the evolution of the standard non-rotating model accreting matter at the same accretion rate is also reported (dashed line).

ergy and angular momentum determines the reduction of the local value of the centrifugal force in a way that the WD experiences an homologous compression which heats-up the whole structure.

We find that for realistic values of the time scale for the energy loses via GWR (in the range $10^3 \div 10^7$ yr - see [10], [11]), the braking structure attains the physical conditions for C-burning ignition at the center. It has to be remarked that different braking efficiencies, *i.e.* different braking time scales, produce just a small variation of the ignition conditions along the ignition curve (see Fig. 2).

The accreting models with high values of both $\dot{M}$ and ω_0 become gravitationally unbound after a small amount of matter has been accreted ($\Delta M \sim 0.1 M_\odot$). In this case the occurrence of the Roche instability does not mean that the accretion process comes to a halt, but only that matter has to be accreted at a lower accretion rate, in such a way to guarantee that the

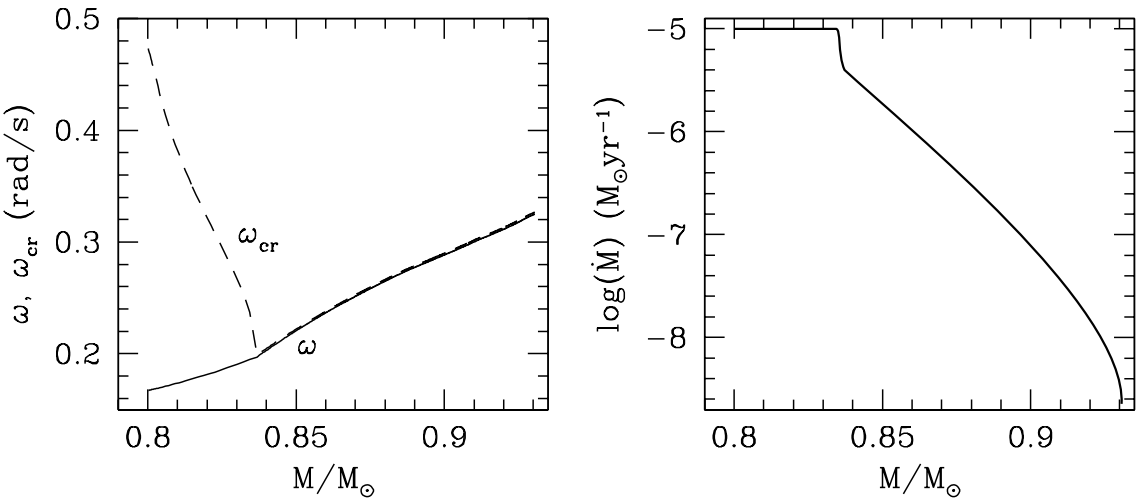

Figure 3: Evolution of the angular velocity compared to the critical angular velocity (left panel) and of the accretion rate (right panel) for a $0.8M_{\odot}$ CO WD rotating with initial angular velocity $\omega_0 = 0.17$ rad/s and initial accretion rate $\dot{M} = 10^{-5}M_{\odot}yr^{-1}$.

centrifugal force does not become greater than the gravitational one. The decrease of the effective accretion rate produced by rotation makes the evolutionary time longer and, as a consequence, the energy excess in the external layers can be efficiently transferred inward so that the WD becomes isothermal.

As it can be noticed in Fig. 3, when the accreting model is going to become gravitationally unbound, the accretion rate decreases in such a way to allow the accreting structure to accept mass. This means that rotation acts as a fine tuning mechanism of the accretion process in a way that the off-center C-burning ignition is prevented and the growth in mass of the CO WD does not come to a halt, the total mass of the accreting structure being limited only by the total mass of the binary system. The other interesting point to remark is that, due to the deposition of angular momentum by the accreted matter, the angular velocity of the WD continues to increase and, when it will be of the order of 1 rad/s the energy loses via GWR will produce the braking of the structure and the homologous compression of the WD as in the case previously discussed. We argue that the efficient braking of the rotating structure will occur when the total mass of the CO WD will be of the order of $1.4M_{\odot}$. The further evolution will produce the physical conditions suitable for central C-burning ignition and the final outcome will

be a SN Ia event.

As a conclusion, DD systems can represent the right solution to the problem of the stellar progenitor of SNe Ia if the lifting effect of rotation is properly taken into account in modeling the thermal evolution of CO WDs accreting CO-rich matter directly as a consequence of a merging process in binary systems.

References

[1] Bragaglia, A., Greggio, L.Renzini, A. & D'Odorico, S., ApJ Lett., **365** (1990) L13

[2] Saffer, R.A., Livio., M. & Yungelson, L.R., ApJ, **502** (1998) 394

[3] Koen, C., Orosz, J.A. Wade, R.A., MNRAS, **200** (1998) 695

[4] Benz, W., Cameron, A.G.W., Press, W.H. & Bowers, R.L., Ap.J, **348** (1990) 647

[5] Rasio, F.A. & Shapiro, S.L., ApJ, **438** (1995) 887

[6] Mochkovitch, R., Guerrero, J. & Segretain, L., 1997, in *Thermonuclear Supernovae*, Eds. P. Ruiz-Lapuente, R. Canal & J. Isern, Kluwer, Dordrecht, p. 187

[7] Nomoto, K.I. & Iben, I.Jr, ApJ, **297** (1985) 531

[8] Saio, H. & Nomoto, K.I., A&A Lett., **150** (1985) L21

[9] Saio, H. & Nomoto, K.I., ApJ, **502** (1998) 394

[10] Shapiro, S.L. & Teukolsky, in *Black Holes, White Dwarfs and Neutron Stars* (1983) Wiley, New York

[11] Ma, F., astro-ph/0202040

Cosmo chronometers and nuclear reactions

O. Straniero[1], *I. Dominguez*[2], *M. Limongi*[3], *A. Chieffi*[4], *G. Imbriani*[1,5], *P. Prada Moroni*[1,6], *L. Piersanti*[1], *and on behalf of the LUNA collaboration*

[1] *Osservatorio Astronomico di Collurania, Italy*
[2] *Dpto. de Fisica Teorica y del Cosmos, Univ. de Granada, Spain*
[3] *Osservatorio Astronomico di Roma, Italy*
[4] *Istituto di Astrofisica Spaziale (CNR), Italy*
[5] *Laboratori Nazionali Gran Sasso (INFN), Italy*
[6] *Dipartimento di Fisica Università di Pisa, Italy*

The age of the various components of the Milky Way are commonly derived from stellar chronometers. Since nuclear reactions are responsible for chemical modifications occurring in stellar interiors and supplies most of the energy irradiated from the stellar surface, the estimated stellar lifetime relays on accurate measurements of thermonuclear reaction rates. In the last few years, many efforts were spent in improving these measurements at low energy, as close as possible to the Gamow peak that represents the relevant energy at which nuclear reactions occur in stars. This is a mandatory requirement for the calibration of stellar ages. By considering two widely adopted stellar chronometers, we have investigated the present level of uncertainty due to the experimental errors of the key nuclear cross sections.

Turn off luminosity and Age

Stellar clusters are groups of stars with similar ages and chemical compositions, but different masses. It was early recognized that the older the cluster, the fainter the tip of the main sequence in the observed color-magnitude diagrams. This occurs because the H-burning is faster in massive stars, so that the main sequence of a stellar cluster becomes progressively depopulated of the brightest (more massive) stars. For this reason, the turn off luminosity, namely the luminosity of the bluest point of the main sequence, is an important age indicator for Globular Clusters, which are among the oldest stellar components of the Galaxy. The method used to date these stellar systems requires the knowledge of the distance, the light extinction along the line of sight and the original chemical composition of the stars. The measure of these parameters is matter for astronomers. In addition we need a reliable theoretical calibration of the age-turnoff luminosity relation. This relays on

our knowledge of the physical processes of energy generation and transport taking place in H-burning low mass stars. An adequate description of the thermodynamic of stellar matter is also required. Finally we have to consider any mechanism capable to modify the internal chemical stratification (nuclear burning, convective mixing, rotational induced mixing, microscopic diffusion and the like). The progress made in this field in the last 30 years is illustrated in figure 1. Theoretical isochrones for GC firstly appeared at

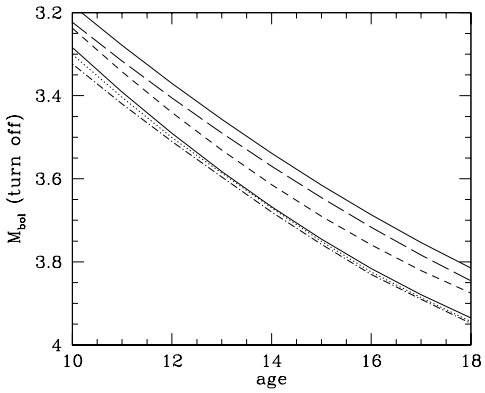

Figure 1: Turn off luminosity-age relations for Z=0.0001: [7] light solid, [4] long dashed, [17] short dashed, [15] heavy solid, [6] dotted, [18] dot dashed

the beginning of the Seventies ([7], [4]). Significative improvements were the paper by [17], in which several inputs physics were revised, and the one by [15], firstly including electrostatic corrections in the equation of state. This last result has been recently confirmed [6], using the more refined OPAL EOS. As a consequence of these improvements, an about 15% reduction of the predicted GC ages has been obtained. At the end of the Eighties and during the Nineties it was progressively realized that the α-elements (O, Ne, Mg, Si, Ca, etc.) are overabundant, with respect to iron in Pop II stars. The effects on the age were deeply studied by [14] and substantially confirmed by [18]. Another important improvement was the inclusion of microscopic diffusion that induces a slow modification of the chemical stratification ([11], [5],[16],[3]). As a consequence a further reduction of the estimated GC ages (about 10%) was found.

By comparing our latest theoretical isochrones [16] with the HR diagrams reported in the database provided by [12], we have obtained ages for 35 GCs of the Milky Way. The distances have been derived from the luminosity of the observed horizontal branches and the chemical compositions have been taken from [2]. The bulk of the GCs is coeval (within a bona fide error

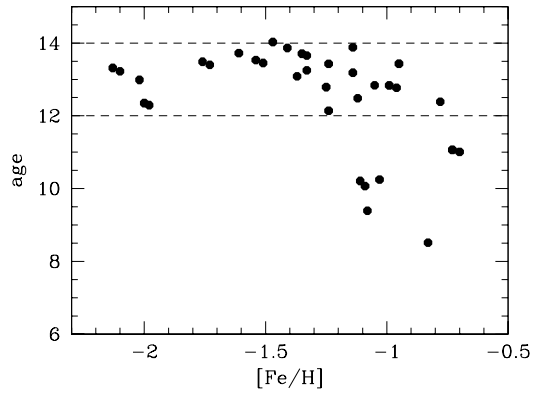

Figure 2: Ages (in Gyr) versus metallicity for 35 Galactic Globular Clusters.

of ±1 Gyr), with interesting exceptions at large metallicity ([Fe/H]>1.2). Once the five Clusters whose age differs by more than 2 Gyr from that of M15 are excluded, an average age of 12.95±0.65 Gyr is found. Note that the quoted error is just the standard deviation and it does not include possible systematic errors due to the adopted distance scale.

This result must be compared with the age of the Universe, as derived from the proposed cosmological models. According to the recent discovery that the geometry of the universe is Euclidean and the space is flat, as demonstrated in detailed measurements of the temperature fluctuations of cosmic microwave background (MAXIMA and BOOMERANG), and taking into account the high redshift supernovae measurements, proving that the matter density $\Omega_M = 0.28$ ($^{+0.08}_{-0.09}$ 1 σ statistical error) [10], one find an age of the Universe of 14.9±1 Gyr (by assuming H_0=63 Km sec^{-1} Mpc^{-1}). Taking into account the time elapsed from the Big Bang and the formation of the galactic halo (more or less 1 Gyr), this age for the Universe is in very good agreement with the age presently estimated for the Galactic Globular Cluster system. However, by taking the latest determination of H_0 (namely 72±8 Km sec^{-1} Mpc^{-1}, [9]), a younger Universe is found, about 13 Gyr. This is only marginally compatible with the ages for the oldest Globulars. A better agreement could be found if $H_O \leq$67 Km sec^{-1} Mpc^{-1}, or $\Omega_{matter} \leq$ 0.23. Note that both these values are inside the respective 1 σ experimental errors.

But how reliable is the calibration of the age/luminosity relation for globular cluster turn off stars? One should note that during most of its life, a low mass star burns H in the center via the pp chain. However, when the central H mass fraction reduces down to ∼0.1, the nuclear energy realized

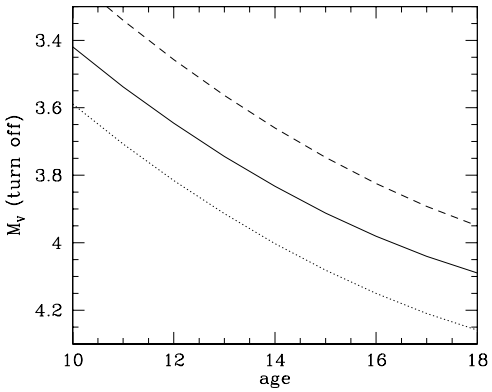

Figure 3: Turn off V magnitude versus age (Gyr) under different assumptions for the ^{14}N(p,γ)^{15}O reaction: NACRE (solid curve), NACRE x 5 (dotted), NACRE / 5 (dashed).

by the H-burning becomes insufficient and the stellar core must contract to extract some energy from its gravitational field. Then, the central temperature (and the density) increases and the H-burning switches from the pp-chain to the CNO-burning. Thus, the departure from the MS is powered by the onset of the CNO-burning, whose bottleneck is the ^{14}N(p,γ)^{15}O reaction. The luminosity of the turnoff depends on the rate of this key reaction: the larger the rate, the fainter the turnoff. On the other hand, the stellar lifetime, which is mainly controlled by the rate of the pp reaction, remains unchanged. In figure 3 we report the variation of the calibrated age as obtained by varying of a factor 5 the rate of the ^{14}N(p,γ)^{15}O. The minimum energy explored in nuclear physics laboratories is $\sim$200 KeV, which is well above the energies of interest for the stellar CNO-burning ($\sim 20 - 80$ KeV), Therefore, the reaction rate used in stellar model computations is largely extrapolated in a region were the resonant structure of the ^{15}O compound nucleus is particularly complex. According to [1], the low energy S factor is dominated by the transitions to the ground state of the ^{15}O and to the sub-threshold resonance located at 6.79 MeV (-0.504 MeV in the center of mass). The rate reported by the popular compilations (Caughlan & Fowler 1988 or NACRE) is based on this data analysis. However, a recent re-analysis performed by [13] reveals that the contribution of the transitions to the ground state of the ^{15}O is significantly smaller then previously reported (about 20 time smaller). As a consequence, the total reaction rate of the ^{14}N(p,γ)^{15}O should be reduced (of about a factor 2). Such a big uncertainty demands a measurement of the astrophysical factor at energy as close as possible to

the effective stellar energy. The LUNA collaboration (an acronym of the Laboratory for Underground Nuclear Astrophysics, operating at the LNGS of Assergi, Italy) has started a new investigation with a 400 KeV accelerator devoted to the low energy measure of the rate of this key reaction (see the contribution presented by Alba Formicola in this proceeding).

Cooling of White Dwarfs

The White Dwarf luminosity is another important age indicator for old stellar populations. White Dwarfs are dead stars, i.e. no energy is produced via nuclear burning and the pressure of degenerate electrons prevents the core contraction. Thus the energy irradiated from the surface is supplied by the thermal reservoir accumulated by the progenitor during its life. The heat consumption causes a drop of the temperature and, in turn, a decrease of the luminosity. Therefore, it exists a luminosity-age relation of WDs, which can be calibrated by means of accurate theoretical cooling sequences. Here we emphasize that the cooling time depends, among the other things, on the internal chemical composition of the WD: the larger the mean molecular weight, the faster the cooling. The majority of the WDs are post-AGB stars. They are made with the ashes of the He-burning, essentially C and O. Figure 4a show the luminosity-age relation for two 0.6 $M_\odot$ WD models, having different internal amount of C and O. Figure 4b shows the corresponding chemical stratification.

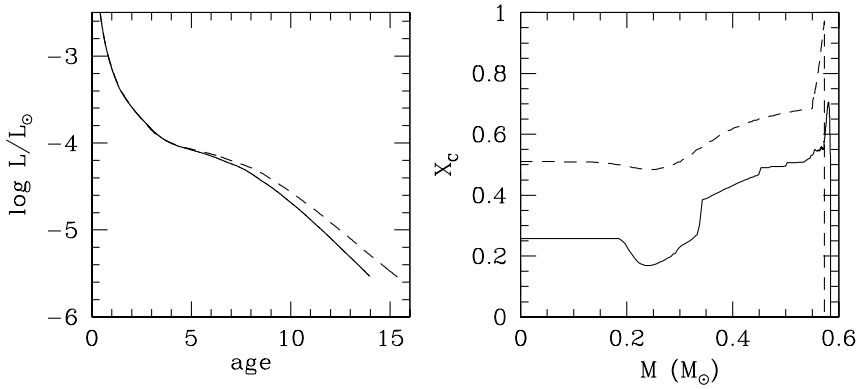

Figure 4: a) Cooling sequences for two 0.6 $M_\odot$ WD. The dashed curve has been obtained by using an "low" rate of the $^{12}C(\alpha,\gamma)^{16}O$ reaction, while the solid corresponds to a "high" rate. b) Carbon internal profiles for the two models in a).

The most internal (flat) region, was left by the central He-burning. Its extension is determined by the maximum size attained by the convective core during this phase. The external region was builded up during the AGB by the advancing He-burning shell. In general, the amount of carbon left in the WD interior depends on the competition between the 3α and the $^{12}C(\alpha,\gamma)^{16}O$ reactions. The rate of the latter is rather uncertain (see the contribution presented by Hammer in this meeting). As extensively discussed by [8], the central amount of C (and O) of a WD also depends on the strength of the convective mixing occurred in the core of the He-burning progenitor. Thus, any extra-mixing taking place during the final part of the central He-burning, like Breathing Pulses, affects the predicted final abundances. In synthesis, one should also account for the uncertainties in the convective theory when discussing the composition of WDs.

Acknowledgements

This work has been partially supported by the Italian grant COFIN2000.

References

[1] Angulo & Descouvemont, 2001, Nucl. Phys. A, 690, 755

[2] Carretta, E. & Gratton, R., 1997, AAS, 121,95.

[3] Castellani et al. 1997, AA, 322,801.

[4] Ciardullo, R.B. & Demarque, P., 1977, Transactions of the Astronomical Observatory of Yale University, (New Haven: Astronomical Observatory).

[5] Chaboyer et al. 1992, 388,372

[6] Chaboyer, B. & Kim, Y., 1995, APJ, 454,767

[7] Iben, I.J., 1971, PASP, 83,697.

[8] Imbriani et al. 2001, APJ, 558,903.

[9] Freedman et al. 2001, APJ, 553,47.

[10] Perlmutter et al. 1999, APJ, 517,565.

[11] Proffit & Vandenberg, 1991, APJS 77,473

[12] Rosemberg et al., 1999, AJ, 118,2036.

[13] Schroder et al., 1987, Nucl. Phys. A, 467, 240

[14] Salaris, M., Chieffi, A. & Straniero, O., 1993, APJ, 414,580.

[15] Straniero, O. & Chieffi, A., 1991, APJS, 76,525.

[16] Straniero, O., Chieffi, A. & Limongi, M., 1997, APJS, 490,425.

[17] Vandenberg, D.A. & Bell, R.A., 1985 APJS, 58,561.

[18] Vandenberg, D.A., Bolte, M. & Stetson, P.B., 1996, ARAA, 34,461

Effects of Rotation on SN Ia Progenitor Models

S.-C. Yoon, N. Langer

Astronomical Institute, Utrecht University, Princetonplein 5, NL-3584 CC, Utrecht, The Netherlands

6.1 Introduction

Although there is a general agreement that the exploding star in a Type Ia supernova (SN Ia) is an accreting CO white dwarf in a close binary system, the exact nature of the progenitor system is still uncertain. Classical studies on mass accreting white dwarfs have assumed spherical symmetry. However, in close binary systems which contain a white dwarf, the matter accreted onto the white dwarf carries angular momentum and spins it up (e.g. [1], [2]). The fast rotation of white dwarfs in CVs [3] supports the idea that white dwarfs are indeed spun up by mass accretion. The recent evidence for asphericity of SN1999by [4] may also suggest a rapidly rotating progenitor for this sub-luminous Type Ia supernova.

If a white dwarf is spun up by mass accretion, the presence of differential rotation in the white dwarf is inevitable and the resulting hydrodynamic instabilities may induce chemical mixing between the accreted matter and the white dwarf core. Futhermore, the centrifugal support may increase the mass required to ignite the degenerate core or shell of a rotating white dwarfs. To investigate these effects of rotation for SN Ia progenitors, we have performed numerical simulations of helium accreting CO white dwarf.

The numerical models have been computed with a hydrodynamic stellar evolution code in which we include the effect of the centrifugal force on the stellar structure and rotation-induced transport of angular momentum and chemical species [5]. We accrete helium rich matter at constant rates onto white dwarfs with initial masses of $1.0\mathrm{M}_{\odot}$ and $0.6\mathrm{M}_{\odot}$. We chose two different accretion rates to investigate the effects of rotation both in the Chandrasekhar mass single degenerate scenario ($\dot{M} = 10^{-6}\mathrm{M}_{\odot}\mathrm{yr}^{-1}$) and in sub-Chandrasekhar mass models ($\dot{M} = 10^{-8}\mathrm{M}_{\odot}\mathrm{yr}^{-1}$) for the SN Ia progenitors. The initial equatorial rotation velocity of white dwarf is set to $1\mathrm{kms}^{-1}$ and the specific angular momentum of the accreted matter is assumed to have the Keplerian value at the white dwarf equator.

6.2 Results

Figure 1a shows the nuclear luminosity ($L_{\rm nuc} = \int \epsilon_{\rm nuc} dM_r$, $\epsilon_{\rm nuc}$ being the nuclear energy generation rate.) due to the helium burning as function of the total mass of white dwarf for the model with $\dot{M} = 10^{-6}{\rm M}_\odot{\rm yr}^{-1}$ and $M_{\rm i} = 1.0{\rm M}_\odot$. In the non-rotating case, after steady helium shell burning until $M \simeq 1.04{\rm M}_\odot$, the white dwarf begins to experience thermal pulses, since the helium shell burning becomes unstable (e.g. [6]). When rotation is considered, the white dwarf accretes matter up to $\simeq 1.48{\rm M}_\odot$ without thermal pulses. The stability of shell burning is determined mainly by two factors: The more degenerate the gas is and the thinner the shell is, the more unstable does the shell burning become [7]. Figure 1b shows that rotationally induced chemical mixing extends the helium layer into the interior of the white dwarf. This effect widens the helium burning shell. The degree of degeneracy is also lowered in the burning layer compared to the non-rotating case, due to the centrifugal force (see [8] for more details). Both effects together provide thermal stability for the helium shell in the rotating model. Furthermore, the mixing of α particles into ^{12}C-rich layers makes the $^{12}{\rm C}(\alpha,\gamma)^{16}{\rm O}$ reaction more active than in the non-rotating model, rendering the C/O ratio lower in the rotating one (Fig. 1b).

The model with $\dot{M} = 10^{-8}{\rm M}_\odot{\rm yr}^{-1}$ and $M_{\rm i} = 0.6{\rm M}_\odot$ gives an example of the so-called sub-Chandrasekhar mass progenitor type for SNe Ia (e.g. [9]). In Figure 2, the chemical structure in the white dwarf is shown when $M_{\rm WD} \simeq 0.99{\rm M}_\odot$. In this model, the degenerate helium shell builds up above the CO core of the white dwarf until helium ignition occurs near $M_{\rm r} \simeq 0.6{\rm M}_\odot$, induced by the $^{14}{\rm N}({\rm e}^-,\nu)^{14}{\rm C}(\alpha,\gamma)^{18}{\rm O}$ reaction when the white dwarf mass reaches $0.99{\rm M}_\odot$. Our model shows that the accreted helium is mixed into the deep interior of the white dwarf due to the rotationally induced mixing. As a consequence the chemical structure becomes quite different from those obtained in standard sub-Chandrasekhar mass models, which show a sharp discontinuity between the helium envelope and the CO core (e.g. [9]).

6.3 Discussion

In the Chandrasekhar mass single degenerate scenario for SN Ia progenitors, a white dwarf in a close binary system burns hydrogen steadily which is accreted from its companion (either a main sequence or a red giant star), making the CO core mass grow to the Chandrasekhar limit. Although this is currently the favored scenario for SN Ia progenitors, it is still not clear whether it can explain the observed SN Ia rate since the accretion rates

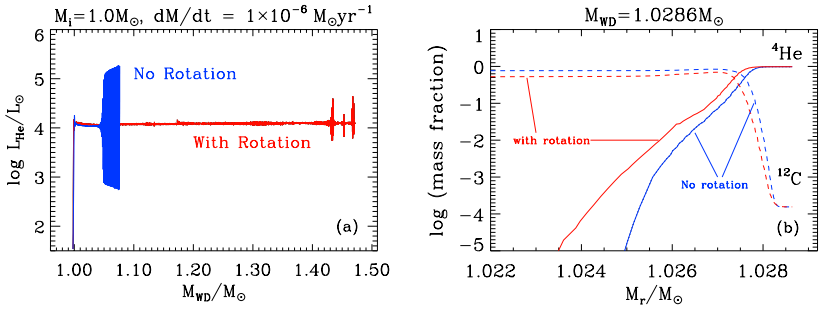

Figure 1: (a) Nuclear luminosity due to helium burning as function of the total mass of the white dwarf, which accretes helium with a constant rate of $10^{-6}\mathrm{M}_{\odot}\mathrm{yr}^{-1}$ starting at $M_{\rm WD} = 1.0\mathrm{M}_{\odot}$. (b) Chemical abundances of the white dwarf models as function of the mass coordinate when the white dwarf mass reaches $1.0286\mathrm{M}_{\odot}$.

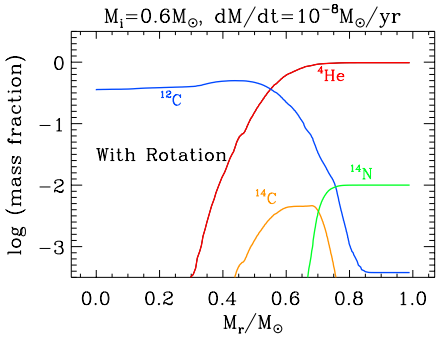

Figure 2: Chemical abundances as function of the mass coordinate when the mass of the white dwarf model reached $0.99\mathrm{M}_{\odot}$. The initial mass of the white dwarf is $0.6\mathrm{M}_{\odot}$ and the accretion rate is $10^{-8}\mathrm{M}_{\odot}\mathrm{yr}^{-1}$

which give the steady burning solutions for hydrogen are limited to a very narrow range (e.g. [10]). Furthermore, accretion rates which allow steady hydrogen shell burning do not guarantee a stable helium shell burning (e.g. [11]). Our calculations show that with an accretion rate of $10^{-6}\mathrm{M}_{\odot}\mathrm{yr}^{-1}$ (for which hydrogen burns steadily with $M_{\rm WD} \simeq 1.0\mathrm{M}_{\odot}$, e.g. [10]), the helium shell burning undergoes thermal pulses soon after the onset of accretion when rotation is not considered (Fig. 1a). The strength of the thermal pulses grows as the white dwarf mass increases and thus we can not expect the white dwarf to grow to the Chandrasekhar mass since the thermal pulses

may induce mass loss and the binary may undergo contact phases due to the expansion of the white dwarf envelope [2]. Our results imply that rotation can suppress the pulses and help the white dwarf to obtain a higher mass for a given accretion rate. Futhermore, our models show that rotationally induced mixing can significantly change the white dwarf chemical structure in the Chandrasekhar mass single degenerate scenario and in the sub-Chandrasekhar mass models (Fig. 1b and 2), which may have interesting consequences for the exlosion characteristics.

Acknowledgement

We are very grateful to Gabriel Martinez for kindly giving us a data table of $^{14}\mathrm{N}(\mathrm{e}^-, \nu)$ reaction rate.

References

[1] N. Langer, A. Deutschmann, S. Wellstein, P. Höflich **362** (2000) 1046.

[2] N. Langer, S.-C. Yoon, S. Wellstein, S. Scheithauer, in the physics of Cataclysmic Variables and Related Objects, in press (2002).

[3] E.M. Sion, PASP **111** (1999) 532.

[4] D.A. Howell,P. Höflich, L. Wang, J.C. Wheeler ApJ **556** (2001) 302.

[5] A. Heger, N. Langer, S.E. Woosley ApJ **528** (2000) 368.

[6] D. Sugimoto, M.Y. Fujimoto PASJ **30** (1978) 467.

[7] R. Kippenhahn, A. Weigert, in Stellar Strucutre and Evolution (1990) Springer.

[8] S.-C. Yoon, L. Langer, S. Scheithauer A&A in preparation (2002).

[9] S.E. Woosley, T.A. Weaver ApJ **423** (1994) 371.

[10] K. Nomoto, Y. Kondo ApJ **367** (1991) L19.

[11] M. Kato, I. Hachisu ApJL **513** (1999) L41.

Investigating the Flame Microstructure in Type Ia Supernovae

F.K. Röpke, W. Hillebrandt, J.C. Niemeyer

Max-Planck-Institut für Astrophysik, Karl-Schwarzschild-Str. 1, D-85740 Garching, Germany

Introduction

Type Ia Supernovae (SN Ia in the following) are the most accurate cosmological distance indicators at the moment. Through light curve shape corrections accuracies of better than 10% in distance are claimed. In addition, claims of an accelerated cosmic expansion and thus a new constituent of the universe are mainly based on supernova observations. It is, however, evident that an understanding of the explosion mechanism is needed in order to validate such interpretations of the data and to control possible evolutionary effects.

One way to perform such investigations is by means of numerical simulations. These simulations should be self-consistent, independent of any phenomenological parameters, and based on models that are in accord with observational constraints. However, the main problem with the numerical approach is the vast range of relevant length scales, 11 orders of magnitude from the flame width to the radius of the star, that remains unresolvable in multidimensional simulations. Following [1], attempts to overcome this difficulty can be classified into large scale calculations (LSCs) and small scale calculations (SSCs). The former try to simulate SN Ia on scales of the radius of the exploding white dwarf star relying on assumptions on the microscale physics, whereas the latter are used to study the flame dynamics through a small window in scale space. In this manner it is possible to isolate specific physical effects and eventually to include the information gained here into LSCs. Examples of LSCs are given in M. Reinecke's contribution to these proceedings. The present work is concerned with SSCs to investigate the dynamics of thermonuclear flames in SN Ia explosions.

The astrophysical model

The SN Ia model adopted in the present study describes them as thermonuclear explosions of Chandrasekhar-mass C+O white dwarf stars. In the

standard model nuclear burning is ignited near or at the star's center. At the typical temperatures of around 10^{10} K the thermonuclear burning rate scales with the temperature as $\dot{S} \propto T^{12}$. Hence the burning takes place in a very thin region which is called a flame.

Flames can travel in two distinct modes: as a supersonic compression (shock) wave in the detonation mode and as a subsonic conductive wave in the deflagration mode. A pure detonation model for SN Ia can be ruled out because the outcome does not match the observed spectra. A more promising model (see M. Reinecke's contribution) is one in which the explosion starts out as a (slow) deflagration, is accelerated by turbulence, and possibly undergoes a transition to a detonation. The questions arising here concern the mechanism of the generation of turbulence as well as the likelihood of a deflagration-to-detonation transition. They are still not answered and are the motivation to study thermonuclear flames at microscopic scales.

In this work we will investigate length scales much larger than the diffusive flame width (less than one millimeter for C+O white dwarfs [2]) but much smaller than the stellar radius. On such scales the so-called discontinuity approximation holds which describes the flame as a discontinuity in temperature and density. This picture does not resolve the inner structure of the flame and it is therefore necessary to prescribe the laminar burning velocity as taken from direct numerical simulations, e.g. [2].

Some theoretical considerations

A laminar flame is subject to various instabilities. In the context of SN Ia explosions the most important ones are the Rayleigh-Taylor instability, the Kelvin-Helmholtz instability, and the Landau-Darrieus instability. While the first two are more important on large scales, the Landau-Darrieus (LD) instability acts unconditionally on all scales provided the flame can be described by the discontinuity approximation. This instability shall be investigated here, and its cause will be described briefly.

As was first discussed by Landau [3] and Darrieus [4] the cause of this instability is the refraction of the streamlines of the flow at the density jump of the flame. Consider a flame front that is perturbed from its originally planar shape. In the vicinity of a bulge of the perturbation the flow tubes are broadened. This leads to a decrease of the local fluid velocity with respect to the velocity far away from the front. Therefore the burning velocity s_l of the flame is higher than the corresponding local fluid velocity leading to an accrual of the bulge. The opposite holds for recesses of the perturbed front. In this way the perturbation keeps growing. By means of a linear stability

analysis Landau found for the growth rate of the perturbation amplitude

$$\omega_{\mathrm{LD}} = k s_l \frac{\mu}{1+\mu}\left(\sqrt{1+\mu-\frac{1}{\mu}}-1\right), \tag{1}$$

where k denotes the perturbation wavenumber and $\mu = \rho_u/\rho_b$ is the expansion across the flame front. In white dwarf matter at densities relevant for SNe Ia, the existence of the LD instability was first demonstrated numerically in [5].

However, the LD instability does not lead to unlimited growth of the amplitudes but is limited in the nonlinear regime. Fig. 1 illustrates this effect which can be described in a geometrical way (following [7]): The

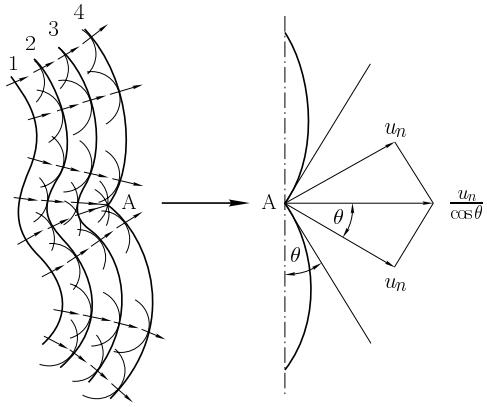

Figure 1: Nonlinear effect stabilizing the flame front (adopted from [6]).

propagation of an initially sinusoidally perturbed flame is first determined by Huygens' principle. But once a cusp forms at point A Huygens' principle breaks down and the flame propagation enters the nonlinear regime. The propagation velocity at the cusps exceeds s_l. This leads to a stabilization of the flame in form of cells which propagated with a velocity not much higher than s_l. Therefore the LD instability is usually ignored in SN Ia simulations. An analytical investigation of the stabilizing effect is given in [8] and is applied to the context of SN Ia in [9]. But there exist the possibility that nonlinear stabilization is destroyed under certain conditions (e.g. certain densities; interaction with turbulent velocity fields). In the following section we present a numerical method that will allow us to study this question.

Numerical methods

The fluid dynamics is described by the reactive Euler equations that are discretized on an equidistant Cartesian grid. To solve these equations a Godunov scheme is applied using the piecewise parabolic method (PPM) [10]. For this we employ the PROMETHEUS implementation [11] with directional splitting in two dimensions.

The equation of state is that of white dwarf matter, including an arbitrarily degenerate and relativistic electron gas, local black body radiation, an ideal gas of nuclei and electron-positron pair creation/annihilation.

Thermonuclear burning as considered here takes place at fuel densities above $10^7\,\mathrm{g\,cm^{-1}}$ and terminates into nuclear statistical equilibrium, consisting mainly of ^{56}Ni. Because of the high computational costs of a full reaction network and because the objective of our SSC is to study flame dynamics rather than to provide an exact nucleosynthetic description we simplified the burning to an net reaction, $14\ ^{12}\mathrm{C} \longrightarrow 3\ ^{56}\mathrm{Ni}$, which gives an energy release of $7 \cdot 10^{17}\,\mathrm{erg\,g^{-1}}$.

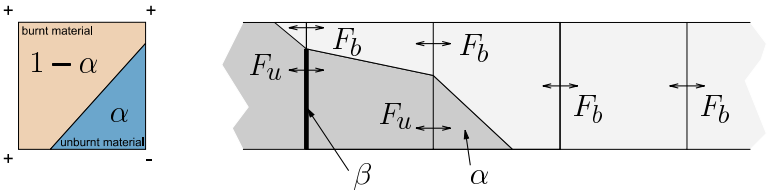

Figure 2: Determination of the unburnt volume fraction α (l.h.s.); flux-splitting method, adapted from [12] (r.h.s.)

The flame is described using the *level set technique*, associating the flame front with the zero level set of a signed distance function G. Details of the implementation of the level set method can be found in [12]. Without additional measures, however, the flame would smear out over 3-4 cells of the computational grid. This is not acceptable for our purposes and therefore we apply the *in-cell reconstruction/flux-splitting scheme* developed by Smiljanovski et al. [13]. This algorithm makes use of the fact that geometrical information on cells containing burnt and unburnt material ("mixed cells") can be obtained from the intersection of the zero level set of the G-function (representing the flame) with the interfaces of the mixed computational cells. In this way one can designate the volume fraction α of the unburnt cell part (Fig. 2, l.h.s.). The conserved quantities U are now interpreted as a linear

combination of unburnt and burnt parts of each cell

$$\overline{U} = \alpha U_u + (1 - \alpha) U_b.$$

Together with the Rankine-Hugoniot jump conditions and the Rayleigh criterion for the flame front, the equation of state, the jump condition for the velocity component normal to the front, and the prescribed burning velocity one obtains a system of equations which allows to compute state variables of unburnt and burnt matter in each mixed cell from the mean values. To describe the energy generation and species conversion consistently it is necessary to treat the source terms in this reconstruction implicitly. The reconstruction equation system is solved with Broyden's method.

The knowledge of the values of the burnt and unburnt quantities makes it possible to treat the hydrodynamic fluxes as linear combinations of "unburnt" and "burnt" fluxes weighted with corresponding parts β of the cell interfaces (see Fig. 2, r.h.s.). These partial fluxes are calculated separately. Therefore it is guaranteed that for instance no unburnt material can flow through the third cell interface from the left in Fig. 2, r.h.s. This feature prevents the flame from smearing out and enables us to describe it as a sharp discontinuity.

Some preliminary results

In order to study the LD instability the flame evolution has been simulated for two values of the fuel density, namely for $\rho_u = 5 \cdot 10^7\,\mathrm{g\,cm^{-1}}$ and for $\rho_u = 5 \cdot 10^8\,\mathrm{g\,cm^{-1}}$. The corresponding expansion coefficients across the front are $\mu = 2.410$ and $\mu = 1.619$, respectively. The simulation runs were performed on a grid of 100×100 cells with a cell length of 500 cm. The physical domain was periodic in the y-direction. On the left boundary of the domain an outflow condition was enforced and on the right boundary we imposed an inflow condition with the unburnt material entering the grid with the laminar burning velocity s_l.

Fig. 3 shows the temporal evolution of the flame fronts. The flame was initially perturbed in a sinusoidal way with a wavelength of $\lambda_{\mathrm{pert}} = 5 \cdot 10^4\,\mathrm{cm}$ and an amplitude of 200 cm (0.4 grid cells). Each contour is shifted artificially in x-direction for better visibility. As expected, in the beginning the perturbation grows exponentially, and the growth rate of the perturbation amplitude meets the theoretical expectations (1). As the flame evolution enters the nonlinear regime the formation of a cusp sets in. The front develops a cellular structure. At the troughs the cells split forming

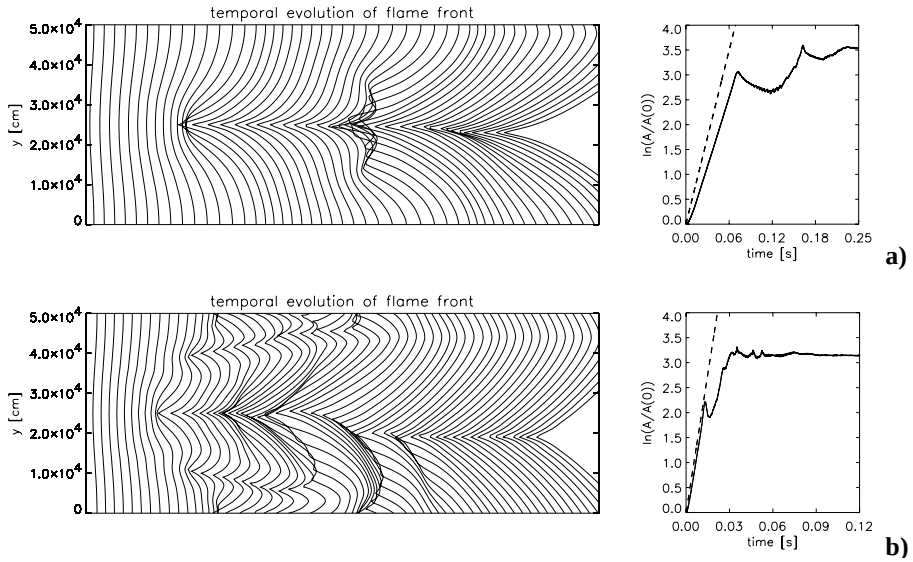

Figure 3: Flame front evolution. a) $\rho_u = 5 \cdot 10^7 \mathrm{g\,cm^{-3}}$, each contour corresponds to a time step of $\Delta t = 2.46 \cdot 10^{-3}\,\mathrm{s}$. b) $\rho_u = 5 \cdot 10^8 \mathrm{g\,cm^{-3}}$, $\Delta t = 1.23 \cdot 10^{-3}\,\mathrm{s}$. The plots on the r.h.s. show the growth of the perturbation amplitude over time (solid) and the prediction of Landau's linear stability analysis (dashed).

new cusps. The new cells move downwards the initial cusp and disappear. Finally this merging process results in a single domain-filling cusp/trough structure which then propagates steadily forward.

We do not reproduce the result of [5] that nonlinear stabilization fails at $\rho_u = 5 \cdot 10^7\,\mathrm{g\,cm^{-1}}$. A detailed discussion of this discrepancy will be presented elsewhere.

Summary and outlook

The presented model was proven to be applicable for studies of the microscale behavior of thermonuclear flames in the discontinuity approximation. The response of the flame to perturbations of its planar shape meets the theoretical expectations. Early stages of the flame evolution are consistent with Landau's stability analysis. The later evolution of the flame is nonlinear, it stabilizes in a cellular structure. Whether the final outcome is always a single domain-filling cell has to be studied in larger simulations. With this new code we are now in a position to investigate the interaction

of thermonuclear flames with imprinted velocity fields such as turbulence and to study the question of nonlinear stability. Moreover, if possible, we want to apply the in-cell reconstruction/flux-splitting technique to full two-dimensional LSCs of SN Ia explosions.

Acknowledgements

We would like to thank Martin Reinecke, Heiko Schmidt, and Sergei Blinnikov for valuable discussions.

References

[1] J.C. Niemeyer and W. Hillebrandt, in *"Thermonuclear Supernovae"*, eds. Ruiz-Lapuente et al., Kluwer Academic Publishers, Dordrecht 1997, p. 441.

[2] F.X. Timmes and S.E. Woosley, ApJ **396** (1992) 649.

[3] L.D. Landau, Acta Physicochim. URSS **19** (1944) 77.

[4] G. Darrieus, communication presented at *La Technique Moderne* (1938), unpublished.

[5] J.C. Niemeyer and W. Hillebrandt, ApJ **452** (1995) 779.

[6] Ya.B. Zeldovich, G.I. Barenblatt, V.B. Librovich, and G.M. Makhviladze, *The Mathematical Theory of Combustion and Explosions*, Nauka, Moscow (1980)

[7] Ya.B. Zel'dovich, Journal of Appl. Mech. and Tech. Physics **1** (1966) 102.

[8] G.I. Sivashinsky, Acta Astronautica **4** (1977) 1177.

[9] S.I. Blinnikov and P.V. Sasorov, Phys. Rev. E **53** (1996) 4827.

[10] P. Colella and P.R. Woodward, J. Comput. Phys. **59** (1984) 174.

[11] B.A. Fryxell, E. Müller, and W.D. Arnett, MPA Preprint **449** (1989)

[12] M.A. Reinecke, Ph.D. thesis, Technische Universität München (2001)

[13] V. Smiljanovski, V. Moser and R. Klein, Comb. Theory and Modeling **1** (1997) 183.

Model atmospheres for type Ia supernovae: Basic steps towards realistic synthetic spectra

D.N. Sauer[1,2], *A.W.A Pauldrach*[2]

[1] *Max-Planck-Institut für Astrophysik, Garching, Germany*
[2] *Institut für Astronomie und Astrophysik der Universität München, Germany*

8.1 Introduction

Analyses and interpretations of the meanwhile enormous database of excellent spectra of type Ia supernovae obtained in key projects and extensive searches still suffer from missing realistic numerical simulations of the physics involved. One of the most important steps towards this objective concerns a detailed simulation of the radiative transfer in the outermost parts of this objects in order to calculate synthetic spectra on the basis of models of the explosion scenario. The priority objective thereby is to construct for the first time consistent models which link the results of the hydrodynamics and nucleosynthesis obtained from the explosion models (see, for example, [7], [8], these proceedings) with the calculations of light curves (see, for instance, [1],[9], these proceedings) and synthetic spectra of SN Ia. After a phase of testing this new tool will provide a method for SN Ia diagnostics, whereby physical constraints on the basic parameters, the abundances, and the hydrodynamic structures of the atmospheric part of the objects can be obtained via a detailed comparison of observed and synthetic spectra. This will also allow to determine the astrophysically important information about the distances of SN Ia.

First results in this direction are presented in Section 1.3. In the preceding sections we will first with regard to our objective briefly summarize the most important observed properties of type Ia supernovae, and then discuss the current status of our treatment of the hydrodynamic expanding atmospheres of SN Ia.

8.2 Observed properties of type Ia supernovae

The classification of supernovae is based on purely empiric observational properties. In this scheme, type Ia supernovae are defined by the absence

of hydrogen and helium spectral lines and a strong absorption feature of Si II lines near 6100 Å in epochs around maximum light. In late phases the SN Ia spectra are dominated by emission of forbidden lines of mainly iron and cobalt.

Prominent features in the early-time spectra of type Ia supernovae – this is the phase we want to analyze at present – are characteristic absorption lines resulting from low ionized intermediate-mass elements (such as Si II, O I, Ca II, Mg II). The formation of these lines results in a pseudo-continuum that is set up by the overlap of thousands of these lines. The absorption lines show characteristic line shapes due to Doppler-broadening resulting from large velocity gradients. In the UV-part of the spectrum, the flux is strongly depleted (compared to a blackbody-fit in the optical range) by line blocking of heavy element lines (especially Fe, Co, Mg). Towards the red and IR, the flux is also low due to the absence of significant line influence in these regions. Towards later phases ($\sim$ 2 weeks after max.), heavier element lines become more prominent as the photosphere recedes deeper into the ejecta. At this time emission features also start to increasingly dominate the spectral characteristics. In the nebular phase ($\sim$ 1 month) the spectrum approaches a typical nebular appearance dominated by lines of heavy element forbidden transitions.

The spectra as well as the light curves of type Ia supernovae show a high degree of homogeneity; however, some intrinsic differences are also observed. The mechanisms leading to these differences have to be understood in order to draw conclusions based on the homogeneity, such as the distance measurements for cosmological applications. (For detailed reviews of the optical properties of SN Ia we refer to [3],[2].)

8.3 Model atmospheres for type Ia supernovae

In early phases, which are considered here, a supernova of type Ia is described by a photosphere in the deeper layers (i.e., the sphere where the optical depth $\tau = 1$) and a superimposed extended atmosphere that expands at high velocities – up to 30000 km/s.

Due to the high radiation energy density and the dominant role of scattering processes the problem we are dealing with is strongly non-local, leading to typical conditions that make consideration of NLTE (non local thermodynamic equilibrium) effects necessary. Additionally, processes of line blocking and blanketing significantly influence the radiative transfer within the ejecta and thus the observed spectral properties (see [5]). This behavior results in the strong depletion of the flux in the UV part and the blue region

of the spectrum due to the influence of thousands of lines of the heavy elements. As the absorbed radiation is partly reemitted towards lower layers ("*backwarming*") the temperature structure is also affected, and in turn the ionization equilibrium and thus the radiation field itself.

Certain properties of supernovae make the full problem of NLTE and radiative transfer calculations even more complicated than in related objects, such as hot stars: The element abundances of type Ia supernovae are entirely dominated by heavy species that have fairly complicated ionic energy level structures with hundred-thousands of transitions. In addition, the high velocities within the ejecta broaden these lines by Doppler-shift and thus cause a strong overlap of sometimes thousands of lines especially in the UV wavelength regions. In contrast to objects with similar physical conditions (for example, hot stars or, in late phases, planetary nebulae), SNe are not illuminated by a central source of radiation, but are heated by the diffuse source of the γ-rays emitted by the radioactive decay of ^{56}Ni and ^{56}Co. Thus, the diffuse field is of primary importance and can not be approximated accurately in a simple way. Another problem concerns the relatively flat density distribution: Even for early phases where the assumption of an underlying photosphere seems to be justified, the radius of this photosphere (defined as the radius where the optical depth $\tau_\nu = 1$) varies strongly with wavelength.

The approach used in this project employs a detailed atmospheric model code which is based on the concept of *homogeneous, stationary, and spherically symmetric radiation-driven winds*, where the expansion of the atmosphere is due to scattering and absorption of Doppler-shifted metal lines. This code provides a detailed and consistent solution of the radiative transfer including a proper treatment of NLTE as well as blocking and blanketing effects in order to calculate realistic synthetic spectra (see [6], [5]). The computation of the NLTE level populations is carried out using detailed atomic models, and including all important contributions to the rate equations. Thomson scattering, bound-free and free-free opacities, line absorption and emission processes as well as dielectronic recombination is included in the radiative transfer. The computation of the NLTE model is based on several iteration cycles of step-wise improving accuracy. In a first step, an opacity sampling method is employed, which results in a approximate solution that is, however, already close to the final solution. An exact treatment of the radiative transfer equation in the observer's frame is performed in a second step. In a final step the occupation numbers, opacities and emissivities from the NLTE model are utilized for calculating a synthetic spectrum via a formal solution of the transfer equation. For a detailed description of the

numerical methods we refer to [6].

8.4 Results

We regard the results obtained so far as not yet suitable for diagnostic purposes, since some physics relevant for SN modelling have been only very roughly included up to now (e.g., the heating by the diffuse source of the γ-rays emitted by the radioactive decay of ^{56}Ni and ^{56}Co). Thus, our present calculations should be considered as preliminary. All models obtained so far are based on the hydrodynamic model W7 by Nomoto et al. [4]. Since radial variation of the chemical composition has not yet been fully implemented in our models described here, the values used for the composition have been averaged over mass shells. Additionally we assume that the energy deposition arises completely from the optically thick part of the atmosphere. Moreover, the expansion of the ejecta is assumed to be homologous (i.e. $r \propto v$).

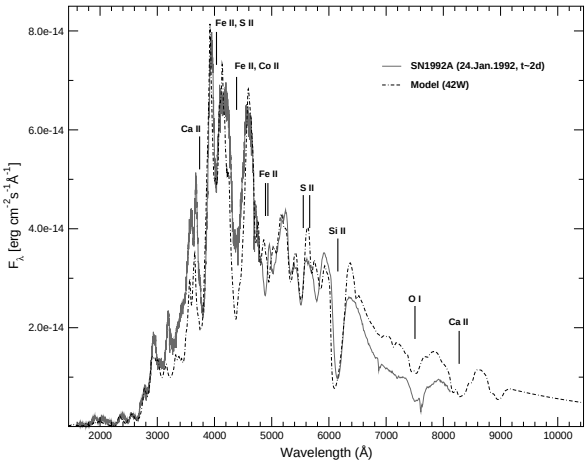

Figure 1: Model calculation compared to observed spectrum of SN1992A

Fig. 1 compares a calculated model spectrum to the observed "standard" type Ia supernova 1992A spectrum. As is shown, the synthetic spectrum reproduces the observed spectrum in the UV and blue wavelength ranges. Thus, our method already produces quantitatively reliable results indicating that the basic physics is obviously treated properly. However, towards the redder part of the spectrum a systematic offset to the observation appears. We regard our treatment of the inner boundary condition (diffusion approximation) and the missing energy deposition above the photosphere

as a possible reason for this behavior. At the inner boundary we apply the diffusion approximation at all frequencies. This approximation is valid for conditions where the mean free path of the photons is very small (i.e. $\tau \gg 1$), which, however, is not guaranteed at longer wavelengths, due to the absence of strong lines in this wavelength range and the relatively flat density distribution that does not provide the required strong increase of the continuum opacities towards our innermost radius grid point. As a consequence, the flux emitted from the inner boundary is too high. In addition, the opacity in this wavelength range is dominated by pure electron (Thomson) scattering that does not couple the radiation field to the thermal pool. In these regions the radiation observed is actually generated in much deeper layers of the ejecta and scattered outwards.

8.5 Near future prospects

Regarding a solid basis for spectral diagnostics of type Ia supernovae the next steps are obvious. Depth-dependent abundances and a proper treatment of the γ energy deposition above the photosphere have to be included. The latter point will also free us from the limitation of currently being able to treat only the photospheric, early-phase epochs around maximum. With these enhancements it seems feasible to obtain synthetic spectra based on hydrodynamic explosion models like those of the hydrodynamics group at MPA, and to compare them directly to observed SN spectra.

Acknowledgements

We wish to thank our collaborators at MPA – the Hydro-Group – and USM for helpful discussions. In particular we thank T. Hoffmann at USM for providing lots of useful tools and active support for this ongoing project. The first author thanks especially his primary supervisor, W. Hillebrandt, for numerous helpful comments, permanent motivation, and financial support.

References

[1] S. Blinnikov, E. Sorokina (2000), A&A, **356**, L30

[2] A.V. Filippenko (1997), ARA&A, **35**, 309

[3] B. Leibundgut (2000), A&A Rev , **10**, 179

[4] K. Nomoto, F. Thielemann, and K. Yokoi (1984), ApJ, **286**, 644

[5] A. Pauldrach, et al. (1996), A&A, **312**, 525

[6] A. Pauldrach, et al. (2001), A&A, **375**, 161

[7] M. Reinecke,W. Hillebrandt, Niemeyer, J. C. (2001), astro-ph/0111475

[8] M. Reinecke, W. Hillebrandt, Niemeyer, J. C. (1999), A&A, **374**, 739

[9] E. Sorokina, S. Blinnikov, & O. Bartunov (2000), Astron.Letters **26**, 67

Recent progress in multidimensional SN Ia simulations

M. Reinecke, W. Hillebrandt, J.C. Niemeyer, F. Röpke, W. Schmidt, D. Sauer

Max-Planck-Institut für Astrophysik, Garching, Germany

This project is a direct continuation of the work presented by [4] and [5], and is therefore concerned with the accurate modeling of the rapid thermonuclear combustion processes which occur in a white dwarf during its explosion as a Type Ia supernova. While the earlier results already gave several new insights into the explosion dynamics of such an event and its dependence on parameters like the ignition conditions, it nevertheless became clear that the numerical models employed at that time were not sufficient to reproduce characteristic properties of SNe Ia that are known from observations; most importantly, the total energy release predicted by the simulations lay consistently below the expectations.

Several potential reasons for this shortcoming have been identified and addressed in the meantime:

- In the early simulations thermonuclear combustion was modeled by the net reaction of ^{12}C and ^{16}O to ^{56}Ni. This ignored the fact that at high densities a mixture of iron-group elements and α-particles in nuclear statistic equilibrium is synthesized, and that the synthesis only reaches intermediate-mass elements like silicon at lower densities. Both effects have been implemented, so that at least the energetical aspects of the burning process should be modeled correctly.

- The model for the turbulent flame propagation velocity as presented in [3] and [4] was only consistent for three-dimensional simulations. This problem has been solved by changing a numerical factor in the two-dimensional case (see [6]).

- Nonetheless, reliable predictions of the total energy relese can only be expected from fully three-dimensional simulations, since in two dimensions axial symmetry is assumed, which artificially inhibits the wrinkling of the flame in the azimuthal direction. This effect leads to an underestimation of the total flame surface and consequently to a lower energy generation rate.

In order to test the improved code, a two-dimensional explosion was simulated several times with identical initial conditions but varying numerical resolution (c3_2d_128 to c3_2d_1024 in table 1). Contrary to our experiences with the original code the energy release and final structure were comparable for all calculations, except for the run with the poorest resolution (see [6]). This allows the conclusion that – at least above a certain minimum resolution – all unresolved small-scale phenomena are appropriately represented by our turbulent sub-grid model for the turbulent flame speed.

As expected, the transition to three spatial dimensions (simulation c3_3d_256 in table 1) caused a significant increase of the released energy. The obtained values for energy, nickel mass and mass of lighter elements lie well within the range deduced from real supernova observations ([1]). The calculated expansion speeds reach values up to 12 000 km/s, and therefore are also compatible with the line widths observed in typical SN Ia spectra.

model name	$\frac{m_{\mathrm{Mg}}}{M_\odot}$	$\frac{m_{\mathrm{Ni}}}{M_\odot}$	$\frac{E_{\mathrm{nuc}}}{10^{50}\,\mathrm{erg}}$
c3_2d_128	0.132	0.348	6.56
c3_2d_256	0.109	0.400	7.19
c3_2d_512	0.151	0.402	7.58
c3_2d_1024	0.152	0.428	8.00
c3_3d_256	0.177	0.526	9.76

Table 1: Overview over element production and energy release of all discussed supernova simulations

Qualitatively, our results for the explosion energetics are in rather good agreement with recent simulations performed by [2], which rely on quite different numerical models and assumptions; most notably the macroscopic flame velocity is determined by the asymptotic rise speed of a Rayleigh-Taylor bubble with size Δ, instead of the turbulent velocity fluctuations.

Further improvements of the SN Ia simulations are planned, both with respect to the underlying models and the realism of the initial conditions. As was pointed out by S. Blinnikov (personal communication), an accurate simulation of light curves and spectra based on the results of the 3D hydrodynamical computation requires not only the total concentration of iron group elements (which have been represented so far by ^{56}Ni), but the amounts of the real ^{56}Ni and the rest of the Fe-group elements. The necessary changes will be implemented in the near future.

It would also be desirable to reach a higher numerical resolution at the beginning of the explosion, which allows a more accurate prescription of

the flame geometry, and, at the same time, to follow the expansion of the star over a longer time period (several seconds), until the ballistic expansion stage has been reached. To achieve both of these goals, an expanding grid must be used instead of the currently employed static one.

Acknowledgements

We thank Sergei Blinnikov, Elena Sorokina, Ken'ichi Nomoto and Hans-Thomas Janka for many helpful discussions and contribution of code and data tables.

References

[1] G. Contardo, B. Leibundgut, W.D. Vacca: Astron. Astroph. **359** (2000) 876.

[2] A.M. Kohokhlov: astro-ph/0008463, submitted to ApJ

[3] J.C. Niemeyer, W. Hillebrandt: ApJ **452** (1995) 769.

[4] M. Reinecke, W. Hillebrandt, J.C. Niemeyer, R. Klein, A. Gröbl: Astron. Astrophys. **347** (1999) 724.

[5] M. Reinecke, W. Hillebrandt, J.C. Niemeyer: Astron. Astrophys. **347** (1999) 739.

[6] M. Reinecke, W. Hillebrandt, J.C. Niemeyer: astro-ph/0111473, accepted by Astron. Astrophys.

Energy exchange inside SN ejecta and light curves of SNe Ia

E.I. Sorokina[1], *S.I. Blinnikov*[2,1]

[1] *Sternberg Astronomical Institute, Moscow, Russia*
[2] *Institute for Theoretical and Experimental Physics, Moscow, Russia*

A treatment of line opacity is one of the most crucial problems for the light curve (LC) modeling of Type Ia supernovae (SNe Ia). Spectral lines are the main source of opacity inside SN Ia ejecta from ultraviolet through infrared range. A lot of work has been done on this subject [1, 3, 6, 7, 8, 9].

The problem itself can be divided into two parts:

- How are flux and energy equations changed in the expanding medium;
- How should one average flux and intensity, as well as extinction and absorption coefficients, over energy bins used in calculations.

Almost all previous research was about flux equation. Here we will focus on the energy equation. We will suppose a free expansion of gas, i.e. linear law for the velocity distribution $v = r/t$. The principal difference between the behavior of flux and intensity in comparison to the static case is that the flux always becomes lower in the expanding media, while the sign of the change of intensity depends on the temperature gradient. It is clear qualitatively. When we are sitting inside the gas and would like to measure a flux and an intensity at a fixed frequency in the static case we should just measure how the surrounding gas emits and absorbs at this frequency. If this specific frequency corresponds to a strong line we will not be able to see distant layers of gas, since rather large optical depth accumulates quite close to the observer. In the continuum we can see rather distant gas layers. So at the frequency of a strong line we observe almost local gas without temperature gradient, hence we measure rather low flux values, and the intensity corresponds to the local blackbody value. In the continuum the flux grows appreciably because of growing gradients, and the intensity corresponds to the blackbody at $\tau \sim 1$, where conditions differ from local ones.

In the expanding case, a photon's mean free path becomes less even at the frequency which corresponds to the continuum at the rest observer frame. If we encounter a strong line blueward before $\tau \sim 1$ in continuum then, most probably, we will not be able to see further out. So the temperature

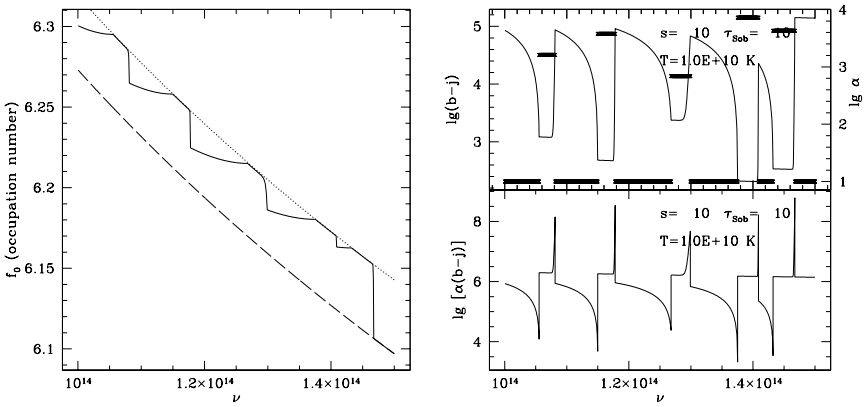

Figure 1: *Left panel:* the zero moment of an occupation number f_0. Dots correspond to the local blackbody value, dashes shows the blackbody at the distance where continuum forms, solid line demonstrates the behavior of f_0 when five spectral lines presents in the frequency interval we are interested in. *Right panel:* logarithms of monochromatic α (thick lines, "top hat" profile), $b - j$, and $\alpha(b - j)$. The main problem is to integrate the last function, especially when the number of lines is not 5, but several hundreds.

gradient at the mean free path of a photon becomes less than in the static case, therefore the flux drops down. The intensity in the expanding medium would then correspond to the blackbody radiation at the distance where the line forms, but it is redshifted by Doppler effect. For a constant temperature and pure continuum, the intensity at any space point and any frequency is less than the local blackbody intensity. A strong nearby line enhances the value of the observed intensity (opposite to the behavior of the flux, which drops down with the comparison to a pure continuum case) and diminishes the difference between intensity and a local blackbody. Fig. 1 shows all these dependencies for the zero moment of an occupation number, which is proportional to an angle averaged intensity (the zero moment of intensity): $J_\nu = \frac{2h\nu^3}{c^2} f_0$; $J_\nu = \frac{1}{2}\int_{-1}^{1} I_\nu d\mu$.

To derive these dependencies formally, we have to solve the Boltzmann equation in the comoving frame for a spherically-symmetrical flow:

$$\frac{1}{c}\frac{\partial f}{\partial t} + \mu\frac{\partial f}{\partial r} + \frac{1-\mu^2}{r}\frac{\partial f}{\partial \mu} - \frac{\nu}{ct}\frac{\partial f}{\partial \nu} = \eta_\nu - \chi_\nu f \ , \qquad (2)$$

where we put $r = vt$, which is quickly established in SN ejecta. When we apply a diffusion limit, so that the space derivatives are negligible, the

solution of the Boltzmann equation is

$$f_0 = \int_{\nu}^{t\nu/t_0} \frac{\nu}{\tilde{\nu}^2}\, \alpha^\star(t\nu/\tilde{\nu}, \tilde{\nu})\, b(t\nu/\tilde{\nu}, \tilde{\nu}) \exp\left[-\int_{\nu}^{\tilde{\nu}} \frac{\nu}{\bar{\nu}^2}\, \alpha^\star(t\nu/\bar{\nu}, \bar{\nu})\, d\bar{\nu}\right] d\tilde{\nu}\ , \tag{3}$$

where b is a blackbody occupation number, and the dimensionless absorption coefficient $\alpha^\star = \alpha ct$.

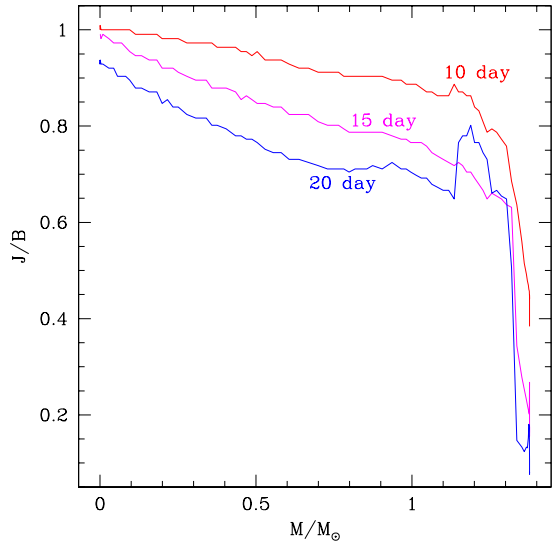

Figure 2: The distribution of J/B inside the ejecta at different time demonstrates how matter and radiation are decoupled.

Last equation gives us an exact solution for a monochromatic value of f_0. Numerical codes which are used for computations of SNe radiative evolution operate with averaged numbers, and each energy bin contains hundreds of spectral lines. During such computations one needs to solve equations for energy exchange between radiation and gas in each bin:

$$\frac{d < j_\nu >}{dt} \ \propto < \alpha_\nu > (< b_\nu > - < j_\nu >). \tag{4}$$

The problem here is to average α correctly inside a bin with hundreds (or thousands) of lines. The right way is to average it so that

$$< \alpha >= \frac{< \alpha(b - f_0) >}{< b > - < f_0 >} \qquad (f_0 \equiv j_\nu). \tag{5}$$

The main difficulty here is to derive an average value of $<\alpha(b-f_0)>$. As we said above, in the strong lines $f_0 = b$. If an optical depth in the continuum is also very high, so that radiation is tightly coupled with matter and $f_0 = b$, then $b - f_0 \approx 0$ and it is not so important how we treat α. It becomes important when radiation is decoupled from matter. As it is seen in the fig. 2, they are decoupled within the entire SN Ia ejecta even before maximum light (which occurs about 20th day after explosion). A similar result was obtained in [5]. So the correct treatment of $<\alpha>$ is essential. We need to take the integral (3) accurately. It is very hard to do numerically, since α jumps up and down by many orders of magnitude hundreds of times. Moreover, where α is high, there $b - f_0$ is extremely small (see fig. 1). Analytically, one can solve this problem, but only for very simple line profiles. We assume that lines have a rectangle shape ("top hat" profile). For rectangle lines in the Rayleigh–Jeans regime and infinite expanding medium (so that at given ν one can observe emission with arbitrary shifted $\Delta\nu$ in the transparent case) we have

$$f_0(\nu) = \frac{kT}{h\nu}\left[\!\!\left[1 - \frac{1}{\alpha^\star_{N_\nu}}\left(1 - e^{-\alpha^\star_{N_\nu}(1-\frac{\nu}{\nu_{N_\nu}})}\right)\right.\right.$$
$$- \sum_{j=N_\nu+1}^{N_{\max}}\left[\frac{1}{\alpha^\star_j}\left(1 - e^{-\alpha^\star_j(\frac{\nu}{\nu_{j-1}}-\frac{\nu}{\nu_j})}\right)\exp\left\{-\sum_{i=N_\nu}^{j-1}\alpha^\star_i\left(\frac{\nu}{\nu_{i-1}} - \frac{\nu}{\nu_i}\right)\right\}\right]$$
$$\left.\left. - \frac{1}{\alpha^\star_{N_{\max}+1}}\left(1 - e^{-\alpha^\star_{N_{\max}+1}\nu/\nu_{N_{\max}}}\right)\exp\left\{-\sum_{i=N_\nu}^{N_{\max}}\alpha^\star_i\left(\frac{\nu}{\nu_{i-1}} - \frac{\nu}{\nu_i}\right)\right\}\right]\!\!\right] \quad (6)$$

To get $<\alpha>$ from (5) we need to integrate this expression once more. This also can be done analytically, and adds the third summation over all lines in the bin. Computing of these long sums is very time consuming. Probably, the efficiency can be improved along the way proposed in [2].

Using our expression for $<\alpha>$, we have computed the opacity tables for standard SN Ia model W7. The results are compared with the absorption derived with the Eastman–Pinto approximation [7] (see fig. 3). Occasionally, they remains almost unchanged at the visual light, while decreases in UV and enhances in IR.

LCs for W7 (fig. 4) were calculated with the help of the code STELLA [4]. UBV LCs remain almost unchanged, while I-band is affected strongly (fig. 4). This is explained by the changes of opacity and spectrum in the I-band.

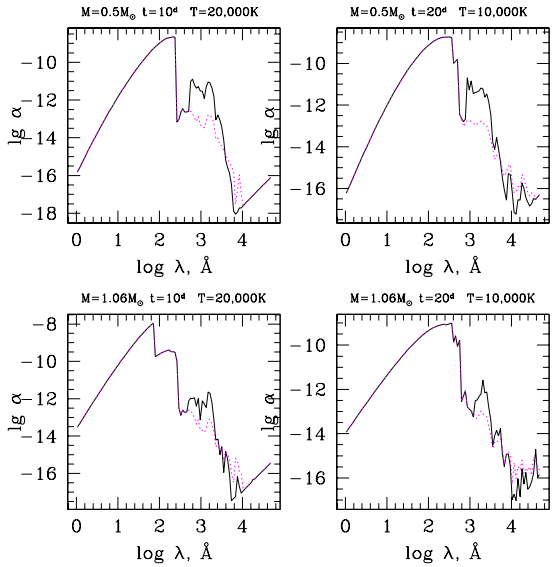

Figure 3: Logarithm of absorption coefficient calculated accordingly to our formulae (solid) and in Eastman–Pinto approximation (dotted). Top panels show the absorption for two sets of (time, temperature) inside the layer of W7 model which consists of mostly ^{56}Ni, while bottom panels correspond to the layer of intermediate mass elements. Decreasing of the number of lines in this layer leads to the disappearance of the difference between two treatments of opacity.

Acknowledgements

We are grateful to the organizers of the Ringberg meeting for their hospitality, to Stan Woosley for supporting our work in the UCSC. Our work in US was supported by grants NSF AST-97 31569 and NASA - NAG5-8128, in Russia RBRF 99-02-16205 and RBRF 02-02-16500.

References

[1] E. Baron, P.H. Hauschildt, A. Mezzacappa, MNRAS **278** (1996) 763.

[2] B. Baschek, W. v. Waldenfels, R. Wehrse, A&A **371** (2001) 1084.

[3] S.I. Blinnikov, Astron.Lett. **22** (1996) 79.

[4] S.I. Blinnikov et al., ApJ **496** (1998) 454.

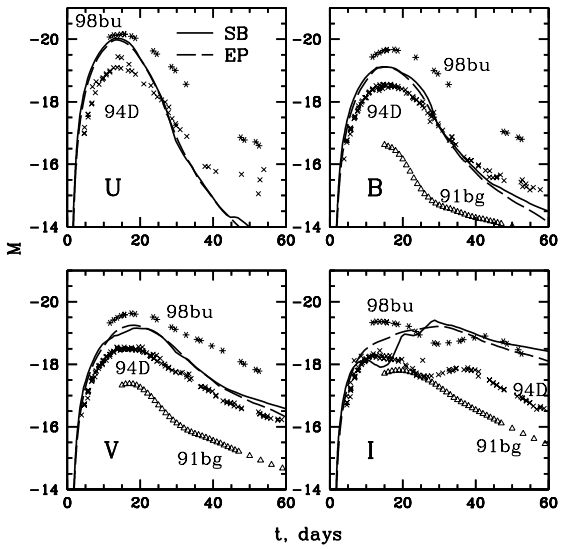

Figure 4: UBVI light curves of the model W7 with two opacity approximations: Eastman–Pinto (dashed) and the way of averaging presented here (solid). UBV bands remain almost unaffected, while I–band shows now a complicated structure similar to that one can observe for the real SNE Ia, though not identical. Crosses, stars and triangles shows the observational LCs for three SNe Ia.

[5] R.G. Eastman, in Thermonuclear Supernovae. Eds. P. Ruis-Lapuente et al. – Dordrecht: Kluwer Academic Pub., (1997) p. 571.

[6] R.G. Eastman and R.P. Kirshner, ApJ **347** (1989) 771.

[7] R.G. Eastman, P.A. Pinto, ApJ **412** (1993) 731.

[8] A.H. Karp et al., ApJ **214** (1977) 161.

[9] R.V. Wagoner, C.A. Perez, M. Vasu, ApJ **377** (1991) 639.

The $^{12}C(\alpha,\gamma)^{16}O$ Reaction Rate and the Rise Time of Type Ia Supernovae

I. Domínguez[1], *P. Höflich*[2], *O. Straniero*[3]

[1] *Universidad de Granada, Granada, Spain*
[2] *University of Texas, Austin, USA*
[3] *Osservatorio Astronomico di Collurania, Teramo, Italy*

In this work we present preliminary results that favour a *high* value of the $^{12}C(\alpha,\gamma)^{16}O$ nuclear cross section based on the rise time of type Ia supernova (SNIa) light curves. This approach is possible thanks to the high quality data obtained for nearby SNIe. These data allow to establish an empirical relation between the magnitude (B and V) at maximum light and the rise time (the time to maximum since the explosion) [1].

Type Ia supernovae are thought to be the result of the thermonuclear explosion of a C-O WD with a mass close to the Chandrasekhar mass. The observations indicate that nearly all the WD is burnt in the explosion.

C-O WDs are the remnants of the evolution of low and intermediate mass stars and their chemical structure is mainly that of their predecessors, the degenerate C-O cores at the TP-AGB phase.

We use the C-O WD structure obtained evolving a 3 $M_\odot$ (Z=0.001 and Y=0.23) from the Pre-MS to the TP-AGB phase. The FRANEC code (see [9], [11] and [7]) is used for these calculations. Two values of the $^{12}C(\alpha,\gamma)^{16}O$ cross section have been assumed: a *high* rate [3] and a *low* rate [2]. In Figure 1 the C profile at the TP-AGB phase adopting these two nuclear reaction rates and the new rate from [5] are displayed.

Three distinct layers are clear in Figure 1, through them C abundance increases outward: (1) the central convective He burning produces the innermost homogeneous C-depleted layer, which is affected by the treatment of turbulent convection; (2) radiative He shell burning during the early-AGB phase produces the intermediate layer with increasing C abundance; (3) He shell burning during the TP-AGB phase produces the thin external layer. Note that the outer spike is just due to the incomplete burning, He has not yet been depleted.

This core is subsequently accreted at a variable rate in order to achieve the explosion conditions at the same central density (2 10^9 g/cm^3) in all the models. Table 1 shows, for the *high* and *low* reaction rates, the central carbon abundance (column 2), the average C-O ratio within the original

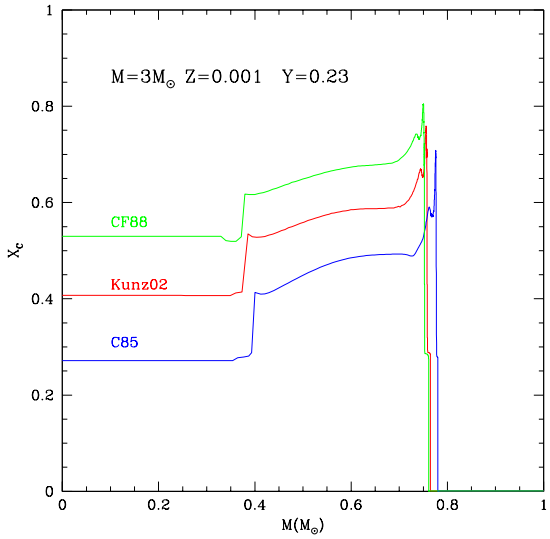

Figure 1: Final chemical Carbon profiles in the central region at the TP-AGB phase for the high rate (C85, [3]), the low rate (CF88, [2]) and the new rate (Kunz02, [5])

C-O core (column 3) and the average C-O ratio within the Chandrasekhar mass WD (column 4).

The explosion and light curves are calculated as in [8], [13], [4] and [7] and references therein. We consider Delayed Detonation (DD) models because they reproduce the optical and infrared light curves and spectra reasonably well [8]. In these models the density at which the deflagration turns into a detonation (the transition density, ρ_{tr}) determines mainly the the amount of ^{56}Ni synthesized. At the other side, the kinetic energy is quite insensitive to the ρ_{tr} because, in agreement with the observations, practically all the WD is burnt. In DD models, changes in the ρ_{tr} allow to reproduce the empirical maximum-decline relation.

In our calculations the transition density is chosen to be 2.3 10^7 g/cm^3. All model parameters are fixed and the adopted values are those that reproduce a *typical* SNIa. Therefore the differences in the light curves may be attributed to the different C-O ratio in the progenitor.

The increase in the C-O ratio when the *low* rate is assumed (see Table 1 column 4) results in a moderate increase in the ^{56}Ni mass (10%) and, as a consequence, a higher maximum magnitude (Table 1 column 5). More

significant is the increase in the kinetic energy (20%), which results in a *faster* light curve. As a consequence, the rise time decreases 3 days (from 18.0 to 15.3 days) when the *low* rate, instead of the *high* rate, is assumed (see column 6 in Table 1). Based on the empirical fit (rise time-maximum magnitude) of [1], for which the spread is found to be 0.4 days, 17.6 and 18.4 days are obtained for the *high* and *low* rate, respectively (column 7).

RATE	C_{cen}	C/O_{core}	C/O_{Mch}	M_V	Rise time (models)	Rise time (calibration [1])
(1)	(2)	(3)	(4)	(5)	(6)	(7)
C85	0.26	0.58	0.74	-19.21	18.0 d	17.6 d
CF88	0.51	1.42	1.22	-19.30	15.3 d	18.4 d

From these numbers we *suggest* that the observed *Long* rise times of SNIa favour a low C-O ratio in the exploding WD, which requires a depletion of C through α captures after He burning. Therefore indicating a *High* $^{12}C(\alpha,\gamma)^{16}O$ nuclear cross section. This result agrees with recent studies of pulsating WDs [6], which also favour a *high* rate.

The strongest limitation of this study is due to the uncertainties in the treatment of convection at the end of the central He burning, in particular the occurrence of breating pulses [10]. However, note that this problem is less severe for SNe Ia than for pulsating WDs. In the model presented here just the inner 0.4 $M_\odot$ (less than 30% of the WD) are affected by the treatment of convection. Out of this central zone, the C-O ratio reflects mainly the $^{12}C(\alpha,\gamma)^{16}O$ nuclear cross section. Other limitations come from the light curve models [5], in particular the opacity.

As a final comment, it is clear that the best way to go is to measure the $^{12}C(\alpha,\gamma)^{16}O$ nuclear reaction rate at the laboratory, as it is nowdays being done ([12], [5] and Hammer et al., this volume). However SNe Ia and C-O WDs models would be *surprised* if a *low* rate (as CF88 [2]) would be obtained.

References

[1] A.G. Riess et al., The Astron. Journal **118** (1999) 2675.

[2] G.R. Caughlan, A.M. Fowler, Atomic Data Nucl. Data Tables, **40** (1988) 283.

[3] G.R. Caughlan, A.M. Fowler, M.J. Harris, B.A. Zimmerman, Atomic Data Nucl. Data Tables **32** (1985) 197.

[4] P. Höflich, J.C. Wheeler, F.K. Thielemann, The Astrophys. Journal **495** (1998) 617.

[5] R. Kunz, M. Fey, M. Jaeger, A. Mayer, J.W. Hammer, G. Staudt, S. Harissopulos, T. Paradellis, The Astrophys. Journal **567** (2002) 643.

[6] T.S. Metcalfe, D.E. Winget, P. Charbonneau, The Astrophys. Journal **557** (2001) 1021.

[7] I. Domínguez, P. Höflich, O. Straniero, The Astrophys. Journal **557** (2001) 279.

[8] P. Höflich, A. Khokhlov, The Astrophys. Journal **457** (1996) 500.

[9] A. Chieffi, M. Limongi, O. Straniero, The Astrophys. Journal **502** (1998) 737.

[10] G. Imbriani, M. Limongi, L. Gialanella, F. Terrasi, O. Straniero, A. Chieffi, The Astrophys. Journal **558** (2001) 903.

[11] A. Chieffi, O. Straniero, The Astrophys. Journal Suppl. **71** (2002) 47.

[12] L. Gialanella et al., Eur. Phys. **11** (2001) 357.

[13] I. Domínguez, P. Höflich, The Astrophys. Journal **528** (2000) 854.

Two key reactions in stellar nucleosynthesis: ^{12}C$(\alpha,\gamma)^{16}$O and ^{22}Ne$(\alpha,n)^{25}$Mg

J.W. Hammer[1], *M. Jaeger*[1], *R. Kunz*[1], *M. Fey*[1], *A. Mayer*[1], *G. Staudt*[2], *S. Harissopulos*[3], *T. Paradellis*[3] †, *K.-L. Kratz*[4], *B. Pfeiffer*[4]

[1] *Institut für Strahlenphysik, Univ. of Stuttgart, Germany*
[2] *Physikalisches Institut, Univ. of Tübingen, Germany*
[3] *Institute of Nuclear Physics, N.C.S.R. Demokritos Athens, Gr*
[4] *Institut für Kernchemie, Univ. of Mainz, Germany*

Abstract

The excitation functions of the key reactions of stellar nucleosynthesis, ^{12}C$(\alpha,\gamma)^{16}$O and ^{22}Ne$(\alpha,n)^{25}$Mg, have been determined with an experimental sensitivity of 10^{-11} barn. For ^{12}C$(\alpha,\gamma)^{16}$O the S_{E1}- and S_{E2}-factors deduced from the γ angular distributions have been extrapolated into the range of helium burning temperatures applying the R-matrix method, which yielded $S_{E1}^{300} = (76 \pm 20)$ keV b and $S_{E2}^{300} = (85 \pm 30)$ keV b. Based on the new data, improved reaction rates were calculated as a function of temperature. For ^{12}C$(\alpha,\gamma)^{16}$O the reaction rate at $T_9 = 0.2$ is $N_A\langle\sigma\, v\rangle = (7.9 \pm 2.5) \times 10^{-15}$ cm^3 (mol s)$^{-1}$ and for ^{22}Ne$(\alpha,n)^{25}$Mg it is $N_A\langle\sigma\, v\rangle = (0.88\,^{+2.6}_{-0.3}) \times 10^{-16}$ cm^3 (mol s)$^{-1}$, improving the accuracy considerably compared to previous determinations.

12.1 Introduction

The ^{12}C$(\alpha,\gamma)^{16}$O reaction is considered to be the key reaction in the helium burning of stars because it determines not only the C/O ratio but also the nucleosynthesis of all heavier elements [1, 2]. The cross section of the ^{12}C$(\alpha,\gamma)^{16}$O reaction at burning temperatures is of the order of 10^{-17} b which can neither be measured with present techniques nor be predicted by theory. In any case the cross section or the S-factor has to be extrapolated and for this purpose information on the different contributions ($E1$, $E2$, cascades and the sign of all possible interferences) to the reaction yield is required to obtain an appropriate modeling of the extrapolation. Especially the separation of the $E1$- and the $E2$-capture is important. In the

† deceased

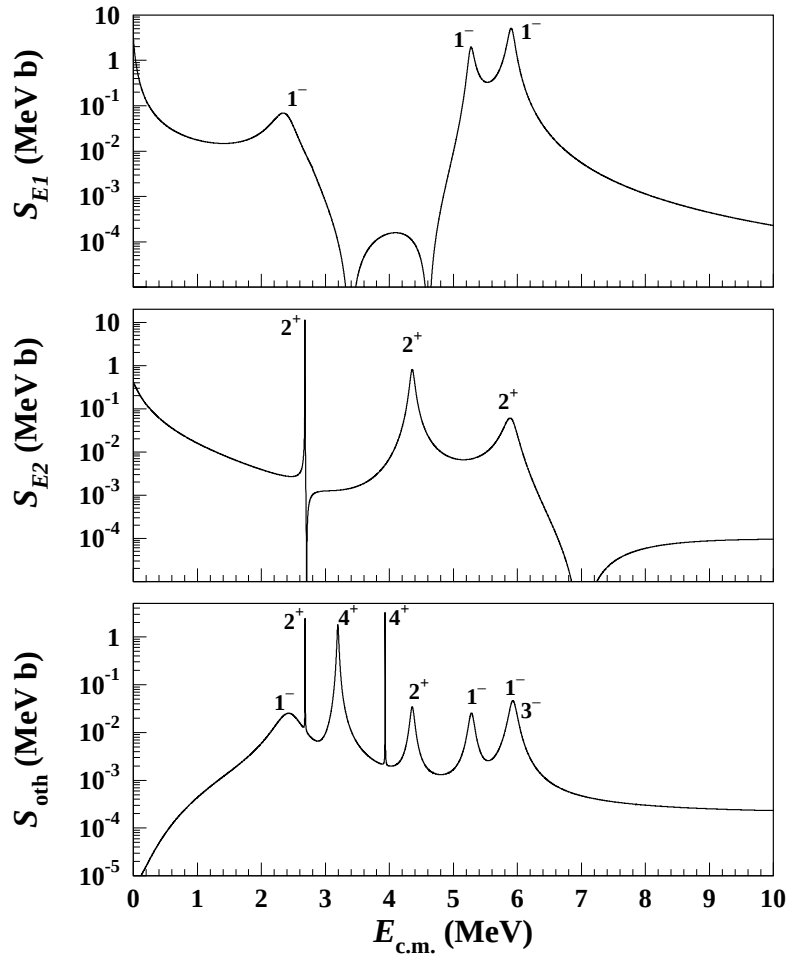

Figure 1: Contributions of different parts of the S-factor of the reaction $^{12}C(\alpha,\gamma)^{16}O$ resulting from R-matrix calculations considering the capture data of this work [3], the elastic scattering data [8, 9], the β-delayed α decay of ^{16}N [10] and the resonance parameters for the higher energy resonances given in [11]. The S_{E1} and S_{E2} curves represent the $E1$- and $E2$-capture to the ground state of ^{16}O with their interference structure. The sign of the interference terms can be read from the graphs. The $S_{\rm oth}$ curve represents captures from the 1^- and 2^+ states followed by cascades and captures from the 4^+ and 3^- states without taking into account the interference effects.

present investigation this information was deduced from the measurement of γ-angular distributions in a wide energy range [3] using an array of large Ge detectors and high α-beam currents of the Stuttgart DYNAMITRON accelerator.
On the other hand the reaction $^{22}\mathrm{Ne}(\alpha,n)^{25}\mathrm{Mg}$ is the dominant source of neutrons for the s-process (neutron capture on a slow time scale) in massive stars with $M > 8\,M_\odot$ ($M_\odot =$ solar mass) destined to become supernovae [4]. Calculations suggest that this range of stellar masses is responsible for producing most of the nuclides attributed to slow neutron capture for atomic masses $A \sim 60-90$ as well as many lighter than $A = 60$ [5]. The uncertainties of the cross section of the reaction $^{22}\mathrm{Ne}(\alpha,n)^{25}\mathrm{Mg}$ were unacceptable high [6] and therefore a new experiment was performed at the Stuttgart DYNAMITRON accelerator with an intense He^+ beam of about 1 mm diameter at the windowless gas target facility RHINOCEROS. A new 4π neutron detector has been designed and tailored for this specific reaction to enhance the sensitivity of this experiment [7].
More information on both experiments and the status of the data can be found in [3] and [7] and the references given therein.

12.2 Results for the reaction $^{12}\mathrm{C}(\alpha,\gamma)^{16}\mathrm{O}$

The $E1$-excitation function deduced from the new capture data has been described by a three-level-R-matrix fit ($E_R =$ - 45.1 and 2400 keV + 'background'-level) assuming a radius $R_0 = 6.5$ fm for the inner space with the nuclear interaction. In a consistent manner also elastic α-scattering data [8, 9] for $l = 1$ and $l = 3$ and the β-delayed α-decay of ^{16}N [10] have been included in our R-matrix fit. The boundary parameter was chosen in a way to obtain physically relevant parameters for the subthreshold levels; so γ-widths and energies from literature [11] could be used. The $E2$-data have been described with a five-level-R-matrix fit (- 245, 2680, 4320, 5650 keV and the 'background'-level) using again the elastic scattering data from literature for $l = 2$ [8, 9], γ-widths [11] and the resonance parameters for the 2^+ resonance [11]. The result of the R-matrix analysis is shown in Fig. 1. The S-factor curves are extrapolated into the range of burning temperature. The following values for the $E1$-, the $E2$-part of the S-factor, the contribution due to γ-cascades and the total S-factor at 300 keV have been extracted [3]:

$$S_{E1}^{300} = (76 \pm 20)\,\mathrm{keV\ b} \qquad S_{E2}^{300} = (85 \pm 30)\,\mathrm{keV\ b}$$

$$S_{\mathrm{casc}}^{300} = (4 \pm 4)\,\mathrm{keV\ b} \qquad S_{\mathrm{tot}}^{300} = (165 \pm 50)\,\mathrm{keV\ b}$$

PARAMETER SET

	Accuracy of Fit		
Parameter	Adopted (7 %)	High (8 %)	Low (14 %)
a_0	1.21×10^8	1.35×10^8	3.2×10^7
a_1	6.06×10^{-2}	5.45×10^{-2}	3.5×10^{-2}
a_2	32.12	32.12	32.12
a_3	1.7	10	8×10^{-2}
a_4	7.4×10^8	9.4×10^8	4.6×10^8
a_5	0.47	0.41	0.262
a_6	32.12	32.12	32.12
a_7	0	0	0
a_8	0	0	0
a_9	1.53×10^4	1.7×10^4	1.4×10^4
a_{10}	2×10^6	2.22×10^6	1.9×10^6
a_{11}	38.534	38.6	38.67
$\tilde{a}_9$	3.06×10^{10}	3.77×10^{10}	2.66×10^{10}

Table 1: Parameter set of the analytic expression according to the equation given above for the adopted, high and low reaction rate of $^{12}\mathrm{C}(\alpha,\gamma)^{16}\mathrm{O}$ determined in this work. "Accuracy of fit" means the maximum deviation of the fit from the determined tabulated reaction rate [12] in the full temperature range $0.001 \leq T_9 \leq 10$. In the temperature range $0.003 \leq T_9 \leq 2$ the maximal deviation is only 3 %.

12.3 Reaction rate of the reaction $^{12}\mathrm{C}(\alpha,\gamma)^{16}\mathrm{O}$

The reaction rate for $^{12}\mathrm{C}(\alpha,\gamma)^{16}\mathrm{O}$ was obtained by numerical integration of the excitation function folded as usual with the Maxwell-Boltzmann distribution of α particles according to the stellar temperature. The reaction rate is presented here as an analytic expression with an appropriate parametrization. The equation of this analytic expression contains 11 parameters. However, the calculations show that two parameters (a_7 and a_8) can be set to zero and two others (a_9 and a_{10}) can be combined to one ($\tilde{a}_9$) for our parameter set given in Table 1. In [12] the rate is also given in tabular form.

$$N_A \langle \sigma v \rangle = \frac{a_0}{T_9^2 \left(1 + a_1 T_9^{-2/3}\right)^2} \exp\left(-\frac{a_2}{T_9^{1/3}} - \left(\frac{T_9}{a_3}\right)^2\right)$$

$$
\begin{aligned}
&+ \quad \frac{a_4}{T_9^2 \left(1 + a_5\, T_9^{-2/3}\right)^2} \exp\left(-\frac{a_6}{T_9^{1/3}}\right) \\
&+ \quad \frac{a_7}{T_9^{3/2}} \exp\left(-\frac{a_8}{T_9}\right) \\
&+ \quad \frac{a_9}{T_9^{2/3}} \left(1 + a_{10}\, T_9^{1/3}\right) \exp\left(-\frac{a_{11}}{T_9^{1/3}}\right)
\end{aligned}
$$

Because $a_{10}\, T_9^{1/3} \gg 1$ one can omit the 1 in that term and reduce it to $\tilde{a}_9\, T_9^{-1/3} \exp(-a_{11} T_9^{-1/3})$ with $\tilde{a}_9 = a_9\, a_{10}$.
The parameters a_0 – a_{11} are listed in Table 1 for the adopted, the high and the low rate and the units of the rate are $\mathrm{cm}^3\,(\mathrm{mol\,s})^{-1}$.
The maximal deviation of the analytic expression from the numerical values in [12] is less than 7 % (adopted), 8 % (high) and 14 % (low). This fit is valid in the temperature range $0.001 \leq T_9 \leq 10$.
In the temperature range $0.003 \leq T_9 \leq 2$ the maximal deviation is only 3 % and in the range $0.001 \leq T_9 \leq 2.3$ it is less than 5 %.

12.4 Reaction Rate of the Reaction ^{22}Ne$(\alpha, n)^{25}$Mg

We have calculated an analytical expression for the reaction rates, employing the same parametrization as NACRE [6]. This expression is valid in the full temperature range of $0.1 \leq T_9 \leq 10$, and reproduces the tabular values within an accuracy of about 8 %. The parameters a_i, b_i, and c_i of this expression are given in Table 2 for the recommended, high, and low rates. In [7] the rates for $^{22}\mathrm{Ne}(\alpha, n)^{25}\mathrm{Mg}$ are also given in tabular form.

$$
N_A \, < \sigma\, v > \;\; = \;\; \sum_{i=1}^{4} a_i \; T_9^{b_i} \; \exp\left(-c_i / T_9\right)
$$

At $T_9 = 0.2$ the uncertainty of the $^{22}\mathrm{Ne}(\alpha, n)^{25}\mathrm{Mg}$ reaction rate given by NACRE [6] was a factor of ~ 500 (high / adopt.). In the present work this uncertainty was reduced to a factor of 5, as shown in Fig. 2. In the compilation of Käppeler *et al.* [13] this ratio was only 2, but at a much higher absolute level of the reaction rate, the rate of Käppeler *et al.* being a factor of 28 higher than the present value. At still lower temperatures the differences and uncertainties get larger, but one has to keep in mind that for $T_9 \leq 0.18$ the competing (α, γ) reaction becomes dominant [13]. For $T_9 > 0.2$, where the

	PARAMETER SET					
i	a_i		b_i		c_i	
1	4.04	3.68 4.55	0	0 0	7.74	7.70 7.781
2	2.302×10^{-4}	9.02×10^{-4} 1.701×10^{-10}	-0.60	-1.70 -5.98	6.14	6.31 6.22
3	6900	10900 8000	3.19	2.853 2.75	11.3	11.6 11.55
4	1.881×10^{7}	5.21×10^{6} 1.003×10^{6}	0.358	1.05 1.50	26.7	23.2 23.0

Table 2: Parameters a_i, b_i, and c_i (with significant digits) for the same analytical expression of the reaction rate of ^{22}Ne$(\alpha, n)^{25}$Mg as employed in the NACRE compilation [6], given for the recommended function (left), and the band of uncertainty with a high rate (upper right) and a low rate (lower right).

^{22}Ne$(\alpha, n)^{25}$Mg neutron production will be large enough to be effective in the *s*-process, the improved rates justify new computations of the *s*-process in massive stars.

12.5 Conclusion

For the reaction rate of the reaction ^{12}C$(\alpha, \gamma)^{16}$O a relative accuracy of $\pm\,30\,\%$ was achieved which improves our knowledge of this important reaction (see also Tab. 1 and 4 in ref. [12]). The precision of the rate of 10 %, as requested by different authors, could be achieved for instance by the use of highly sensitive ball detectors for the measurement of the γ-angular distributions.
In the case of the reaction ^{22}Ne$(\alpha, n)^{25}$Mg the present experimental means have been exhausted. Only an experiment in an underground laboratory will improve the sensitivity because there the limiting background will be reduced considerably. For the ^{12}C$(\alpha, \gamma)^{16}$O case this effect would be much smaller because a not negligible fraction of the background events are beam induced and that would be the same in an underground laboratory.

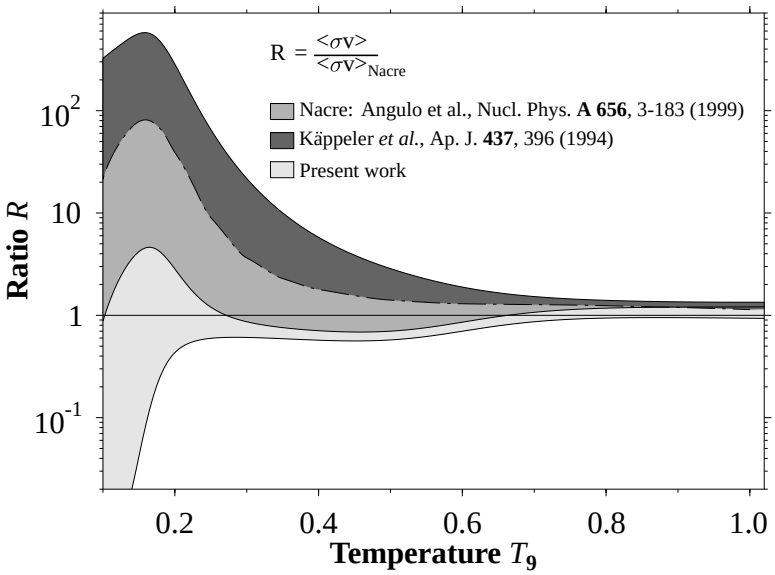

Figure 2: Comparison of the bands of uncertainty, marked with different grey scales, obtained for the reaction rate of ^{22}Ne$(\alpha, n)^{25}$Mg from the determination of this work and the compilations of NACRE [6] and Käppleler *et al.* [13]. All rates have been normalized here to NACRE. At $T_9 = 0.2$ the reduction of the uncertainty obtained in the present work is about a factor of 100.

Acknowledgements

We are indebted to U. Kneissl for supporting this project. This work was subsidized by the Deutsche Forschungsgemeinschaft.

References

[1] W.A. Fowler, in: *Les Prix Nobel – 1983* (Almquist a. Wiksell Int., Stockholm, Sweden, 1984), p. 88

[2] K. Langanke and C.A. Barnes, in: Adv. in Nucl. Phys. **22**, Eds. J.W. Negele and E. Vogt (New York, 1996), p. 173–263

[3] R. Kunz, M. Jaeger, A. Mayer, J.W. Hammer, G. Staudt, S. Harissopulos, T. Paradellis, Phys. Rev. Lett. **86** (2001) 3244.

[4] F. Käppeler *et al.*, Rep. Progr. Phys. **52** (1989) 945.

[5] S.E. Woosley and T.A. Weaver, Astrophys. J. Supp. **101** (1995) 181.

[6] C. Angulo *et al.*, Nucl. Phys. **A 656** (1999) 3.

[7] M. Jaeger, R. Kunz, A. Mayer, J.W. Hammer, G. Staudt, K.-L. Kratz, B. Pfeiffer, Phys. Rev. Lett. **87** (2001) 202501-1.

[8] R. Plaga *et al.*, Nucl. Phys. **A 465** (1987) 291.

[9] M. D'Agostino Bruno *et al.*, Nuovo Cimento Soc. Ital. Fis. **27** (1975) 1.

[10] R.E. Azuma *et al.*, Phys. Rev. C **50** (1994) 1194.

[11] D.R. Tilley *et al.*, Nucl. Phys. **A 564** (1993) 1.

[12] R. Kunz, M. Fey, M. Jaeger, A. Mayer, J.W. Hammer, G. Staudt, S. Harissopulos, T. Paradellis, Astrophys. J. **567** (2002) 643.

[13] F. Käppeler *et al.*, Astrophys. J. **437** (1994) 396.

Reaction Rates for Helium Burning

J. Görres[1], *S. Dababneh*[2], *C. Ugalde*[1], *F. Käppeler*[2], *M. Wiescher*[1]

[1] *University of Notre Dame, Department of Physics*
[2] *Forschungszentrum Karlsruhe, Institut für Kernphysik*

The synthesis of heavy elements in the s-process takes place during the He-burning phases of the stars. Core He-burning of massive stars is the site of the weak s-process which is responsible for the nucleosynthesis of the light s-process nuclei, A= 60-90 [1, 2]. The main neutron source for this process is the ^{22}Ne(α,n)^{25}Mg reaction. The site for the synthesis of the heavier s-process nuclei, the main s-process, are thermally pulsing, low-mass asymptotic giant branch (TP-AGB) stars [3, 4]. In this case the main neutron source is the ^{13}C(α,n)^{16}O reaction. A second small neutron burst is produced by the ^{22}Ne(α,n)^{25}Mg during thermal pulses. This second neutron exposure is important for the understanding of several branching points along the s-process path [4]. In both cases the ^{22}Ne is produced by the reaction sequence ^{14}N$(\alpha,\gamma)^{18}$F$(\beta^{+}\nu)^{18}$O$(\alpha,\gamma)^{22}$Ne. The initial ^{14}N abundance has been produced in the CNO cycle during the preceding H-burning.

We have investigated both (α,γ)-reaction leading to the formation of ^{22}Ne to reduce the uncertainties for both reaction ration rates. The reaction rate at temperatures of interest for the ^{14}N(α,γ)-reaction is dominated by the contribution of a low energy resonance at an α-energy (in the laboratory system) of 573 keV. The strength of this resonance has been measured by Couch et al. [5] but considerable uncertainty remained about its absolute strength [6]. For this reason we have measured the strength of the resonance and the strong resonance at 1136 keV using an activation technique (details can be found in reference [6]). The reaction product, ^{18}F, has a half life of 110 minutes and decays by β^{+}-decay producing two 511 keV γ-rays. TiN targets were activated for two half lives using high-intensity α-beams (100 μA) and then placed between two Ge-clover detectors which faced each other in close geometry The resulting decay curve of ^{18}F was measured by counting the 511 keV annihilation γ-rays in coincidence. Because of the high granularity of the setup it was possible to reduce the background using the directional correlation of the two 511 γ-ray, 180^{o}, while maintaining a high counting efficiency. The observed activities lead to a resonance strength of (45 $\pm$ 3) μeV which is about a factor of two lower than the previous value of (96 $\pm$ 14) μeV [5]. In addition to the strength we also measured the resonance energy leading to a value of (573 $\pm$ 3) keV in contrast to the previous value of 559

keV [5, 7]. With these results the present reaction rate for the ^{14}N(α,γ)-reaction rate is now a factor of 2-5 smaller than the previous rate [7] in the astrophysical important temperature range of 0.1 to 0.4 GK. The complete results of this experiment have been published in reference [6].

For the ^{18}O$(\alpha,\gamma)^{22}$Ne reaction rate strong contributions arise from the low energy resonances at 218, 470, and 566 keV. None of these resonances has been observed directly. Only upper limits are reported for the two higher resonances [8, 9], while the expected strength of the lowest resonance is too small to allow a direct measurement. These resonances have been observed indirectly using an α-transfer reaction [9]. Their alpha spectroscopic factor were determined which allowed an extraction of the alpha width of these resonances and to calculate their resonance strengths. However, no unique spin assignments were possible leading to large uncertainties in the resonance strength. The latest compilation of reaction rates [7] adopted spins of 0^+ and 4^+ for the two higher resonances with resonance strengths of 0.61 and 0.01 μeV. To resolve this uncertainty we have measured the ^{18}O$(\alpha,\gamma)^{22}$Ne reaction at α-energies between 420 and 800 keV. In contrast to the previous experiment no activation measurement is possible and a Ge clover detector was placed in close geometry at 0^o with respect to the beam axis. The back hemisphere was surrounded by 4 BGO detectors. The detectors were shielded against environmental background with Pb and two large area plastic detectors were used for active shielding against background induced by cosmic radiation. The background was further reduced by requiring a coincidence between the Ge and an event in any of the BGO detectors with an energy above 3 MeV. With this setup is was possible to observe the 566 keV resonance for the first time and to obtain an upper limit for the 470 keV resonance. A first, preliminary analysis suggests that the 566 keV resonance has a strength of approximately 1 μeV and thus a spin of 2^+ while the upper limit for the lower resonance, combined with the results of reference [8], indicates a spin of 1^- and therefore a strength of 0.2 μeV [9]. This result would lower the reaction rate at temperatures of interest by a factor of two compared to the Nacre rate [7]. However, these results are preliminary until the analysis of the data has been finalized.

We have started to investigate the reaction ^{19}F(α,p)^{22}Ne which is related to the production of Fluorine in TP-AGB stars. Jorissen et al. [10] observed ^{19}F/^{16}O ratios in AGB stars which are correlated with the ^{12}C/^{16}O ratio. This implies that Fluorine is produced in TP-AGB stars. Neutrons produced by the ^{13}C(α,n) reaction produce protons via the ^{14}N(n,p) reaction. This protons combine with ^{18}O to produce ^{19}F by the reaction sequence ^{18}O(p,α)^{15}N$(\alpha,\gamma)^{19}$F [11]. In this scenario ^{19}F can be destroyed by the

^{19}F(α,p)^{22}Ne reaction. The reaction rate for this reaction is experimentally not known and has been calculated using the Hauser-Feshbach formalism. We have started first test measurements at higher α-energies, 1200 to 2000 keV, and we will extend these measurements in the near future to lower energies to obtain reaction rates for the temperature range of interest, 0.1-0.4 GK. CaF_2 targets on thin C-backings were bombarded with an α-beam of 1-3 μA. The targets were surrounded by several Si detectors in close geometry. The detectors were covered by Au or Ni foils to stop the intense flux of elastically scattered α-particles. In addition a tightly collimated detector at backward angle allowed to monitor the target stability using the Rutherford backscattering method. The high energy data were used to calculate a reaction rate which is only valid around T = 1 GK. This first result indicates that the reaction rate might be larger than predicted by the Hauser-Feshbach calculations. However, any conclusions have to wait for the conclusion of the low energy measurements.

In conclusion, the present results put the reaction rates for the α-capture on ^{14}N and ^{18}O on a firm experimental basis. First measurements of the ^{19}F(p,α)-reaction indicate a larger reaction rate than obtained by statistical model calculations. The experiments showed that the use of modern detection technologies such as Ge clover detectors and compact detector arrays (NaI or BGO) together with active and passive shielding and high intensity particle beams can significantly increase the sensitivity for proton- and α-induced reactions.

Acknowledgements

We appreciate the active help during the experiments by C. Arlandini, M. Heil, R. Reifarth, A. Couture, J. Daly, and H.-Y. Lee and like to thank the technical staffs at Karlsruhe and Notre Dame for their excellent support. This work was supported by the National Science Foundation, by the Deutscher Akademischer Austauschdienst, and by the Graduate School of the University of Notre Dame.

References

[1] C.M. Raiteri, M. Busso, R. Gallino, G. Picchio, and L. Pulone, Astrophys. J. **367** (1991) 228.

[2] F. Käppeler, M. Wiescher, U. Giesen, J. Görres, I. Baraffe, M.id, C.M. Raiteri, M. Busso, R. Gallino, M. Limongi, and A. Chieffi, Astrophys. J. **437** (1994) 398.

[3] O. Staniero, A. Chieffi, M. Limongi, M. Busso, R. Gallino, and C. Arlandini, Astrophys. J. **478** (1997) 332.

[4] R. Gallino, C. Arlandini, M. Busso, M. lugaro, C. Travaglio, O. Straniero, A. chieffi, and M. Limongi, Astrophys. J. **497** (1998) 388.

[5] R.G. Couch, H. Spinka, T.A. Tombrello, and T.A. Weaver, Nucl. Phys. **A175** (1971) 300.

[6] J. Görres, C. Arlandini, U. Giesen, M. Heil, F. Käppeler, H. Leiste, E. Stech, and E. Wiescher, Phys. Rev. **C62** (2000) 055801

[7] C. Angulo et al., Nucl. Phys. **A656** (1999) 3.

[8] R.B. Vogellar, T.R. Wang, and R.W. Kavanagh, Phys. Rev. **C42** (1990) 753

[9] U. Giesen, C.P. Browne, J. Görres, J.G. Ross, M. Wiescher, R.E. Azuma, J.D. king, J.B. Vise, and M. Buckby, Nucl. Phys. **A567** (1994) 146

[10] A. Jorissen, V.V. Smith, and D.L. Lambert, Astron. Astrophys. **261** (1992) 164

[11] J. Lattanzio, M. Forestini, in 'Asymptotic Giant Branch Stars', IAU Symposium #191, Edited by T. Le Bertre, A. Lebre, and C. Waelkens. p. 31 (1999).

First Gamma-Spectroscopic Study of the r-Process Waiting-Point Nucleus ^{130}Cd

A. Wöhr[1], A. Ostrowski[2], K.-L. Kratz[2], I. Dillmann[2], A.M. El-Taher[2,3], V. Fedoseyev[4], L. Fraile[4], H. Fynbo[4], U. Köster[4], B. Pfeiffer[2], H.L. Ravn[4], M. Seliverstov[5], J. Shergur[1], L. Weissman[4], W.B. Walters[1], and the ISOLDE Collaboration[4]

[1] *Department of Chemistry, University of Maryland, Maryland, USA*
[2] *Institut für Kernchemie, Universität Mainz, Mainz, Germany*
[3] *Al-Azhar University, Assiut, Egypt*
[4] *CERN, Geneva, Switzerland*
[5] *Russian Academy of Sciences, Institut of Spectroscopy, Troitzk, Russia*

The understanding of explosive nucleosynthesis processes in stars requires various nuclear properties of about 6000 nuclei from β-stability to the drip lines. To use exclusively nuclear model predictions for astrophysical calculations is one way to proceed, but the question of reliability comes up. A more reasonable approach is, however, to **measure** as many nuclear properties as possible. For example, experimental studies of very neutron-rich nuclides lying in or near the projected r-process path – in particular the classical "waiting-point" isotopes at the magic neutron shells N=50, 82 and 126 – in general serve two purposes, (i) provision of direct data for use in r-process calculations, and (ii) testing current theories from which nuclear properties of far-unstable isotopes are derived when no experimental data exist.

The N=82 r-process waiting-point isotope ^{130}Cd was first identified by Kratz et al. in 1986 [1] at CERN/ISOLDE, thus starting the era of experiments **in** the r-process path. At that time, with model predictions still varying between 30 ms and 1.2 s, its β-decay half-life ($T_{1/2}$) was measured with great experimental difficulties via multiscaling of so-called β-delayed neutrons to be (195±35) ms. It was quite satisfying to see that this value turned out to be in reasonable agreement with the $N_{r,\odot}(Z)\times\lambda_\beta \simeq$ const. waiting-point expectation of (180±20) ms, derived independently at that time by Hillebrandt. This correlation between the $T_{1/2}$ of ^{130}Cd and the observed solar r-abundance of its stable isobar ^{130}Te immediately became essential to constrain the equilibrium conditions of an r-process. And this

success strongly motivated our further experimental and theoretical nuclear-structure investigations, as well as detailed astrophysical r-process parameter studies (see, e.g. [2, 3]). It took more than a decade to repeat the above measurement at the new PS-Booster ISOLDE at CERN [4], now yielding a more precise $T_{1/2}$=(162±7) ms for ^{130}Cd. Since our first identification, several technical developments were necessary in order to perform the new experiments. The most important one has been the development and installation of a resonance-ionization laser ion source (RILIS) to achieve chemical selectivity for elements with high ionization potentials, such as Ag, Cd and Sn. For details of this technique, see e.g. [3]. Earlier, these elements could only be ionized by means of completely non-selective plasma ionization of the whole isobaric chain of the delivered mass. A further step to obtain the new results has been the application of a so-called neutron converter, which acts as a kind of "mini-spallation-source". With this set-up, the 1 GeV proton-beam of the PS-Booster is impinging on a Ta rod in close proximity of the ^{238}U target. The fast neutrons produced by the proton beam then induce fission of uranium. The big advantage of this method is, that no or very little of the proton-rich spallation products are produced in the target (for details. see e.g. [5]). In the case of A=130, in this way most of the five orders of magnitude higher, surface-ionized isobaric contamination of 29-m ^{130}Cs could be avoided. Only with this additional step of "selectivity" was it possible to perform the β- and γ-specroscopic measurements outlined below. After mass separation at the ISOLDE facility, the A=130 beam was transported to the detection position, where 3 HPGe detectors and a ΔE-E β-telescope were installed.

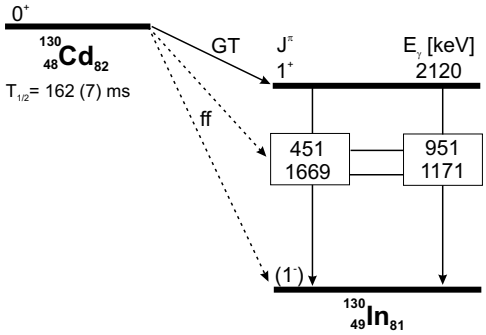

Figure 1: Proposed level scheme of ^{130}In.

Gamma-singles spectra, $\gamma\gamma$- and $\beta\gamma$-coincidence data were taken at A=130 for two different operation modes of the ion source. In surface-ionization mode ("laser-off") only indium was ionized. Hence, the corresponding spectra showed the (already known) γ-lines from the ^{130}In isomers and their β-decay daughters. Whereas with laser ionization ("laser-on") in addition to In also Cd was ionized and then mass-separated, too. By comparing the two types of spectra, the γ-lines from ^{130}Cd decay to ^{130}In could be identified unambiguously. From our preliminary data analysis, so far five new γ-lines at 451, 950, 1171, 1669 and 2120 keV and their coincidence relationships were observed. The resulting tentative decay scheme is shown in Fig. 1. It is clear that the main β-feeding (of Gamow-Teller (GT) type) from the $J^\pi=0^+$ ground state of ^{130}Cd goes to the level at 2120 keV. This $J^\pi=1^+$ state decays (i) directly and (ii) via the 451–1669 keV and the 950–1171 cascades to the ground state of ^{130}In. Since the coincident γ-lines of both cascades have similar intensities, we are not yet able to place their sequences unambiguously in the level scheme. There are several other candidates of Cd γ-lines, however their intensities are too weak to verify any coincidence relationships. It should be pointed out to the non-expert reader in this context, that the neutron-magic nuclide ^{130}Cd lies 14 units away from the heaviest stable isotope ^{116}Cd. Hence, ^{130}Cd is produced at least seven orders of magnitude less than the most abundant isotope in the Cd chain. We are thus faced with the situation to perform nuclear spectroscopy truely at the limits of both production and detection. Only a decade ago, such experiments were still believed to be impossible!

The most important and in fact surprising result is the position of the $\pi g_{9/2}$,$\nu g_{7/2}$, two-quasi-particle (2QP) 1^+ state at 2120 keV. It lies considerably higher than most models have predicted. This even includes the most recent full shell-model approaches [6, 7], which use large model spaces and fine-tuned residual interactions to reproduce known spectra around doubly-magic ^{132}Sn. The excitation energy of the lowest 2QP 1^+ state in ^{130}In and its feeding by GT-decay are of particular nuclear-structure interest for several reasons. First, it contains information about the proton-neutron interaction of the spin-orbit partners $\pi g_{9/2}$ and $\nu g_{7/2}$; furthermore, it will tell us about the sequence and spacing of the neutron single-particle (SP) states below the N=82 shell closure, in particular the $\nu h_{11/2}$ orbital. Finally, the combination of three correlated quantities, i.e. the Q_β value of ^{130}Cd, the GT-decay energy (Q_β–E_{1^+}) and the GT-feeding of the 1^+ state, will yield a complete nuclear-structure understanding of the β-decay half-life ($T_{1/2}$) of the probably most important r-process waiting-point nuclide ^{130}Cd.

Mass model predictions of the Q_β value of ^{130}Cd range from about 7.4 MeV (e.g. [8, 9]) up to about 8.5 MeV (e.g. [10, 11]), where recent experimental evidence seems to favour the "high" values (see, e.g. [3, 4]). Using these values in our standard QRPA shell-model calculations [12], with all other input parameters kept constant, results in an uncertainty of the predicted $T_{1/2}$ of a factor of about 3. Staying within the QRPA model, additional uncertainties are introduced by the choice of the nuclear potential (Nilsson, Woods-Saxon or Folded-Yukawa) and the pairing model (BCS or Lipkin-Nogami) when calculating the GT-decay. Depending on the actual choice of parameters, the position of the lowest 1^+ state in ^{130}In varies between 1.2 MeV and 2.8 MeV, the corresponding GT-feeding between 84% and 60%, and the respective log(ft) values between 4.1 and 4.4. With the Q_β value kept constant, this introduces another uncertainty factor of about 3.5. Taken together, we thus can "predict" any ^{130}Cd half-life between 100 ms and 1.15 s. When exclusively relying on the measured half-life, several model versions succeed to reproduce (or "predict") the required $T_{1/2}$ value with the correct (Q_β–E_{1^+}) energy difference, however with both individual parameters being wrong as we know by now. But, it should also be admitted that one of the oldest QRPA parameterizations using the Nilsson/BCS model with the Bengtsson–Ragnarsson κ- and μ-parameters [13], and a $Q_\beta \simeq 8.5$ MeV from [12], did predict the lowest 2QP 1^+ level in ^{130}In at 2.07 MeV as well as the GT-decay energy (Q_β–E_{1^+})$\simeq$6.43 MeV correctly, and consequently yielded a physically reliable $T_{1/2}$ prediction of 174 ms.

Recently and repeatedly, nuclear-structure theoreticians have argued that QRPA models were too simplistic, and that fully microscopic, selfconsistent shell-model approaches would be by far superior, also in their predictive power far from stability (see, e.g. [6]). Martinez-Pinedo has kindly provided us with the necessary details (in particular the Q_β value used and the E_{1^+} obtained), so that we can "check" the $T_{1/2}$ prediction for ^{130}Cd within his interacting shell model with our present experimental results. He uses the rather low Q_β=7.41 MeV from [9], and calculates an E_{1^+}=1.55 MeV and a $T_{1/2}$=161ms. Hence, in this case the GT-decay energy to the lowest 1^+ state is 5.86 MeV. Recently, also Brown et al. have performed shell-model calculations of nuclei in the ^{132}Sn region using the OXBASH code [7]. They use their selfconsistent Q_β=8.21 MeV and initially calculate an E_{1^+}=1.38 MeV, resulting in an 1 MeV higher GT-decay energy of 6.83 MeV than obtained by Martinez-Pinedo. After having been informed about our experimental E_{1^+}, in a second step Brown et al. lowered the $\nu h_{11/2}$ orbital by 200 keV

compared to what was assumed so far in ^{131}Sn and renormalized parts of the proton-neutron interaction. With this, they now were able to reproduce the E_{1^+} in ^{130}In within 180 keV, hence obtaining a GT-decay energy of 6.27 MeV. To remember, with the Q_β value from the mass evaluation of Audi et al. [12], we obtain an *"experimental"* GT-decay energy of (6.38±0.40) MeV.

To summarize, our new results on ^{130}Cd decay have added another nuclear-structure "surprise" in the ^{132}Sn region. With the inclusion of the new information about masses, SP levels and residual interactions, we plan to improve our local model predictions of so far unknown nuclear properties and test their implications of the formation of the A≃130 r-process abundance peak.

References

[1] K.-L. Kratz et al., Z. Physik **A325** (1986) 489.

[2] K.-L. Kratz et al., Ap. J. **403** (1993) 216.

[3] K.-L. Kratz et al., Hyperfine Interact. **129** (2000) 185.

[4] M. Hannawald et al., Phys. Rev. **C62** (2000) 054301.

[5] I. Dillmann et al., Eur. Phys. J. **A13** (2002), in print.

[6] G. Martinez-Pinedo et al., Phys. Rev. Lett. **83** (1999) 4502; and priv. comm.

[7] B.A. Brown et al., to be publ. (2002); and priv. comm.

[8] P. Möller et al., ADNDT **59** (1995) 185.

[9] J. Duflo and A.P. Zuker, Phys. Rev. **C52** (1995) R23.

[10] J.M. Pearson et al., Phys. Lett. **B387** (1996) 455.

[11] G. Audi et al., Nucl. Phys. **A624** (1997) 1.

[12] P. Möller and J. Randrup, Nucl. Phys. **A514** (1990) 1.

[13] T. Bengtsson and I. Ragnarsson, Nucl. Phys. **A436** (1985) 14.

Beta decay studies of neutron-rich $_{21}$Sc - $_{26}$Fe nuclei at GANIL

O. Sorlin[1], C. Donzaud[1], J. C. Angélique[2], F. Azaiez[1], C. Bourgeois[1], V. Chiste[1], Z. Dlouhy[3], S. Grévy[2], D. Guillemaud-Mueller, F. Ibrahim[1], K.-L Kratz[4], M. Lewitowicz[5], S.M. Lukyanov[6], J. Mrasek[3], Yu.-E. Penionzhkevich[6], F. de Oliveira Santos[5], B. Pfeiffer[4], F. Pougheon[1], M.G. Saint-Laurent[5], M. Stanoiu[5]

[1] *Institut de Physique Nucléaire, IN2P3-CNRS, F-91406 Orsay Cedex, France*
[2] *LPC, ISMRA, F-14050 Caen Cedex, France*
[3] *Nuclear Physics Institute, AS CR, CZ 25068, Rez, Czech Republic*
[4] *Institut für Kernchemie, Universität Mainz, D-55128 Mainz, Germany*
[5] *GANIL, B. P. 5027, F-14076 Caen Cedex, France*
[6] *FLNR, JINR, 141980 Dubna, Moscow region, Russia*

Recent astronomical observations of old stars in the galactic halo reveal the probable existence of a "weak" r-process component which would produce nuclei of masses below A=130 from neutron-rich progenitors [1, 2]. This "weak" r-process could extend down to light masses, and be responsible for the observation of correlated isotopic anomalies in the neutron-rich ^{48}Ca-^{50}Ti-^{54}Cr-^{58}Fe-^{64}Ni-^{66}Zn in certain inclusions of meteorites. Two entropy conditions can reproduce the correlated overabundances of Ca-Ti-Cr [3], observed in the EK1-4-1 inclusion.

At low entropy (S=10 $k_B/baryon$), the Ca-Ti-Cr isotopes are synthesized in an α-rich freeze out where essentially no free neutrons are available for subsequent neutron captures. The neutron-rich stable ^{48}Ca is formed directly, as calculated in an earlier study of B. Meyer et al [4].

At higher entropy (S=150 $k_B/baryon$), a weak r-process may be triggered by the presence of free neutrons after the charged-particle reactions freeze out. Under such conditions, ^{48}Ca is mainly generated by β-decay of neutron-rich progenitor ^{48}Ar. Similarily, the progenitor of ^{64}Ni would be possibly found at mass number 64 in the Cr isotopic chain if the beta-decay time of ^{64}Cr is shorter than its the neutron-capture time. In such a case, the neutron-capture flow would be depleted at the "turning point" ^{64}Cr to the higher Z chain.

The two processes mentionned above produce considerably different pat-

terns of abundances as a function of the mass number A (see Fig.2 of ref [3]). In particular, the low entropy scenario provides a somewhat low abundance of ^{64}Ni as compared to ^{48}Ca, a large overabundance of ^{66}Zn, and no nuclei synthesized beyond A=90. These three points seems contradictory to the observations of some FUN inclusions of the Allende meteorite ([5, 6, 7]). The high entropy scenario better fulfill the observations. It was calculated by W. Böhmer [8] using the code of C. Freiburghaus [9] in which the latest nuclear physics data for the neutron-rich progenitors have been included. However, the existing half-lives measurements did not extend far enough from stability in the region where the progenitors of ^{58}Fe, ^{64}Ni and ^{66}Zn should be found. The present contribution show new half-lives measurements in the neutron-rich Sc-Fe nuclei, aiming to found where the turning points at mass number A=58, 64, and 66 can be found in each isotopic chain.

The neutron-rich $^{57,58}_{21}$Sc, $^{58-60}_{22}$Ti, $^{60-63}_{23}$V, $^{62-66}_{24}$Cr, $^{64,68}_{25}$Mn and $^{68-70}_{26}$Fe isotopes have been produced at GANIL by the fragmentation of a 61.8 A.MeV ^{76}Ge^{30+} beam, of mean intensity 1 eμA, onto a ^{58}Ni target of 118 μm thickness. The nuclei of interest were separated by the LISE3 achromatic spectrometer which was tuned to optimize the transmission rate of very neutron-rich nuclei. The nuclei transmitted through the spectrometer were identified by means of 3 consecutive 300, 300, 1500 μm silicon detectors. The two first served for the energy loss and time-of-flight measurements. The last one, into which the nuclei were implanted, determined their residual energies. It was divided in sixteen 3 mm wide, 46 mm height vertical strips. The rate of nuclei implanted was about ten per minute in each strip. Each time a nucleus was implanted in one of the strips, the primary beam was switched off during 1 second to collect the beta-rays of its decay in the same strip. Beta-decay time spectra correlated with the implantation of $^{63-66}$Cr are shown in Fig 1. From the beta-decay studies of ^{60,62}V to ^{60,62}Cr, it has been found that the Cr isotopes are strongly deformed when approaching the neutron subshell closure N=40. This unexpected feature result in beta-decay half-lives which differ by up to an order of magnitude with the theoretical predictions of P. Möller. The half-lives of the Ti and Cr isotopes are reported on Fig 2 and compared to neutron-capture times calculated by Th. Rauscher et al. [10] for neutron density condition of d_n=6.10^{20} cm^{-3}. It is seen that a turning point occurs in the Cr chain at ^{64}Cr, the beta decay time of ^{64}Cr being shorter than its neutron capture time. As a consequence, the Cr chain will mainly feed the ^{64}Ni isotope, and to a much weaker extend the ^{66}Zn isotope since the major part of the neutron-capture flow is already depleted at the mass number 64. Since no branching point at A=66 is expected in any of the higher Z isotopic chains, it is surmised that the

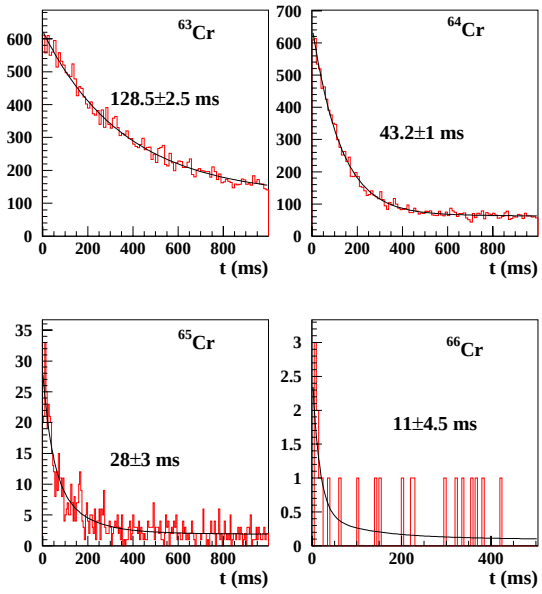

Figure 1: Beta-decay curves of Cr isotopes. The corresponding half-lives are included for each isotope.

^{66}Zn will be underproduced by this process. Similarly, a branching point occurs at ^{58}Ti, which would be reinforced a somewhat weaker neutron density. The most probable progenitor of the neutron-rich stable ^{58}Fe is ^{58}Ti. This process naturally explains large correlated overabundances of ^{58}Fe and ^{64}Ni, and an underabundance of ^{66}Zn. It is, therefore, a very promising scenario to account for the observed isotopic anomalies in the FUN inclusions of meteorites.

References

[1] C. Sneden et al., Astroph. J. **496** (1998) 235.

[2] J.W. Truran et al., Nucl. Phys. A **688** (2001) 330c.

[3] K.L. Kratz et al., proceedings in Memorie della Societa Astronomica Italiana (2000) **72** N2 (2001).

[4] B.S. Meyer et al., Astroph. J. **462** (1996) 825.

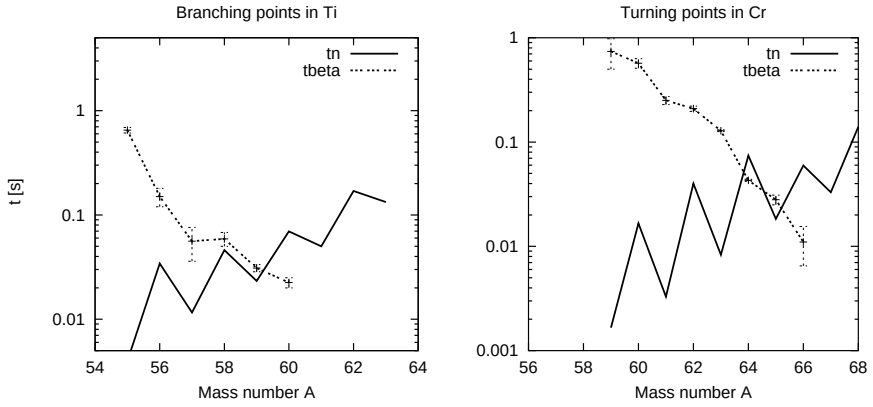

Figure 2: Comparisson between neutron-capture times (tn) and beta-decay times (tbeta) in the Ti and Cr isotopic chains.

[5] J.L. Birck and G. W. LugmairEarth and Planetary Science Letters 90 (1988) 131.

[6] R.D. Loss and G.W. Lugmair, Astroph. J. **360** (1990) L59.

[7] G.W. Lugmair et al., Lunar and Planetary Science **IX** (1978) 672.

[8] W. Böhmer, Diploma Thesis, University of Mainz 1996.

[9] C. Freiburghaus, Diploma Thesis, University of Basel 1995.

[10] T. Rauscher et al., in proceedings of the ENAM95 conference, Editions Frontieres, eds. M. de Saint Simon and O. Sorlin, Arles, France, June 1995, page 683.

An s-Process Origin of ^{180}Ta^m?

K. Wisshak[1], F. Voss[1], C. Arlandini[1], F. Bečvář[2], R. Gallino[3], M. Heil[1], F. Käppeler[1], M. Krtička[2], S. Masera[3], R. Reifarth[1], O. Straniero[4], and C. Travaglio[5]

[1]Forschungszentrum Karlsruhe, Institut für Kernphysik, D-76021 Karlsruhe, Germany
[2]Charles University, Prague, Czech Republic
[3]Dipartimento di Fisica Generale, Università di Torino and INFN, Sezione di Torino, Via P. Giuria 1, I-10125 Torino, Italy
[4]Osservatorio Astronomico di Collurania, I-64100 Teramo, Italy
[5]Max-Planck Institut für Astrophysik, Karl-Schwarzschild-Str. 1, D-85748 Garching, Germany

16.1 Introduction

For two reasons ^{180}Ta^m is a unique nucleus: it is the rarest stable isotope found in the solar system, and it is the only isotope that is stable in the isomeric state. The rarity of ^{180}Ta^m reflects the difficulty of its production. In fact, at first glance the common processes for synthesizing the heavy elements, including the s, r, and p processes, seem to fail in this case.

This is illustrated in Fig. 1, which shows that the decay chains from the r- and p-process regions end at the stable isobars ^{180}Hf and ^{180}W, and that main s-process reaction path (indicated by thick arrows) is completely bypassing ^{180}Ta^m via the (n,γ) sequence along the stable hafnium isotopes.

Marginal feeding of ^{180}Ta^m can be achieved, however, by two minor branchings of the s path. The decay of the 8^- isomeric state in ^{180}Hf, which is weakly populated by neutron capture on ^{179}Hf has been shown to account for about 20% of the observed ^{180}Ta^m abundance [1, 2]. This contribution is well determined by the partial cross section to the ^{180}Hf isomer.

The second branching to ^{180}Ta^m [3, 4] occurs, because the $7/2^-$ state at 214 keV in ^{179}Hf, which can be thermally populated in the hot stellar photon bath, is unstable against β-decay to ^{179}Ta. This mechanism results in a small ^{179}Ta abundance which acts as a seed for neutron captures feeding ^{180}Ta^m. In contrast to the first branching, this route depends strongly on temperature, indicating that the ^{180}Ta^m abundance may be interpreted as a sensitive stellar thermometer [5].

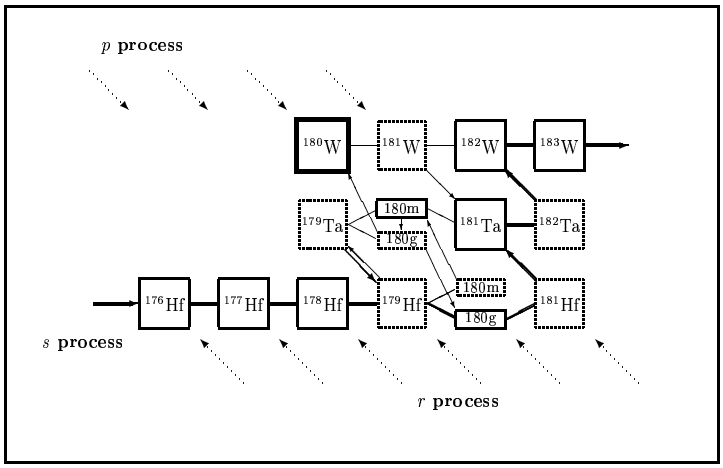

Figure 1: The reaction path of the s process in the Hf/Ta/W region. Though the main reaction path (thick arrows) is bypassing $^{180}\mathrm{Ta}^m$, this rare isotope can in fact be produced by neutron captures on ^{179}Ta and through β-decays of a weakly populated isomer in ^{180}Hf, which are the result of minor branchings at A=179 and 180.

Since the second branching opens only at relatively high temperatures, its efficiency for producing $^{180}\mathrm{Ta}^m$ is challenged by the possibility that the freshly produced $^{180}\mathrm{Ta}^m$ may be immediately destroyed by thermally induced depopulation to the short-lived ground state [5]. Though direct IT decay can be excluded because of selection rules, this depopulation can be achieved by excitation of an intermediate state with decay channels to the ground state. Many attempts have been made to locate the position of the lowest intermediate state.

Several mediating states could be identified by a Munich - Stuttgart - Darmstadt - Karlsruhe collaboration, the lowest being located at 1.01 MeV excitation energy [6]. That this state can already be reached at typical s-process temperatures, implies that $^{180}\mathrm{Ta}^m$ can not survive in the constant temperature scenario of the classical approach. Instead, it was found that the highly convective situation during He shell flashes in thermally pulsing low mass AGB stars favors the s-process production of $^{180}\mathrm{Ta}^m$ due to rapid mixing of freshly synthesized material into cooler outer zones, where temperatures are too low for affecting the half-life of $^{180}\mathrm{Ta}^m$.

After the temperature-dependence of the $^{180}\mathrm{Ta}^m$ half-life yield had been settled, the important next problem was to measure the stellar (n,γ) cross

section of $^{180}Ta^m$, which determines the expected abundance. Since tantalum is situated in a mass region where the so-called local approximation ($\langle\sigma\rangle N_s$ = const.) holds, the primary production yield is to good approximation inversely proportional to the cross section. While experimental data were completely missing, the available data from statistical model calculations differed by almost a factor two [5, 7, 8].

16.2 The (n,γ) measurement

The measurement was carried out in the neutron energy range from 10 to 100 keV using gold as a standard. Neutrons were produced via the ^{7}Li(p,n)^{7}Be reaction with the pulsed proton beam of the Karlsruhe 3.7 MV Van de Graaff accelerator. The neutron energy was determined by time of flight (TOF), the samples being located at a flight path of 79 cm. The proton energy was adjusted 30 keV above the reaction threshold resulting in a continuous neutron spectrum from 10 to 100 keV. Capture events were detected with the Karlsruhe 4π BaF_2 array [9] by registration of the prompt capture γ-ray cascades. The detector array consists of 41 hexagonal and pentagonal crystals forming a spherical shell of BaF_2 with 10 cm inner radius and 15 cm thickness. It is characterized by a resolution in γ-ray energy of 7% at 2.5 MeV, a time resolution of 500 ps, and a peak efficiency of 90% at 1 MeV. The sum energy spectrum of the capture cascades was taken with a 1.7 MeV threshold, corresponding to efficiencies of 99% and 95% for capture events in $^{180}Ta^m$ and gold, respectively.

Together with the $^{180}Ta^m$ sample (the same as in the photoactivation experiment, i.e. 150 mg oxide powder with 5.5% enrichment in $^{180}Ta^m$), a set of additional samples in identical graphite containers was mounted on a sample ladder: a gold sample for determining the neutron flux, a natural tantalum sample for simulating the effect of ^{181}Ta, as well as an empty container and an empty position in the sample ladder for measuring various background components. The total beam time of the experiment was 45 days.

Fig. 2 shows the γ-ray spectrum of capture events in the enriched Ta-sample, which is dominated by the 6.06 MeV line from captures on ^{181}Ta, but $^{180}Ta^m$ events are clearly visible as well. The separation of the two components was carried out in two different ways: (i) by subtracting the ^{181}Ta contribution by means of the data recorded with the natural sample, and (ii) by fitting both components independently using a parameter systematics for the line shapes which was derived from corresponding analyses of more than 50 isotopes measured with the 4π BaF_2 detector so far. The

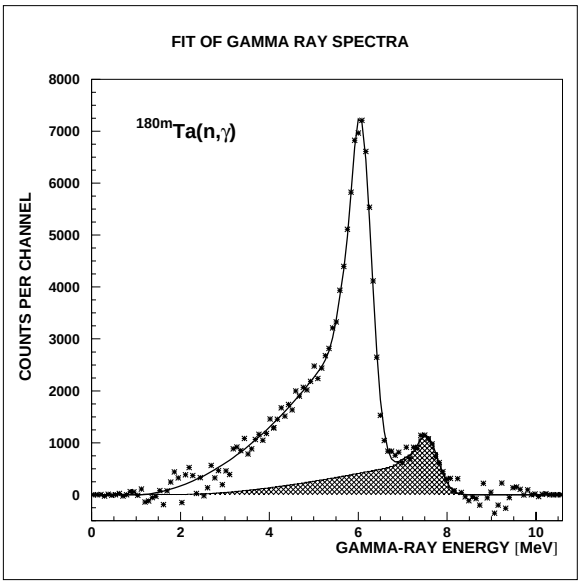

Figure 2: The γ-ray spectrum of capture events in the enriched tantalum sample, showing the two components due to captures on $^{180}\mathrm{Ta}^m$ (dashed area) and ^{181}Ta.

Table 1: Stellar neutron capture cross section of $^{180}\mathrm{Ta}^m$

kT (keV)	$<\sigma v>/v_T$ (mbarn)	Uncertainty (mbarn)		
		stat.	syst.	tot.
8	3059	185	156	242
10	2695	153	137	205
15	2143	109	109	154
20	1824	88	93	128
25	1613	75	82	111
30	1465	66	75	100

result of the second technique is indicated by the shaded area in Fig. 2. The cross sections obtained in these ways agree within $\pm 2.5\%$. More details on the numerical results and the respective uncertainties can be found in Refs. [10, 11].

The Maxwellian average cross sections, which are summarized in Table 1, exhibit uncertainties of about 5%. It is important to note that the measured values are significantly lower compared to all theoretical predictions.

16.3 Production of $^{180}Ta^m$ in Red Giants

The canonical approach for describing the s process [12] can not account for the origin of $^{180}Ta^m$. The photoactivation experiment [6] showed that the half-life of $^{180}Ta^m$ is reduced to less than 10 yr for temperatures in excess of T_8=2 (T_8 = temperature in units of 10^8 K). In view of the physical conditions characteristic for the classical approach, i.e. temperatures of T_8=2.5±0.4 and a duration of 10^4 y [13], this implies that $^{180}Ta^m$ could not survive the s process.

For the more complex stellar s-process model, however, the fate of $^{180}Ta^m$ is completely different. It is currently accepted that the main s-process component between A=90 and 209 is produced during recurrent thermal instabilities in the AGB phase of 1.5 to 3 $M_\odot$ mass stars [14, 15, 16]. In this scenario, about 95% of the neutron irradiation occurs via the $^{13}C(\alpha, n)^{16}O$ reaction between thermal instabilities at comparably low temperatures of T_8=1, where ^{179}Hf and $^{180}Ta^m$ are both stable. During thermal instabilities, however, temperatures of T_8=2.5 - 3 are reached for a few years, resulting in a second neutron burst due to the activation of the $^{22}Ne(\alpha, n)^{25}Mg$ reaction. At these higher temperatures, ^{179}Hf becomes unstable, thus opening the neutron capture sequence from ^{179}Ta to $^{180}Ta^m$. Since the prolific energy production in these He shell flashes creates a highly convective zone with turnover times of less than a few hours [11], freshly produced $^{180}Ta^m$ is effectively mixed into cooler regions where it survives and from where it is eventually mixed into the stellar envelope.

The large gradient in temperature ($0.2 \leq T_8 \leq 3$) and density ($10 \leq \rho \leq 10^4$ g cm^{-3}) implies that - according to the result of the photoactivation measurement [6] - the effective lifetime of $^{180}Ta^m$ varies by more than 15 orders of magnitude between the top and the bottom of the convective zone. The production and survival of $^{180}Ta^m$ was followed in detail by dividing this convective zone into 25 meshes of equal extension, where the physical conditions could be considered constant per each time-step. The time evolution of each mesh was obtained by the stellar evolution model, which accounts also for the respective changes from pulse to pulse along the AGB evolution [16]. The nucleosynthesis was followed in each mesh separately, and the resulting abundances were periodically mixed to account for the typical turnover time of the convective zone.

It is evident that high temperatures prevail only in a relatively small zone near the bottom of the convective zone, where also the s-process takes place. As long as the turnover time is short compared to the actual half-life, most of the produced $^{180}Ta^m$ is rapidly brought to the outer and cooler zones of

the convective region where it survives unaltered. For this scenario, it was found that ∼85% of the solar $^{180}\mathrm{Ta}^m$ abundance can be produced, almost independent of the stellar mass or metallicity. Hence this value determines also the average over galactic chemical evolution at the epoch of solar system formation, strongly suggesting an *s* process origin of $^{180}\mathrm{Ta}^m$.

The main residual uncertainties in the *s*-process yield of ^{180m}Ta are due to the stellar half-life of ^{179}Hf and the (n,γ) cross section of ^{179}Ta. Variation of these quantities within plausible limits of ±30% would change the ^{180m}Ta abundance by 15 and 25%, respectively. While the part of the half-life might be difficult to improve, a measurement of the ^{179}Ta cross section remains an experimental challenge for a conclusive analysis of the *s*-process origin of ^{180m}Ta.

References

[1] H. Beer and R. Ward, Nature **291**, 308 (1981).

[2] S. Kellogg and E. Norman, Phys. Rev. C **46**, 1115 (1992).

[3] K. Yokoi and K. Takahashi, Nature **305**, 198 (1983).

[4] K. Takahashi and K. Yokoi, Atomic Data Nucl. Data Tables, **36** 375 (1987).

[5] Z. Németh, F. Käppeler, and G. Reffo, Ap. J. **392**, 277 (1992).

[6] D. Belic *et al.*, Phys. Rev. Lett. **83**, 5242 (1999).

[7] H. Beer and R. Macklin, Phys. Rev. C **26**, 1404 (1982).

[8] J. Holmes, S. Woosley, W. Fowler, and B. Zimmerman, Atomic Data and Nucl. Data Tables **18**, 305 (1976).

[9] K. Wisshak *et al.*, Nucl. Instr. Meth. A **292**, 595 (1990).

[10] K. Wisshak *et al.*, Technical report, Report FZKA-6362, Forschungszentrum Karlsruhe.

[11] K. Wisshak *et al.*, Phys. Rev. Lett. **87**, 251102 (4) (2001).

[12] F. Käppeler *et al.*, Ap. J. **354**, 630 (1990).

[13] F. Käppeler, K. Toukan, M. Schumann, and A. Mengoni, Phys. Rev. C **53**, 1397 (1996).

[14] O. Straniero *et al.*, Ap. J. **440**, L85 (1995).

[15] O. Straniero *et al.*, Ap. J. **478**, 332 (1997).

[16] R. Gallino *et al.*, Ap. J. **497**, 388 (1998).

Astrophysical implications of Xe(n,γ)-measurements

R. Reifarth[1], *R. Gallino*[2], *F. Käppeler*[1], *F. Voss*[1], *K. Wisshak*[1]

[1] *Forschungszentrum Karlsruhe, Institut für Kernphysik, Postfach 3640, D-76021 Karlsruhe, Germany*
[2] *Dipartimento di Fisica Generale, Università di Torino and INFN, Sezione di Torino, Via. P. Giuria, I-10125 Torino, Italy*

17.1 Introduction

About 50 % of the elements beyond iron are produced via slow neutron capture nucleosysnthesis (s process). Starting at iron seed, the s-process mass flow follows the valley of stability. If different reaction rates are comparable, the s-process path branches and the branching ratio reflects the physical conditions in the interior of the star.
Xenon is one of the six elements with two s-only isotopes. If one of these isotopes is partly bypassed by the s-process reaction flow, these cases are best suited for quantitative branching analyses. The actual branching at ^{128}I is independent of the neutron flux, but is completely determined by competition between β^- and electron capture decays (see Figure 1). Accordingly, the resulting abundance pattern represents a sensitive test for the temperature and electron density profiles predicted by various s-process models.

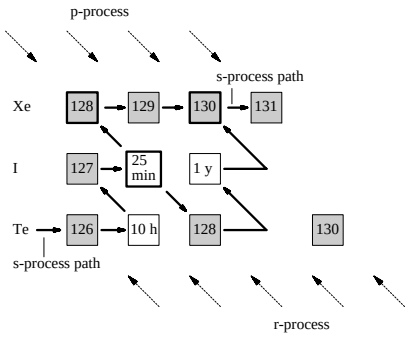

Figure 1: Simplified picture of the s-process path in the iodine region. The s-only isotopes ^{128,130}Xe are affected by the temperature dependent branching at ^{128}I. In contrast to ^{130}Xe ^{128}Xe is partly bypassed by the reaction flow.

17.2 Astrophysical facts

Figure 2 shows the Maxwellian averaged neutron capture cross sections of the *s*-only Xe-isotopes 128 and 130 derived from Ref. [1]. The cross section ratio $^{128}\sigma/^{130}\sigma$ could be determined with a typical uncertainty of 2 % over the whole astrophysically interesting energy range between 8 and 100 keV. For the solar abundance ratio N_{128} / N_{130} one finds 0.510 ± 0.005 [2]. While

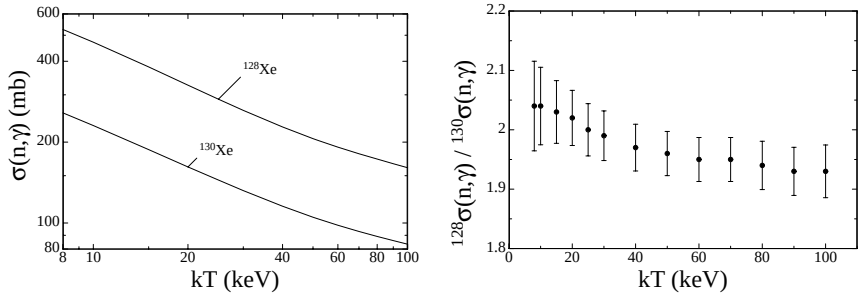

Figure 2: The Maxwellian averaged cross sections of ^{128,130}Xe as a function of the stellar temperature (left), and the cross section ratio ^{128}Xe / ^{130}Xe, which is important for *s*-process analyses (right).

the solar ratio contains *s*- and *p*-process contributions, the average isotopic ratio of 0.447 ± 0.003 found in presolar SiC grains [3] is considered to be *s*-only. The temperature and electron density dependence of the branching ratio has been adopted from Ref. [4].

17.3 ^{128,130}Xe during the *s* process

A classical *s*-process analysis with kT=30 keV predicts an abundance ratio N_{128} / N_{130} of 0.51 ± 0.02. This would imply that the branching at ^{128}I is closed and that there are equal *p*-process contributions to both *s*-only isotopes, in clear contradiction to the *p*-process models which predict *p* contributions of 10 % for ^{128}Xe and only 2 % for ^{130}Xe, respectively.
The stellar model [5] yields an *s*-process abundance ratio of 0.485 ± 0.015 leaving a 5 % higher *p*-process contribution to ^{128}Xe than to ^{130}Xe. Within uncertainties this value is in fair agreement with the *p*-model predictions. However, the very low abundance ratios found in some presolar grains of *s*-process origin [3] are difficult to explain with the stellar model.

17.4 The solar Xe abundance

Based on the *s*-process analysis it is possible to normalize the ^{130}Xe abundance to the well defined abundances in the rare earth region. Applying this method the classical approach and the stellar model differ by less than 1.5 %. Given the isotopic abundance of ^{130}Xe [2] one can determine the solar xenon abundance with almost ten times better accuracy than previously achieved. We suggest a solar xenon abundance of $N_{\odot} = 5.39 \pm 0.22$ relative to 10^6 Si atoms.

References

[1] R. Reifarth, F. Käppeler, F. Voss, K. Wisshak, *Nucl. Phys.* **A688** (2001) 229.

[2] R.O. Pepin , R.H. Becker , P.E. Rider , *Geochim. et Cosmochim. Acta* **59** (1995) 4997.

[3] R.S. Lewis, S. Amari, E. Anders, *Geochim. et Cosmochim. Acta* **58** (1994) 471.

[4] K. Takahashi, K. Yokoi, *Atomic Data and Nuclear Data Tables* **36** (1987) 375.

[5] R. Gallino et al., *Ap. J.* **497** (1998) 388.

Weak Interactions in the Supernova Environment

J.M. Sampaio

Institut for Fysik og Astronomi, Århus Universitet, Denmark

18.1 Weak interactions on nuclei

The role of weak interactions in the evolution of a core collapse supernova is twofold. They determine the energy transport during the collapse and they are responsible for the evolution of the matter composition inside the core [1]. Therefore, a robust simulation of core collapse supernovae, requires a good knowledge of nuclear and weak interactions physics in the supernova environment.

In the low-energy limit it is sufficient to consider only the allowed transitions. The allowed Fermi (F) and Gamow-Teller (GT) operators are:

$$F^{\pm,0} = \sum_{n=1}^{A} \tau^{\pm,0}(n) \qquad GT^{\pm,0} = g_A \sum_{n=1}^{A} \sigma(n)\tau^{\pm,0}(n) \tag{7}$$

where $\tau^{\pm,0}(n)$ and $\sigma(n)$ are the 1-nucleon isospin and spin spherical operators and g_A is the axial coupling constant. The F operator commutes with all parts of the nuclear Hamiltonian, excluding the weak coulomb term. Thus, the F strength is well concentrated in a single state known as the Isobaric Analogue State (IAS). The GT operator mixes the spin and isospin spaces and does not commute with the nuclear Hamiltonian. Thus, the GT strength is scattered through several states. However, most of the strength is concentrated at excitation energies around the GT Giant Resonance (GTGR).

In our work the GT strength distributions were derived from large-scale shell-model calculations within the complete pf shell [2]. A reliable description of the weak interaction rates at low temperatures and densities can be obtained by considering explicitly the GT distributions built on the low-lying states. However, at higher temperatures and densities regimes, states at higher excitation energies become increasingly important. A complete shell-model calculation of the GT distributions for all relevant states in a given nucleus is not feasible with the present computer capabilities. Therefore we introduced the backresonances in our calculations [3]. These are

important transitions due to the large matrix elements and increased phase-space. They were obtained from the inversion of the GT distributions built on the low-lying states of the daughter nucleus [4].

18.2 Neutrino spectra from electron captures

Core collapse simulations require detailed bookkeeping of the neutrino spectra. Fig. 1 shows the shell-model calculations of the neutrino spectra (solid lines) for the six nuclei that dominate the electron captures in the presupernova model of a $15M_\odot$ star [5]. Furthermore we provide a parametrization to easily implement them in collapse codes (dashed lines) [6]:

$$n(E_\nu) = E_\nu^2 (E_\nu - q)^2 \frac{N}{1 + \exp(\frac{E_\nu - q - \mu_e}{T})} \tag{8}$$

where E_ν is the neutrino energy, μ_e is the electron chemical potential, N a normalization constant and q was taken as a fit parameter adjusted to the average neutrino energy. For comparison we show the parametrization of Bruenn [7] where it is assumed a 3 MeV splitting between the f orbitals (dot-dashed lines).

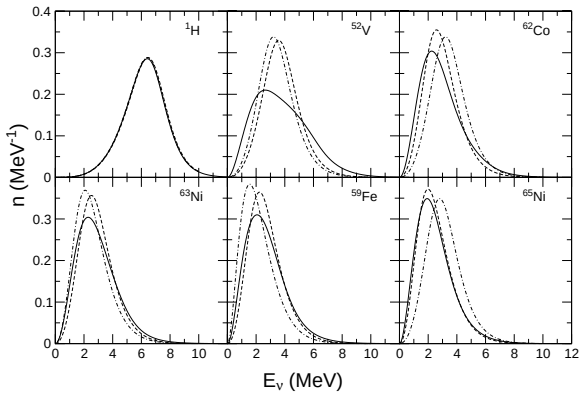

Figure 1: Normalized neutrino spectra from stellar electron captures in the presupernova model of a $15M_\odot$ star. The stellar parameters are $T = 1.2\times10^9$ K, $\rho = 9.1 \times 10^9$ gcm^{-3} and $Y_e = 0.43$. The resulting chemical potential is then $\mu_e = 8.1$ MeV.

Eq. (8) can be derived assuming: (i) the electron capture on the parent nucleus ground-state leads to a single state in the daughter nucleus at an energy E_i and (ii) the Brink hypothesis is valid, that is, if the capture is on

an excited state in the parent at an energy E_i, then the final state in the daughter is at $E_f + E_i$. This proposal reproduces, in general, the shell-model spectra rather well. However, we note that for ^{52}V the shell-model spectrum is wider than the parametrization. This is due to the fact that some specific states in this nucleus do not follow the Brink hypothesis.

18.3 Neutrino reactions on nuclei

To evaluate the effects of finite temperature on the neutrino-induced reactions, we split the cross sections into two parts. One describes the states that follow the Brink hypothesis and the second describes the backresonances contribution. If the Brink hypothesis is valid, it can be shown that the nuclear response is independent of the temperature. Therefore the temperature-dependence of the cross sections is solely related to the excitation of the backresonances.

Fig. 2 shows the temperature-dependence of the electron neutrino absorption cross sections for ^{59,61}Fe and ^{60,62}Co. In all cases the low-energy cross sections are enhanced relative to the ground-state. However, for the collapse conditions, the cross sections are dominated by the final electron Pauli blocking. Therefore they are strongly suppressed and it is not expected that neutrino absorption can compete with inelastic neutrino scattering on electrons and nuclei. Neutrino absorption at higher energies is also important during the collapse, but our calculations show that the temperature effects are negligible [8].

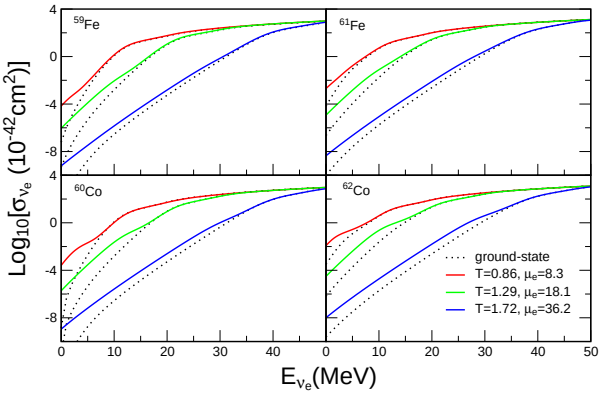

Figure 2: Absorption cross sections of electron neutrinos on selected neutronrich nuclei, including the final electron Pauli blocking. Temperatures T and chemical potentials μ_e are in MeV.

Fig. 3 shows the temperature-dependence of the neutrino scattering cross sections for ^{56,59}Fe and ^{56,59}Co. In all cases the low-energy cross section are enhanced relative to the ground-state. This is particularly remarkable for ^{56}Fe due to pairing structure effects. For even-even nuclei (like ^{56}Fe) there are no low-lying transitions available in the GT_0 distribution built on the ground-state. Consequently, at $T = 0$, the cross section drops rapidly to zero as the energy approaches the reaction threshold (dotted line). At finite-temperature the gap below this threshold is then filled up by thermal population of the backresonances. For the odd-A nuclei and odd-odd nuclei there are sizable low-lying transitions in the GT_0 distribution built on the ground-state. Thus, there is essentially no threshold at $T = 0$ and the increase of the low-energy cross section with temperature is much less dramatic than for even-even nuclei [9]. Nevertheless, our results seems to imply that inelastic neutrino-nucleus scattering is larger at low energies than assumed in [10] by more than an order of magnitude.

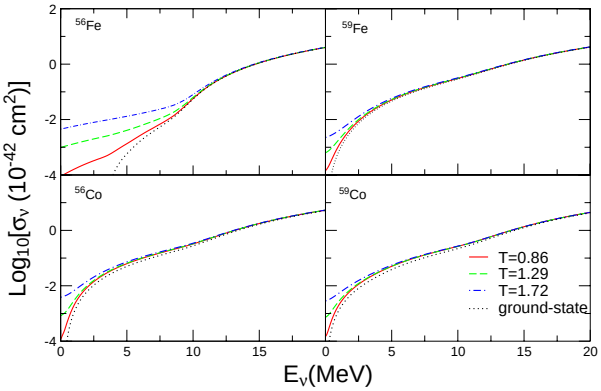

Figure 3: Scattering cross sections of neutrinos on selected neutronrich nuclei. Temperatures T are in MeV.

We further note that the cross sections for the ^{59}Fe, ^{56}Co and ^{59}Co are quite similar at finite-temperature, while for ^{56}Fe, the low-lying states of the GT_0 distribution breaks this similarity at low energies. This indicates that neutrino-nucleus scattering, at least for odd-A and odd-odd nuclei, can be represented by an "average nucleus" for easy implementation in core collapse simulations. Therefore the GT_0 systematics for the relevant nuclei is currently being investigated.

Finite-temperature allows for neutrino upscattering through nuclear de-excitation of the backresonances. The neutrino spectra as a function of the

outcoming neutrino energy shows the relative importance of the down- and upscattering components. This is shown in Figs. 4 for incoming $E_\nu = 7.5$ MeV and $E_\nu = 20$ MeV neutrinos. For $E_\nu = 7.5$ MeV neutrinos the GT_0 resonances can not be reached in the downscattering direction. Thus, upscattering is quite remarkable due to the thermal population of the backresonances. For the other three nuclei almost all of the neutrinos are downscattered by the low-lying GT_0 ground-state strength. Therefore upscattering is negligible. The $E_\nu = 20$ MeV neutrinos can always reach the GT_0 resonances (at excitation energies around 10 MeV) in all four cases. Consequently neutrino downscaterring dominates the cross sections independently of the temperature. We note, however, that quantitative calculations of neutrino cross sections for these energies must include forbidden transitions, but they do not change our conclusion that finite-temperature effects can be neglected for $E_\nu > 10$ MeV.

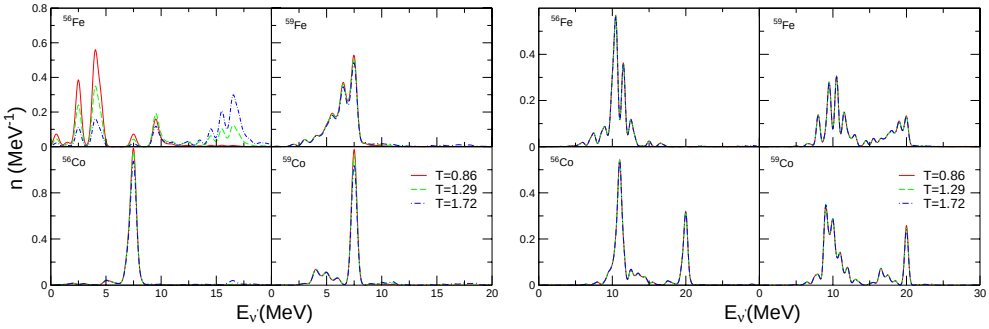

Figure 4: Normalized neutrino spectra from neutrino scattering on nuclei at finite-temperature. Left figure corresponds to $E_\nu = 7.5$ MeV neutrinos. Right figure corresponds to $E_\nu = 20$ MeV neutrinos. Temperatures T are in MeV.

18.4 Electron captures on neutronrich nuclei

Electron captures during the collapse drives the matter to more neutronrich nuclei. Current models predict that the electron captures stop for nuclei with neutron numbers above the pf shell closure $N = 40$. Since GT transitions can only change the nucleons inside a major shell, those transitions are Pauli blocked for nuclei with $N > 40$ and $Z < 40$. This picture is wrong for two reasons: (i) Thermal excitation can promote protons and neutrons to the gds orbitals and (ii) The residual interactions between nucleons mixes the $g_{9/2}$ orbital with the pf shell. Both mechanisms unblock the GT transitions.

Shell-model diagonalization of the full pf+gds shells is not feasible with the present computer capabilities due to the large model space. A hybrid model has been proposed in [11] to carry out this task. The capture rates are calculated within the Random Phase Approximation (RPA) model. The occupation numbers are provided as a function of the temperature by Shell-Model Monte Carlo calculations (SMMC), including an appropriate pairing+quadrupole interaction. In this way we can incorporate relevant features of the nuclear structure, avoiding the sign problem associated with SMMC calculations.

Calculations of electron captures rates on the relevant nuclei above $A = 65$ are currently undergoing. The rates will be provided along a stellar trajectory as a function of the final neutrino energy.

Acknowledgements

The work has been supported by the Danish Research Council. The author acknowledges the financial support of the Portuguese Foundation for Science and Technology.

References

[1] H.A. Bethe, Rev. Mod. Phys **62** (1990) 801.

[2] E. Caurier *et al*, Nucl. Phys. A **653** (1999) 439.

[3] G. M. Fuller, W. A. Fowler, M. J. Newman, Ap. J. S. **42** (1980) 447 and **48** (1982) 279.

[4] K. Langanke and G. Martínez-Pinedo, Nucl. Phys. A **673** (2000) 481.

[5] A. Heger *et al*, Ap. J. **560** (2001) 307.

[6] K. Langanke, G. Martínez-Pinedo and J. M. Sampaio, Phys. Rev. C **64** (2001) 055801.

[7] S. W. Bruenn, Ap. J. S. **58** (1985) 771.

[8] J. M. Sampaio, K. Langanke and G. Martínez-Pinedo, Phys. Lett. B 511, 11 (2001).

[9] J. M. Sampaio *et al*, Phys. Lett. B (accepted).

[10] S. W. Bruenn and W. C. Haxton, Ap. J. **376** (1991) 701.

[11] K. Langanke, E. Kolbe and D. J. Dean, Phys. Rev. C **63**, (2001) 032801.

New Measurement of the $^7Be(p,\gamma)^8B$ NuclearCross Section and Impact on the Solar Neutrino Fluxes

Gianluca Imbriani [1,2], *Oscar Straniero*[3] *and Filippo Terrasi*[2,4]
for the NABONA collaboration

[1] *Institut für Physik mit Ionenstrahlen, Ruhr-Universität-Bochum, Bochum (Germany)*
[2] *Istituto Nazionale di Fisica Nucleare sezione di Napoli, Napoli (Italy)*
[3] *Osservatorio Astronomico V.Cerulli, Collurania, Teramo (Italy)*
[4] *Dipartimento di Scienze Ambientali, Seconda Universitá di Napoli, Caserta (Italy)*

The Sun is burning hydrogen mostly ($\simeq 99\%$) by means of the p-p chain. Five of the reactions involved in this chain produce neutrinos:

$$\begin{cases} p + p & \rightarrow {}^2H + e^+ + \nu & \mathbf{pp} \\ p + e^- + p & \rightarrow {}^2H + \nu & \mathbf{pep} \\ {}^3He + p & \rightarrow {}^4He + e^+ + \nu & \mathbf{hep} \\ {}^7Be + e^- & \rightarrow {}^7Li + \nu \quad (90\%) & \mathbf{^7Be} \\ {}^7Be + e^- & \rightarrow {}^7Li^* + \nu & \mathbf{^7Be^*} \\ {}^8B & \rightarrow {}^8Be + e^+ + \nu & \mathbf{^8B} \end{cases}$$

In the center of the sun the CNO cycle is also partially active, and so we have to add three other neutrinos coming from the ^{13}N, ^{15}O and ^{17}F decays. The flux and the energy distribution of ν's emitted from the Sun is of course dependent on the number of each of the above reactions taking place, and then on the details of the present state of the evolutionary path of the star (solar model). We performed solar model calculations using the FRANEC code adopting updated input physics and taking into account element diffusion [1]. To reproduce the sun we evolve a model trying to fit two experimental data: we have for the sun a luminosity $L_\odot = (3.844 \pm 0.004) \cdot 10^{33} erg\ s^{-1}$ and a radius $R_\odot = 6.961 \cdot 10^{10}\ cm$. For nuclear reaction rates, we have used both the NACRE [2] and Caughlan and Fowler (CF'88) [3] compilation with the exception of $^7Be(p,\gamma)^8B$.

Helioseismic data help us to verify the goodness of the model. Figure 1 shows the comparison between experimental and model sound velocity. We reproduce the experimental data with a difference smaller than 0.5%: note

that for $R < 0.6\ R_{\odot}$, where 99% of neutrinos are producted, the difference is of the order of 0.2%.

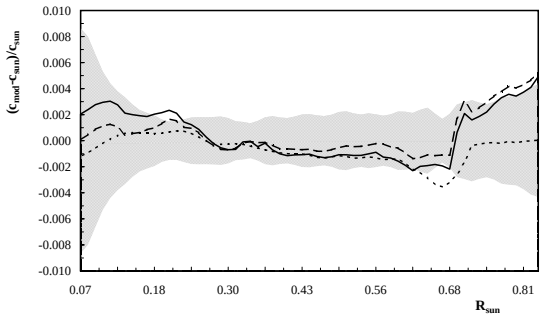

Figure 1: **Comparison between experimental and model sound velocity using FRANEC code and NACRE (solid line) and CF'88 compilation (dashed line) and BP01 [4] data (dotted line).**

Using our value for the flux we calculate the spectrum assuming the standard electroweak theory (see figure 2).

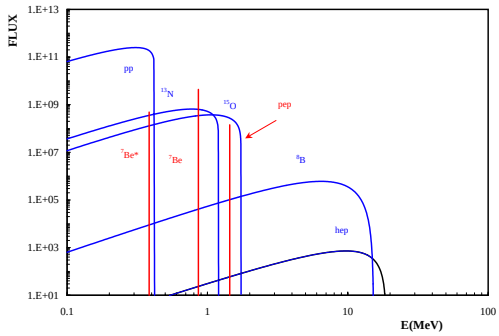

Figure 2: **Solar Neutrino Spectrum is shown in the figure. The neutrino fluxes for continuum sources are given in the units of number per cm^2 per second per MeV at one astronomical unit; while line fluxes are given in number per cm^2 per second.**

Solar neutrino experiments measure the flux using radiochemical or water Cherenkov detectors. Homestake [5], SAGE [6] and GALLEX [7] belong to the first group. They used chlorine and gallium detectors exploiting the reactions: $\nu_e + {}^{37}Cl \rightarrow {}^{37}Ar + e$ (**Homestake**) which has an energy

threshold at 0.814 MeV; $\nu_e + {}^{71}Ga \rightarrow {}^{71}Ge + e$ (**SAGE and GALLEX**) which has an energy threshold at 0.233 MeV. SAGE and GALLEX experiments are sensitive to almost all the solar neutrino energy window, then they should measure almost all the flux expected. They measure **only** 75^{+8}_{-7} SNU and 74^{+7}_{-8} SNU, instead of the 130.6 SNU expected: this is usually called **the missing neutrino** problem.

Super Kamiokande [8] and SNO [9] are water Cherenkov experiments: SK detects solar neutrinos by virtue of their elastic scattering on the electrons bound in the water molecules ($\nu_{e,\tau,\mu} + e \rightarrow e + \nu_{e,\tau,\mu}$) and SNO using heavy water detects simoultaneusly the previous elastic scattering and the reaction $\nu_e + d \rightarrow p + p + e^-$. The two experiments are able to measure the energy spectrum with an energy threshold of about $6MeV$. Therefore these experiments measure only the neutrinos coming from ${}^8B$ decay. The expected flux at the earth surface, considering the energy range from 0 to 15 MeV, is $5.18 \cdot 10^6$ cm^{-2} s^{-1}. The measured value of SNO charged current is $(1.70 \pm 0.15) \cdot 10^6$ cm^{-2} s^{-1} while that of SK elastic scattering is $(2.32 \pm 0.09) \cdot 10^6$ cm^{-2} s^{-1}. The discrepancy between elastic scattering and charged current data shows that neutrino changes flavor.

In the framework of the MSW [10, 11] theory for neutrino oscillation it is very important to reduce the uncertainty on the nuclear reaction rates. We have considered the error on luminosity (0.4%), age (0.4%), metallicity (3.3%) and some nuclear reaction rates: ${}^3He({}^3He, 2p){}^4He$ (known with 6% uncertainty)[12]; ${}^3He({}^4He, \gamma){}^7Be$ (9%) and ${}^7Be(p, \gamma){}^8B$.

As regards the lasrt process in 1995 we have started at the 3 MV tandem accelerator in Naples a renewed measurement of the absolute $\sigma(E)$ value of $p({}^7Be, \gamma){}^8B$ (using a radioactive ${}^7Be$ beam and an H_2 gas target, i.e. inverted kinematics) in the non-resonant energy region, i.e. at $E_{cm} \sim 1MeV$ ($E_{lab} \sim 8MeV$) [13, 14]. The aim of the present measurement was to determine the cross section using a different technique with respect to previous ones, thus searching for possible systematic uncertainties. Indeed, the knowledge of the cross section - based essentially on measurements of the β-delayed α-decay of ${}^8B$, performed using radioactive ${}^7Be$ targets produced by hot chemistry - could be significantly affected by the backscattering of the recoiling ${}^8B$ nuclides (a loss up to 15% was predicted). We collected 13 counts of ${}^8B$ in a Recoil Mass Separator, measuring concurently the ${}^7Be+p$ elastic scattering for normalization purposes. The absolute cross section of the ${}^7Be(p, \gamma){}^8B$ reaction turned out to be: $\sigma(990keV) = 0.40 \pm 0.12 \mu b$, which corresponds to an astrophysical factor at zero energy of $S(0) = 15.3 \pm 4.5$ eVb [15]. Performing a weighted average with the three most recent results, one

obtains: $S(0) = 19.5 \pm 1.0\ eVb$ which means a 5% error.

A good fit to the solar neutrino experiments data is found both for large mixing angles (LMA) and small mixing angles (SMA). In our work we have studied the dependence of the solutions from the theoretical uncertainty in the solar model, perfoming a χ^2 analysis. We have define a χ^2 function as: $\chi^2 = \sum_{i,j}(F_i^{exp} - F_i^{meas})V_{i,j}^{-1}(F_j^{exp} - F_j^{meas})$, where F_{exp} and F_{meas} are the expected and measured fluxes for each neutrino experiment (SAGE, GALLEX, HOMESTAKE, SNO and SUPERKAMIOKANDE) and $V_{i,j}$ is the error matrix which takes into account both theoretical uncertainties on parameters α_k (luminosity, age, metallicity and nuclear reaction rates) and the experimental errors σ_i:

$$V_{i,j} = \left[\sum_k \frac{\partial F_i^{exp}(\alpha_k)}{\partial \alpha_k}\frac{\partial F_j^{exp}(\alpha_k)}{\partial \alpha_k}\Delta(\alpha_k)\Delta(\alpha_k)\right] + \left[cov(F_i^{exp}, F_j^{exp})\right] \quad (9)$$

where $cov(F_i^{exp}, F_i^{exp}) = \sigma^2_{F_i^{exp}}$ We have found as small mixing solution $sin^2 2\theta = 6.63\times10^{-3}$ and $\Delta m^2 = 4.00\times10^{-6}\ eV^2$ with a $\chi^2 = 1.71$ ($\nu = 3$) and as large mixing solution $sin^2 2\theta = 8.10 \times 10^{-1}$ and $\Delta m^2 = 7.67 \times 10^{-5}\ eV^2$ with a $\chi^2 = 4.61$ ($\nu = 3$). Figure 3 shows the contour plots on the $(\sin^2 2\theta, \Delta m^2)$ plane of the two solution with 1-σ acceptance.

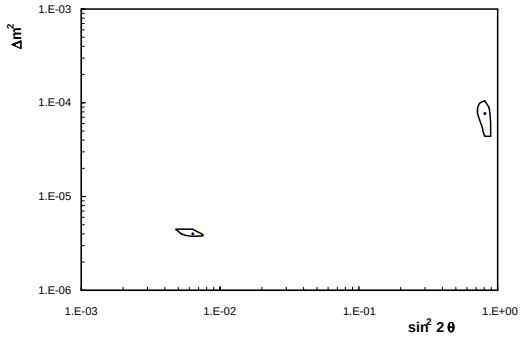

Figure 3: **Figure shows the contour plots on the** $(\sin^2 2\theta, \Delta m^2)$ **plane of the two solution with 1-**σ **acceptance.**

As a last step we have performed a numerical test to establish which is the model parameter that mostly influnce the solutions. We have artificially halved the errors on luminosity, age, metallicity and on $p + p$, $^3He +^3 He$, $^3He +^4 He$ and $^7Be + p$ reaction rates to calculate the change on the χ^2. In table 1 we summarize the results. Finally our conclusions are that at

Table 1: **Results of numerical test.**

	SMA			**LMA**		
	χ^2 $\nu = 3$	$\sin^2 2\theta$ $[10^{-3}]$	Δm^2 $[10^{-6} eV^2]$	χ^2 $\nu = 3$	$\sin^2 2\theta$ $[10^{-1}]$	Δm^2 $[10^{-5} eV^2]$
SSM	1.711	6.361	3.998	4.612	0.810	7.673
$\mathbf{\Delta\alpha/2}$						
L	1.714	6.361	3.996	4.633	0.809	7.673
age	1.712	6.361	3.997	4.615	0.810	7.692
Z/H	1.712	6.361	3.997	4.612	0.810	7.671
$\mathbf{p + p}$	1.713	6.361	3.997	4.615	0.809	7.697
$\mathbf{^3He + ^3He}$	1.713	6.361	3.997	4.617	0.809	7.607
$\mathbf{^3He + ^4He}$	1.726	6.361	3.990	4.652	0.807	7.968
$\mathbf{^7Be + p}$	1.711	6.361	3.998	4.672	0.811	7.846

present now the uncertainties on $(\sin^2 2\theta, \Delta m^2)$ in LMA and SMA solutions are essentially determined by neutrino experiment errors and only the uncertainties on $^3He + ^4He$ and $^7Be + p$ have not negligible influence on the LMA and SMA solutions. The incoming information from running experiments (SNO, BOREXINO...) will probabibly change the situation, thus it is important to improve the information on the above processes.

References

[1] Straniero. O., Chieffi, A. and Limongi, M. 1997, ApJ, 490, 425

[2] C. Angulo *et al.*, Nucl. Phys. A656(1999)3

[3] Caughlan, G.R. & Fowler, W.A., 1988, Atomic and nuclear data tables, 40, 283

[4] Bahcall J.N., Pinsoneault M.H. and Basu S., 2001 ApJ, 555, 990

[5] Davis, R.Jr., Prog. Part. Nucl. Phys., 1994, 32 , 13

[6] SAGE Collaboration, V. Gavrin et al., in Neutrino 96, Proceedings of the XVII International Conference on Neutrino Physics and Astrophysics, Helsinki, edited by K. Huitu, K. Enqvist and J. Maalampi

(World Scientific, Singapore, 1997), p. 14; V. Gavrin et al., inNeutrino 98, Proceedings of the XVIII International Conference on Neutrino Physics and Astrophysics, Takayama, Japan, June 1998, edited by Y. Suzuki and Y. Totsuka

[7] GALLEX Collaboration, P. Anselmann et al., 1995, Phys. Lett. B 342 , 440; GALLEX Collaboration, W. Hampel et al., 1996, Phys. Lett. B 388 , 364

[8] Fukuda, S. *et al.*, 2001, PRL, 86

[9] Ahmad, Q. R. *et al.*, 2001, PRL, 87

[10] Mikheyev, SP and Smirnov A, 1985, Sov. J. Nucl. Phys., 42, 913

[11] Mikheyev, SP and Smirnov A, 1986, Nuovo Cimento 9C, 17

[12] R. Bonetti *et al.* 1999 Phys. Rev. Lett., 82, 5205

[13] L. Gialanella *et al.* Nucl. Phys. B (Supp. Series), in press

[14] F. Terrasi, L.Gialanella, G. Imbriani, *et al.* 2001, Nucl. Phys. A 688, 514

[15] F. Strieder *et al.* 2001, Nucl. Phys. A 696, 219S

Re-investigation of the $^{14}\mathrm{N}(p,\gamma)^{15}\mathrm{O}$ reaction within LUNA collaboration

Alba Formicola [1],[2] *for the LUNA collaboration*

[1] *Institut für Physik mit Ionenstrahlen, Ruhr-Universität-Bochum, Bochum (Germany)*
[2] *Laboratori Nazionali del Gran Sasso, INFN, Assergi (Italy)*

During most of its life, a low mass star burns H in the center via the pp chain. However, when the central H mass fraction reduces down to 0.1, the nuclear energy produced by the H-burning becomes not sufficient and the stellar core must contract to extract some energy from its gravitational field. Then, the central temperature (and the density) increases and the H-burning switches from the pp-chain to the more efficient CNO-burning. Thus, the escape from the main sequence is powered by the onset of the CNO burning, whose bottleneck is the $^{14}\mathrm{N(p,\gamma)^{15}O}$ reaction. A modification of the rate of this reaction alters the turn off luminosity, but leaves almost unchanged the stellar lifetime, which is mainly determined by the rate of the pp reaction.

The minimum energy explored in nuclear physics laboratories for this reaction is $\simeq$ 200 keV [1], well above the region of interest for the CNO burning in astrophysical condition ($20-80$ keV), so that the values used in stellar model computations are largely extrapolated. The most recent stellar models of low mass stars have been obtained by using the compilation of the nuclear reaction rates by Caughlan and Fowler (CF88 [2]). The $^{14}\mathrm{N(p,\gamma)^{15}O}$ rate reported by the most recent compilation (NACRE collaboration [3]) does not substantially differ from the one tabulated by CF88.

At solar energies the cross section of $^{14}\mathrm{N(p,\gamma)^{15}O}$ is dominated by a subthreshold resonance at -504 keV. Recently some indirect measurements of this subthreshold resonance have been performed employing the Doppler Shift Attenuation Method [5] and there are also some new calculations about its influence at solar energies [4]. At energies higher than 100 keV the cross section is dominated by the resonance at $E_R = 278$ keV with transitions to the excited states at E_x = 6793, 6176, 5183 keV, and the ground state in ^{15}O. According to Schröder et al., that extend the measurements over a wide energy range, for laboratory energies $\mathrm{E}_p = 0.2 \pm 3.6$ MeV, the main contribution to the total S-factor at zero energy comes from transitions to the ground state in ^{15}O and to the subthreshold state at $\mathrm{E}_x = 6793$ keV. They found [1] for the total S-factor: $\mathrm{S}(0) = 3.20 \pm 0.54$ keV-b. Angulo et al. [4]

re-analyzed Schröder's experimental data using the R-matrix model; and the main difference concerns the S(0) factor for capture to the ^{15}O ground state: they found a factor of 19 lower than the value of Schröder. From the R-matrix analysis, the total S factor at zero energy is S(0) = 1.77$\pm$0.20 keV-b; which is a factor of 1.7 lower than the values used in the recent compilations. In summary, new measurements of the ^{14}N$(p,\gamma)^{15}$O cross section at energies E $\leq$ 200 keV are necessary, in particular measurements of the transition to the ground state in ^{15}O.
In order to investigate the very low energies of the ^{14}N$(p,\gamma)^{15}$O, the LUNA collaboration has installed an 400 kV underground accelerator facility at Laboratori Nazionali del Gran Sasso exploiting the strong suppression of cosmic background. Before going into details of the ^{14}N$(p,\gamma)^{15}$O measurements, some preliminary tests are performed. Due to the strong dependence of the cross section from the energy it is important to have a precise knowledge of the beam energy (to a precision better 1 keV), and a measurement of the energy spread and stability of the beam. Without going into details about these tests, briefly we will comment the results for the beam energy spread. A resonance in ^{25}Mg$(p,\gamma)^{26}$Al at E$_R$ = 389 keV, which has a very small natural width (Γ < 20 eV) was used to measure the energy spread. The energy of the beam impinging on the target was changed around the resonance energy in very small steps. An accurate analysis of the yield of the reaction as a function of the voltage applied to the target yielded a total experimental width of 72 eV (figure 1).

The peculiarities of the 400 kV facility are particulary well suited for the ^{14}N$(p,\gamma)^{15}$O, where reaction γ-ray lines up to $\simeq$ 7.5 MeV have to be measured with very low intensities. High beam intensities and high detection resolutions have to be coupled to high target stability and purity, and thus low beam-induced background, as cosmic background is strongly suppressed and low intrinsic activity detectors are employed. An extensive study of the quality of N targets has then been performed, using implanted, evaporated, and sputtered targets. In all cases during the experiments targets were water-cooled directly on the backing. In the target chamber the target ladder was shadowed by a collimator, so that a uniform circular beam spot (Φ = 4 cm) was obtained within the target area by magnetic wobbling of the beam. In order to prevent build-up of impurities of the target, a LN-cooled copper cold finger was used. A Pb-shielding 120 % efficiency Ge detector was used in close geometry at 0^o with respect to the beam direction. Repeated measurements of the resonance profile during long-term high power beam bombardments allow for monitoring of target quality and stability. We are able to conclude that sputtered targets of TiN on

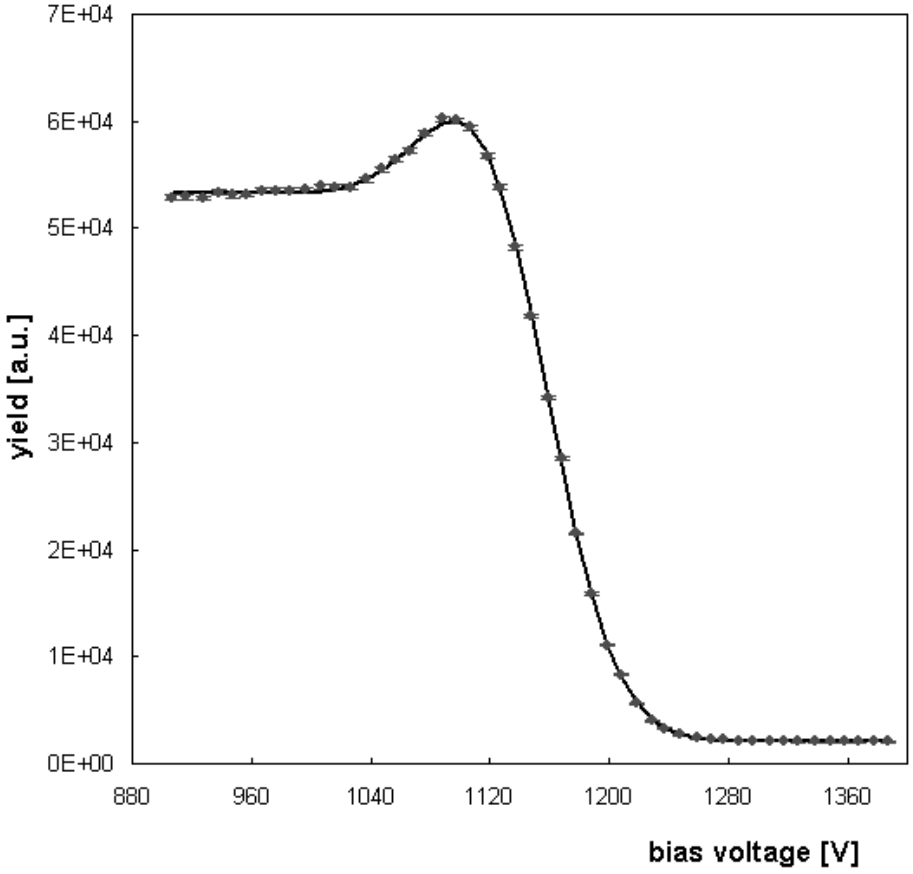

Figure 1: The beam energy spread was studied with a resonance in $^{25}\mathrm{Mg}(p,\gamma)^{26}\mathrm{Al}$ at $\mathrm{E}_R = 389$ keV. The resulting excitation function (straight line) was fitted with a thick target yield curve (dashed line) and a gaussian shaped

Ta backings have the most uniform number density profile and withstand many days of beam bombardment with several hundreds of μA without any significant deterioration.
Figure 2 shows the excitation functions of the $^{14}\mathrm{N}(p,\gamma)^{15}\mathrm{O}$ reaction to four different final states as measured running a thick target ($\sim$ 110 keV at $\mathrm{E}_p = 278$ keV). Below the resonance energy the yields from the reaction drops by more than three orders of magnitude. The analysis of the data in terms of a superposition of direct and resonant amplitude is under course,

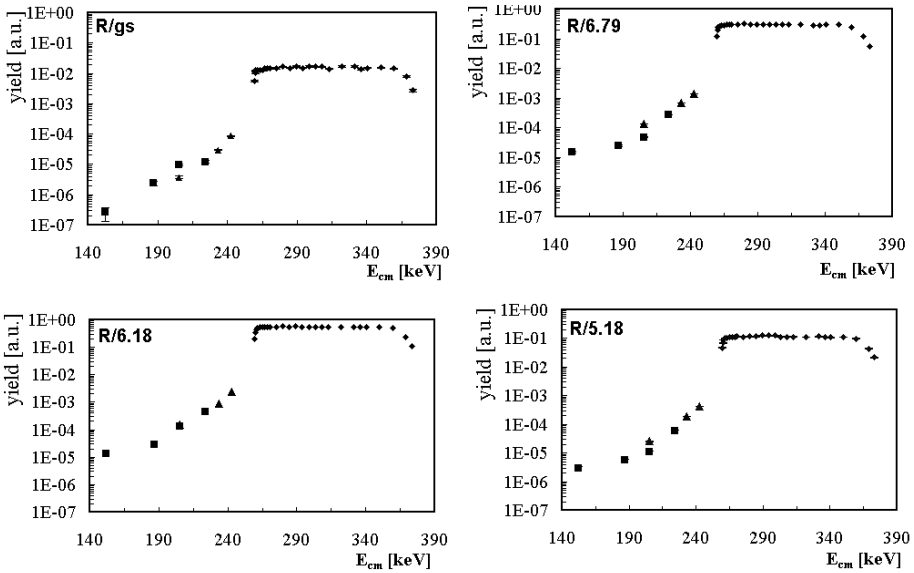

Figure 2: Excitation function of primary γ-rays from the $^{14}\mathrm{N}(\mathrm{p},\gamma)^{15}\mathrm{O}$ for different transitions.

as well as an attempt to extend measurements to as low as possible energy.

References

[1] U.Schröder et al., Nucl. Phys. A 467 (1987) 240

[2] Caughlan, G.R. & Fowler, W.A., 1988, Atomic and nuclear data tables, 40, 283

[3] C. Angulo et al., Nucl. Phys. A 656 (1999) 3

[4] C. Angulo et al., Nucl. Phys. A 690 (2001) 775

[5] P.F.Bertone et al., Phys. Rev. Lett. 87 (2001) 155201

Search for rp-Process Trigger Reactions

A.N. Ostrowski[1], *A.M. Laird*[2], *M. Aliotta*[2], *F. Cappuzzello*[4], *S. Cherubini*[3], *A. Cunsolo*[4], *T. Davinson*[2], *P. Figuera*[4], *W. Galster*[3], *J.S. Graulich*[3], *D. Groombridge*[2], *J. Hinnefeld*[3], *P. Leleux*[3], *A. Musumarra*[4], *A. Ninane*[3], *A. Di Pietro*[4], *A.C. Shotter*[2], *C. Spitaleri*[4], *A. Tumino*[4], *J. Vervier*[3], *P.J. Woods*[2]

[1] *Dept. of Physics, Johannes Gutenberg-Universität, D-55099 Mainz, Germany*
[2] *Dept. of Physics and Astronomy, University of Edinburgh, UK*
[3] *Institut de Physique Nucléaire, Université Catholique de Louvain,Belgium*
[4] *Dipartimenti di Fisica, Universitá di Catania, Italy*

Introduction

At even temperatures found in cataclysmic variable stellar environments the so–called hot carbon–nitrogene–oxygene cycle is initiated and the isotope with the longest half-life in this reaction chain ^{15}O will become highly abundant. Further rises in temperature and pressure can ignite a thermonuclear runaway in which charged particle induced capture reactions become more likely than β–decays and conversion of the remaining nuclei into heavier proton-rich isotopes sets in rapidly [1]. The $^{15}(\alpha,\gamma)^{19}$Ne reaction is generally considered as the potential breakout reaction from the hot CNO cycle [2]. The ^{19}Ne-nuclei produced can be converted further via subsequent radiative capture reactions into ^{20}Ne and heavier proton–rich elements. However, the radiative α–capture on ^{15}O is the least well known of these reactions. Hence, this reaction chain could be bridging the gap between the CNO mass region and the beginning of the rapid proton capture process, i.e. the rp-process. At high enough densities, the ^{18}Ne(α,p)-reaction might offer an alternative route.

Under the typical conditions found e.g. in X-ray novae the ^{15}O(α,γ) reaction rate depends dominantly on the properties of a single sub–Coulomb resonance at $E_{c.m.} = 504$keV which corresponds to a $\frac{3}{2}^+$ resonance in ^{19}Ne at 4.033 excitation energy. No direct measurements of this reaction have been reported up to know. However, since the partial α–decay width Γ_α is small compared with the total resonance width Γ [3], knowledge of the

resonance energy E_R, the spins involved ($\mathbf{I}_{^{19}Ne}=\mathbf{I}_\alpha+\mathbf{I}_{^{15}O}+\ell$)[1], the branching ratio Γ_α/Γ and Γ is sufficient to calculate the reaction rate coefficient $<\sigma v>$ as a function of temperature T using the expression given in 10.

$$<\sigma v> \propto \left(\frac{2\pi}{\mu kT}\right)^{3/2} \hbar^2 \frac{2I_{^{19}Ne}+1}{(2I_\alpha+1)(2I_{^{15}O}+1)} \quad \frac{\Gamma_\alpha}{\Gamma} \quad \Gamma \quad \exp\left(-\frac{E_R}{kT}\right) \qquad (10)$$

A study of the ^{19}F(^{3}He,t)^{19}Ne$^*(\alpha)^{15}$O reaction gave some useful information concerning the α-decay for states in ^{19}Ne above 4.5MeV excitation energy [4]. Indirect methods have used transfer reactions on mirror nuclei [5] to determine the branching ratios of interest. However, the validity of such approaches seems to be questionable [6].

Experimental Set-up

An exploratory measurement has been performed in order to study the potential of populating resonances of astrophysical interest in ^{19}Ne via a ^{18}Ne induced neutron stripping reaction on deuterated polythene targets. The experiment took place at the first generation radioactive nuclear beam facility of the Cyclotron Research Center at Louvain-la-Neuve, Belgium. A ^{18}Ne beam having E_{lab}=44.1 MeV and an average beam intensity of 5×10^5 was impinging on 0.7mg/cm^2 thick $(CD_2)_n$ targets and reaction products were detected using three single sided silicon strip **L**ouvain **E**dinburgh **D**etector **A**rrays. A total of 320 detector elements have been used and both energy and time-of-flight with respect to the cyclotron frequency have been recorded for each strip to allow for the identification of the light reaction products.

The detector arrays have been carefully positioned around the target to measure the particles that are produced in the d(^{18}Ne,^{19}Ne*)p reaction and subsequent α-particle decays of the excited states in ^{19}Ne. The protons that tag the formation of excited states in ^{19}Ne were detected in a recoil detector array covering an laboratory angular range from 131 to 154 degrees in ≈1.4 degree steps. A heavy residue and an α-particle detector array were positioned such as to cover 15 to 35 and 5 to 10 degrees, respectively.

Experimental Results

The 4.033MeV state – among other resonances of astrophysical interest – was clearly populated in this experiment. However, no decay events are detected

[1] ℓ denotes the transferred angular momentum.

for the 4.033 MeV state, which is expected given the the branching ratio is predicted to be less than 10^{-4} [3]. The background in the proton spectra obtained originating from fusion evaporation is featureless and exponentially falling off. It has been determined by performing a reference measurement on a $(CH_2)_n$ target.

Summary and Outlook

Preliminary analysis of a subset of the data for the 4.600 MeV state, however, gives $\Gamma_\alpha/\Gamma = 0.28 \pm 0.13$ to be compared with 0.25 ± 0.04 given in Ref. [4]. Consequently, despite the much lower beam intensity of only 5×10^5pps, the higher cross-section and the larger solid angle subtended allow this radioactive nuclear beam experiment to compare favorably with the stable beam approach. Moreover, assuming the ^{18}Ne beam intensities expected to become available at a second generation radioactive nuclear beam facility, e.g. ISAC at TRIUMF, a measurement of the Γ_α/Γ for the 4.033 MeV state using the aforementioned techniques will become feasible in the near future [7].

Acknowledgements

The authors wish to thank the the technical staff at the Cyclotron Research Centre at Louvain–la-Neuve, Belgium, for their outstanding efforts to provide the post-accelerated radioactive ^{18}Ne-beam.

References

[1] G.Wallerstein, I.Iben, P.Parker, A.M.Boesgaard, G.M.Hale, A.E.Champagne, C.A.Barnes, F.Käppeler, V.V.Smith, R.D.Hoffman, F.X.Timmes, C.Sneden, R.N.Boyd, B.S.Meyer, D.L.Lambert, Rev. Mod. Phys. **69** (1997) 995.

[2] R.K.Wallace and S.E.Woosley, Astr. J. Suppl. **45** (1981) 389.

[3] K. Langanke, M.Wiescher, W.A.Fowler, J.Gorres, Astro. J. **301** 629 (1986).

[4] P.V.Magnus, M.S.Smith, A.J.Howard, P.D.Parker, A.E.Champagne, Nucl. Phys. **A506**, (1990) 332.

[5] S.Wilmes, P.Mohr, U.Atzrott, V.Kolle, G.Staudt, A.Mayer, J.W.Hammer, Phys.Rev. **C52**, R2823 (1995).

[6] F.de Oliveira, A.Coc, P.Aguer, G.Bogaert, J.Kiener, A.Lefebvre, V.Tatischeff, J.-P.Thibaud, S.Fortier, J.M.Maison, L.Rosier, G.Rotbard, J.Vernotte, S.Wilmes, P.Mohr, V.Kolle, G.Staudt, Phys.Rev. **C55**, 3149 (1997).

[7] A.N. Ostrowski and L. Buchmann, approved experiment E874,TRIUMF.

Core-collapse supernova simulations: Variations of the input physics

M. Rampp[1], *R. Buras*[1], *H.-Th. Janka*[1], *G. Raffelt*[2]

[1] *Max-Planck-Institut für Astrophysik, Karl-Schwarzschild-Str. 1, D-85741 Garching, Germany*
[2] *Max-Planck-Institut für Physik, Föhringer Ring 6, D-80805 München, Germany*

Abstract

Spherically symmetric simulations of stellar core collapse and post-bounce evolution are used to test the sensitivity of the supernova dynamics to different variations of the input physics. We consider a state-of-the-art description of the neutrino-nucleon interactions, possible lepton-number changing neutrino reactions in the neutron star, and the potential impact of hydrodynamic mixing behind the supernova shock.

Improvements of the neutrino-nucleon interaction rates

Recently, spherically symmetric Newtonian [1, 2], and general relativistic [3] hydrodynamical simulations of stellar core-collapse and the post-bounce evolution including a Boltzmann solver for the neutrino transport have become possible. No supernova explosions were obtained.

Having reached a new level of accuracy of the numerical treatment, it is a natural next step to reconsider the input physics that enters the models, remove imponderabilities of their description and also test possible alternatives. Within the set of so-called "standard" neutrino opacities [4] which have been widely used in supernova models so far, for example, the rates of charged-current interactions of electron neutrinos and antineutrinos with free nucleons as well as neutral-current scatterings of neutrinos off free nucleons were calculated with the assumption that the nucleons can be considered as isolated, infinitely massive particles at rest. It is, however, well known that these interaction rates are significantly changed when energy transfer between the nucleons and leptons ("recoil"), nucleon-nucleon correlations due to Fermi statistics and nuclear forces, and other so far disregarded effects like weak magnetism corrections, are adequately taken into account (see Ref. [5]). Effectively, at densities $\rho \gtrsim 10^{13}\,\mathrm{g/cm^3}$, the opacities become

considerably smaller than in the "standard" approximation. Correspondingly, neutrino diffusion through the nascent neutron star and the emission from the neutrinosphere are enhanced and higher neutrino luminosities must be expected.

Figure 1 shows results of Newtonian simulations of iron core-collapse and the post-bounce evolution of a $15\,M_\odot$ star [6] using Boltzmann neutrino transport [7]. One model was calculated with an improved description of neutrino-nucleon interactions, which includes the detailed reaction kinematics and nucleon phase-space blocking, nucleon-nucleon correlations in the dense medium [8, 9], weak magnetism [5] and the possible quenching of the axial coupling g_A in nuclear matter [10]. For a reference calculation the conventional "standard" opacities [4] were used. In both simulations we also included nucleon-nucleon bremsstrahlung $NN \rightleftharpoons \nu\bar{\nu}\,NN$ ($N \in \{n, p\}$ denotes a free nucleon), which is the dominant production reaction of μ and τ neutrinos and antineutrinos in the denser regions of the newly formed neutron star [11, 12].

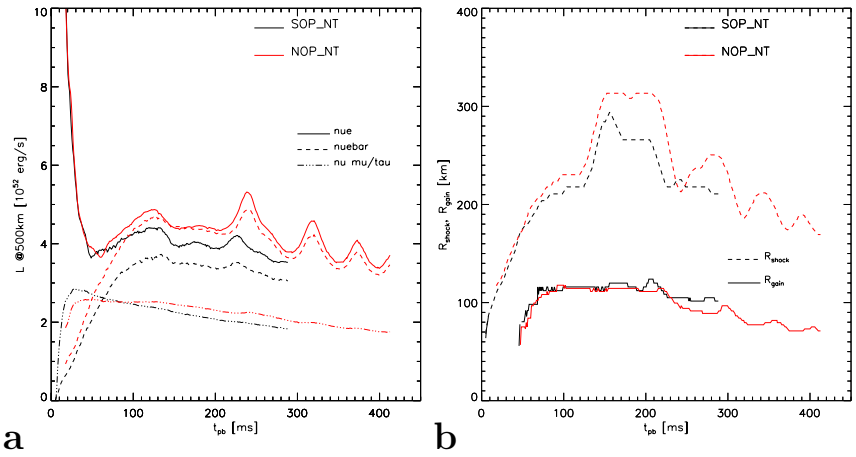

Figure 1: Comparison of the post-bounce evolution of a model computed with "standard" neutrino opacities (black lines) and a model which employs the improved description of neutrino-nucleon interactions (red lines). Panel **a** shows the luminosities of ν_e (solid lines), $\bar{\nu}_e$ (dashed lines), and ν_μ, ν_τ, $\bar{\nu}_\mu$, $\bar{\nu}_\tau$ (individually; dash-dotted lines) as functions of time. In Panel **b** the radial positions of the shock (dashed lines) and the gain radius (solid lines) of the two models are compared.

As expected from the arguments above, the model calculated with the

new implementation of the opacities shows enhanced luminosities for ν_e and, even more pronounced, for $\bar{\nu}_e$. This is caused by the fact that for ν_e and $\bar{\nu}_e$ recoil and nucleon correlations have the strongest effect at high densities, while for $\bar{\nu}_e$ the weak magnetism reduces the opacities also at moderate densities $\rho \lesssim 10^{13}\,\mathrm{g/cm^3}$ [5], where most of the neutrino emission is produced during the time of consideration. In contrast, for ν_e both "corrections" counteract and almost cancel each other [5]. The higher luminosities (see Fig. 1a) and somewhat larger mean energies of ν_e and $\bar{\nu}_e$ increase the neutrino heating in the gain region below the hydrodynamic shock. Consequently, the shock propagates to larger radii when compared with the reference model (see Fig. 1b).

In view of the appreciable differences between both models we consider the inclusion of a state-of-the-art description of neutrino-nucleon interactions as a mandatory step towards more realistic supernova simulations, although the improved opacities *alone* do not lead to a successful supernova explosion in spherical symmetry.

Lepton-number changing neutrino reactions

Lepton-number changing interactions are expected in various extensions of the particle-physics standard model, notably in R-parity violating models of supersymmetry; see Ref. [13] for an overview and current experimental limits. Such processes might significantly affect the supernova dynamics [14]. As a proxy for this class of interactions we implemented the reaction $\nu_e + N \rightleftharpoons \bar{\nu}_e + N$ which opens a channel for "internal deleptonization", i.e. quickly running down electron lepton number without diffusion to the stellar surface. This effect leads to a corresponding increase of the temperature of the stellar plasma by conversion of degeneracy energy to thermal energy (Fig. 2). The relevant time scale is fixed by the effective strength of the lepton-number changing reaction. We parametrize it by $\sigma/\sigma_{\mathrm{SM}}$, which is the lepton-number changing cross section normalized to the standard-model one for $\nu_e + N \rightleftharpoons \nu_e + N$. We have calculated one model with $\sigma/\sigma_{\mathrm{SM}} = 10^{-7}$ where the deleptonization time scale is too slow to be effective during infall, and an extreme case where $\sigma/\sigma_{\mathrm{SM}} = 10^{-3}$ and where coherent enhancement by the scattering off heavy nuclei is allowed, $\nu_e + A \rightleftharpoons \bar{\nu}_e + A$. Despite of sizeable differences in the physical conditions in the core of the nascent neutron star (Fig. 2) we find a remarkable insensitivity of the overall dynamical evolution of the models to the dramatic modifications of the microphysics. In both models the hydrodynamic shock reaches a maximum radius of about 300 km at $\approx$ 200 ms after bounce. These values are very close to the reference

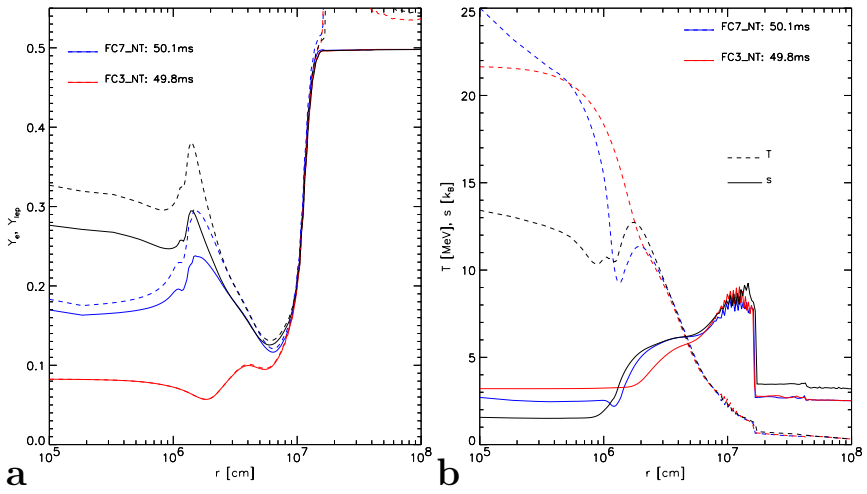

Figure 2: Radial profiles of the electron fraction (Panel **a**, solid lines), total lepton fraction (Panel **a**, dashed lines), temperature (Panel **b**, dashed lines) and specific entropy (Panel **b**, solid lines) 50 ms after core bounce. Results of the models with lepton-number changing reactions are plotted as red ($\sigma/\sigma_{\rm SM} = 10^{-3}$) and blue lines ($\sigma/\sigma_{\rm SM} = 10^{-7}$). For comparison quantities of the reference model ($\sigma/\sigma_{\rm SM} = 0$) are shown as black lines.

calculation with $\sigma/\sigma_{\rm SM} = 0$. This finding is probably explained by the accelerated deleptonization and heating being confined to the innermost ≈ 20 km of the neutron star (Fig. 2), because only there the lepton-number changing reactions are fast enough and the optical depth for these processes is larger than unity. During the first few hundred milliseconds after bounce most of the neutrino luminosity, on the other hand, originates from regions beween 50 km and 100 km where the temperature is essentially the same in all models (Fig. 2b). Continuing the simulations over a period of nearly one second, we find slightly enhanced neutrino luminosities and mean energies and thus heating in the gain region at later times after bounce, but not to a degree that the conditions for explosions [15] would become more favourable.

Successful explosions by convective processes ?

Multi-dimensional hydrodynamic simulations, coupled with simplified treatments of the neutrino physics, have shown that large-scale convective overturn behind the supernova shock *can* aid the neutrino-driven mechanism and cause an explosion even if models fail in spherical symmetry (see Ref. [16] for

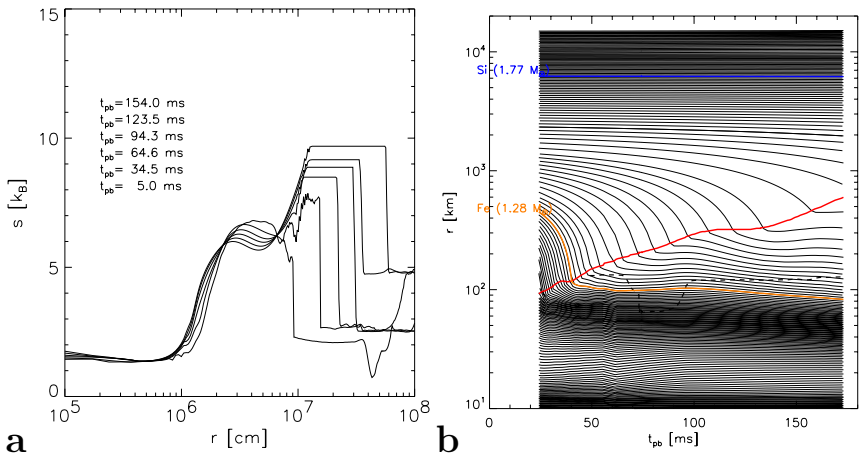

Figure 3: Panel **a** shows the effect of our "mixing" algorithm on the temporal evolution of the radial profile of the specific entropy. From bottom to top the times correspond to profiles with increasing values of the postshock entropy. For the same model the trajectories of different mass shells (with a spacing of 0.02 $M_\odot$) are plotted as black lines in Panel **b**. The red line traces the radial position of the supernova shock. Note that the model includes only ν_e and $\bar{\nu}_e$, and can be directly compared with the simulation published in Ref. [1].

an overview and references to original work). However, because of the uncertainties and approximations in the description of the neutrino sector, the actual role of convection in supernova models is not yet clear. Self-consistent and multi-dimensional simulations with a sufficiently accurate treatment of the neutrino transport have still to be carried out.

Convective overturn has the helpful influence of suppressing energy losses by the reemission of neutrinos, because neutrino-heated matter expands outward instead of being advected through the gain region into the cooling layer. In addition, part of the matter falling through the shock can still accrete onto the neutron star, which helps keeping up a high value of the accretion luminosity. Furthermore, the expanding, neutrino-heated matter raises the pressure immediately behind the shock and thus drives the shock farther out. We try to mimick the latter effect of a multi-dimensional fluid flow between the shock and the gain radius by artificially (and instantaneously) mixing layers of negative entropy gradient behind the shock in our spherically symmetric simulations. This leads to a flattening of the entropy profile. We achieve this behaviour by setting the entropy in such a region

to a constant value $s(t, r) = s_0(t)$ (see Fig. 3a), which is calculated in each timestep from the requirement that the internal (and thus also the total) energy in the affected region is conserved. Of course, this algorithm cannot accout for all the above mentioned effects associated with multi-dimensional fluid motions, but at least one can test the sensitivity of the post-bounce supernova evolution to such a manipulation.

As a consequence of the mixing and the thus increased postshock pressure, the hydrodynamic shock — which in the absence of mixing reached a maximum radius of about 350 km before it started to recede again — is indeed pushed out to a radius beyond 600 km (Fig. 3b), presumably leading to a weak supernova explosion. We interpret this result as an interesting hint that successful neutrino-driven supernova explosions might be in reach when state-of-the-art neutrino physics and a Boltzmann treatment of the neutrino transport are eventually combined in self-consistent multi-dimensional simulations.

Acknowledgements

It is a pleasure to thank K. Takahashi for implementing the improved treatment of the neutrino-nucleon cross sections and Ch. Horowitz for providing correction formulae for the weak magnetism. We thank the Institute for Nuclear Theory at the University of Washington for its hospitality and the Department of Energy for support during a visit of the Summer Program on Neutron Stars. This work was also supported by the Sonderforschungsbereich 375 on "Astroparticle Physics" of the Deutsche Forschungsgemeinschaft. The computations were performed on the NEC SX-5/3C of the Rechenzentrum Garching and on the CRAY T90 of the John von Neumann Institute for Computing (NIC) in Jülich.

References

[1] M. Rampp and H.-T. Janka, ApJ **539** (2000) L33.

[2] A. Mezzacappa, M. Liebendörfer, O. Messer, et al., Phys. Rev. Lett. **86** (2001) 1935.

[3] M. Liebendörfer, A. Mezzacappa, F. Thielemann, et al., Phys. Rev. D **63** (2001) 3004.

[4] S.W. Bruenn, ApJS **58** (1985) 771.

[5] C.J. Horowitz, Phys. Rev. D **65** (2002) 043001.

[6] S. Woosley, personal communication (1999).

[7] M. Rampp and H.-T. Janka, preprint astro-ph/0203101 (2002).

[8] S. Reddy, M. Prakash and J.M. Lattimer, Phys. Rev. D **58** (1998) 3009.

[9] A. Burrows and R.F. Sawyer, Phys. Rev. C **58** (1998) 554.

[10] G.W. Carter and M. Prakash, Physics Letters B **525** (2002) 249.

[11] S. Hannestad and G. Raffelt, ApJ **507** (1998) 339.

[12] T.A. Thompson , A. Burrows and J.E. Horvath, Phys. Rev. C **62** (2000) 035802.

[13] S. Bergmann, H.V. Klapdor-Kleingrothaus and H. Päs, Phys. Rev. D **62** (2000) 113002.

[14] G.M. Fuller, R. Mayle and J.R. Wilson, ApJ **332** (1988) 826.

[15] H.-T. Janka, A&A **368** (2001) 527.

[16] H.-T. Janka, K. Kifonidis and M. Rampp, in Proc. Workshop on Physics of Neutron Star Interiors, ed. D. Blaschke N. Glendenning and A. Sedrakian Lecture Notes in Physics **578** (Springer, 2001) 333–363; preprint astro-ph/0103015.

The Importance of Neutrino Opacities for the Accretion Luminosity in Spherically Symmetric Supernova Models

M. Liebendörfer[1,2], *O. E. B. Messer*[1,2,3], *A. Mezzacappa*[1], *W. R. Hix*[1,2,3], *F.-K. Thielemann*[4], *K. Langanke*[5]

[1] *Physics Division, Oak Ridge National Laboratory, Oak Ridge, TN-37831*
[2] *Department of Physics and Astronomy, University of Tennessee, Knoxville, TN37996*
[3] *Joint Institute for Heavy Ion Research, Oak Ridge National Laboratory, Oak Ridge, TN37831*
[4] *Department of Physics and Astronomy, University of Basel, CH4056 Basel*
[5] *Institut for Fysik og Astronomi, Århus Universitet, DK8000 Århus C*

General Relativistic Boltzmann Neutrino Transport

Spherically symmetric simulations of stellar core collapse and postbounce evolution do not lead to explosions if they are based on "standard" [1, 10] nuclear and weak interaction microphysics. This widely anticipated statement achieved a completely new level of justification with the technically complete and self-consistent treatment of neutrino transport in the highly dynamical evolution after core collapse and bounce [16, 14] in general relativity [2, 11]. Multidimensional models for core collapse supernovae, which allow non stratified hydrodynamics at the cost of reliable neutrino transport, present the neglect of convection as a plausible cause for the failure to reproduce supernova explosions in spherical symmetry (e.g. see Ref. [6] and references therein). In our spherically symmetric models, neutrino absorption adds only weakly to the entropy of the shock-dissociated material after shock stagnation because of high infall velocities. Nevertheless, spherically symmetric models provide a field for further studies: The realistic neutron star structure and the accurate evolution of angle- and energy-resolved neutrino distribution functions enable the investigation of the influence of nuclear and weak interaction physics on the models. Complete implicit radiation hydrodynamics also provides insight into many tightly coupled processes with strong feedback in the evolution of a core collapse supernova.

In the following, we compare the postbounce evolution of five different initial stellar progenitors, simulated with general relativistic three-flavor Boltzmann neutrino transport. The chosen progenitors have masses of 13 $M_\odot$ and 20 $M_\odot$ [15]; and 15 $M_\odot$, 25 $M_\odot$, and 40 $M_\odot$ [17]. We present in Fig. 1 the shock position for these different models as a function of time, as solid lines. We find similar trajectories for all progenitors, with a shock radius maximum around 150 km. We also plot the shock position in terms of enclosed mass in Fig. 2b: Before the existence of a shock during core collapse, we plot the deleptonization-dependent position of the sonic point where the shock will form after bounce. In a later stage, the gradient of the shock trajectory reflects the accretion rate given by the radial density profile of the progenitor star. Also shown are the electron neutrino luminosities and rms energies in Fig. 2a. Among the chosen progenitors, which represent the full progenitor mass range of expected type II events, the most striking feature is the clear separation into a quantitatively similar evolution up to the electron neutrino burst and a distinctively different one afterwards.

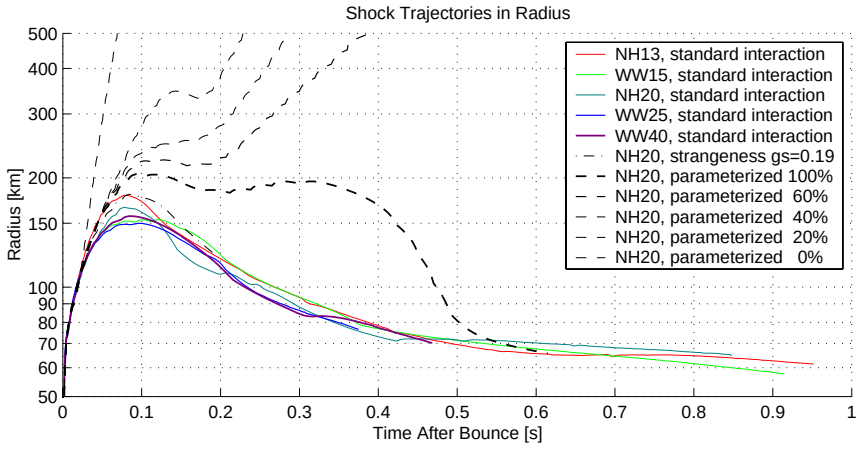

Figure 1: Shown in solid lines are the shock trajectories with standard input physics. Dash-dotted is the shock trajectory of the 20 solar mass progenitor with nucleon strangeness content included. The experimental dashed trajectories (based on transport with lowest angular resolution) show explosions as a function of parametrized isoenergetic scattering on free nucleons.

Feedback in the Deleptonization during Core Collapse

When the inner core of the progenitors reach the Chandrasekhar mass, they have comparable density and temperature profiles. The electron fraction determines the location of the sonic point at the surface of the inner core, which is causally connected by electron pressure (Fig. 2b). During collapse, the electron fraction decreases by electron capture on nuclei and protons until trapped neutrinos block further deleptonization. A regulation mechanism establishes similar electron fractions in all models [1, 12]: The small abundance of free protons, Y_p, is given by the Lattimer-Swesty equation of state as a function of the electron fraction, Y_e. The sensitivity $d\ln(Y_p)/dY_e \sim 30$ is large enough that a small deviation, $\Delta Y_e = 0.01$, from a "normal" Y_e-evolution changes the proton abundance, and therewith the number of electron captures on free protons, by a third. This negative feedback drives the electron fraction back to the "norm"-evolution whenever electron captures on free protons dominate. In our simulations, capture on heavy nuclei is suppressed as soon as the $N = 40$ shell is closed [1]. Thus, the described self-regulation sets in at this point, leading to very small differences in the evolution of the different progenitors up to shock breakout. The extent to which this regulation survives extension of electron capture rates to heavier nuclei, when these rates are computed with improved nuclear shell models, remains to be investigated.

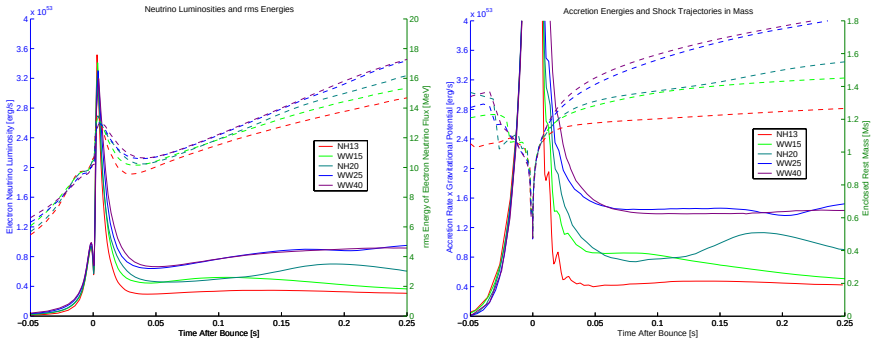

Figure 2: The left hand side shows the electron neutrino luminosities (solid) and rms energies (dashed). On the right hand side are the accretion energy rate (solid) and the sonic point/mass trajectories in enclosed mass (dashed).

Accretion Luminosities and Neutrino Opacities

The accretion luminosity, which dominates over the core diffusion luminosity soon after shock stall, is produced by the compression of infalling material at the surface of the PNS. The available energy can roughly be estimated by the rate of infalling material, multiplied by the gravitational potential at the neutrino sphere. The result is an energy deposition rate that qualitatively relates the modulation in the observable neutrino luminosities to accretion rates (Fig. 2ab), i.e. to variations in the initial density profiles of the progenitor stars. A relation of this kind might be linked to analytical supernova models that present conditions for shock revival as a function of independent luminosities and accretion rates [3, 7]. The main influence of nuclear input physics to the evolution of the shock position resides in how the high density equation of state determines the size of the PNS on the one hand, and how the neutrino opacities at moderate densities ($\sim 10^{13}$ g/cm^3) affect the energy loss rate by neutrino emission on the other:

Indeed, reduced isoenergetic scattering opacities at moderate densities have led to explosions in spherical symmetry and suggested a search for an exploration of the physical limits. However, a physically justifiable opacity reduction by taking into account the strangeness content of nucleons (see e.g. [9]) did not produce explosions, even if it had a positive effect in exploratory runs (Fig. 1). A detailed discussion of the degrees of freedom in the nuclear input in this regime has been given in Ref. [5]. A parameter study with decreased opacities beyond physical limits (Fig. 1) shows an interesting side effect: In exploding models, we find electron fractions close to 0.5 in the inner layers of ejecta as soon as the electron degeneracy is lifted in the neutrino heated, expanding material. The electron fraction changes during mass ejection will be considered in upcoming nucleosynthesis calculations of supernova yields [4].

With standard opacities at moderate densities, the microphysics above nuclear densities affects the postbounce evolution more by influencing the size and stability of the PNS than by influencing the diffusive neutrino flux. A more compact PNS puts the accretion/heating cycle deeper into the gravitational potential, resulting in higher infall velocities and luminosities [2, 11]. An explosion-enhancing effect from the deeper gravitational potential can only be obtained if the PNS contraction is fast enough to produce very high luminosities before the heating region has adjusted to the smaller PNS radius, or if the outer layers are kept at a distance by a yet unidentified mechanism. PNS convection may provide a more visible consequence of changes in the high density physics [8, 13]. However, a definitive conclusion regard-

ing the effect of convection below and around the neutrino sphere awaits a more refined equation of state and the inclusion of detailed multidimensional neutrino transport.

Acknowledgements

M.L. is supported by the National Science Foundation under contract AST-9877130. O.E.B.M. is supported by funds from the DoE HENP Scientific Discovery through Advanced Computing Program. A.M. is supported at the Oak Ridge National Laboratory, managed by UT-Battelle, LLC, for the U.S. Department of Energy under contract DE-AC05-00OR22725. W.R.H. is supported by NASA under contract NAG5-8405 and by funds from the Joint Institute for Heavy Ion Research and a DoE HENP PECASE Award. F.-K.T. is supported in part by the Swiss National Science Foundation under contract 20-61822.00. K. L. is supported in part by the Danish Research Council. We thank the Institute for Nuclear Theory at the University of Washington for its hospitality and the Department of Energy for partial support. Our simulations were carried out on the National Energy Research Supercomputer Center Cray SV-1.

References

[1] S. W. Bruenn, ApJS **58**, 771 (1985).

[2] S. W. Bruenn, K. R. DeNisco, and A. Mezzacappa, ApJ **560**, 326 (2001).

[3] A. Burrows and J. Goshy, ApJL **416**, L75 (1993).

[4] P. Hauser et al., in preparation, (2002).

[5] C. J. Horowitz, Phys. Rev. D **65**, 043001 (2002).

[6] H.-T. Janka, K. Kifonidis, and M. Rampp, Proc. Workshop on Physics of Neutron Star Interiors, ed. D. Blaschke, N. Glendenning, and A. Sedrakian, Lecture Notes in Physics, 333 (Springer, 2001).

[7] H.-T. Janka, A&A **368**, 527 (2001).

[8] W. Keil, H.-T. Janka, and E. Müller, ApJL **473**, L111 (1996).

[9] E. Kolbe, K. Langanke, S. Krewald, and F.-K. Thielemann, ApJL **401**, L89, (1992).

[10] J. Lattimer and F. D. Swesty, Nuc. Phys. **A535**, 331 (1991).

[11] M. Liebendörfer, A. Mezzacappa, F.-K. Thielemann, O. E. B. Messer, R. W. Hix, S. W. Bruenn, Phys. Rev. D **63**, 103004, (2001).

[12] O. E. B. Messer et al., in preparation, (2002).

[13] A. Mezzacappa, A. C. Calder, S. W. Bruenn, J. M. Blondin, M. W. Guidry, M. R. Strayer, and A. S. Umar, ApJ **493**, 848 (1998).

[14] A. Mezzacappa, M. Liebendörfer, O. E. B. Messer, R. W. Hix, F.-K. Thielemann, and S. W. Bruenn, Phys. Rev. Lett. **86**, 1935 (2001).

[15] K. Nomoto and M. Hashimoto, Phys. Rep. **163**, 13 (1988).

[16] M. Rampp and H.-T. Janka, ApJL **539**, L33 (2000).

[17] S. E. Woosley and T. A. Weaver, ApJS **101**, 181 (1995).

Asymmetric Supernovae

C.L. Fryer, M. S. Warren, A. L. Hungerford

Los Alamos National Laboratory

The evidence for asymmetries in core-collapse supernovae (SNe) continues to grow: e.g. neutron star kicks, polarization, the outward mixing of ^{56}Ni in supernova 1987A (see [1]-[3] for reviews). Some observational asymmetries, such as the rings in SN 1987A, do not reflect asymmetries in the explosion mechanism, but in the progenitor star. To truly test what the observations mean about the nature of the explosion mechanism, theorists must work back from the time of observations, when the explosion shock has gone beyond the edge of the star, down to the time when the explosion is at and around the iron core. In this brief note, we show preliminary results of studies both of the explosion mechanism itself and our latest attempts to connect what we learn near the core during the launch of the explosion with the actual observations of asymmetric effects.

The entropy driven convection in the region just beyond the proto-neutron star core has often been invoked as a mechanism to produce asymmetries in supernovae (e.g. [4]). This convective instability is also believed to help produce the supernova explosion itself. Although a lot of attention has been devoted to modeling these explosions in 2-dimensions ([5]-[8]), very few studies have probed this convection in 3-dimensions. To study asymmetries, 3-dimensional simulations are critical! We have run the first 3-dimensional calculations from collapse, through bounce, to explosion of a $15 M_\odot$ star. In figure 1, we plot the isosurface of material with radial velocities of $1000\,\mathrm{km\,s^{-1}}$. These are the upwelling bubbles (the blank spaces denote the downflows). Note that, even in the high resolution simulation, the number of modes is low, and it is plausible that when this small mode convection eventually develops into an explosion, it can drive an asymmetric supernova. However, in our simulations, the explosion occurs very quickly (within 100 ms) and no significant asymmetries develop. It is possible, however, that if this convection could occur over a longer time, one large outflow could develop, driving a strongly asymmetric supernova explosion.

We have also studied the evolution of the explosion from 100 s out to 1 year. With an initial condition where the polar explosion velocity is a factor of 2 stronger than the velocity in the equator, we follow the distribution of the ^{56}Co to better determine the gamma-ray line profiles that are produced in asymmetric explosions (see Fig. 18.4). The left panel shows the isosurface

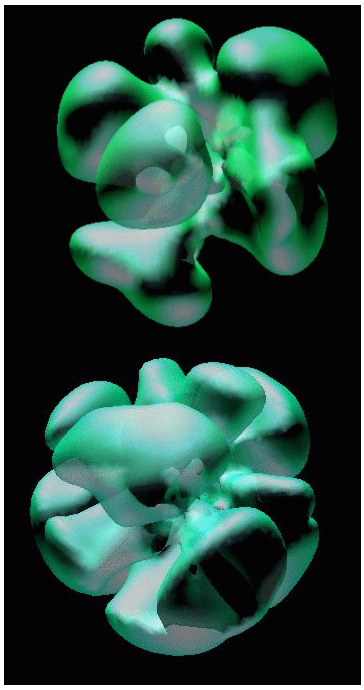

Figure 1: The isosurface of material with radial velocities of $1000\,\mathrm{km\,s^{-1}}$ for a simulation with 300,000 particles (upper) and one with 1 million particles (lower) 75 ms after the bounce of a $15\,\mathrm{M_\odot}$ star. The isosurface outlines the outward moving convective bubbles. The open spaces mark the downflows. Note that the upwelling bubbles are large and have very similar size-scales to the 2-dimensional simulations.

of the ^{56}Co distribution and the color shading shows the density profile. Note that although the ^{56}Co is very asymmetric 1 year after the explosion, the density of the material retains a fairly symmetric profile. The asymmetry in the explosion allowed the ^{56}Co to mix much further out than would be

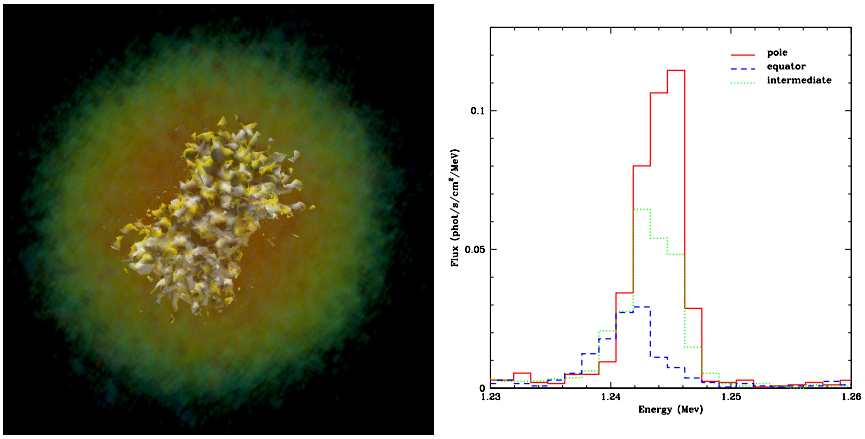

Figure 2: left panel: Isosurface of the ^{56}Co distribution (the actual isosurface denotes material with 10^5 ^{56}Co atoms cm^{-3}) 1 year after the explosion. The shaded colors denote the density distribution. Note that although the ^{56}Co (the source of the gamma-rays) is very asymmetric, the actual density distribution is symmetric. right panel: The corresponding gamma-ray line profile for a range of viewing angles: along the pole, 45° from the pole, and along the equator. The flux is calculated assuming the supernova is located at the distance of SN 1987A.

possible with a symmetric explosion, and such asymmetries will manifest themselves in the gamma-ray line profile. The right panel of figure 18.4 shows the line profile of the 1.238 MeV decay line from 3 different viewing angles. With an independent measurement of the viewing angle, we may well be able to determine the asymmetry in the supernova explosion.

Clearly, we are now poised to begin detailed studies of asymmetries in core-collapse supernovae and the next few years should see many new results in this exciting aspect of supernova theory.

Acknowledgements

It is a pleasure to thank the conference organizers, E. Müller and W. Hillebrandt for organizing such a wonderful workshop. C.L.F. would also like to thank H.-Th. Janka (and the hospitality of the Max Planck Institute for Atrophysics in Garching) for a productive and educating visit. This work has been funded by Feynman Fellowship at LANL and the Scientific Discovery through Advanced Computing (SciDAC) program of the DOE, grant number DE-FC02-01ER41176.

References

[1] C.L. Fryer, A. Burrows & W. Benz, ApJ **496** (1996) 333.

[2] D. C. Leonard, A. V. Filippenko, PASP **113** (2001) 920.

[3] S. Nagataki, ApJS, **127** (2000) 141.

[4] M. Herant, Space Sci. Rev., **74** (2000) 335.

[5] M. Herant, W. Benz, W. R. Hix, C.L. Fryer, S.A. Colgate, ApJ, **435** (1994) 339.

[6] A. Burrows, J. Hayes, B.A. Fryxell, ApJ, **450** (1995) 830.

[7] H.-Th. Janka, E. Müller, A&A, **306** (1996) 167.

[8] A. Mezzacappa, A.C. Calder, S.W. Bruenn, J.M. Blondin, M. W. Guidry, M.R. Strayer, A.S. Umar, ApJ, **493** (1998) 278.

Ionization freeze-out and barium problem in supernova 1987A

V.P. Utrobin[1,2], *N.N. Chugai*[3]

[1] *Institute for Theoretical and Experimental Physics, 117259 Moscow, Russia*
[2] *Max-Planck-Institut für Astrophysik, D-85741 Garching, Germany*
[3] *Institute of Astronomy of Russian Academy of Sciences, 109017 Moscow, Russia*

Abstract

We have shown that in the atmosphere of SN 1987A level populations of hydrogen are mostly controlled by an ionization freeze-out and ion-molecular processes up to $\sim$ 40 days. The ionization freeze-out effects are important for normal SNe II-P as well. The time dependent effects and the mutual neutralization between H^- and H^+ may result in a non-monotonic radial dependence of the Sobolev optical depth for Hα and then in a blue emission satellite of Hα observed in SN 1987A spectra at Bochum event phase. The relative abundance of molecular hydrogen $n(H_2)/n(H) \sim 10^{-4}$–10^{-3} is high enough for the photospheric phase of SN 1987A. We emphasize that the poor knowledge of the far UV radiation field in the envelope of SN 1987A still forbids a truly reliable estimate of the Ba abundance but well-constructed and tested models may improve this situation.

25.1 Introduction

As time goes on an impression strengthens that almost everything is well understood with respect to supernova (SN) 1987A in the Large Magellanic Cloud (LMC). But it is not the case. Let us consider merely two neighbor lines: Hα and Ba II 6142 Å. At early times (during 20–100 days) the Hα line exhibits a striking fine structure called "Bochum event" [1]. This phenomenon was originally described as two additional emission-like features, a red emission satellite (RES) and a blue emission satellite (BES). Such an Hα profile was supposed to result from a superposition of an asymmetric and a spherically symmetric component [2].

The asymmetric component responsible for the RES detail consisted of the bright core with the radial velocity of +4000 km s^{-1} and the extended

halo of a lower brightness. A transversal velocity of the core of 2400 km s^{-1}, estimated with the effect of the occultation of the asymmetric component by the photosphere, together with the radial velocity gave the absolute velocity of 4700 km s^{-1}. It was evident that the core of the asymmetric component coincided with the ^{56}Ni clump, which should have the same absolute velocity of 4700 km s^{-1}. The amount of ^{56}Ni in the fast clump was estimated as $\sim 10^{-3} M_{\odot}$. The symmetric component was adapted to match the BES feature of Hα and was characterized by the non-monotonic radial dependence of the Sobolev optical depth which had no physical explanation.

The unusually strong Ba II 6142 Å line in early spectra of SN 1987A is a distinctive feature of this supernova [3], which still remains a subject of great concern after first studies [4, 5] claimed the large (up to a factor of 20) Ba overabundance derived from the line strength. The problem is that the *s*-process nucleosynthesis in massive stars evolving to the presupernova star of SN 1987A [6] is not able to yield the Ba overabundance in the hydrogen envelope by more than a factor of 1.4 assuming that a total ejecta mass is 15 $M_{\odot}$, a mass-cut is at 2 $M_{\odot}$ [7], and the synthesized Ba is completely mixed over the ejecta.

More naturally is to consider the large strength of Ba II 6142 Å as the outcome of specific conditions in the SN 1987A atmosphere. It was recognized that if Ba in the envelope of SN 1987A was mostly in Ba II ion form then the Ba II 6142 Å line might be reproduced with the Ba abundance typical for the LMC [8]. The absence of strong Ba lines in normal SNe II-P was explained then by the fact that Ba in the atmosphere of these supernovae was mostly in Ba III form. An atmosphere model based on solving the radiation transfer equation with the Monte Carlo technique was able to account for the low strength of Ba II lines in normal SNe II-P for the solar abundance, but failed to produce strong Ba II lines in SN 1987A for the LMC abundance [9]. It was acknowledged that this atmosphere model of SN 1987A used for Ba II lines simulation was presumably not adequate enough because of a poor agreement in hydrogen Balmer line intensities.

Generally, until recently the modelling of hydrogen lines in SN 1987A at the photospheric epoch has remained a challenging problem for spectrum synthesis (e.g. [10]). Situation has changed recently, when it has become clear that the major drawback of standard atmosphere models for SNe II-P was an assumption of the statistical equilibrium. It has been shown in the frame of time dependent chemical kinetics that an ionization freeze-out plays a crucial role in the ionization and excitation of hydrogen in the atmosphere of SNe II-P at the photospheric epoch [11, 12]. Moreover, in the atmosphere of SN 1987A ion-molecular processes might become essential in producing

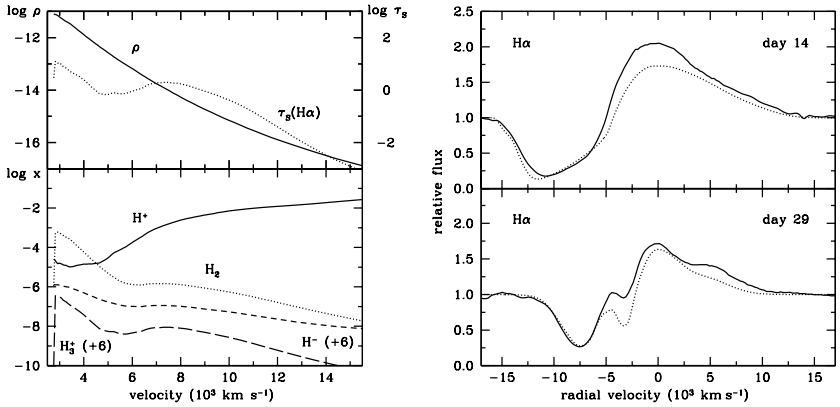

Figure 1: Upper left panel: Density (solid line) and the Sobolev optical depth of Hα (dotted line) as a function of velocity for day 29. Lower left panel: Velocity dependence of the following fractional abundances for day 29: x(H^+) (solid line), x(H_2) (dotted line), x(H^-) (short dashed line), and x(H_3^+) (long dashed line). Dashed lines are shifted by a +6 order of magnitude. Right panel: Observed (solid line) and calculated (dotted line) Hα profile for days 14 and 29.

ionization of hydrogen. In view of these results a motivation of the work is to take time dependent effects into account, to construct an adequate model, to succeed in reproducing Hα profile, and then to study the Ba II 6142 Å line in SN 1987A at the photospheric epoch.

Model and Input Physics

A full model should be based on the hydrodynamic model and time-dependent radiation transport, and should include self-consistent electron temperature evolution and full reaction network.

Our present model is based on the hydrodynamic model [13] which has an ejecta of mass $15M_\odot$ and a kinetic energy of 1.44×10^{51} erg. The radiation field is treated in the approximation of clear-cut photosphere and above atmosphere. For t<1.8 days the radiation field in continuum is described by the photospheric radius and effective temperature, taken from the hydrodynamic model, and then by those observed [14] and by the approximated UV and optical observations [15]. The line radiation transfer is treated in the modified Sobolev approximation [16, 17] as a purely local process. Instead of solving the energy equation we use two regimes for the electron temperature:

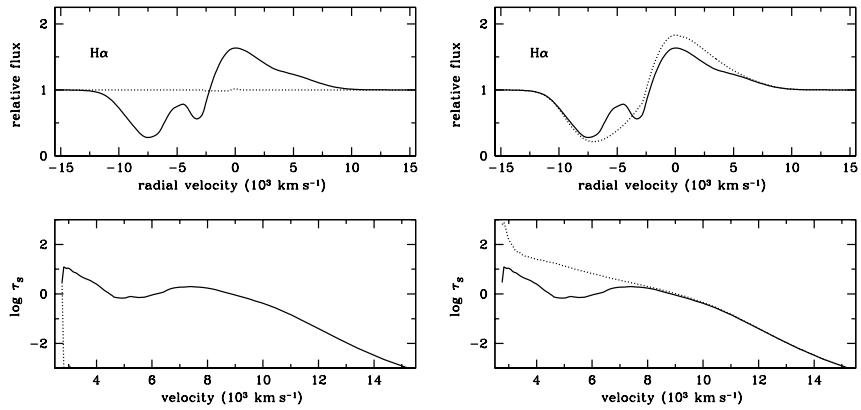

Figure 2: Calculated Hα profile and the Sobolev optical depth as a function of velocity for day 29. Influence of non-stationarity (left panel) and molecules (right panel) is shown by dotted line.

radiative equilibrium and adiabatic approximation.

The following elements and molecules are calculated in non-LTE chemical kinetics: H, He, C, N, O, Ne, Na, Mg, Si, S, Ar, Ca, Fe, Ba, H^-, H_2, H_2^+, and H_3^+. All elements but H are treated with the three ionization stages. The level populations of H and Ba II are calculated for 15 and 17 levels, respectively, and the rest of atoms and ions are assumed to consist of the ground state and continuum. The reaction network involves all bound-bound and bound-free, radiative and collisional processes for atoms and ions, and 7 radiative and 37 collisional processes for molecules. To reproduce the chemical composition typical to the LMC situation [18] all metal abundances are scaled to 1/2.88 their solar values.

Results

We have developed a time dependent chemistry model for supernova envelope at photospheric phase and investigated spectra of SN 1987A. On day 29 Fig. 1 shows the specific non-monotonic radial dependence of the Sobolev optical depth of Hα over envelope with minimum near the photosphere. Just such a distribution we need to reproduce the BES feature of Hα profile. Note that the fractional abundance of molecular hydrogen of the order of 10^{-4} is high enough for the photospheric phase of SN 1987A. The fit between the observed and calculated Hα profiles on days 14 and 29 is fairly good in Fig. 1 indicating that we have constructed a correct model.

The influence of time dependent effects on the Hα profile is shown in Fig. 2. It is clear that the ionization freeze-out plays a key role in producing the ionization and excitation of hydrogen for times nearly up to day 40 when the non-thermal ionization and excitation resulting from radioactive ^{56}Ni decays become essential [13]. In addition, from Fig. 2 it is evident that molecules are mainly responsible for the formation of the minimum of the Sobolev optical depth above the photosphere and, as a consequence, for the BES feature at Bochum event phase. A leading reaction in the neutralization of ionized hydrogen is mutual neutralization between H^- and H^+: $H^- + H^+ \rightarrow 2\ H$.

Now when we have got a confidence in reproducing the observed Hα profile we can study the barium line. In Fig. 3 there is a good fit between the observed and calculated Ba II 6142 Å line but the approximated UV and optical observations result in the Ba overabundance ratio ≈ 12 for the time-dependent solution and ≈ 16 for the steady one. The point is that the fractional abundance of Ba II in the supernova envelope turns out too low to produce the strong barium line with the low Ba overabundance ratio. We have analyzed this situation and found out that, it is evident, the fractional abundance of Ba II is very sensitive to the radiation flux at photon energies responsible for Ba II ionization from ground state and excited levels.

Discussion

To evaluate the influence of the radiation flux on the Ba II fractional abundance we calculate a toy model with the Ba abundance ratio of 1.4 as predicted from the *s*-process nucleosynthesis. In this model the calculated Ba II 6142 Å line matches the observed one as shown in Fig. 3 assuming a reduction of the radiation flux by a factor of ≈ 17 in the far UV region.

So, the far UV radiation field plays a vital role in estimating Ba abundance in SN 1987A. A crucial question is whether the observed flux is an intrinsic flux of SN 1987A or not. Taking a number of uncertainties in measuring the far UV flux of SN 1987A into account it is reasonable to assume that the observed flux is presumably not related to the radiation field in the region where the barium line forms. Thus we have at least two alternatives: pessimistic and optimistic. If we consider the observed flux as responsible for the Ba II ionization in supernova envelope we should accept the Ba abundance as large as 12 or so. And there is nothing more to do. This is the pessimistic alternative. In opposite case we can solve the radiation transfer equation in far UV region, check the solution in some way, and estimate Ba abundance in SN 1987A. It is the optimistic alternative.

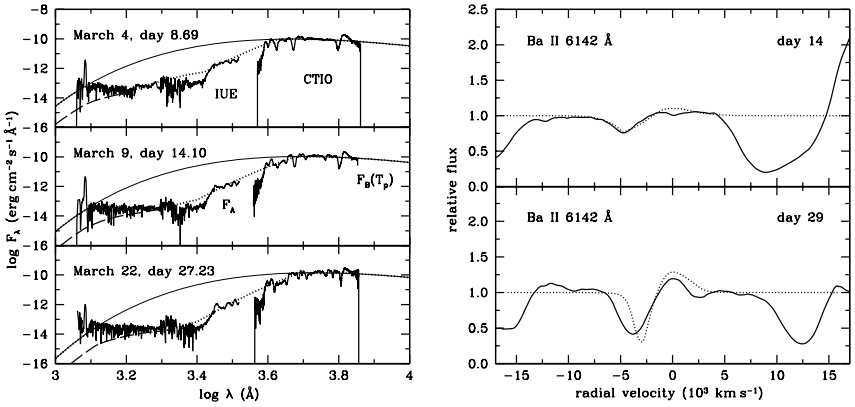

Figure 3: Left panel: The combined UV (IUE) and optical (CTIO) spectra of SN 1987A [15] (thick solid line), the black-body flux at the effective temperature (thin solid line), the approximated emergent flux (dotted line), and the approximated emergent flux reduced by a factor of ≈ 17 at log $\lambda < 3.2-3.3$ (long dashed line) for days 8, 14, and 27. Right panel: Observed (solid line) and calculated (dotted line) Ba II 6142 Å line for days 14 and 29.

Conclusions

We have developed a time dependent chemistry model for supernova envelope at photospheric phase that, in connection with hydrodynamic models, provides a powerful tool to investigate supernova spectra.

We have shown that level populations of hydrogen are mostly controlled by an ionization freeze-out and ion-molecular processes up to ~ 40 days in the atmosphere of SN 1987A. The ionization freeze-out effects are important for normal SNe II-P as well.

The time dependent effects and mutual neutralization between H^- and H^+ may result in a non-monotonic radial dependence of the Sobolev optical depth for Hα and then in a blue emission satellite of Hα observed in SN 1987A spectra at Bochum event phase.

It should be noted that the relative abundance of molecular hydrogen $n(H_2)/n(H) \sim 10^{-4}$–10^{-3} is high enough for the photospheric phase of SN 1987A.

We emphasize that the poor knowledge of the far UV radiation field in the envelope of SN 1987A still forbids a truly reliable estimate of the Ba abundance but well-constructed and tested models may improve this

situation.

Acknowledgements

V.P.U. is grateful to W. Hillebrandt and E. Müller for hospitality, for giving an opportunity to participate in the Eleventh Workshop on Nuclear Astrophysics, and for the financial support of his participation at this workshop and staying at the MPA, and also would like to thank Keith Butler for providing him with atomic data on the once-ionized barium. The work in Russia is partially supported by the RFBR (project 01-02-16295).

References

[1] R.W. Hanuschik and J. Dachs, Astron. and Astrophys. **205** (1988) 135.

[2] V.P. Utrobin, N.N. Chugai, and A.A. Andronova, Astron. and Astrophys. **295** (1995) 129.

[3] R.E. Williams, Astrophys. J. **320** (1987) L117.

[4] R.E. Williams, In: K. Nomoto. (ed) Atmospheric Diagnostics of Stellar Evolution: Chemical Peculiarity, Mass Loss, and Explosion. Springer-Verlag, Berlin (1988) p. 274.

[5] P. Höflich, Proc. Astron. Soc. Australia **7** (1988) 434.

[6] N. Prantzos, M. Hashimoto, and K. Nomoto, Astron. and Astrophys. **234** (1990) 211.

[7] S.E. Woosley and T.A. Weaver, Astrophys. J. Suppl. Ser. **101** (1995) 181.

[8] N.N. Chugai, Sov. Phys. Usp. **31** (1988) 775.

[9] P.A. Mazzali and N.N. Chugai, Astron. and Astrophys. **303** (1995) 118.

[10] R.C. Mitchell et al., Astrophys. J. **556** (2001) 979.

[11] N.N. Chugai, In: S.E. Woosley. (ed) Supernovae. Springer-Verlag, New York (1991) p. 286.

[12] V.P. Utrobin and N.N. Chugai, Sov. Astron. Lett. (2002) in press.

[13] V.P. Utrobin, Astron. and Astrophys. **270** (1993) 249.

[14] R.M. Catchpole et al., Mon. Not. Roy. Astron. Soc. **229** (1987) 15P.

[15] C.S.J. Pun et al., Astrophys. J. Suppl. Ser. **99** (1995) 223.

[16] V.V. Sobolev, Moving envelopes of stars. Harvard University Press, Cambridge (1960).

[17] J.I. Castor, Mon. Not. Roy. Astron. Soc. **149** (1970) 111.

[18] R.J. Dufour, In: S. van den Bergh and K.S. de Boer. (eds) Proc. IAU Symposium 108, Structure and Evolution of the Magellanic Clouds. D. Reidel Publishing Co., Dordrecht (1984) p. 353.

Shock breakouts in SNe Ib/c

S.I. Blinnikov[1], *D.K. Nadyozhin*[1], *S.E.Woosley*[2] *and E.I.Sorokina*[3]

[1] *Institute for Theoretical and Experimental Physics, Moscow*
[2] *UCO/Lick Observatory, University of California, Santa Cruz*
[3] *Sternberg Astronomical Institute, Moscow*

It was realized long ago that a shock propagating along the profile of decreasing density should accelerate [1, 2]. In compact presupernovae, like SNe Ib/c, the shock can become relativistic [3] and is able to produce a burst of X-ray and even γ-ray radiation [4, 5, 6]. The case of a peculiar type Ic SN1998bw, probably related to GRB980425, has shown that SNe Ib/c may have the highest explosion energy and highest production of ^{56}Ni among core-collapsing supernovae [8, 7]. Supernovae of type Ib/c are also interesting for theory due to problems with their light curve modeling. Their understanding may serve as a diagnostics of mass loss from massive stars at the latest phases of evolution.

Numerical modeling of shock breakout in SNe Ib/c was done previously using some simplifying approximations [9]. Our method, realized in the code STELLA, allows us to get more reliable predictions for the outburst. Improvements in the theory done in the current work:

- multi-energy-group time-dependent radiation transfer,
- taking into account of (some) relativistic effects.

A representative presupernova in our runs was a WR star built by the code KEPLER [10] (model 7A). Late light curves and spectra for this model were studied in [11]. We present UBV light curves found for the same model by STELLA in Fig. 1.

The Model 7A has mass 3.199 $M_\odot$(including the mass of the collapsed core). Its radius prior to explosion is not strictly fixed because the outer mesh zones in KEPLER output actually model the strong stellar wind and are not in hydrostatic equilibrium. So, we fixed the radius by hand and we got four models with radii from 0.76 up to 2 $R_\odot$ which *are* in hydrostatic equilibrium. Our results are summarized in the Table.

Explosions with KEPLER [11] gave maximum temperature of photons $T \sim 5 \times 10^5$ K at shock breakout. We have much finer mesh zoning at the edge of the star (down to $1{\times}10^{-12}$ $M_\odot$) and better physics and we find higher values of T. The Fig. 2 shows the difference between effective

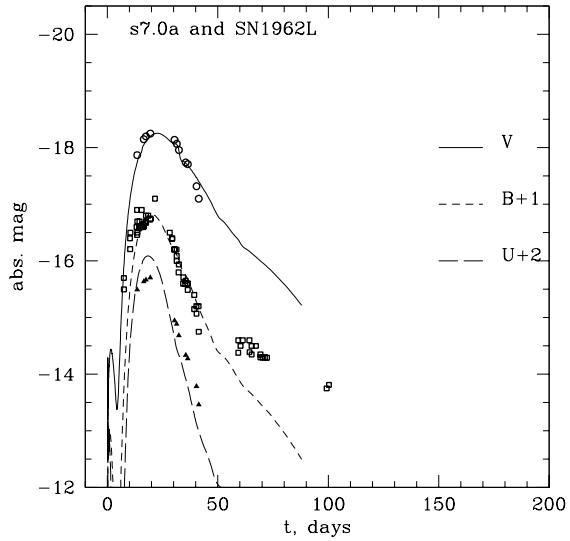

Figure 1: Theoretical UBV fluxes for the model 7A, exploded with $E_{\rm kin} = 1.47 \times 10^{51}$ erg in comparison with observations of SN1962L of type Ib.

and color temperatures (labels 'e' and 'c', respectively, in the Table). One should note that the peak values of luminosity and temperature given in the table and plots in Fig. 2 do not contain the light travel time correction. Models, labeled as 3.5N were computed by D.K.Nadyozhin in 1992 with the equilibrium radiation diffusion hydrocode SNV. Left plot in Fig. 3 shows one of his results. Dashed lines in Fig. 3 demonstrate the effect of averaging the light curve due the light travel time correction.

Parameters of shock breakouts

M	R_0	$E_{\rm kin}$	$L_{\rm p}$	$T_{\rm p}$	Δt
$M_\odot$	$R_\odot$	foe	erg/s	10^6K	s
3.2	0.76	1.24	4.2×10^{44}	4.2c	0.021
3.2	1.00	1.32	5.8×10^{44}	4.3c	0.026
3.2	1.23	1.30	6.8×10^{44}	4.3c	0.043
3.2	2.	1.39	9.4×10^{44}	4.3c	0.12
3.2	2.	4.36	3.6×10^{45}	5.3c	0.028
3.2	2.	8.86	4.8×10^{45}	7.2c	0.020
3.5N	0.76	1.30	1.4×10^{45}	5.1e	0.028
3.5N	1.23	1.30	8.1×10^{44}	3.5e	—

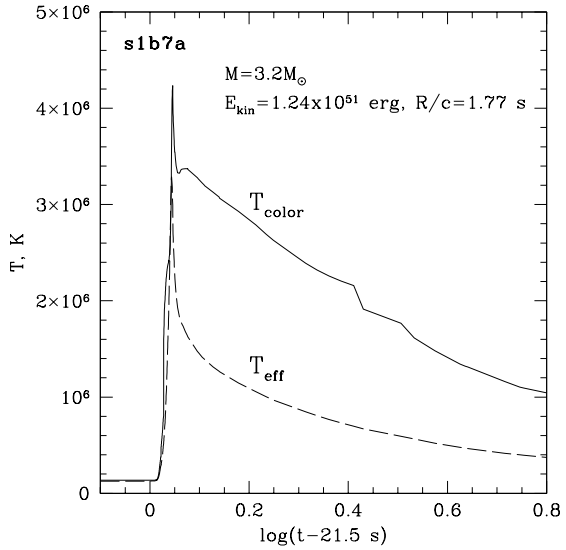

Figure 2: Effective and color temperatures of emerging radiation in one of the runs.

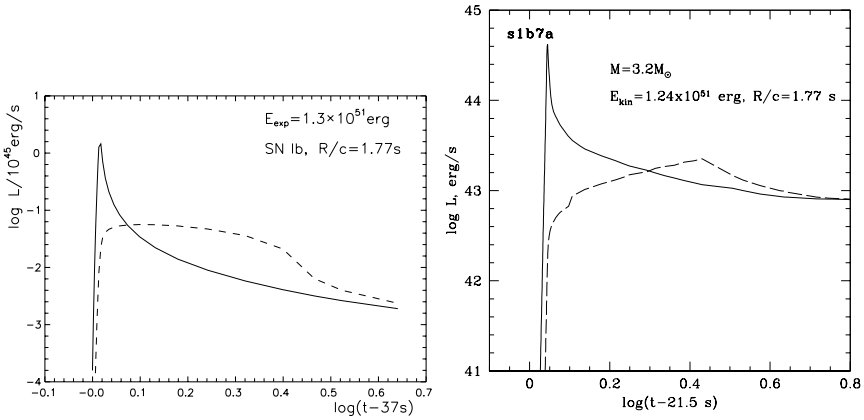

Figure 3: The left figure shows the results for shock breakout luminosity by the equilibrium radiation diffusion hydrocode SNV; the right one: a similar presupernova model, results obtained by STELLA. Dashed lines show the light travel time corrected luminosity.

M and R_0 — presupernova mass and radius, respectively, in solar units
$E_{\rm kin}$ — the kinetic energy at infinity in 10^{51} ergs

L_p and T_p — the peak luminosity and temperature
Δt is the width of the light curves at 1 stellar magnitude below L_p

We conclude that photon spectra at shock breakouts in SNe Ib/c peak near $3kT \sim 1$ keV and the X-ray fluences predicted can be observed by future missions up to tens of Mpc.

We are grateful to MPA staff for permanent and generous support. Our work in US was supported by grants NSF AST-97 31569 and NASA - NAG5-8128, in Russia RBRF 99-02-16205 and RBRF 02-02-16500.

References

[1] G.M. Gandel'man, D.A. Frank-Kamenetskij, Doklady AN SSSR **107** (1956) 811.

[2] A. Sakurai, Commun. Pure Appl. Math. **13** (1960) 353.

[3] M.H. Johnson, C.F. McKee, Phys.Rev.D **3** (1971) 858.

[4] S.A. Colgate, Can.J.Phys. **46** (1969) 476.

[5] G.S. Bisnovatyi-Kogan et al. Ap.Space Sci.**35** (1975) 23.

[6] S.E. Woosley, Astron.Ap.Suppl., **97** (1993) 205.

[7] S.E. Woosley, R.G. Eastman, B.P. Schmidt ApJ, **516** (1999) 788.

[8] K. Iwamoto et al. Nature, **395** (1998) 672.

[9] L.M. Ensman, Type Ib supernovae and a new radiation hydrodynamics code, PhD Thesis – California Univ., Santa Cruz, 1991.

[10] S.E. Woosley, N. Langer, T.A. Weaver ApJ, **448** (1995) 315.

[11] S.E. Woosley, R.G. Eastman, Thermonuclear Supernovae, eds. P. Ruiz-Lapuente, R. Canal, J. Isern (1997) 821.

SNII-Plateau 1999em in NGC 1637: a lower ^{56}Ni mass event.

A. Elmhamdi[1], *I.J. Danziger*[2]

[1]*SISSA / ISAS , via Beirut 4 - 34014 Trieste, Italy*
[2]*Osservatorio Astronomico di Trieste, via G.B. Tiepolo 11,34131 Trieste, Italy*

Abstract

In this short presentation we summarize our main results from the study of SN 1999em in NGC 1637, using the spectroscopic and photometric characteristics to determine the chemical composition as well as its progenitor star properties. For more details of the work see Elmhamdi et al (2002, in preparation).

27.1 Main results

A sample of the spectral evolution of SN 1999em is shown in figure 1(left) at three different phases, namely, $\sim +8^d$ after explosion with a clear blue-continuum indicating a temperature exceeding 10^4K with broad P-Cygni profiles(high velocities) of the hydrogen Balmer lines, HeI lines, and the $NaID$ and $CaII$ lines, and the $\sim +40^d$ spectrum during the photospheric phase where the temperature has cooled to $\sim$ 5000-6000K, and the $\sim +312^d$ spectrum dominated by emission lines of $[OI]$, $H\alpha$, $[CaII]$ and the near IR triplet $CaII$ characterizing the nebular phase.

We note a blue-shifted emission peaks at early phases, clearer for $H\alpha$, decreasing as the SN evolves in time. Similar behaviour was reported for SN 1987A and has been interpreted as beingdue to reflection of photons from the photosphere [1]. Some fine structure bumps are seen on the blue and red sides of the emission component of $H\alpha$ P-Cygni profile as shown in figure 1(right), these features are also evident in $NaID$ profile. In analogy with SN 1987A (Bochum event; Utrobin, this workshop) one might conclude that mixing of radioactive material has occurred in SN 1999em, but at a later phase [10] .

The light curves show a clear plateau phase, lasting about 80 days in the V band, then display a steep decline signaling the onset of the nebular phase and the starting of the exponential decline (figure 2). We measure the decline

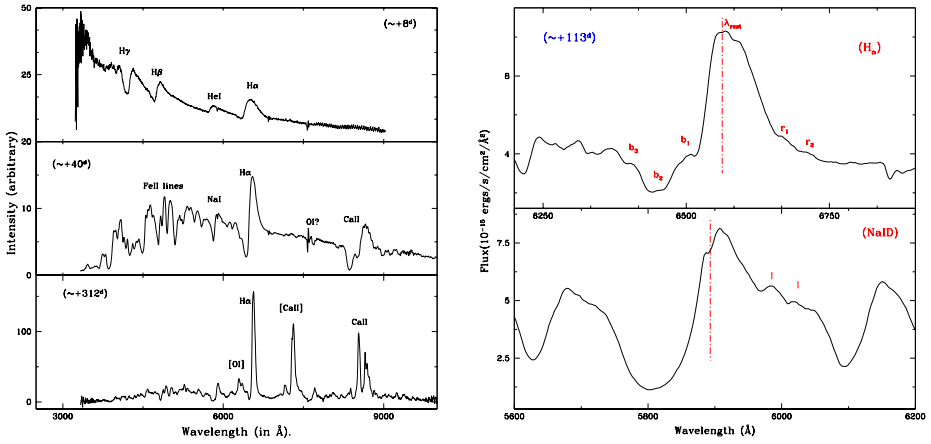

Figure 1: Left: a sample of spectra during different phases of evolution with some line identifications. Right: the $H\alpha$ and $NaID$ line profiles at $\sim +113^d$ after explosion. The rest wavelengths are also shown. The short bars in $NaID$ profile correspond to the derived velocities from the features seen in the $H\alpha$ profile .

rate in V-band at these later phases to be $\sim$0.97 mag $(100d)^{-1}$, indicating that radioactive decay of ^{56}Co with consequent trapping of $\gamma - rays$ is the main source of energy powering the light curve at late times for SN 1999em, at least until $\sim$ 510 days after explosion. The (B-V) colour evolution exhibits a steep and rapid decline from blue to red as the supernova envelope expands and cools as shown in figure 2(right), and at later phases as the light curve settles into the exponential tail, the colour becomes bluer again as a result of the particular distribution of emission lines with a clear similarity to SN 1987A.

We apply the Expanding Photosphere Method(EPM) to our spectrophotometric data in order to estimate the explosion time of SN 1999em. More detailed works concerning the use of this method in the case of SN 1999em were made by Hamuy et al [2] and by Leonard et al [3], who used broad band colours rather than spectrophotometry. Note that the case of SN 1999em provides a check of the consistency of the EPM since, from observations, it is already known that the supernova exploded between Oct 20.45 and the discovery date Oct 29($IAUC$ 7294). We found $t_0 \sim JD2451476(\pm 1\text{day})$ corresponding to 1999 October 24.5 and a distance of the order 7.82 $\pm$0.461 Mpc in good agreement with the values derived by other independent work

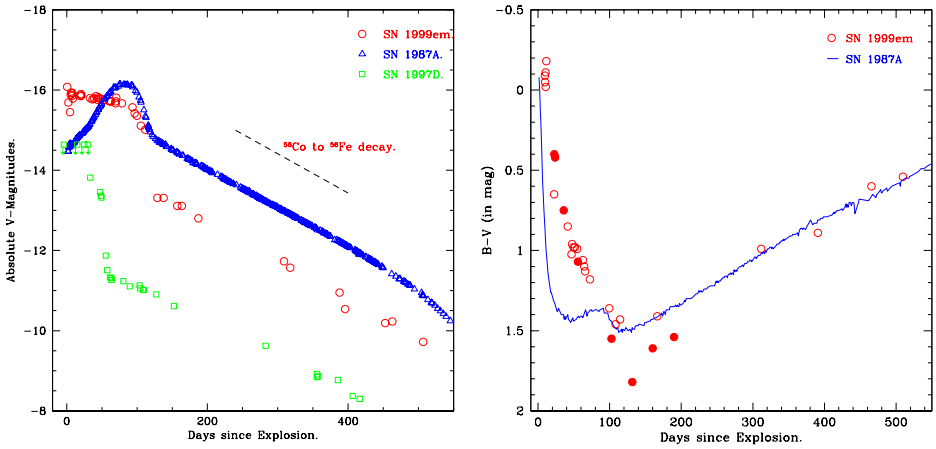

Figure 2: Left: the absolute V-light curve of SN 1999em with those of SN 1987A and SN 1997D;^{56}Co to^{56}Fe decay is also reported. Right: Comparison of the B-V color curve of SN 1999em with the one of SN 1987A. Filled circles represent data from Hamuy et al [2]

[4].

In order to obtain information about the progenitor star of SN 1999em, we apply the analytical two-zone model for type II-P SNe of Popov [5] . The model allows us to estimate the basic SN parameters, namely the mass of ejected envelope, explosion energy and the initial radius for Type II-P supernovae, from observational data (the duration of the plateau and its V magnitude).

We obtained constraints on the mass and radius suggesting an $(F_5 - G_2)$ supergiant star as the pre-supernova progenitor. The results are consistent with what was observed in the pre-explosion frame as well with stellar evolutionary theory. Therefore as a conclusion, we believe that the progenitor of SN 1999em was a $(F_8 - G_2)$supergiant having the following characteristics :
$M \approx 9$ -12 $M_\odot$, $R \approx 100$ -150 $R_\odot$ with energy $E_{exp} \approx 1$ -1.5$\times$ 10^{51} ergs. These estimates provide one with the main parameters of the SN progenitor, as a starting point for more detailed computations. The low mass progenitor nature is supported observationally by the $[OI]$ 6300,64$\mathring{A}$ integrated flux evolution, as well as by the behaviour of $[CaII]$ 7291,7324$\mathring{A}$ to $[OI]$ 6300,64$\mathring{A}$ flux ratio evolution when compared with that of SN 1987A. We estimate the oxygen mass produced by SN 1999em to be $\sim 0.15 M_\odot$.

Figure 2(left) displays the absolute light curve of SN 1999em in the V band together with that of the double-peaked SN 1987A and the peculiar type II-P SN 1997D for comparison. These plots display the different behaviour of the photometric evolution of the three SNe, from the explosion until about 550 days. They provide constraints on the explosion energy of SN 1999em as well as on the radioactive nickel mass ejected. All the radioactive tails of the three SNe follow the ^{56}Co decay slope suggesting that it is the main energy source powering the late phases of the light curves.

The fainter object SN 1997D ($M_V^{max} \geq -14.65$, [6]) ejected an extremely small amount of radioactive ^{56}Ni, about $0.002M_{\odot}$, with a low explosion energy of $\sim 10^{50}$ ergs derived from modelling the spectra [7] , while the mass of ^{56}Ni ejected by the well studied SN 1987A and the explosion energy are $\sim 0.075M_{\odot}$ and $\sim 1.04 \times 10^{51}$ ergs, respectively [8]. We therefore conclude that SN 1999em produced a mass of ^{56}Ni intermediate between 0.002 and 0.075 $M_{\odot}$.

For more accurate estimation we constract the UBVRI bolometric light curve of SN 1999em, and when comparing with that of SN 1987A (figure 3) we infer an amount of the ejected ^{56}Ni mass to be about $0.022M_{\odot}$.

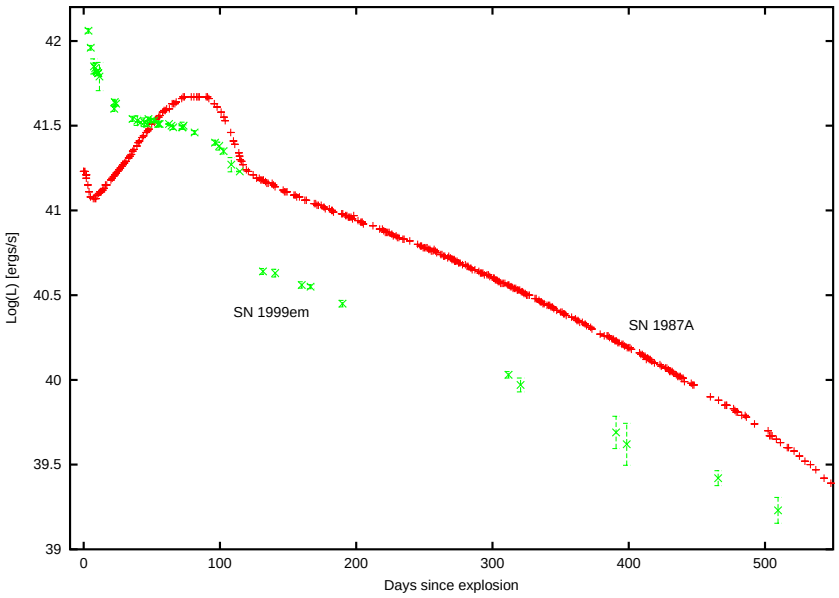

Figure 3: The UBVRI bolometric light curve of SN 1999em with that of SN 1987A for comparison.

27.2 Discussion

SN 1999em provided a good opportunity to test our understanding of core collapse events from an observational point of view. For instance, when comparing with other events it transpires that although the explosion energy is normal ($\sim 10^{51}$ ergs), the nickel mass is smaller than typical type II-P SNe 1969L and 1988A ($0.07 M_{\odot}$) and similar to the peculiar SNII-P 1991G. Therefore whether in fact there is any correlation between the amount of ^{56}Ni ejected and the explosion energy [9] remains unclear and its clarification will require a larger sample. SNII-P 1997D with its low explosion energy and very low mass of ^{56}Ni ($0.002 M_{\odot}$) has been interpreted to have a relatively low mass progenitor (a main-sequence mass $\sim$ 8 - 12 $M_{\odot}$) adopted by Chugai & Utrobin [7], leaving a neutron star. On the other hand SN 1997D and SN 1999em have different nickel masses and explosion energies while their progenitor masses could be similar. This indicates that the full range of parameter space for supernova progenitors is not yet understood nor well-defined. But taken at face value nickel mass seems to be a steeply rising function of progenitor mass near 10 $M_{\odot}$. Moreover the fact that SN 1999em probably resulted from the explosion of an F8 supergiant also indicates, as did SN 1987A, that the evolutionary stage at which massive stars can explode is not well understood.

Our results, namely the progenitor main sequence mass (9 - 13 $M_{\odot}$) and the ejected ^{56}Ni mass ($\sim 0.022 M_{\odot}$) also satisfy the constraints on the iron yield as function of core collapse SNe progenitor mass derived from the scatter in $[O/Fe]$ and $[Mg/Fe]$ abundance ratios observed in metal-poor halo stars (see Argast, this workshop).

We have noted some flattening in the light curves (clearer for the blue bands) at the start of the exponential tail after the steep decline from the plateau phase. This behaviour is also noted in other objects, namely SN 1997D [6] , SN 1991G [9]and SN 1999eu (Pastorello et al, in preparation). On the other hand these events have some common characteristics, being type II-P SNe and all having lower nickel mass. In addition there may be a hint of a correlation between the duration of this feature and the amount of the ejected nickel. However more statistics and samples of this class of *low nickel mass* events are required in order to confirm or rule out this behaviour.

Acknowledgements

A.Elmhamdi is greatful to the workshop organizers for hospitality and for providing an excellent environment for this scientific meeting.

References

[1] Chugai N.N. 1988, SvAL, 14, 334

[2] Hamuy M. et al. 2001, ApJ, 558, 615

[3] Leonard D.C. et al. 2002, PASP, 114, 35

[4] Sohn Y.J. and Davidge T.J. 1998, AJ, 115:130-143

[5] Popov D.V. 1993, ApJ, 414, 712

[6] Turatto M. et al. 1998, AJ, 498, L129-L133

[7] Chugai N.N., Utrobin V.P. 2000, A&A, 354, 557-566

[8] Danziger I.J. et al. 1988, in SN 1987A in the Large Magellanic Cloud, eds. Kaplan M. & Michlitsianos A.G., Cambridge University Press, Cambridge p.37

[9] Blanton E.L. et al. 1995, AJ, 110.2868

[10] Lucy L.B. 1988, in SN 1987A in the Large Magellanic Cloud, eds. Kaplan M. & Michlitsianos,A.G., Cambridge University Press

Disturbance Ecology from Nearby Supernovae

D.H. Hartmann[1], *K. Kretschmer*[2], *and R. Diehl*[2]

[1] *Clemson University, Department of Physics & Astronomy, Clemson, SC 29634-0978*
[2] *Max-Planck Institut für Extraterrestrische Physik, PO Box 1312, 85741 Garching*

The Hammer of God

"Kali 2 entered the atmosphere just before sunrise, a hundred kilometers above Hawaii. Instantly, the gigantic fireball brought a false dawn to the Pacific, awakening the wildlife on its myriad islands. But few humans; not many were asleep this night of nights, except those who had sought the oblivion of drugs" [12].

This grim description of an asteroid impact by Arthur C. Clarke was inspired by the famous paper "Extraterrestrial Cause for the Cretaceous-Tertiary Extinction" by Nobel Laureate Luis Alvarez and his geologist son, Walter Alvarez [1]. That great extinction episodes in geological history are tightly connected to asteroid/comet impacts is now firmly established [5][2]. Whether impact events are (quasi)periodic or random is not yet clear, and it is also not yet established if some external agent (e.g., a hypothetical Nemesis companion star of the Sun or modulated Oort cloud pertubations via solar oscillations in the Galactic disk; [34][37]) is required to explain the extinction record. While the idea of repeated blows by some "Hammer of God" has found widespread acceptance, a paradigm shift is underway with regards to the way we think about such catastrophes. Was the extinction of the dinosaurs a bad day in our history? From the point of view of the dinosaurs it sure counts as a bad day, but from our present-day perspective we can appreciate how this impact promoted evolutionary changes that benefited humans and other species.

Disturbance Ecology on Grand Scales

Ecology is the study of the interrelationships between organisms and their environment. In the past interactions between predators and prey and be-

tween herbivors and plants held the preeminent status among all ecological processes, with the environment merely providing the stage on which the ecological play takes place. This view has changed dramatically in recent decades. The "New Ecology" endowes the environment with an active role. Fires, floods, hurricanes, tornadoes, tsunamis, land-slides, vulcanic eruptions, storms, and lightning strikes are all key agents of the new "disturbance ecology" [38][14]. The destructive power of nature is now viewed as essential for maintaining biodiversity. This new persepective can be expanded by considering that changes in the solar system environment can directly affect the Earth, and that such changes can be driven by gentle or catastrophic events in the solar neighborhood. Long term evolution of the Sun will steadily increase the equilibrium temperatures of the planets on time scales of billions of years (melting the ice caps and eventually boiling the oceans and evaporating the atmosphere), while solar flares occur frequently and occasionally can be so energetic that global planetary atmospheres and the interplanetary space environment become severely polluted with energetic particles that can significantly alter atmospheric chemistry [10] [42][27]. Other dangers lurk just outside the solar system.

As the Sun moves around the Galactic center in a nearly circular orbit the Galactic environment in general changes slowly, but "sudden" (10^{3-4} years) modifications of the planetary environments can take place when the Sun encounters local density fluctuations in the interstellar medium [48] [52] or local field stars [23]. The latter situation can disturb the Oort cloud, increasing the cometary impact rates in the solar system, while the former situation can modulate the properties of the heliosphere and thus the local cosmic ray environment, with potential consequences for planetary climates. Still more damaging could be encounters with very massive stars, black holes, novae, super- novae, and hypernovae (aka Gamma Ray Bursts, GRBs).

Exposure to Nearby Gamma Ray Bursts

The largest energy releases in the Universe due to supernovae and gamma-ray bursts ([32] and [49] discuss both phenomena and their possible connections) do take place with somewhat predictable rates. A core collapse supernova occurs about once every second in the Universe. The Milky Way's present star formation rate is a few solar masses per year, which for a Salpeter-like IMF translates into a Galactic supernova rate of about once per century. The GRB rate is of order 1 day^{-1}, and we know that bursts are truly cosmological (typical redshifts of order unity, with a present

record at z $\sim$ 4.5 for GRB000131). Afterglow observations point towards a direct link between GRBs and supernovae so that bursts are also expected to occur in the Milky Way, although with a lower rate. The relative frequency of SNe and GRBs depends on the uncertain beaming pattern of bursts. The observations imply significant beaming corrections, but suggest that GRB rates are still much lower than supernova rates. Long-duration GRBs and SNe are expected to have similar spatial distributions. The amount of energy released into the surrounding medium is of order 1 foe (10^{51} ergs) in both cases, but GRBs focus energy into narrow jets while SNe impact their environments $\sim$isotropically.

Hartmann [26] and Thorsett [46] considered the possibility that a GRB was responsible for the demise of the dinosaurs and perhaps other mass extinctions. Thorsett studied in detail the effect of the gamma-ray flux on Earth's atmosphere, especially the reduction of ozone and the subsequent effects of enhanced solar UV radiation on the surface. Thorsett concluded that the critical distance was $D_{crit} \sim 1$ kpc, and estimated a rate of events closer than this distance of about $1/10^8$ yrs. In 1998 Dar, Laor, and Shaviv [15] investigated the effects of cosmic ray exposure for planet Earth located inside the jet of a galactic GRB. These authors concluded that ozone destruction and radioactive pollution of the Earth could have contributed to mass extinctions, and that biological effects due to ionizing radiation could also have caused the fast appearance of new species. More recently Dar & DeRujula [16] considered the potential dangers from Eta Carina as a future nearby GRB source (concluding that the direction of the possible jet is not aiming at us), and determined that jet-sterilization per life-supporting planet could happen as often as every 100 million years. Such a high rate might provide an answer to Fermi's famous question about alien visitors: "Where are they?". Depressing thoughts along these lines were the theme of the recent NOVA show "Death Star" [36]; nothing seems to sell better than sex and doomsday predictions [31].

A less sensational approach to the possible biological effects of nearby bursts was recently presented by Scalo and Wheeler [40], who investigated in great detail the effects of ionizing GRB radiation on DNA alterations and chemical modifications of the atmosphere. The emphasis of this work is thus not on catastrophes but smaller (more frequent and perhaps cumulative) events that can alter evolution through enhanced mutagenesis. Scalo and Wheeler estimate the "critical " X-γ-fluence required for a significant increase in DNA alteration, $F_{crit} = 5\ 10^5$ ergs cm^{-2}. From observed GRB spectral properties the sphere of influence of a galactic GRB is found to be $\sim$ 10 kpc, so that many galactic GRBs can have a potential impact on Earth's

ecology. Scalo and Wheeler estimate that at least one thousand biologically significant Galactic GRB irradiations should have occurred stochastically during the 4.4 Gyr history of life on Earth. The direct effect of one burst (GRB830801) on the ionosphere was recorded via changes in the VLF radio transmissions between distant sites [22], and this event most likely occured at a cosmological distance. Although GRBs are very luminous, their short duration provides a moderating factor in comparison to other potential sources of ionizing radiation (massive stars, supernovae, etc), and causes only one half of the Earth to be affected in any given exposure.

Exposure to Nearby Supernovae

The rate of nearby Galactic supernovae is a rather uncertain quantity, and estimates date back to the sixties [44]. The impact of a close supernova on the biosphere was considered in the seventies [39][28][50] and subsequent studies zoomed in on particular supernovae (e.g., Vela [8], and Geminga [24]) or nearby star forming regions (Sco-Cen [4]). The potential identification of such events through specific isotopic anaomalies (e.g., ^{60}Fe) was pointed out by Ellis and collaborators [19][21]. A recent search for ^{60}Fe anomalies in deep-ocean ferromanganese crust samples was sucessful [30] and estimates of the distance and epoch of the putative supernova give D $\leq$ 30 pc and age $\leq$ 5 Myrs [21], based on standard yields of $M_{ej}(^{60}Fe) \sim 10^{-5}$ $M_{\odot}$ [47]. The decay of ^{60}Fe (mean life $\sim$ 2 Myrs) produces gamma-ray lines at 1.17 MeV and 1.33 MeV. The diffuse glow of the galactic disk from the many supernovae that occur during a few mean life times may soon be detected with INTEGRAL, an ESA mission to be launched later this year [51] [43]. Tracing the orbits of the Sun and nearby stars back in time Benitez et al. [4] find that massive stars born in the Sco-Cen association produced supernovae at the right time and distance to be responsible for the ^{60}Fe observed in the ocean crust. According to these authors $\sim$ 2 Myrs ago a "Sco-Cen supernova" as close as D $\sim$ 40 pc could have done serious damage to the Earth' ozone layer, provoking or contributing to the Pliocene- Pleistocene boundary marine extinction. A very recent (or perhaps near future) supernova impact may be associated with "Vela-Junior" [3], for which ^{44}Ti gamma-ray line observations [29] were used to argue for a distance of D $\sim$ 150 pc and an age of t $\sim$ 700 yrs [11].

While dramatic events such as the demise of the dinosaurs and other mass extinctions may in some cases be linked to nearby supernovae [10], more moderate alterations of evolutionary paths through the enhanced UV

exposure were only recently considered in detail [41]. Core collapse supernovae launch a strong shock that propagates through the star for a few hours, depending on the progenitor size and mass and ejecta energy. The shock-breakout leads to a short UV-flash [17] [20][7] that delivers of order 10^{47} ergs in the 200-300 nm UV band. Scalo et al estimate that a "critical" fluence for enhanced mutagenesis in this crucial energy window is $\mathrm{F_{crit}} \sim 600$ ergs/cm^2. Taking into account absorption in the atmosphere the relevant value at the top of the atmosphere is about three times as large. The critical distance for shock breakout UV-flashes to affect the biosphere is thus of order 1 kpc. The effect of galactic extinction must also be taken into account, as emphasized by Scalo et al. In the UV band considered here the average differential midplane UV-extinction is $\partial_r \mathrm{A}_{UV} \sim 5$ mag kpc^{-1}. In addition, one should consider the spatial distribution of the absorbing dust relative to the spatial distribution of supernovae.

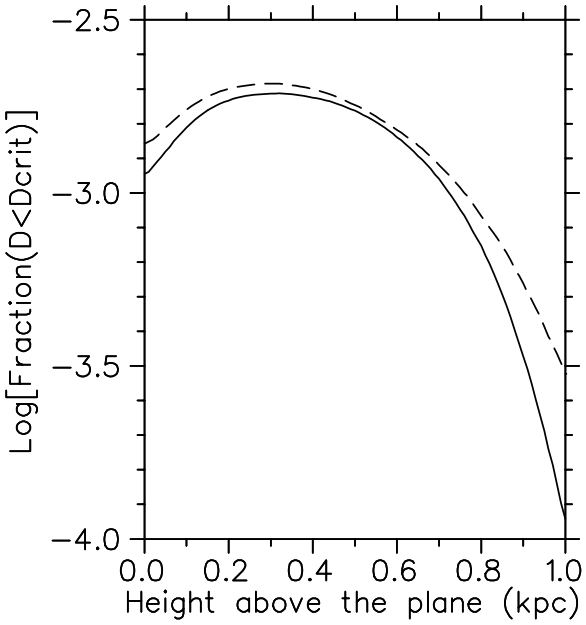

Figure 1: The fraction of Galactic Supernovae closer than the critical distance (see text) as a function of position above the midplane. The solid line assumes the same vertical profile for dust and supernovae, while the dashed curve is for a supernova distribution with doubled scale height.

What is the frequency of supernovae that generate UV fluences at Earth that exceed the critical value? A galaxy-wide star formation rate of a few

solar masses per year is associated with a supernova rate of a few events per century (many papers have been written about the value of "few" in both of these quantities). If the fraction of events closer than D_{crit} is f, the time between "events that cause a disturbance" is $\Delta T \sim 100/\text{few}\ f^{-1}$ years, where "few" is about 1−3 [45]. We find that f is of order 10^{-3}, so that dangerous UV-flashes from nearby supernovae occur as often as every ∼100,000 years. Scalo et al. provide an estimate of this time scale as a function of fluence and peak flux.

We now consider a modification of these rate estimates due to the solar motion in the Galaxy. The Sun is currently located $\sim$ 10 pc above the midplane (this number is uncertain, but everyone agrees that it is not zero [33][25][35][13]), but its perpendicular velocity relative to the local standard of rest W = 7.2 ± 0.4 km/s [6] will eventually carry us to a maximal height H $\sim$ 100 pc (depending on the galactic mass model) above the plane. The sun, like most stars, will spend most of its time above the Galactic dust layer, so that this effect should be included in estimates of the extinction to supernovae. The figure shows the variation of f with height above the Galactic plane. For the Sun the change in Δ T is less than a factor two, but for planets around high-velocity stars the effect can be significant (making damaging exposure ten times less frequent if vertical motion carries the star to z $\sim$ 1 kpc above the plane. The effect seen in the figure is due to the exposure asymmetry (events above/below the plane) for small heights but simply the result of larger distances from supernovae as the star moves away from the disk. For heights well in excess of 1 kpc none of the galactic supernovae is ever close enough to have an effect. As the stars oscillate in the Milky Way with periods of order 50−100 Myrs plane passages would lead to increased exposure, but less time is spend in the "critical midplane zone". A Monte Carlo simulation using these constraints could evaluate the time-averaged UV-exposure as a function of position and kinematics in the Galaxy.

We also investigated the effects of a larger scale height of supernovae relative to the dust (dashed line in the figure). The standard model assumes an exponential scale height of H_z = 60 pc for both components, while the model with larger extent of the supernova layer assumes H_z = 120 pc. The effect of "puffing up" the SN distribution is reduced extinction and thus a slightly larger fraction of critical events, but the effect is obviously not very strong. The radial distribution of supernovae probably is a more critical parameter. It is however rather uncertain and we describe it by a gaussian function, centered at R = 4 kpc, the location of the well known molecular ring [6]. If the width of this gaussian drops below 3 kpc, the fraction of

"deadly SN" decreases rapidly. Clearly, a delta function at R = 4 kpc generates no SN close enough to damage the biosphere. If the gaussian width exceeds 3 kpc, the fraction saturates as the local SN density profile becomes flat (as was assumed by Scalo et al.). While the time between SN that are "too close for comfort" depends on many properties of the Galaxy, the solar orbit, the shock breakout properties, and assumptions about what constitutes a biologically significant exposure, the perhaps surprising fact remains that close calls happened many times along our path around the galactic center.

Conclusions and Outlook

Can a nearby GRB or Supernova ruin your day ? You bet! Does this happen frequently? Yes and no, depending on your point of view. On a present-day human history time scale the answer is no (fortunately), but on a long-term- history-of-life time scale the answer is yes. Over the past billions of years there must have been a large number of close encounters of the undesired kind - UV jolts from supernovae and GRBs, and longer exposures to passing luminous and hot stars. Disturbance ecology is driven by events taking place on Earth and in the immediate Galactic environment of the solar system. Mutagenesis can be stimulated by exposure to external UV sources, and despite the long time intervals between events (ten thousand years to perhaps millions of years) these "rare" events may have domiated the path of evolution on Earth as well as other inhabited planetary systems throughout the Galaxy. The killing of the dinosaurs was indeed spectacular, but perhaps more impressive is the realization that the evolution of life throughout the Universe is so closely intertwined with the violent history of the Universe. Once every second a supernova and once every minute a GRB sends a UV flash into some galactic environment, jolting mildly or vehemently life in its path. It happened many times in Earth's history, and it will happen again. We hope that the next nearby jolt in our path contributes to a better global future for most lifeforms on Earth.

Acknowledgements

With pleasure we thank the organizers and the staff for outstanding hospitality and a very stimulating meeting.

References

[1] L. Alvarez, W. Alvarez, F. Asaro, and H. Michel (1980), Science, 208, 1095.

[2] W. Alvarez (1997), "T Rex and the Crater of Doom" (Princeton Univ. Press).

[3] B. Aschenbach, et al. (1998), Nature **396**, 141.

[4] N. Benitez, J. Maiz-Apellaniz, and M. Canelles (2002), Phys. Rev. Lett. **88**, 081101.

[5] L. Becker (2002), Scientific American, **286**, 76.

[6] J. Binney and M. Merrifield (1998) "Galactic Astronomy" (Princeton Univ. Press).

[7] S. Blinnikov, et al. (2000) ApJ **532**, 1132.

[8] G.R. Brakenridge (1981), Icarus **46**, 81.

[9] E. Cappellaro, et al. 1997, A&A **322**, 431.

[10] C.A. Chapman and D. Morrison (1998) "Cosmic Catastrophes" (Plenum Press).

[11] W. Chen, and N. Gehrels (1999) ApJ **514**, L103.

[12] A. C. Clarke (1993) "The Hammer of God" (Bantam Books, NY).

[13] M. Cohen 1995, ApJ **444**, 874.

[14] V. Courtillot (1999) "Evolutionary Catastrophes" (Cambridge Univ. Press).

[15] A. Dar, A. Laor, and N.J. Shaviv (1998), PRL 80, 5813.

[16] A. Dar, and A. DeRujula (2001), astro-ph/0110162.

[17] M.A. Dopita, S.J. Meatheringham, P. Nulsen, and P.R. Wood (1987) ApJ **322**, L85.

[18] J. Ellis, and D. N. Schramm (1995), Proc. Natl. Acad. Sci. **92**, 235.

[19] J. Ellis, B.D. Fields, and D.N. Schramm (1996), ApJ **470**, 1227.

[20] L. Ensman and A. Burrows (1992) ApJ **393**, 742.

[21] B.D. Fields, and J. Ellis (1999), New Astr. **4**, 419.

[22] G.J. Fishman and U.S. Inan (1988) Nature **331**, 418.

[23] J. Garcia-Sanchez, et al. (2001) A&A **379**, 634.

[24] N. Gehrels and W. Chen (1993) Nature **361**, 706.

[25] R.L. Hammersley, F. Garzon, T. Mahoney, and X. Calbet 1995, MNRAS **273**, 206.

[26] D. H. Hartmann (1995), Nature (unpublished).

[27] D.V. Hoyt and K.H. Schatten (1997) "The Role of the Sun in Climate Change" (Oxford Univ. Press).

[28] G.E. Hunt (1978) Nature **271**, 430.

[29] A. Iyudin, et al. (1998) Nature **396**, 142.

[30] K. Knie, G. Korschinek, T. Faestermann, C. Wallner, J. Scholten, and W. Hillebrandt (1999), Phys. Rev. Lett. **83**, 18.

[31] P.J.T. Leonard and J.T. Bonnell (1998), Sky & Telescope, February.

[32] M. Livio, N. Panagia, and K. Sahu (2001), "Supernovae and Gamma-Ray Bursts", Space Telescope Science Institute Symposium Series No. 13, (Cambridge University Press).

[33] T. Minezaki, et al. 1998, AJ **115**, 229.

[34] R. Muller (1988) "Nemesis the Death Star" (Weidenfeld & Nicolson, N.Y.).

[35] Y.K. Ng, G. Bertelli, C. Chiosi, and A. Bressan 1997, A&A **324**, 65.

[36] "Death Star", NOVA(2002) video, (WGBH Ed. Found., Boston).

[37] D. M. Raup (1986) "The Nemesis Affair" (W.W. Norton).

[38] S.R. Reice (2001) "The Silver Lining" (Princeton Univ. Press).

[39] M.A. Ruderman (1974), Science **184**, 1079.

[40] J. Scalo, J.C. Wheeler (2002) ApJ **566** 723.

[41] J. Scalo, J.C. Wheeler, and P. Williams (2001) astro-ph/0104209.

[42] B.E. Schaefer, J. R. King, and C.P. Deliyannis (2000) ApJ **529**, 1026.

[43] V. Schönfelder (2001) "The Universe in Gamma Rays" (Springer Verlag).

[44] I.S. Shklovsky (1968), "Supernovae" (Wiley, N.Y.).

[45] G.A. Tammann, W. Löffler, and A. Schröder 1994, ApJ Suppl. **92**, 487.

[46] S. E. Thorsett (1995) ApJ **444**, L53.

[47] F.X. Timmes, et al. (1995) ApJ **449**, 204.

[48] G.L. Verschuur (1978) "Cosmic Catastrophes" (Addison-Wesley)./bibi

[49] J.C. Wheeler (2000) "Cosmic Catastophes" (Cambridge Univ. Press).

[50] R. C. Whitten, J. Cuzzi, W.J. Borucki, and J.H. Wolfe (1976) Nature **263**, 398.

[51] C. Winkler, et al. (1997), "The Transparent Universe", ESA SP-382.

[52] G.P. Zank, & P. C. Frisch (1999) ApJ **518**, 965.

Pop III Hypernova Nucleosynthesis and Abundance in Very Metal-Poor Halo Stars

Hideyuki Umeda[1], *Ken'ichi Nomoto* [1]

[1] *Department of Astronomy, School of Science, The University of Tokyo, 7-3-1 Hongo, Bunkyo-ku, Tokyo 113-0033, Japan*

Abstract

We calculate evolution and nucleosynthesis in massive Pop III stars with $M = 13 \sim 270 M_\odot$, and compare the results with abundances of very metal-poor halo stars. The observed abundances can be explained by the energetic core-collapse supernovae with $M \lesssim 130 M_\odot$ ("hypernovae") but not by pair-instability supernovae (PISNe) with $M \sim 140 - 270 M_\odot$. This result constrain the IMF for the Pop III and very metal-poor Pop II stars.

Observed Abundance and Hypernova Nucleosynthesis

The observed abundances of metal-poor halo stars show quite interesting trends. There are significant differences between the abundance patterns in the iron-peak elements below and above [Fe/H]~ -2.5. For [Fe/H]$\lesssim -2.5$, the mean values of [Cr/Fe] and [Mn/Fe] decrease toward smaller metallicity, while [Co/Fe] and [Zn/Fe] increases (McWilliam et al. 1995; Ryan et al. 1996; Primas et al. 2000; Blake et al. 2001; see also Fig.4). The Galaxy was not well mixed in such a early stage, and the abundance pattern of each supernova (SN) may be kept in the very metal-poor stars. However, these trend could not be explained with the previous results of nucleosynthesis by core-collapse SNe such as Woosley & Weaver (1995), Nomoto et al. (1997) and Limongi et al. (2000). Therefore, we need reconsideration for the nucleosynthesis of very metal-poor stars.

We found that these trends are explained simultaneously in the context of Fe core-collapse SNe, if the mass from complete Si-burning is relatively large compared with that from incomplete Si-burning (Nakamura et al. 1999). However, all previous model calculations including Nakamura et al. (1999) underproduced the Zn/Fe ratio significantly (Fig. 1 left). In Umeda & Nomoto (2002, UN02 hereafter), we find that [Zn/Fe] is larger for deeper mass-cuts, smaller neutron excess, and larger explosion energies. Among them the large explosion energy is most important to realize the

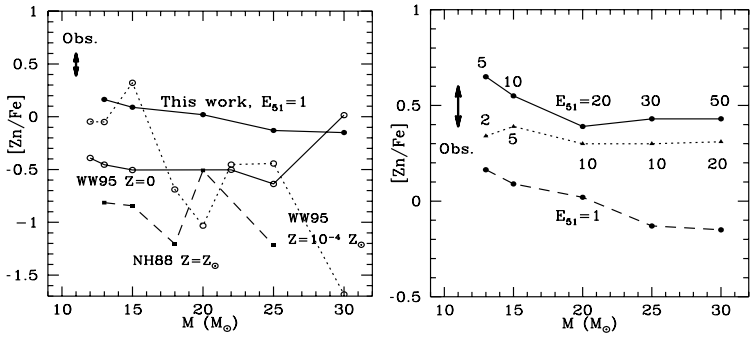

Figure 1: Observed range of [Zn/Fe] for the very metal-poor stars ([Fe/H] $\lesssim -3$) compared with the yields of theoretical models with low explosion energy $E_{51} = E_{\rm exp}/10^{51}$ erg =1 (left) and with high energies $E_{51} = 2 \sim 50$ (right panel). The observed large [Zn/Fe] value and also other unexpected trends in [Co, Mn, Cr/Fe] can be explained with this high energy ("Hypernova") models.

large [Zn/Fe] ratio (Fig. 1 right). The observed trends of the abundance ratios among the iron-peak elements are better explained with this high energy ("Hypernova") models than the simple "deep" mass-cut effect, because the overabundance of Ni can be avoided in the hypernova models.

Pair Instability Supernovae

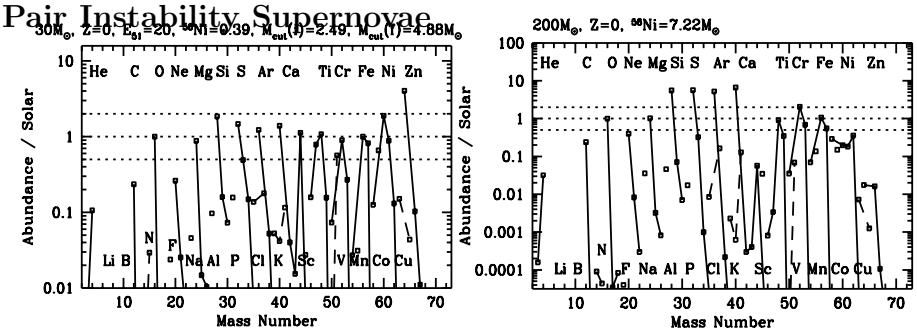

Figure 2: The abundance pattern of a hypernova (left) and a PISN model (right panel), normalize to the solar abundance. For PISNe with initial masses $M \simeq 140 - 300 M_\odot$ [Zn/Fe] is small, so that the abundance features of very metal-poor halo stars cannot be explained by these SNe.

We also investigate the yields of pair-instability supernova explosions of

$M \simeq 140 - 300 M_\odot$ stars. In Fig.2 we compare the abundance pattern of a hypernova and a PISN model. As can be seen [Zn/Fe] of PISNe are always small, because relatively large incomplete Si-burning region is formed in the explosion (UN02). Therefore, the abundance features of very metal-poor stars cannot be explained by pair-instability supernovae.

[Fe/H] and SNe Mass, Energy

We have discussed that the large [Zn/Fe] ratio can be explained with hypernova nucleosynthesis of $M \lesssim 130 M_\odot$ stars. However, in order to explain the observed trend for [Fe/H], it is necessary to explain why hypernova contribution is dominant for lower [Fe/H]. Suppose that the star-formation is induced by the supernova shock. Then the [Fe/H] of the next generation stars is determined by the ratio of Fe mass synthesized by the SN and the hydrogen mass swept by the supernova shock. Since the latter is inversely proportional to the explosion energy E, the following relation is obtained (Ryan et al. 1996; Shigeyama & Tsujimoto 1998):

$$\mathrm{Fe/H} \propto \mathrm{M}(^{56}\mathrm{Ni})/E. \tag{11}$$

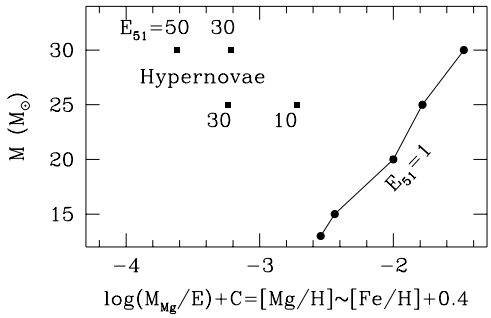

Figure 3: [(Mg, Fe)/H] determined by the relation (1) as a function of SN mass and energy. The constant C is chosen to normalize the ($20 M_\odot$, $E_{51} = 1$) case to be [Mg/H]= -2.

In Fig.3 we show the similar relation for Mg as a function of the mass and energy of SNe. Although the ejected Fe mass is theoretically uncertain, in most of the observed stars, Mg/Fe ratio is roughly the same and typically [Mg/Fe] $\simeq$ 0.4. Thus [Mg/H]$\sim$ [Fe/H]+0.4. As shown in this figure, if the explosion energy E_{51} is fixed, [(Mg, Fe)/H] increases with mass, because more Mg is ejected for more massive stars. However the energy factor is much more important, and hence massive hypernova models have smaller

[(Mg, Fe)/H] than less massive normal SNe II. In this way, hypernova like nucleosynthesis patterns can be seen in the very metal-poor stars.

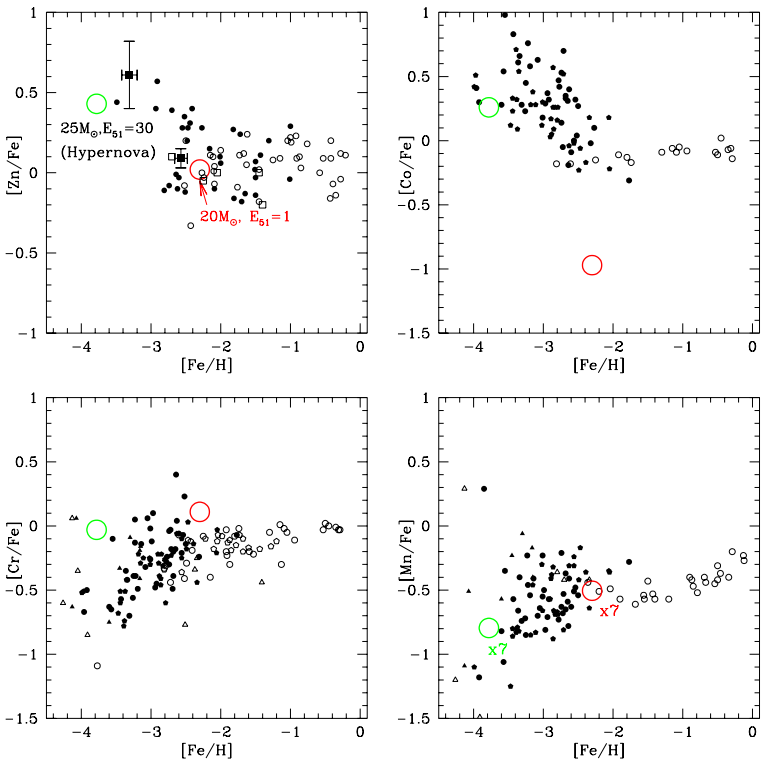

Figure 4: Observational points of Fe-peak elements (small symbols) and the theoretical abundance patterns for a normal SNe II ($20M_\odot$, $E_{51} = 1$) and a hypernova ($25M_\odot$, $E_{51} = 30$) models in UN2002 (large open circles). Here, Mn abundance is multiplied by 7.

Finally in Fig.4, together with the observation points, we plot the abundance pattern of Fe-peak elements for a normal SNe II ($20M_\odot$, $E_{51} = 1$) and a hypernova ($25M_\odot$, $E_{51} = 30$) models in UN02. Here the relative position in [Fe/H] is determined by the relation (1). Although there are some inconsistencies between the model and observations, we can explain the trend in the observation. As discussed in UN02, the Mn abundance is very sensitive to Y_e of the progenitor, and thus the enhancement of factor 7 is not so difficult to realize. The remaining problem is the overproduction of Cr and underproduction of Co, which should be investigated further in future work.

References

[1] Blake, L.A.J., Ryan S.G., Norris, J.E., & Beers, T.C. 2001, Nucl.Phys.A., 688, 502

[2] Limongi, M., Straniero, O., & Chieffi, A. 2000, ApJS, 129, 625

[3] McWilliam, A., Preston, G. W., Sneden, C., & Searle, L. 1995, AJ, 109, 2757

[4] Nakamura, T., Umeda, H., Nomoto, K., Thielemann, F.-K., & Burrows, A. 1999, ApJ, 517, 193

[5] Nomoto, K., Hashimoto, M., Tsujimoto, T., Thielemann, F.-K., Kishimoto, N., Kubo, Y., & Nakasato, N. 1997, Nucl. Phys. A616, 79

[6] Primas, F., Reimers, D., Wisotzki, L., Reetz, J., Gehren, T., & Beers, T.C. 2000, in The First Stars, ed. A. Weiss, T. Abel, & V. Hill (Berlin: Springer), 51

[7] Ryan, S. G., Norris, J. E., & Beers, T. C. 1996, ApJ, 471, 254

[8] Shigeyama, T., & Tsujimoto, T. 1998, ApJ, 507, L135

[9] Umeda, H., Nomoto, K. (2002), ApJ, 565, 385 (UN02)

[10] Woosley, S.E., & Weaver, T.A. 1995, ApJS, 101, 181

R-Process Chronometers: Calculations versus Observations

K.–L. Kratz and B. Pfeiffer

Institut für Kernchemie, Universität Mainz, Germany

Nuclear chronometers in terrestrial and meteoritic probes have always played an important role in the determination of the ages of the Solar System and our Milky Way. Particularly useful in this context are the long-lived actinides ^{232}Th, ^{235}U and ^{238}U, all of which are products of the rapid neutron-capture nucleosynthesis (the r-process). Earlier studies were based on models of galactic chemical evolution and the primordial abundances of Th and U in solar system matter. More recently, spectroscopic studies of extremely metal-deficient stars have made possible a quite different approach: age determinations for individual halo-field and globular-cluster stars from nuclear chronometers. Since such stars were formed in the very earliest epoch of star formation and nucleosynthesis in our Galaxy, their ages provide a **direct** measure of the age of the Galaxy and a lower limit of the age of the Universe itself. The observed relative abundance ratio of radioactive Th to the stable r-process-"only" element Eu was commonly used as the appropriate chronometer. However, theoretical modeling of r-process nucleosynthesis is required to determine the "initial" production ratios of the chronometric nuclei. Recent calculations use the observed solar-system isotopic r-abundances ($N_{r,\odot}$) to constrain these determinations [1, 2]. This was motivated by increasing evidence of a universal ("scaled") solar elemental abundance pattern in the oldest stars, at least for the heavy elements beyond Ba. As an example, in Fig. 1 the observed neutron-capture element abundances in BD+17°3248 [3] are compared to scaled solar-system values and our r-process calculations.

It is still true, that r-process calculations require nuclear physics input data of thousands of far unstable nuclei, in general not available from experiment. Hence, far reaching theoretical extrapolations from the known isotopes near β-stability to the neutron drip-line are needed, which may affect the calculated initial production ratios, thus introducing uncertainties in the age determinations that are not easy to quantify. Therefore, it was proposed to replace the $_{90}$Th/$_{63}$Eu chronometric pair by abundance ratios of elements with a smaller difference in the atomic numbers, as for example ratios between the actinides and 3^{rd} r-process peak elements ($_{76}$Os,

Table 1: Comparison of ($N_\odot$–N_s)$\simeq N_{r,\odot}$ "residuals" [2, 8, 9] of $^{206-208}$Pb and ^{209}Bi with our calculated r-abundances.

Isotope	Pb-206	Pb-207	Pb-208	Bi-209	ΣPb	ΣPb,Bi
$N_\odot$(s+r)	0.593	0.644	1.828	0.146	3.065	3.211
$N_{r,\odot}$						
Ref. [2]	0.240	0.254	0.158	0.144	0.652	0.766
Ref. [8]	0.178	0.171	0.133	0.101	0.482	0.583
Ref. [9]	0.178	0.116	0.091	0.118	0.385	0.503
$N_{r,calc.}$						
Ref. [2]	0.158	0.146	0.135	0.103	0.439	0.542
Fe-seed	0.163	0.151	0.138	0.111	0.452	0.564
Zr-seed	0.213	0.163	0.142	0.132	0.518	0.650

$_{77}$Ir, $_{78}$Pt) or even $_{90}$Th/$_{92}$U. Although Th abundances have been determined for several halo stars, only upper limits had been reported for U so far. The very recent determination of U abundances in CS31082-001 [4] and BD+17°3248 [3] (see Fig. 1) now makes it possible to use also the Th/U pair as a chronometer. A quite sensitive consistency check for the calculated initial abundances of this actinide pair can be given by a successful reproduction of the observed Pb and Bi r-abundances, which originate to more than 80% from α-decay of the Th and U isotopes (for details, see e.g. [2]). We have therefore examined in great detail problems and constraints associated with the above Th/3^{rd} peak and Th/U chronometers, such as uncertainties in the underlying atomic and nuclear physics (see, e.g. [5, 6, 7]). Table 1 summarizes our recent (so far unpublished) results of Th/X ratios from our site-independent r-abundance calculations assuming two different seed compositions, (i) the classical Fe-seed, and (ii) an A$\simeq$90 seed composition (here denoted "Zr-seed"). The latter simulates the possible r-process seed after the α-rich freeze-out of the high-entropy wind scenario of a core-collapse SN II. A detailed discussion of these results will be given in a forthcoming paper [10]. Table 2 compares the solar-system r-process "residuals" ($N_r, \odot$ $\simeq$ N$\odot$–N_s) [2, 8] for the Pb and Bi isotopes with our earlier [2] and recent theoretical predictions. It is clear from this table, that - at least within our present r-process model parameterization - we consistently obtain Pb and Bi abundances, which are lower than the old recommended solar values (used e.g. in [2]), but agree much better with the recent evaluations of Beer et al. [8] and Gallino et al. [9]. Again, more details about the predictions

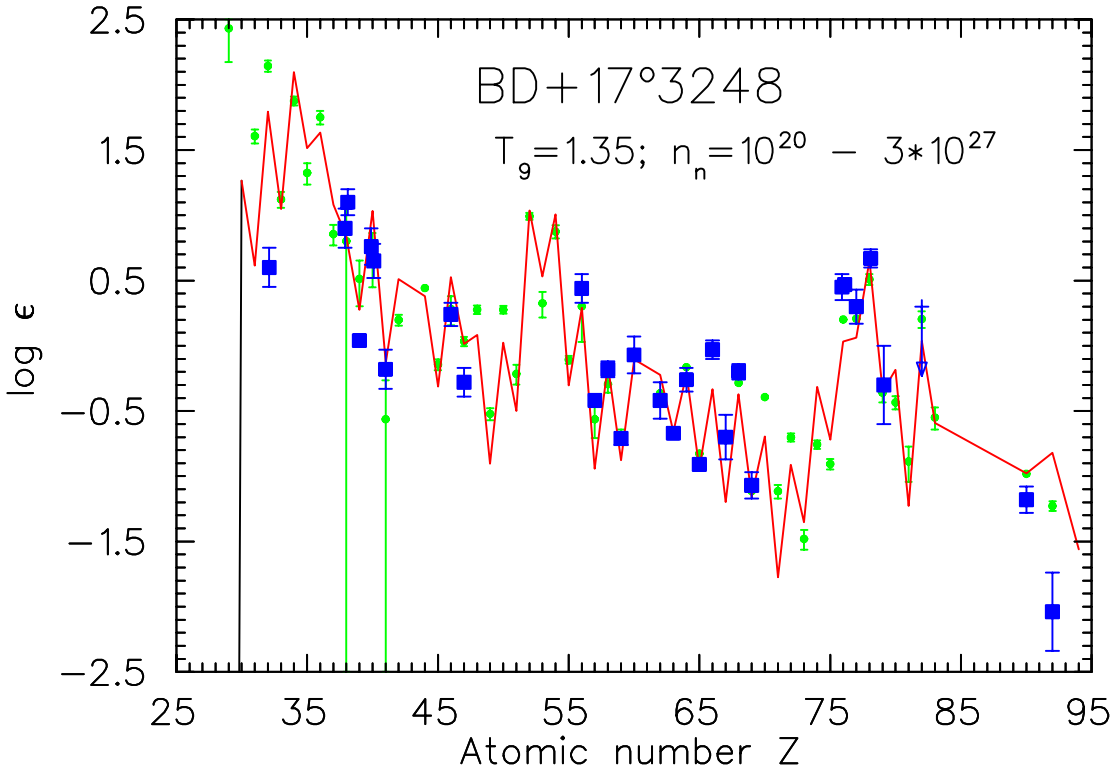

Figure 1: Observed neutron-capture element abundances in BD+17°3248 (squares) compared to scaled $N_{r,\odot}$ values (dots) and our calculated r-abundances (full line). The upper limit on the Pb abundance is denoted by an inverted triangle. Note also the Th and U detections.

of Pb and Bi r-abundances will be given in a forthcoming paper [10]. Further progress in the understanding of r-process chronometry will soon be obtained from the determination of Pb abundances with the Hubble Space Telescope (HST). Already for the next cyle later this year, 40 orbits of HST are dedicated to the spectroscopy of CS31082-001 [11].

So far, only **elemental** abundances could be determined in very metal-poor, neutron-capture-rich halo stars and were compared with their values in the solar system. However, very recently Sneden et al. [11] have, for the first time, succeeded to measure the **isotopic** abundances of the rare-earth element (REE) Eu in three of these metal-poor giant stars. Europium consists of only two, nearly "r-only" nuclides, i.e. ^{151}E and ^{153}Eu. In all 3 stars, the authors found a consistent abundance ratio of ^{153}Eu/^{151}Eu$\simeq$1.0,

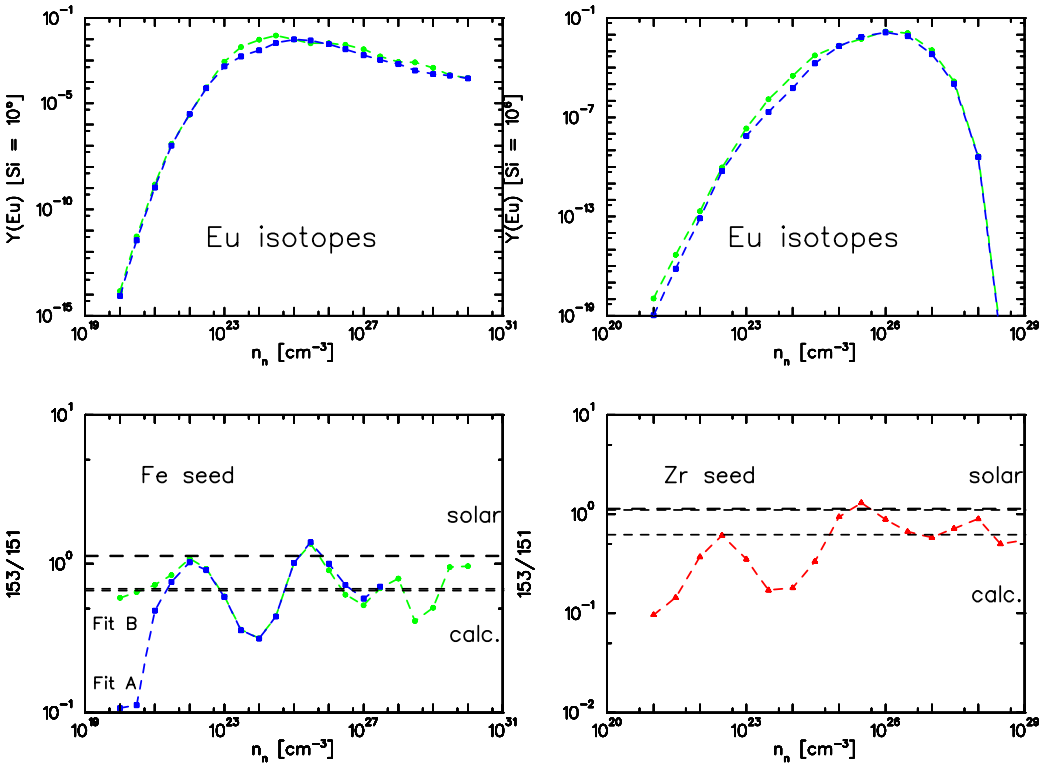

Figure 2: R-process abundances of Eu isotopes as a function of neutron-densities for two different assumptions on r-process seeds (upper part); and ^{153}Eu/^{151}Eu ratios (lower part) compared to the overall calculated and solar system isotopic ratio.

in very good agreement with the solar-system r-process abundance ratio of 1.13. Motivated by the above authors, we have used our r-process model to investigate under which astrophysical conditions (in particular the neutron-density (n_n) regimes at freeze-out) **detectable** abundances of ^{151}Eu and ^{153}Eu can be produced. As is shown in the upper part of Fig. 2, over a wide r-process n_n-range roughly equal amounts of both isotopes are formed. However, measurable quantities (at the 1% level of the strongest n_n-component) can only be obtained for $n_n \geq 5\times10^{24}$[cm^{-3}]. These are typical conditions of the "main" r-process, under which the matter flow has already passed the A$\simeq$130 abundance peak and forms the REE region.

Because of the possibility of determining in the near future also the isotopic abundance fractions of Ba in the one or other metal-poor halo star,

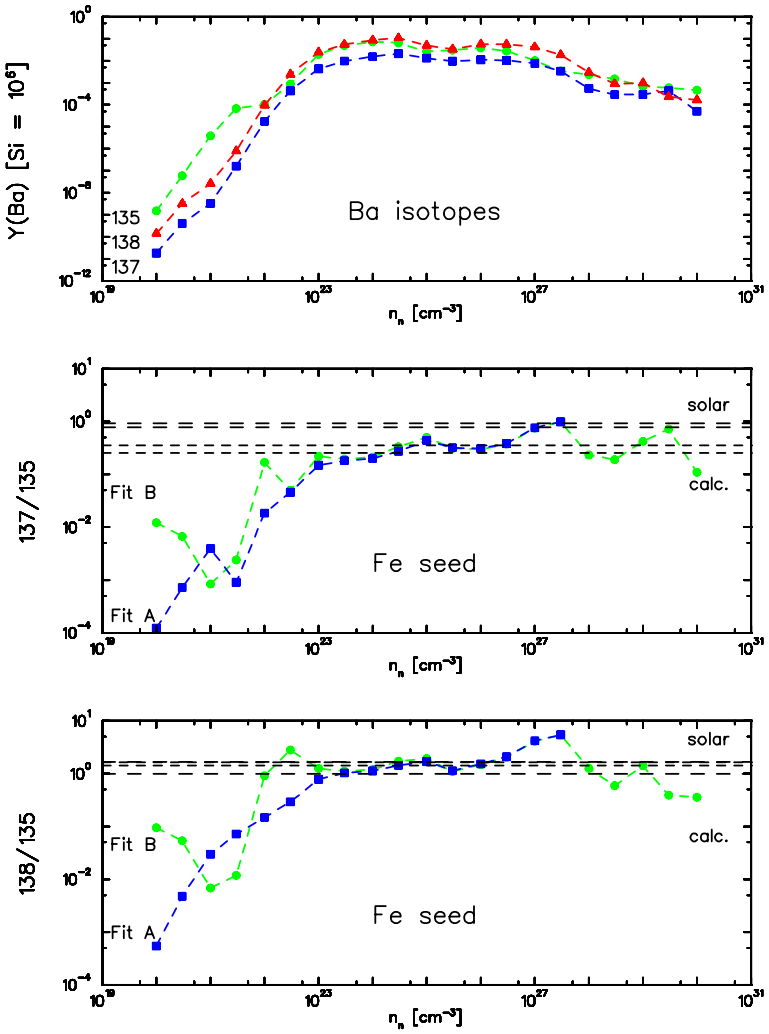

Figure 3: R-process abundances of Ba isotopes as a function of neutron-density (upper part); and ^{137}Ba/^{135}Ba (middle part) and ^{138}Ba/^{135}Ba (lower part) ratios compared to the respective overall caculated and solar-system isotopic ratios.

we also have calculated the r-process yields of the 3 nuclides ^{135}Ba, ^{137}Ba and ^{138}Ba, which lie just beyond the 2^{nd} r-peak. In this case, the two heaviest isotopes are mainly of s-process origin whereas ^{135}Ba is formed to $\geq$70% by the r-process. Hence, the observed ^{137,138}Ba/^{135}Ba abundance ratios are much more sensitive to the underlying nucleosynthesis process

Table 2: Abundance ratios of r-chronometer pairs using different fit criteria and seed compositions

Chron.-pair	Fe-seed				Zr-seed
	Old fit [2]	New fit A	New fit B	Th(B)/$X_\odot$	New fit
Th/U-238	1.805(3)	1.557(11)	1.568(11)		1.475(1)
U-235/U-238	1.602(6)	1.464(14)	1.464(14)		1.758(2)
Th/Os	0.0990(24)	0.0980(11)	0.0927(14)	0.0750	0.0735(16)
Th/Ir	0.0923(19)	0.0948(30)	0.0890(31)	0.0703	0.0676(11)
Th/Pt	0.0239(6)	0.0255(11)	0.0235(11)	0.0360	0.0316(5)
Th/3^{rd}peak	0.0159(4)	0.0167(6)	0.0155(6)	0.0181	0.0166(3)
Th/Eu	0.481(23)	0.530(23)	0.453(17)	0.422	0.479(18)

than the above Eu data. Figure 3 shows our model predictions of the 3 Ba nuclides as a function of n_n, together with the two isotopic abundance ratios. Similar to the case of Eu, **detectable** amounts of Ba with roughly the solar-system values of ^{137}Ba/^{135}Ba$\simeq$0.86 and ^{138}Ba/^{135}Ba$\simeq$1.33 are obtained for $n_n \geq 5\times10^{22}$[cm^{-3}]. These are the conditions under which the "main" r-process is just forming the full A$\simeq$130 peak and the matter flow starts to overcome this bottle-neck. This also shows that the full solar-like r-abundance of Ba cannot be produced without simultaneous r-process nucleosynthesis of ^{129}I/Xe and ^{130}Te. Therefore, it would be extremely important if optical spectroscopy of these elements could be performed in halo stars.

References

[1] B. Pfeiffer et al., Z. Phys. **A357** (1997) 235.

[2] J.J. Cowan et al., Ap. J. **521** (1999) 194.

[3] J.J. Cowan et al., Ap. J. (2002) in print; and these Proc.

[4] R. Cayrel et al., Nature **409** (2001) 691.

[5] M. Hannawald et al., ASP Conf. Ser. **245** (2001) 310.

[6] S. Burles et al., to be subm. to Ap. J.

[7] H. Schatz et al., subm. to Ap. J. (2002).

[8] H. Beer et al., in: "*Hadrons, Nuclei, and Applications*", World Scientific (2001), 372.

[9] R. Gallino et al., priv. comm. (2001), and to be publ.

[10] K.-L. Kratz et al., to be publ.

[11] C. Sneden et al., Ap. J. **566** (2002) L25.

The r-Process and Chronometers

John J. Cowan [1], *Christopher Sneden* [2] *and James W. Truran* [3]

[1] *Department of Physics and Astronomy, University of Oklahoma, Norman, OK 73019*
[2] *Department of Astronomy and McDonald Observatory, University of Texas, Austin, TX 78712*
[3] *Department of Astronomy & Astrophysics, University of Chicago, Chicago, IL 60637*

Introduction

We have been examining the abundance distributions in metal-poor Galactic halo stars trying to identify, and understand, the signatures of the slow- and rapid-neutron capture processes (*i.e.*, the *s*- and the *r*-process). Detailed studies have been made of the stars CS 22892–052 [1, 2] and HD 115444 [3]. In our latest work we have added to this list the metal-poor ([Fe/H] = –2.0) halo star BD +17°3248 [4].

Observations and Abundance Trends in BD +17°3248

Using both ground-based (Keck and McDonald) and space-based (Hubble Space Telescope, HST) observations we have obtained high resolution, high signal-to-noise spectra of BD +17°3248. The element gold has been detected in BD +17°3248 as shown in Figure 1. This HST STIS observation shows a comparison between BD +17°3248 and HD 122563. While the spectra appear somewhat similar in this region, this is due to the complex set of absorption lines that contribute to the total feature near this wavelength. Specifically, there is an OH line near the 2675.94 Å gold line. This results in some blending of the gold feature for BD +17°3248. The OH absorption, however, is much stronger throughout the UV spectrum of HD 122563 and is solely repsonsible for the strong line at 2676.0 Å in this star. We note that the this gold detection in BD +17°3248 is the first in any metal-poor halo stars.

We show in Figure 2 the entire abundance distribution of BD +17°3248. This includes the element uranium. We have detected a weak line at 3859.60 Å

in the spectrum of BD +17°3248 that we tentatively identify with this element. This would be only the second such detection, after Cayrel *et al.*[5], in any metal-poor halo stars.

We note in Figure 2 that the heavier neutron-capture elements, Z≥ 56, including now the 3rd *r*-process peak elements, all fall on the scaled solar system *r*-process distribution. This is the same pattern that was seen previously in CS 22892–052 and HD 115444 [6]. This strongly suggests a robust process for the production of these heavier neutron-capture elements. Very recently the europium isotopic abundance fractions have been determined for BD +17°3248, CS 22892–052 and HD 115444 [7]. Those fractions are all in excellent agreement with each other and with their values in the solar system. Thus, there appears to be a consistency in the production of the heavier neutron-capture elements and, at least for europium, the isotopes.

We also note the trend of the lighter neutron capture elements in Figure 2. Similarly to the case of CS 22892–052, the elements with Z = 40–50 in BD +17°3248 fall below the scaled solar system curve that fits the heavier neutron-capture elements. This might be explained by a single *r*-process site with two regimes or sets of conditions, or perhaps two different sites for the lighter and heavier neutron-capture elements (see [4]).

r-Process Chronometers

The long-lived radioactive nuclei, such as ^{232}Th and ^{238}U, can be used as chronometers (or clocks) to determine the ages of stars. Thus, the detection of thorium in a number of halo stars has led to stellar radioactive age estimates. To minimize observational errors the ratio of the radioactive element thorium (formed entirely in the *r*-process) is normally compared to the stable (*r*-process) element europium. The detection of 3rd *r*-process peak elements such as Pt provides additional chronometric pairs, with the advantage that these elements are closer in atomic mass (than Eu) to Th. Furthermore, new stellar detections of U can provide a second chronometer and help constrain age determinations. Employing the newly detected Th, U and 3rd *r*-process peak element abundances Cowan *et al.*[4] made chronometric age estimates for BD +17°3248. The average value of the various chronometric pairs suggests an age of 13.8 ± 4 Gyr for this star. This age estimate is consistent, within error limits, with other chronometric age determinations for metal-poor Galactic halo stars.

The still relatively large uncertainties reflect the sensitivity of the age estimates to both the observed and predicted (initial) abundance ratios.

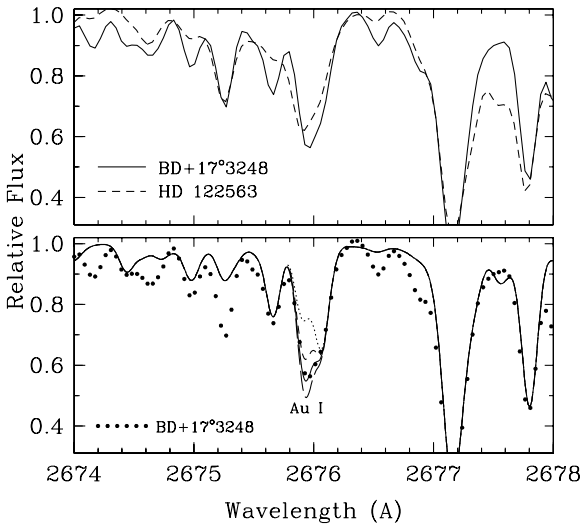

Figure 1: Observed HST-STIS and synthetic spectra in region surrounding the Au I 2675.94 Å line. In the top panel, the observed BD +17°3248 spectrum is compared to that of HD 122563. In the bottom panel, the observed BD +17°3248 spectrum is compared to four synthetic spectra, shown in order of increasing abundance by dotted, short dashed, solid, and long dashed lines computed for log ϵ(Au) = $-\infty$, –0.8, –0.3, +0.2.

Additional stellar observations will help to reduce observational uncertainties. Even in cases where only upper limits on uranium may be avaialable (perhaps the norm for most stars), the upper limits to the U/Th ratio can already provide lower limits on the age estimates for the most metal-poor stars and hence constrain age determinations for the Galaxy [8]. Additional theoretical studies, see [8, 9], will also help to reduce the errors in the theoretical predictions for the initial abundances of the radioactive elements produced in the r-process. Despite any current uncertainties, this radioactive dating technique offers promise. It is independent of chemical evolution or cosmological models. It offers an alternative means of placing lower lmits on the ages of the Galaxy and the Universe.

Acknowledgements

We thank our colleagues and collabortors for many helpful discussions. This research has been supported in part by STScI grants GO-8111 and GO-08342, NSF grants AST-9986974 (JJC), AST-9987162 (CS), and by

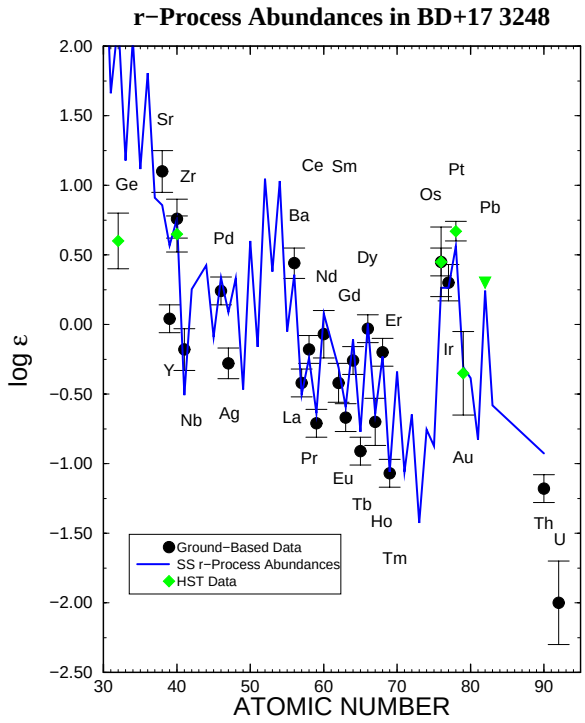

Figure 2: Neutron-capture element abundances in BD +17°3248, obtained by ground-based and HST observations, compared to a scaled solar system r-process abundance curve. The upper limit on the lead abundance is denoted by an inverted triangle. Note also the thorium and uranium detections.

the ASCI/Alliances Center for Astrophysical Thermonuclear Flashes under DOE contract B341495 (JWT).

References

[1] C. Sneden, *et al.*, ApJ **467** (1996) 819.

[2] C. Sneden, *et al.*, ApJ **533** (2000) L139.

[3] J. Westin, *et al.*, ApJ **530** (2000) 783.

[4] J. Cowan, *et al.*, ApJ (2002) in press.

[5] R. Cayrel, *et al.*, Nature **409** (2001) 691.

[6] J. Cowan, *et al.*, ApJ **521** (1999) 194.

[7] C. Sneden, *et al.*, ApJ (2002) in press.

[8] S. Burles, *et al.*, ApJ (2002) in preparation.

[9] H. Schatz, *et al.*, ApJ (2002) submitted.

Nucleosynthesis Gamma-Rays

Roland Diehl

Max Planck Institut für extraterrestrische Physik, D-85740 Garching, Germany

Introduction

Cosmic sites of nucleosynthesis produce radioactive by-products, the decay of which leads to gamma-ray line emission which can be observed with current telescopes. Among the seven candidate isotopes for such measurements, this presentation reports about ^{26}Al (and ^{60}Fe) from diffuse interstellar space, and ^{56}Co gamma-rays from the ^{56}Ni decay chain from supernovae of type Ia. Such gamma-ray line observations are more direct than, e.g., atomic transitions observed in X-rays, UV, or optical, because radioactive decay is independent of conditions in the post-nucleosynthesis environment such as density or temperature. On the other hand, gamma-ray telescopes have sensitivities of about 10^{-5} ph cm^{-2}s^{-1} and angular resolutions of $\simeq$ 1 degree, which limits diffuse emission studies to nearby (Galactic) nucleosynthesis, and supernova studies to distances less than $\simeq$10 Mpc.

^{26}Al

The sky survey from 9 years of COMPTEL observations resulted in an all-sky map in the 1809 keV gamma-ray line from ^{26}Al [7, 6, 8]. Prominent emission along the plane of the Galaxy (see Fig. 1) is structured in a way which suggests that massive stars in young starforming regions are the dominating sources. ^{60}Fe emission from these same regions will be searched for with INTEGRAL (launch Oct 2002, [11]). This will help to discriminate between core-collapse supernovae and Wolf-Rayet stars as sources of ^{26}Al, since only the former are expected to produce both ^{26}Al and ^{60}Fe at comparable intensities, while Wolf-Rayet stars may be the dominant sources of ^{26}Al but do not produce ^{60}Fe.

The 1809 keV map shows that distinct regions of the Galaxy are prominent sites of current ($\simeq 10^6$ y) nucleosynthesis. Most of these are detected at sufficient significance for detailed study: The inner Galaxy as a whole, probably including the 3 kpc molecular ring as dominating region (but note

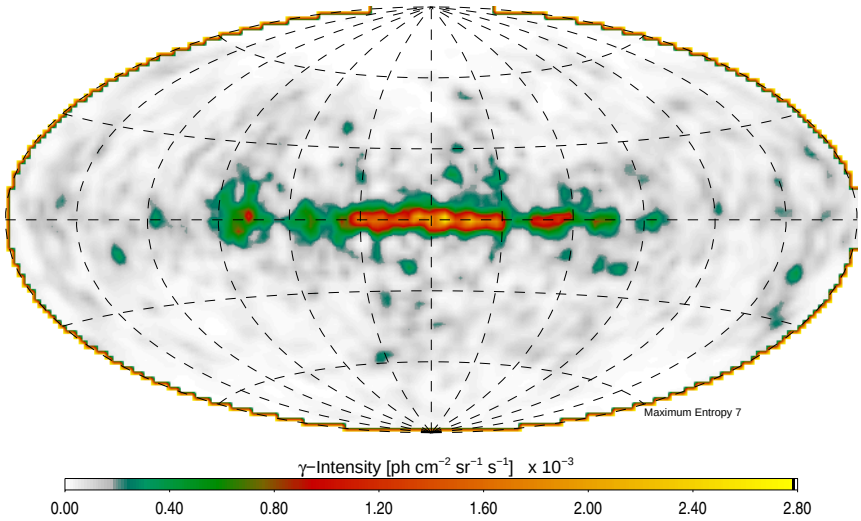

Figure 1: COMPTEL map of 1809 keV emission from radioactive ^{26}Al (decay time 10^6y), derived from the 9 year COMPTEL survey with the MaxEnt imaging method [7]

that the Galactic Center itself is not prominent) [8], the Cygnus region [7], the Carina/Vela region [3], and some regions at higher Galactic latitudes (which hence must be nearby) [2].

For the Cygnus region, an inventory of candidate sources identified 9 OB associations and a few single Wolf Rayet stars, all at distances between 0.5 and 2.5 kpc [7]. A population-synthesis estimate of the ^{26}Al emission predicted by these sources reveals a significant deficiency, which seems to point to a deficit in the stellar census of massive stars even in this nearby region [7, 5].

In the Orion region at less than 500 pc distance, the observed ^{26}Al emission (see Fig. 2) extends towards the south away from the Orion molecular clouds, following the Eridanus cavity which extends from the Orion clouds towards the Sun over several hundred parsecs [1, 2]. It is believed that the massive stars in older subgroups of the Orion OB1 association are responsible for the formation of the Eridanus cavity, from their massive-star winds and supernovae, as constrained by the density structure of interstellar matter in this region. More recently, massive stars in younger OB1 subgroups produced ^{26}Al, which appears blown preferentially into the cavity (see Fig. 2 and caption). This region provides an illustrative example of successive star formation activity which destroys its parental molecular cloud and forms

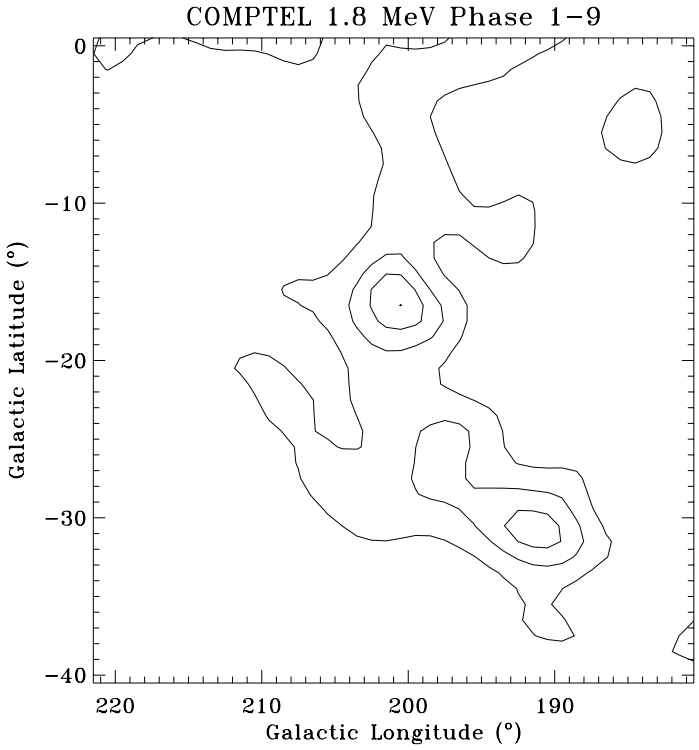

Figure 2: COMPTEL map of 1809 keV emission from radioactive ^{26}Al in the Orion region. The Orion molecular clouds extend from l=210^o, b=-20^o to about l=203^o, b=-12^o, with the Orion OB1 association around (l,b)=(205^o,-18^o), and the Eridanus cavity stretching down to (l,b)=(200^o,-50^o)

cavities in the interstellar medium, which are filled with hot gas and nucleosynthesis products. The spectrometer SPI on the INTEGRAL mission [11] will have sufficient spectral resolution to measure Doppler broadening from such kinematics, which had been indicated at even 500 km s^{-1} by an earlier balloon experiment [10].

Supernovae Ia

The gamma-ray line emission from SN1991T indicated in COMPTEL data [9] stimulated hope that such gamma-ray measurements could help to calibrate the primary power source of SN Ia for events less distant than 10 Mpc. SN1998bu seemed to be *the* opportunity, with a distance between

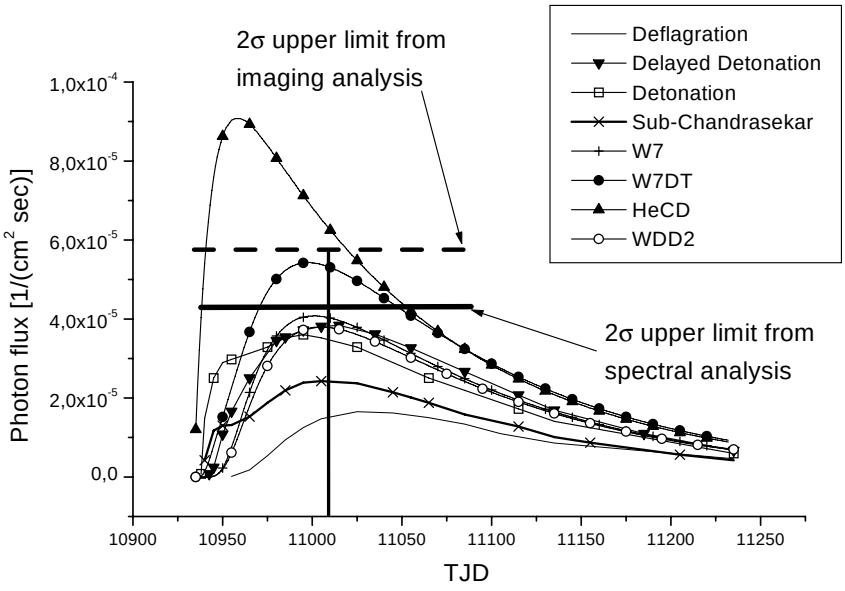

Figure 3: COMPTEL limits of ^{56}Co γ-rays from SN1998bu, compared to predicted emission time profiles from typical models, for the 847 keV line from ^{56}Co decay [4].

8 and 12 Mpc (depending on the distance determination method for its parent galaxy M96). The Compton Observatory spent 14 weeks of observing time on this object, yet none of its instruments saw any indication of gamma-ray lines from the ^{56}Ni decay chain. The COMPTEL upper limit of $\leq 3.3\ 10^{-5}$ ph cm^{-2}s^{-1} (see Fig. 3) for these lines limits the ^{56}Ni mass of this supernova to less than 0.35 M$_\odot$ [4]. Predicted gamma-ray light curves of the supernova are in conflict with these limits for the "faster" models, which have radioactive ejecta in their outer regions, such as He cap models or highly-mixed detonation models.

Acknowledgements

It is a pleasure to thank my colleagues in the COMPTEL Team for stimulating and collaborative science analysis on gamma-ray lines.

References

[1] Burrows D.N.*et al.* (1993) ApJ **406**, 97

[2] Diehl R. *et al.* (2002) in preparation for A&A

[3] Diehl R. *et al.* (1999) Astrop.Lett.Comm. **38**, 357

[4] Georgii R. *et al.* (2002) submitted to A&A

[5] Knödlseder J. (2001) A&A **360**, 539

[6] Knödlseder J. *et al.* (1999), A&A **345**, 813

[7] Plüschke S. (2001) PhD Thesis TU München

[8] Prantzos, N. & Diehl, R. (1996) Phys. Rep. **267**, 1

[9] Morris D. J. *et al.* (1997) AIP **410**, 1084

[10] Naya J.E. *et al.* (1996) Nat. **384**, 44

[11] http://astro.estec.esa.nl/SA-general/Projects/ Integral/integral.html

Mixing by Wave Breaking at the Surface of a White Dwarf

J.W. Truran[1,2,3], A. Alexakis[1,2], A.C. Calder[1,2] L.J. Dursi[1,2], M. Zingale[4], B. Fryxell[1], P. Ricker[1,2], F.X. Timmes[1,2], K. Olson[1,5], and R. Rosner[1,2,3]

[1] *Center for Astrophysical Thermonuclear Flashes, The University of Chicago, Chicago, IL 60637 USA*
[2] *Department of Astronomy and Astrophysics, The University of Chicago, Chicago, IL 60637 USA*
[3] *Enrico Fermi Institute, The University of Chicago, Chicago, IL 60637 USA*
[4] *Department of Astronomy and Astrophysics, The University of California, Santa Cruz, CA 95064 USA*
[5] *UMBC/GEST Center, NASA/GSFC, Greenbelt, MD 20771*

Classical Novae result from the explosive thermonuclear burning of material accreted from a companion star onto the surface of a white dwarf. Observed abundances and explosion energies estimated from observations indicate that there must be significant mixing of the heavier material of the C/O or O/Ne white dwarf into the lighter accreted material (H/He). This mixing is critical because otherwise hydrogen burning would be too slow to reproduce observed nova characteristics in outburst. Further, without this mixing it is difficult to understand the observed abundances of intermediate-mass nuclei in the ejecta. Accordingly, nova models must incorporate a mechanism that will dredge up the heavier white dwarf material [5, and references therein].

A recently proposed mixing mechanism is the breaking of nonlinear resonant gravity waves at the C-O surface [4, 1, 5]. The gravity waves, driven by the "wind" of accreted material can break, forming a layer of well-mixed material. This mixed layer can then be transported upward by convection, thereby enriching the accreted material. Because the length scale of this mixed layer may be very small (much smaller than the length scale of convection), previous precursor simulations have not captured this effect.

We present preliminary calculations of linear gravity waves in a flat, periodic domain driven by two different winds – a step-function wind, and a more realistic boundary-layer profile. The simulations were performed with FLASH, a parallel, adaptive-mesh simulation code for the compressible, reactive flows found in many astrophysical environments [3]. Both winds

have the same maximum velocity of 2×10^8 cms^{-1}. Hydrostatic boundary conditions were used at the lower boundary, periodic conditions on the sides, and an outflow condition was used at the upper boundary.

The theory of gravity waves assumes an incompressible medium (originally air over water) [2], which may not be assumed for a white dwarf. The simulations began with the similar initial conditions consisting of a simple $\gamma = 5/3$ gas. The density and pressure profiles were obtained by integrating the equation of hydrostatic equilibrium,

$$\frac{dp}{dy} = -\rho g \hat{\mathbf{k}} \, , \tag{12}$$

which for the case of a compressible, gamma-law gas gives

$$\rho = \rho_i \left[1 - (\gamma - 1) \frac{g \rho_i y}{P_0 \gamma} \right]^{\frac{1}{\gamma - 1}} \tag{13}$$

and

$$P = P_0 \left[1 - (\gamma - 1) \frac{g \rho_i y}{P_0 \gamma} \right]^{\frac{\gamma}{\gamma - 1}} \, . \tag{14}$$

Here P_0 is the pressure at the interface and ρ_i is the density immediately above or below the interface. The density discontinuity was a factor of 10, gravity was constant, and periodic boundary conditions were used on the horizontal boundaries. The wave was created by forcing the interface to be sinusoidal, perturbing the pressure, and adding a velocity.

The simulations shown here demonstrate that the step-function wind profile immediately induces a Kelvin-Helmholtz instability. This immediately introduces mixing; however, because the Kelvin-Helmholtz instability is driven by the velocity shear between the layers [2], there may be a limit to how much material can be dredged up by the wind.

The second sets of simulation results show that a wind which goes to zero velocity at the interface can interact with a gravity wave, driving the wave towards breaking. However, the current sets of simulations have not been evolved far enough to see the non-linear evolution of the wave-flow interaction, so that mixing rates cannot be measured. If a non-zero mixing rate can be sustained, however, there is no reason to assume that this mixing will saturate [1], so that over long timescales, this may be a more promising mixing mechanism than Kelvin-Helmholtz.

While the details of operation of this mixing mechanism in nova environments remain to be explored, we interpret our results to date as indicating that such "wind" driven gravity wave instabilities may play a significant role.

Acknowledgments

This work is supported in part by the U.S. Department of Energy under Grant No. B341495 to the Center for Astrophysical Thermonuclear Flashes at the University of Chicago. J. W. Truran acknowledges partial support from DOE grant DE-FG02-91ER40606. L. J. Dursi is supported by the Krell Institute CSGF. K. Olson acknowledges partial support from NASA grant NAS5-28524.

References

[1] A. Alexakis, Y.-N. Young, & R. Rosner Phys. Rev. E **65** (2002) 026313.

[2] S. Chandrasekhar, Hydrodynamic and Hydromagnetic Stability (New York: Dover) 1981.

[3] B. Fryxell, et al., ApJS **131** (2000) 273.

[4] R. Rosner, et al., Bull. AAS **32** (2000) 1538.

[5] R. Rosner, A. Alexakis, Y.-N. Young, J.W. Truran, & W. Hillebrandt, ApJ **562** (2001) L177.

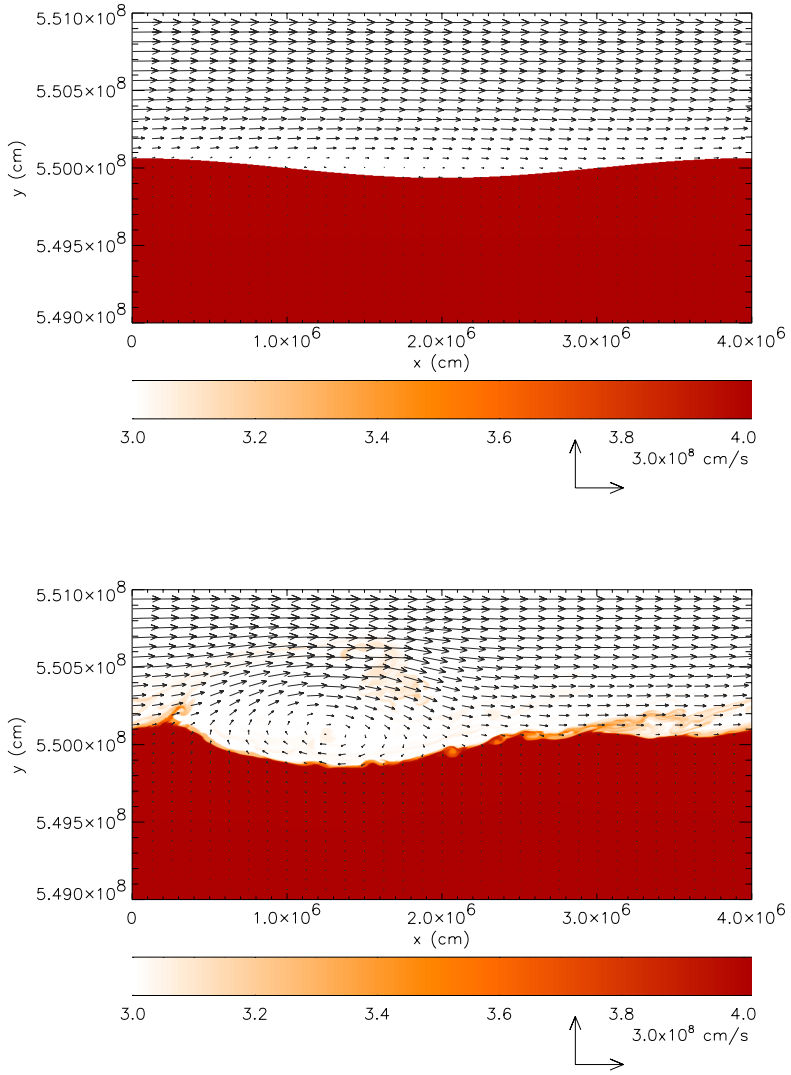

Figure 1: Preliminary simulation results showing a gravitational wave on the interface between a C/O white dwarf and a H/He atmosphere. Plotted is density, with velocity vectors. These figures represent evolution of a wave driven by a 'step-function' wind, which immediately drives a Kelvin-Helmholtz instability. The top figure is the initial condition; the bottom figure shows the state after 59 ms of evolution.

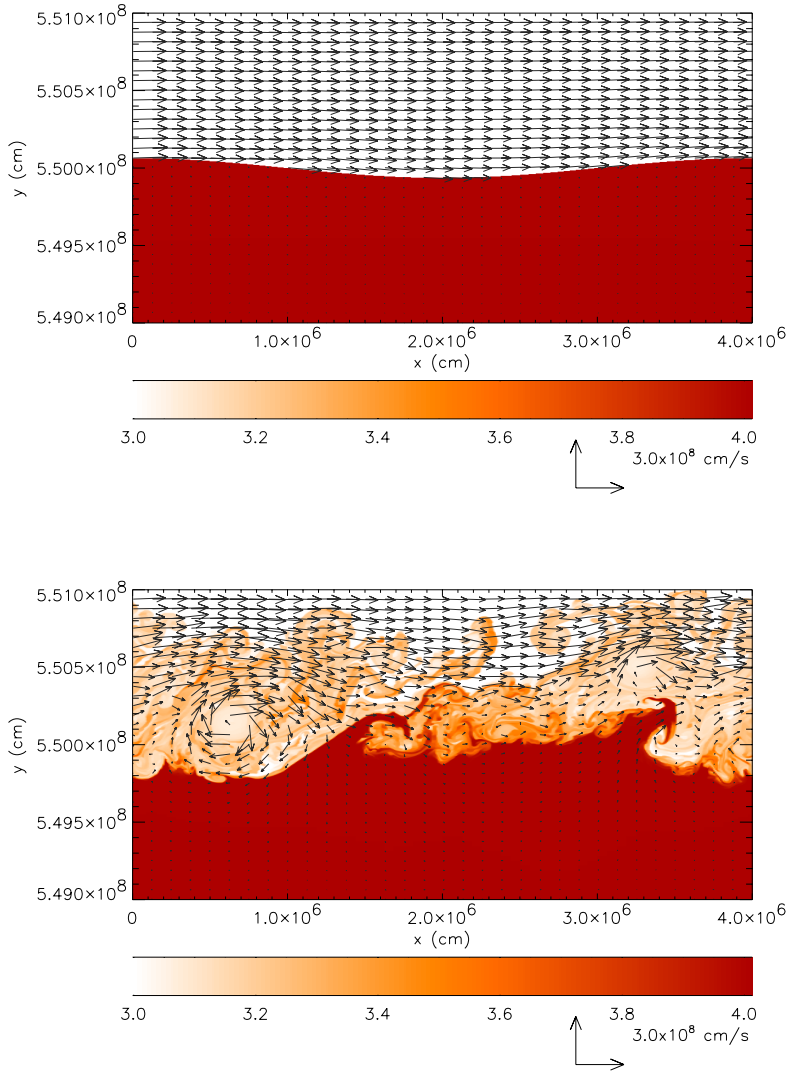

Figure 2: Same as Figure (1), but with a boundary-layer wind profile. The top figure is the initial condition, while the bottom figure shows the computational domain at 197 ms.

Classical Novae: observations of X-ray emission

M. Hernanz, G. Sala

Institut d'Estudis Espacials de Catalunya (IEEC) and Instituto de Ciencias del Espacio (CSIC), Gran Capità 2-4, E-08034 Barcelona, Spain

A classical nova explosion occurs as a consequence of the explosive burning of hydrogen, through a thermonuclear runaway, on top of an accreting white dwarf in a close binary system (cataclysmic variable). The outburst causes the expansion of the envelope, with large velocities, up to some thousands of km.s^{-1}, to large radii. During this phase, the rise to maximum visual luminosity occurs. Theoretical models predict the ejection of a fraction of the accreted envelope, between $\sim 10^{-6}$ and 10^{-4} M$_\odot$ (José & Hernanz, 1998, Starrfield et al. 1998, Prialnik & Kovetz, 1995). The remaining envelope returns to hydrostatic equilibrium after the explosion and it enters into a steady nuclear burning phase, with constant bolometric luminosity close to the Eddington value (Starrfield, 1989). Multiwavelength observations of novae have shown that this constant bolometric luminosity phase occurs in all novae after optical decline. As the envelope mass is depleted, the photospheric radius decreases at constant luminosity and, therefore, the effective temperature increases, leading to a hardening of the spectrum from optical to ultraviolet, extreme ultraviolet and soft X (MacDonald, 1996). So, classical novae are expected to emit in the soft X-ray band (up to ~ 1.5 keV), due to the remaining nuclear burning at their surface and the contemporaneous mass-loss. This emission is expected to be of the blackbody type, although realistic models of hot white dwarf atmospheres, taking into account their particular composition, are required to interpret the observations (MacDonald & Vennes, 1991).

There is another mechanism through which novae can emit X-rays: internal shocks in the ejecta or external ones with the circumstellar material around the expanding envelope can be at the origin of hard X-ray emission, with thermal bremsstrahlung being the most favored emission mechanism. It had also been suggested that the comptonization of the gamma-rays produced in ^{22}Na decay could be responsible of it (Livio et al. 1992), but this has been shown not to be the case after detailed modelling of gamma-ray spectra of classical novae, since there are no photons with lower energies than 20-30 keV from this scattering (Hernanz et al., 1997, Gómez-Gomar et

al 1998). Finally, old novae also emit X-rays originated in the re-established accretion process (emission as a cataclysmic variable) and/or in the nova shell, which is interacting with the circumstellar material.

Observations of classical novae in X-rays have been performed since the 70's, mainly with Einstein, EXOSAT and ROSAT (see for instance Ögelman et al. 1984, 1987, 1993, Ögelman & Orio 1995, Orio et al. 1996, 2001, Orio & Greiner, 1999, Lloyd et al. 1992, Shanley et al. 1995, Krautter et al. 1996, Balman et al. 1998, Balman & Krautter 2001). The conclusions extracted from those observations leave many unanswered questions. For instance, the deduced duration of the constant bolometric luminosity phase is too short to be compatible with the evolution of the envelope on a purely nuclear timescale (MacDonald et al. 1985), indicating some extra mechanism of mass loss, related to the interaction with the companion star and/or to an optically thick wind (Kato & Hachisu, 1994). In addition, the spectral energy distribution (SED) is not well known in general, due to the low resolution and/or the limited spectral range of the past detectors; therefore, flux determinations and model parameters are not very accurate, leaving the origin of the emission unclear. Finally, it should also be mentioned that the lack of detection of many novae that had exploded not much earlier than their observation time with ROSAT is puzzling. A larger sample and observations with better sensitivity are necessary to clarify this problem.

The unprecedented sensitivity and spectral resolution of the EPIC cameras on board the ESA XMM-Newton satellite, makes it very suitable for studies of novae in optical decline. With this aim, we have done observations of five recent Galactic classical novae (Nova Sco 1997, Nova Sco 1998, Nova Sgr 1998, Nova Mus 1998, Nova Oph 1998) with XMM-Newton. Each object has been observed at two or three different epochs (see table 1, where we also indicate if the sources have been detected or not by the first still preliminary analysis of data). Three out of five observed sources have been detected at least twice after their explosion, at epochs as large as 3.5 years after the explosion. In all cases there is emission spanning the energetic range from 0.3 up to 8.0 keV. This has important consequences for nova models, because it indicates a longer duration of the post-explosion steady burning phase. In addition, our observations unambiguously indicate that there is simultaneous hard emission, being its origin not completely clear yet (either shocked ejecta or re-established accretion).

Table 1: List of targets observed.

Target	Discovery date	Date of XMM observation	EPIC detection
Nova Sco 1997 (V1141 Sco)	June 5, 1997	October 11, 2000	No
		March 24, 2001	No
		September 7, 2001	No
Nova Sgr 1998 (V4633 Sgr)	March 22, 1998	October 11, 2000	Yes
		March 9, 2001	Yes
		September 7, 2001	Yes
Nova Oph 1998 (V2487 Oph)	June 15, 1998	February 25, 2001	Yes
		September 5, 2001	Yes
		February 2002	-
Nova Sco 1998 (V1142 Sco)	October 21, 1998	October 11, 2000	No ?
		March 24, 2001	No ?
		September 7, 2001	-
Nova Mus 1998 (LZ Mus)	December 29, 1998	December 28, 2000	Yes ?
		June 26, 2001	Yes
		December 26, 2001	Yes

Acknowledgements

This work is based on observations obtained with XMM-Newton, an ESA science mission with instruments and contributions directly funded by ESA Member States and the USA (NASA).This research has made use of the SIMBAD database, operated at CDS, Strasbourg, France. We thank the Spanish MCYT for funding (project AYA2001-2360).

References

[1] Balman, S., Krautter, J. 2001, MNRAS, **326**, 1441

[2] Balman, S., Krautter, J., & Ögelman, H. 1998, ApJ, **499**, 395

[3] Gómez-Gomar, J., Hernanz, M., Jose, J., & Isern, J. 1998, MNRAS, **296**, 913

[4] Hernanz, M., Gómez-Gomar, J., Jose, J., & Isern, J. 1997, in 2nd INTEGRAL Workshop, The Transparent Universe. ESA SP-382, Noordwijk, p. 47

[5] José, J., & Hernanz, M. 1998, ApJ, **494**, 680

[6] Kato, M., & Hachisu, I. 1994, ApJ, **437**, 802

[7] Krautter, J., Ögelman, H., Starrfield, S., Wichmann, R., & Pfeffermann, E. 1996, ApJ, **456**, 788

[8] Livio, M., Mastichiadis, A., Ögelman, H., & Truran, J.W. 1992, ApJ, **394**, 217

[9] Lloyd, H.M., O'Brien, T.J., Bode, M.F., Predehl, P., Schmitt, J.H.M.M., Trümper, J., Watson, M.G., & Pounds, K.A. 1992, Nature, **356**, 222

[10] MacDonald, J. 1996, in Cataclysmic Variables and Related Objects, Kluwer, Dordrecht, p. 281

[11] MacDonald, J., Fujimoto, M.Y., Truran, J.W. 1985, ApJ, **294**, 263

[12] MacDonald, J., & Vennes, S. 1991, ApJ, **373**, L51

[13] Ögelman, H., Beuermann, K., & Krautter, J. 1984, ApJ, **287**, L31

[14] Ögelman, H., Krautter, J., & Beuermann, K. 1987, A&A, **177**, 110

[15] Ögelman, H., Orio, M., Krautter, J., & Starrfield, S. 1993, Nature **361**, 331

[16] Ögelman, H., & Orio, M. 1995, in Cataclysmic Variables, Kluwer, Dordrecht, p. 11

[17] Orio, M., Balman, S., Della Valle, M., Gallagher, J., & Ogelman, H. 1996, ApJ, **466**, 410

[18] Orio, M., & Greiner, J. 1999, A&A, **344**, L13

[19] Orio, M., Covington, J., Ögelman, H. 2001, A&A, **373**, 542

[20] Prialnik, D., & Kovetz, A. 1995, ApJ, **445**, 789

[21] Shanley, L., Ogelman, H., Gallagher, J., Orio, M., & Krautter, J. 1995, ApJ, **438**, L95

[22] Starrfield, S. 1989, in Classical Novae, Wiley, New York, p. 39

[23] Starrfield, S., Truran, J.W., Wiescher, M.C., Sparks, W.M. 1998, MNRAS, **296**, 502

Gravitational radiation from neutron star mergers as a function of the equation of state

R. Oechslin[1], *S. Rosswog*[2], *F. K. Thielemann*[1]

[1] *Department of Physics and Astronomy, University of Basel, Klingelbergstrasse 82, 4056 Basel, Switzerland*
[2] *Department of Physics and Astronomy, University of Leicester, LE1 7RH, Leicester, UK*

35.1 Introduction

Coalescing neutron star (NS) binaries are expected to be one of the most promising sources of gravitational radiation for laser interferometer detectors like LIGO, VIRGO, GEO600, and TAMA. Since emission of gravitational waves (GW) is sensitive to mass distributions it provides additional information on the astrophysical object that is not available from observations based on electromagnetic radiation.

Different groups have already considered the neutron star merger problem numerically. Approximations range from Newtonian gravity to full general relativity (GR) and from a simplifying polytropic EOS model to models including a nuclear EOS and a neutrino emission scheme (For references, see e.g. [1], for a general review, see [2]).

In our model, we chose an approximation to GR, the so-called conformally flat (CF) approximation ([3]), which is numerically less demanding than full GR but still reproducing main relativistic features to a good precision. On the microphysical side, we chose a simple polytropic model with the adiabatic index Γ as a free parameter since the nuclear EOS is still very poorly constrained. This allows us to investigate the merger process depending on the polytropic EOS. The code we developed is based on smoothed particle hydrodynamics (SPH), combined with a multigrid scheme to solve the field equations resulting from the CF formalism.

35.2 Results

Three runs were performed, with adiabatic indices $\Gamma = 2.0$, $\Gamma = 2.6$, and $\Gamma = 3.0$. Starting with a corotating binary in equilibrium, the loss of energy

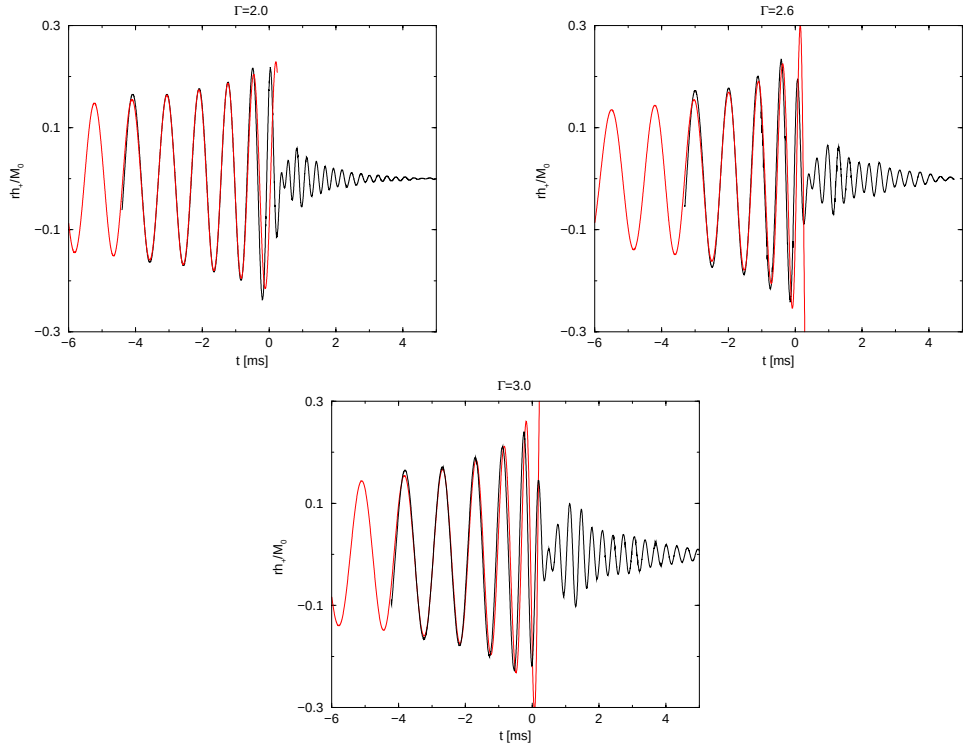

Figure 1: Gravitational waveforms of the three models normalised to the rest mass M_0. The height and decay time of the second maximum, produced by the non-axisymmetric remnant, is highly depending on the adiabatic index. The dashed lines correspond to waveforms from a pointmass binary with the same initial parameters.

and angular momentum due to gravitational radiation carries the binary over the innermost stable circular orbit which results in a tidal instability and a disruption of the individual stars. The two cores merge to a new rapidly rotating central object, either a neutron star or a black hole.

In the GW signal (see Fig. 1), two components are present, an inspiral signal which results from the quadrupole of the binary configuration prior to merging, and a ringdown signal that is produced after the merger by the quadrupole oscillations of the final remnant. While the inspiral signal is fairly independent of the internal structure of the NS's, the ringdown signal strongly depends on the adiabatic index. A soft EOS results in a weak signal that rapidly decays while the stiff-EOS model produces a strong, slowly

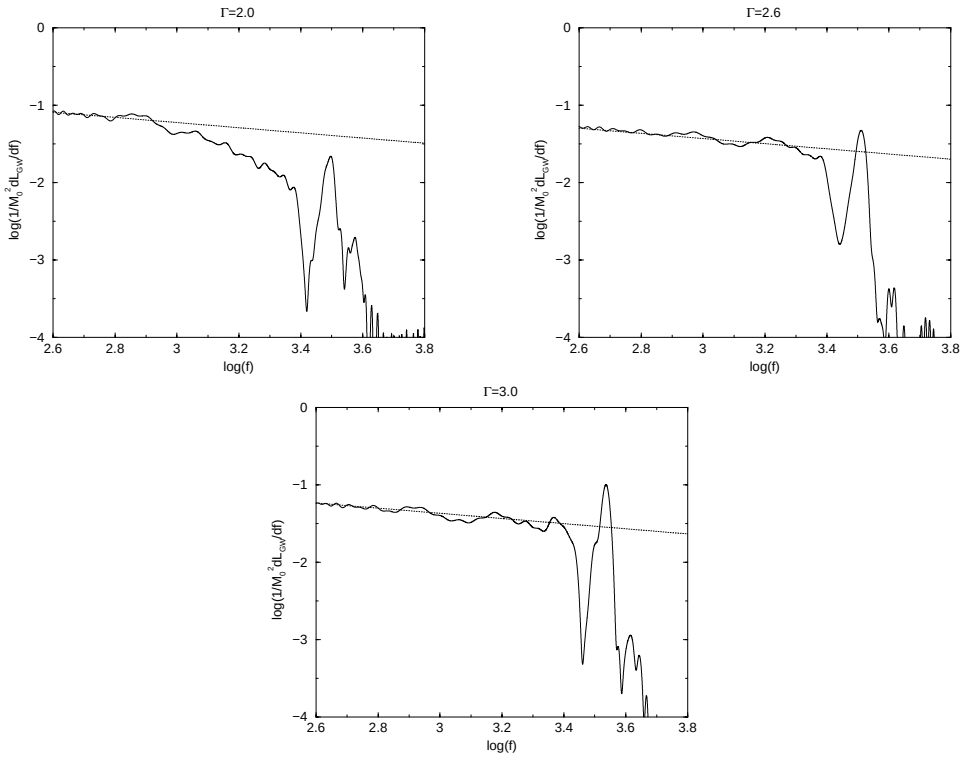

Figure 2: Frequency spectra for the three different models. The dashed line shows the pointmass spectrum $dE/df \simeq f^{-1/3}$. Due to a build-up of a non-axisymmetric central object, the stiff-EoS model produces a much higher quadrupole oscillation peak than the soft-EoS model, whose central object quickly relaxes to axisymmetry.

decaying signal. *Therefore, if some day a GW signal is measured to that precision, information on the EOS could be extracted.* The reason is that the soft-EOS model has a more centrally condensed and more axisymmetric remnant than the stiff-EOS models.

The same effect appears in the luminosity frequency spectrum (Fig. 2) which indicates the amount of energy emitted in GW per frequency bin. Similar to above, the main difference between the three models can be found in a peak around the remnant's quadrupole oscillation frequency of about $f_{QPole} \sim 3.2$ kHz. The deviation from the pointmass spectrum in the $\Gamma = 2.0$ model is a numerical artefact caused by our limited resolution.

References

[1] R. Oechslin, S. Rosswog, F. K. Thielemann, Phys. Rev. D, in press, gr-qc/0111005.

[2] F. A. Rasio, S. L. Shapiro, Class. Quant. Grav., **16**, R1 - R29 (1999).

[3] J. R. Wilson, G. J. Mathews, P. Marronetti, Phys. Rev. D, **54**, 1317 (1996).

Accuracy of Stellar Atmosphere Parameters

R. Wehrse[1,2], *J. Schrage*[1,2]

[1] *Institut f. Theoret. Astrophysik, Tiergartenstr. 15, D-69121 Heidelberg, Germany*
[2] *Interdisziplin. Zentrum f. Wissenschaftliches Rechnen, Im Neuenheimer Feld 368, D-69120 Heidelberg, Germany*

Abstract

After a discussion of the main sources of uncertainties in stellar parameters a new algorithm is introduced that allows an objective determination of the parameters together with the corresponding errors from spectra. First results are presented and discussed.

36.1 Introduction

Although the first fine-analysis of a stellar spectrum has been performed already 60 years ago and much progress has been achieved since, the corresponding error analysis is still in its infancy. At first glance this is surprising since a good knowledge of stellar parameters is of fundamental importance for the understanding in a variety of astronomical fields such e.g. as stellar evolution, galactic structure, cosmic abundances.

The main reason for this situation is the complexity of spectral analysis (see below) and an insufficient knowledge on the accuracy of the input data: spectral analysis seems sometimes to be more an art than science still!

A comprehensive overview about error estimates of stellar parameters based on spectra has been given in [1]. Certainly, during the last decade many more data of high quality have been acquired and the use of the Poisson point process (cf. [2],[3], [4]) to describe line spectra has allowed to estimate much better the consequences of missing and uncertain line-center wavelengths, transition probabilities, damping constants etc. But many problems of the end-eighties –as e.g. the influence of the signal-to-noise ratio on the element abundances– still persist.

In this paper we first summarize the main sources of errors (Sects. 36.2 and 36.3) and then present a new algorithm for an objective determination of both the parameters and the corresponding errors that can deal with such

difficult problems and that provides fast, accurate, and consistent results. The method has originally been developed as an parameter identification algorithm in applied mathematics for use in chemical engineering but has been applied to inverse problems in various fields during the last years.

36.2 Sources of errors in spectral analysis

The accuracy of stellar atmosphere parameters depends on a variety of factors. They can broadly be divided into the following classes:

- Observation
  - *spectral resolution*: intrinsic line profiles resolved?
  - *signal-to-noise ratio*: visibility of weak lines?
  - *available wavelength-range*: all relevant lines included?
  - *calibration of the spectrum*: absolute/normalized spectrum, height of continuum?
- model
  - *dimensionality of the model:* plan-parallel, spherical geometry, horizontal inhomogeneities, time dependencies ?
  - *hydrodynamics:* convection, consequences for the radiation fields ?
  - *thermodynamics:* LTE, NLTE, general distribution functions?
  - *radiative transfer:* type of radiative transfer, treatment of scattering, polarisation?
  - *atomic/molecular data:* accuracy, completeness?
- inversion process

36.3 Accuracy of "conventional" estimates

Parameter identification is an inverse problem, and thereby belongs to a class of mathematical problems that is notoriously hard to handle. Up to now parameters for stellar atmospheres are essentially found by "eye ball estimates", i.e. by tuning parameters by rule of thumb until the simulation more or less fits the observation. This method, does not yield necessarily good parameter estimates and reliable error estimates are hardly available at all. Instead, accuracy is estimated by comparing analyses by different authors. The discussion on the first carbon dwarf star G77-61 (cf. [5]) and on the iron abundance of Vega (see [6]) illustrate the problem.

36.4 Parameter identification

In order to avoid the problems briefly addressed above we now turn to the alternative scheme of parameter identification. It is based on the well known Gauß method of minimizing an objective function $Z(P)$ that depends on the parameter vector P and gives some measure of the difference between observation and model. In our stellar atmosphere case we use the sum of weighted squared differences between observed and calculated fluxes

$$Z(P) = \sum_i \frac{(F^{obs}(\lambda_i) - F^{mod}(\lambda_i, P))^2}{\sigma(\lambda_i)^2}. \tag{15}$$

The scatter in the observational data are taken into account by the wavelength dependent $\sigma(\lambda_i)$.

Unlike to the usual unconstrained minimization techniques, in our parameter identification scheme the stellar structure equations (as the hydrostatic equation and the transfer equation, condition of radiative equilibrium etc.), a differential-algebraic system of equations, are used as constraints to the minimization problem. In addition, other non-spectroscopic information can, if relevant and available, be included as additional inequality constraints of the form

$$g < 0 \tag{16}$$

$$h \leq 0. \tag{17}$$

For the estimation process we use a generalized Gauß-Newton algorithm implemented in the software package `Parfit++` [7]. Convergence of this method is superlinear. The stellar structure equations are parameterized with a boundary value approach using multiple shooting [8]. This method is gradient-based. The needed derivatives are computed with internal numerical differentiation combined with efficient update schemes in the multiple shooting context. The quadratic subproblems that must be solved possess a structure that is exploited in a tailored condensing and decomposition procedure. Convergence behaviour and quality of the method are illustrated in Fig. 1.

36.5 First results: the accuracy of the effective temperature

We have carried out a parameter study varying both the starting point T_0 for the estimation process and the perturbance σ for a grey atmosphere at $T = 6500K$. The mean of the perturbation is always 0 and the total flux is in

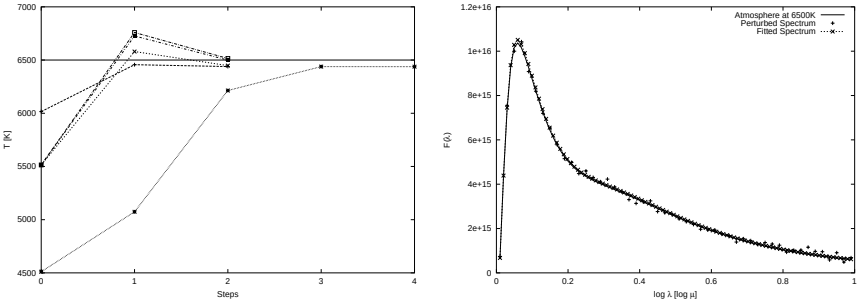

Figure 1: Convergence of the parameter identification algorithm for various starting temperatures T_0 with varying scatter σ (left). Note that the computer time for the solution of the inverse problems is only about that of 3 - 5 forward problems, a feature of the algorithm that is also found in cases with many parameters. Right: comparison of the exact grey flux distribution, the perturbed data and the corresponding fit from the perturbed flux distribution. The relative magnitude of the perturbations is less than < 0.002, the local perturbations are much larger (see text).

no case modified by more than 0.2%. The starting point plays no role for the quality of the fit, as can be seen from Fig. 1. σ varies between approximately 3% and 10% at $\lambda \simeq 4\mu$. Figure 2 shows the resulting estimated effective temperatures T_{eff} and the variance χ^2 of the fits. We clearly see a trend to slightly overestimate the temperature for small perturbances σ which becomes a trend to very much underestimate the temperature as σ gets larger. With σ getting larger the resulting χ^2 of the fit grows unproportionally, as does the spread in the estimated effective temperatures.

For a single parameter, i.e. the case we treat here, the optimization problem is convex, which means that our algorithm is guaranteed to yield the globally optimal result. It is clear that this behaviour is a property of the stellar structure equations, and all attempts at determining parameters by fitting spectra or just looking at them are subject to it.

In consequence observational data with large uncertainties will lead to estimated effective temperatures that are likely to be systematically too low. In our study the average for larger perturbances was 50K below the effective temperature of the model, and two of the estimates were even too low by more than 100K. For the estimation of element abundances in turn even a $\Delta T = 100$K may lead to an error of up to $\Delta \log \epsilon \simeq 0.2$.

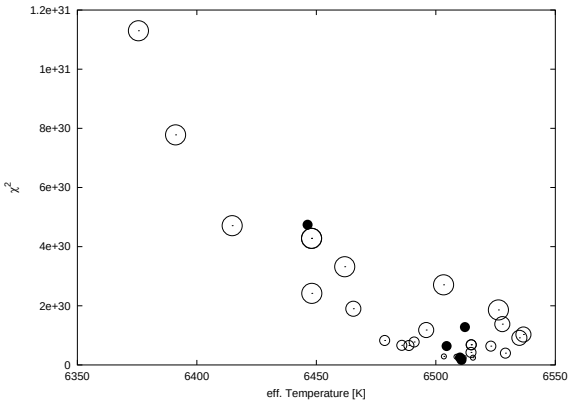

Figure 2: χ^2 versus T_{eff} for a grey stellar atmosphere with an effective temperature of $T_{\text{eff}} = 6500$K. The total flux is in no case perturbed by more than 0.002 of the total flux. Larger circles mean larger perturbations. The filled circles denote the respective average values of (T_{eff}, χ^2).

36.6 Advantages and disadvantages of parameter identification

The main disadvantage of formal parameter identification is the complexity of the algorithm and the effort it takes to implement it. This single disadvantage, however, is outweighed by far by the advantages of the method, such as

- highly efficient numerics,
- indication of parameters that cannot be determined simultaneously,
- a fully consistent error ellipsoid,
- the Jacobi matrix is available, e.g. for optimization of future observations,
- convergence to a global minimum (as far as we know),
- a sound mathematical basis.

Acknowledgements

This work has been supported by the Deutsche Forschunggemeinschaft (Graduiertenkolleg "Modellierung und Wissenschaftliches Rechnen in Mathematik und Naturwissenschaften"; Sonderforschungsbereich 359, Teilprojekt C2).

References

[1] Wehrse, R., ed., Accuracy of element abundances from stellar atmospheres, Lecture Notes in Physics, Springer (1990)

[2] Wehrse, R., von Waldenfels, W., Baschek, B. JQSRT **60**, 963 (1998)

[3] Baschek, B., von Waldenfels, W., Wehrse, R. A&A 371, 1084 (2001)

[4] Wehrse, R., Baschek, B., von Waldenfels, W. in preparation

[5] Gass, H., Liebert, J., Wehrse, R. A&A **189**, 194 (1988)

[6] Sadakane, K, in: Accuracy of element abundances from stellar atmospheres, Lecture Notes in Physics, Wehrse, R., ed., Springer (1990)

[7] Kraus, C., private communication (2001).

[8] Bock, H.G. Bonner Mathematische Schriften **183** (1987).

New Kr cross sections and astrophysical constraints on presolar grains

R. Gallino [1], *M. Lugaro* [2], *P. Mutti* [3], *O. Straniero*[4], *R. Reifarth,* [5], *F. Käppeler* [5], *R.S. Lewis,* [6], *A.M. Davis,* [6], *J. Wagemans* [7]

[1] *Dipartimento di Fisica Generale, Universitá di Torino and INFN, Sezione di Torino, Via P. Giuria 1, I-10125 Torino, Italy*
[2] *Institute of Astronomy, Cambridge University, Madingley Road, Cambridge, CB3 0HA, UK*
[3] *Institut Laue Langevin, 6 rue Jules Horowitz, BP 156, 38042 Grenoble, CEDEX 9, France*
[4] *Osservatorio Astronomico di Collurania, I-64100 Teramo, Italy*
[5] *Forschungszentrum Karlsruhe, Institute für Kernphysik, Postfach 3640, D-76021 Karlsruhe, Germany*
[6] *Enrico Fermi Istitute, University of Chicago, Chicago, IL 60637-1433, USA*
[7] *IRRM, Geel, Belgium*

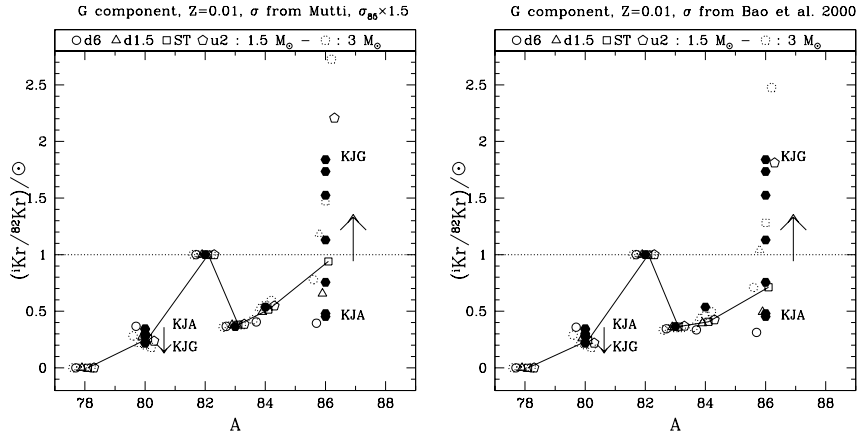

Figure 1: Kr isotopic G-components for bulk mainstream SiC grains of different sizes (full hexagons) are compared with AGB stellar model predictions of 1.5 and 3 $M_{\odot}$ and half-solar metallicity. The full line connects predictions for the ST case [1]. Left panel: updated Kr cross sections by [2]; right panel: Kr cross sections by [3]. Open symbols correspond to different choices of the ^{13}C-pocket efficiency.

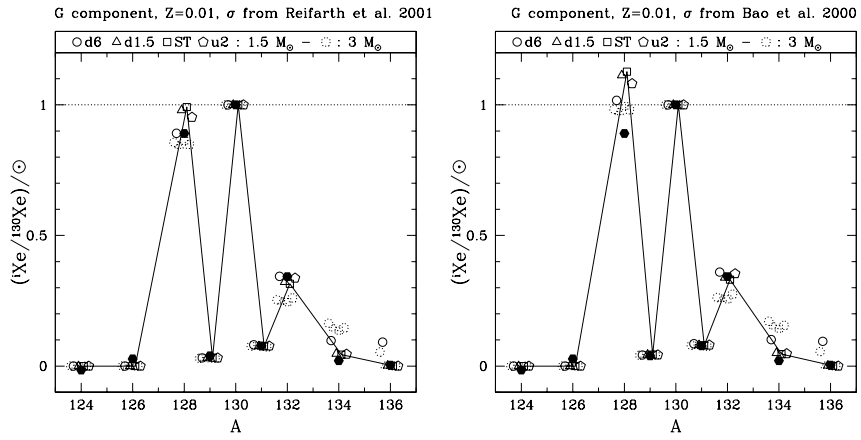

Figure 2: The same as Figure 1 for the meteoritic Xe isotopic G-component. The left panel is for Xe cross sections by [5], while the right panel shows AGB model predictions using the previous recommended cross sections by [3].

Presolar grains extracted from carbonaceous meteorites carry the nucleosynthesis signature of their astrophysical parent sources. There is general consensus that mainstream SiC grains (95% of presolar SiC) condensed in the carbon-rich extended envelopes of Asymptotic Giant Branch (AGB) stars [4]. Trace heavy elements at neutron magic number peaks $N = 50$ (Sr, Y, Zr, Nb, Mo) and $N = 82$ (Ba, La, Ce, Pr, Nd, Sm) are present in relatively large abundance, with an isotopic distribution characteristic of the s-process, as measured in aggregates of many grains [6] and more recently in single grains [7]. Mainstream SiC grains have been identified as the carriers of the Ne-E(H) meteoritic anomalous component [8]. These mainstream grains are assumed as well to be the carriers of the Kr-s and Xe-s components [9]. In the framework of a program to revisit AGB predictions for all noble gases, Figures 1 and 2 compare the pure-s Kr and Xe isotopic signature (G-component) shown by aggregate SiC grains [9] with updated predictions using a spread of ^{13}C pocket efficiencies in agreement with spectroscopic s-element abundances in carbon-rich stars [1]. New cross sections for ^{82,84,86}Kr, with a typical uncertainty of 5% [2], and for ^{128,129,130}Xe, with a typical uncertainty of 2% ([5]; Reifarth, these Proceedings), have been included in the neutron capture network. In the case of Kr, the meteoritic G-component might in principle be determined by extrapolating the ^{78}Kr/^{82}Kr ratio to zero, because the p-only isotope ^{78}Kr is fully destroyed

by the s-process. However, the measurement of this ratio is prevented by isobaric interferences. Besides ^{82}Kr, a second isotope, ^{83}Kr, has to be chosen as normalisation. According to Figure 2, the best candidate is ^{83}Kr, because of the almost constant ^{83}Kr/^{82}Kr predicted ratio. The ^{82}Kr cross section at 30 keV by [2] is higher by only 2% with respect to [3], while the ^{84}Kr cross section is lower by 20%. The s-process production of ^{86}Kr in AGB stars is strongly dependent on the neutron density because of the s-process branching at the unstable ^{85}Kr. This dependence is affected by both the ^{13}C-pocket efficiency and by the marginal activation of the ^{22}Ne neutron source during the thermal pulse. The initial metallicity also plays an important role. The results presented in Figure 1 are for AGB stellar models of half-solar metallicity. For AGB models of solar metallicity and initial mass 1.5 and 3 $M_{\odot}$, the highest ^{86}Kr/^{82}Kr ratio (Case u2) would be 0.83 and 1.24, respectively. In case of AGB models of metallicity 1/3 solar, these ratios would be 3.99 and 4.75. In this framework, it is tempting to assign the origin of the larger size grains to ABG stars of around half-solar metallicity. The cross section of ^{85}Kr is highly uncertain since only discrepant theoretical estimates are available. The recommended cross section from [3] is given at a tentative 80% uncertainty (1 s.d.). The predictions shown in Figure 1 (left panel) have been obtained by increasing the recommended cross section of ^{85}Kr of [3] by a factor of 1.5. This corresponds to an increase by a factor of 1.3 in the ^{86}Kr production. A second temperature-dependent branching at ^{79}Se affects the production of the s-only isotope ^{80}Kr, whose predicted abundance depends linearly on the uncertainty of the theoretical neutron capture cross section (by 20% [3]) and of the β-decay rate at stellar temperatures of ^{79}Se (by 30% [10]). The much higher meteoritic abundance ratio of neutron-magic ^{86}Kr relative to s-only ^{82}Kr for the coarser grains, as well as the strong non-solar ratio of the of s-only pair ^{80}Kr and ^{82}Kr are fundamental characteristics of AGB stellar models. Most solar ^{80}Kr and about 50% of solar ^{82}Kr are to be ascribed to the weak s-component occurring in massive stars. Solar ratios are from [11].

Concerning the Xe-s component, the meteoritic ratio $(^{128}\mathrm{Xe}/^{130}\mathrm{Xe})_G = 0.90$ is in agreement with an estimated p-process contribution by about 10% of solar ^{128}Xe. There is a satisfactory match with AGB models of half-solar metallicity, while for solar metallicity a predicted ratio higher by 5% in the average would be obtained. Notice that the use of the Xe cross sections by [3] would provide a discrepant ratio $(^{128}\mathrm{Xe}/^{130}\mathrm{Xe})_G = 1.1$, as shown in Figure 2 (right panel). Further analysis is in progress, including the use of a more representative solar system Xe isotope composition by [12].

References

[1] Busso, M. et al. ApJ, **557** (2001) 802.

[2] P. Mutti, et al. in Int. Conf. on Nuclear Data for Science and Technology, Oct 7-12 2001, Tsukuba, Ibaraki, Japan, in press.

[3] Bao Z. Y., et al., Atom. Data Nucl. Data Tab., **76** (2000) 70.

[4] Zinner, E., in Astrophysical Implications of the Laboratory Study of Presolar Material, ed. T.J. Bernatowicz and E. Zinner, AIP, Woodbury, New York (1997), p. 3.

[5] Reifarth, R., Käppeler, Voss, F., and Wisshak, K., Nucl. Phys, **A688** (2001) 229.

[6] Hoppe, P. and Ott, U. in Astrophysical Implications of the Laboratory Study of Presolar Material, ed. T.J. Bernatowicz and E. Zinner, AIP, Woodbury, New York (1997), p. 27.

[7] Davis, A., et al. in Nuclei in the Cosmos V, eds. N. Prantzos & S. Harissopoulos, Editions Frontières, Paris, p. 563.

[8] Nichols, R.H. Jr, Hohenberg, C.M., Hoppe, P., Amari, S. and R. Lewis R.S. (1992) LPSC **23**, 989.

[9] Lewis, R. S., Amari, S. and Anders E. Geochim. Cosmochim. Acta, **58** (1994) 471.

[10] Klay, N., and Käppeler, F. Phys. Rev. **C38** (1988) 295.

[11] Anders, E. and Grevesse, N. Geochim. Cosmochim. Acta, **53** (1989) 197.

[12] Pepin. R.O., Becker, R.H., Rider, P.E. Geochim. Cosmochim. Acta, **59** (1995) 4997.

The s-Process Nucleosynthesis and the Mass of Carbon Stars

C. Abia[1], *I. Domínguez*[1], *M. Busso*[2], *R. Gallino*[3], *O. Straniero*[4], *J. Isern*[5], *P. de Laverny*[6], *B. Plez*[7]

[1] *Dpto. Física Teórica y del Cosmos. Universidad de Granada, Granada (Spain)*
[2] *Universita di Perugia, Perugia (Italia)*
[3] *Universita di Torino, Torino (Italia)*
[4] *Osservatorio Astronomico di Collurania, Teramo (Italia)*
[5] *Institut D'Estudis Spacials de Catalunya-CSIC, Barcelona (Spain)*
[6] *Observatoire de la Cote d'Azur, Nice (France)*
[7] *Universite de Montpellier, Montpellier (France)*

We present new spectroscopic observations for a sample of C(N)-type red giants [1]. These objects belong to the class of Asymptotic Giant Branch stars, experiencing thermal instabilities in the He-burning shell (thermal pulses). Mixing episodes called *third dredge-up* enrich the photosphere with newly synthesized ^{12}C in the He-rich zone, and this is the source of the high observed ratio between carbon and oxygen (C/O ≥ 1 by number). Our spectroscopic abundance estimates confirm that, in agreement with the general understanding of the late evolutionary stages of low and intermediate mass stars, carbon enrichment is accompanied by the appearance of *s*-process elements in the photosphere. We discuss the details of the observations and of the derived abundances, focusing in particular on rubidium, a neutron-density sensitive element, and on the *s*-elements Sr, Y and Zr belonging to the first *s*-peak. The critical reaction branching at ^{85}Kr, which determines the relative enrichment of the studied species, is discussed. Subsequently, we compare our data with recent models for *s*-processing in Thermally Pulsing Asymptotic Giant Branch stars, at metallicities relevant for our sample. A remarkable agreement between model predictions and observations is found. Thanks to the different neutron density prevailing in low and intermediate mass stars, comparison with the models allows us to conclude that most C(N) stars are of low mass ($M \leq 3\ M_{\odot}$). Figure 1 shows this fact: the area occupied by our stars in the [ls/M] vs. [Rb/Y] (M represents the mean metallicity of the star) diagram is well reproduced by s-process nucleosynthetic predictions [2] corresponding to an AGB star of $M = 1.5\ M_{\odot}$, while predictions for a $M = 5\ M_{\odot}$ are far away (considering the error bars) of the

observational data. We also analyze the $^{12}C/^{13}C$ ratios measured, showing that most of them cannot be explained by canonical stellar models (see Figure 2). This fact would require the operation of and *ad hoc* additional mixing, currently called Cool Bottom Process, operating only in low mass stars during the first ascent of the red giant branch and, perhaps, also during the asymptotic giant branch.

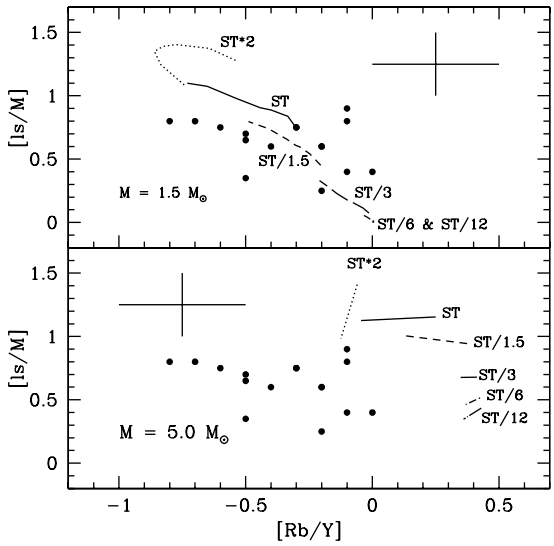

Figure 1: Comparison of the observed mean low-mass s-element (Y,Zr) enhancement (signature of the neutron exposure) against [Rb/Y] (signature of the neutron density) with theoretical predictions for a 1.5 $M_\odot$ (upper panel) and 5 $M_\odot$ (lower panel) TP-AGB star for different parameterizations of the ^{13}C pocket (lines). The theoretical predictions are for stellar models with C/O $\sim$ 1 and metallicity [M/H] ≥ -0.3, which is the metallicity of most of the stars studied here. Only stars in the sample with metallicity above this value are plotted. Note that several stars coincide in the same data point.

Acknowledgments

This work has been partially supported by the Spanish grant AYA2000-1574.

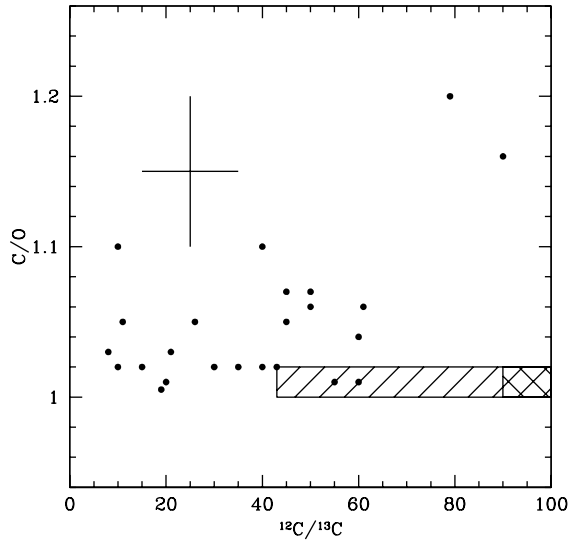

Figure 2: C/O vs. $^{12}C/^{13}C$ ratios derived in our stars. Note that most of the stars have a C/O ratio only slightly higher than 1 and that a significant number shows $^{12}C/^{13}C < 40$. Carbon isotopic ratios lower than about this value in an AGB star with C/O$\sim$ 1 cannot be explained by the standard models of stellar evolution and nucleosynthesis. Dashed bins correspond to theoretical predictions for low-mass ($^{12}C/^{13}C > 40$) and intermediate mass AGB models ($^{12}C/^{13}C > 90$). An extra-mixing mechanism seems to be required both during the RGB and AGB phases of evolution. An average error bar is show.

References

[1] Abia, C., Busso, M., Gallino, R., Domínguez, I., Straniero, O., Isern, J., ApJ, **559**, (2001), 1117

[2] Busso, M., Gallino, R., Lambert, D.L., Travaglio, C., & Smith, V.V., ApJ, **557** (2001) 902.

O and Mg abundances in metal-poor halo stars and their implications for stellar Fe yields

D. Argast[1]

[1] *Astronomisches Institut der Universität Basel, Venusstrasse 7, CH–4102 Binningnen*

Inhomogeneous chemical evolution models that try to reproduce the scatter seen in element-to-iron ratios ([el/Fe]) of metal-poor halo stars are heavily dependent on theoretical nucleosynthesis yields of core-collapse supernovae (SNe II). Hence inhomogeneous chemical evolution models present themselves as a test for stellar nucleosynthesis calculations. Applying such a model to our Galaxy reveals a number of shortcomings of existing nucleosynthesis yields. One problem is the predicted scatter in [O/Fe] and [Mg/Fe] which is too large compared to the one observed in metal-poor halo stars [1]. This can be either due to the oxygen or magnesium yields or due to the iron yields (or both). However, oxygen and magnesium are α-elements that are produced mainly during hydrostatic burning and thus are not affected by the theoretical uncertainties afflicting the collapse and explosion of a massive star. Stellar iron yields, on the other hand, depend heavily on the choice of the mass-cut between ejecta and proto-neutron star and are therefore very uncertain [2].

In Fig. 1, oxygen and magnesium abundances of metal-poor halo stars from different authors (squares and triangles) and model stars (dots) are plotted. Also visible as circles are [O/Fe] and [Mg/Fe] ratios predicted by nucleosynthesis calculations (yields are taken from [2]). The numbers in the circles give the mass of the progenitor star in solar masses. In the picture of inhomogeneous chemical evolution, a single SN event enriches the primordial ISM locally (in our model by mixing with $5 \times 10^4\,\mathrm{M}_\odot$ of ISM) with its nucleosynthesis products. Depending on the mass of the progenitor star, the resulting [O/Fe] and [Mg/Fe] ratios in these isolated patches of ISM cover a range of over two dex and as long as the ISM is dominated by these local inhomogeneities, newly formed stars will show the same range in their [el/Fe] ratios. In particular, this means that stars with [O/Fe] and [Mg/Fe] as small as -1.0 are inevitably produced by our model (see Fig. 1). This is in contrast to the bulk of observed metal-poor halo stars, which show [O/Fe] and [Mg/Fe] ratios in the range between 0.0 and 1.2, and is a strong

indication that existing nucleosynthesis models may correctly account for IMF averaged abundances but fail to reproduce stellar yields as function of progenitor mass.

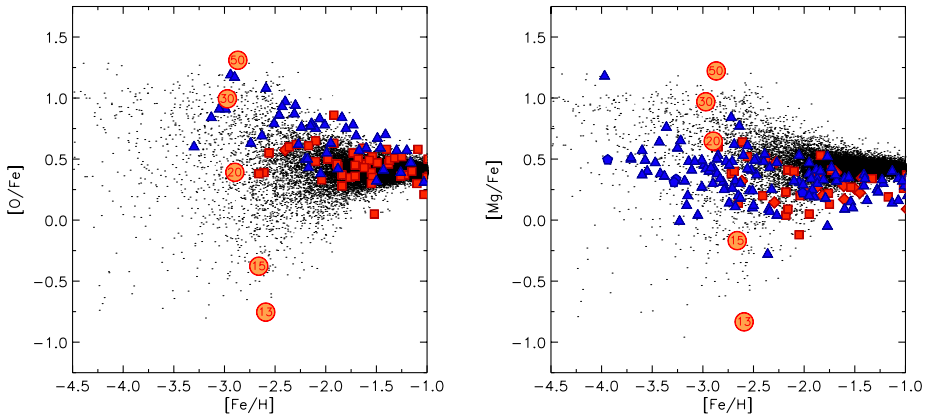

Figure 1: [O/Fe] and [Mg/Fe] ratios vs. metallicity [Fe/H] of metal-poor halo stars (squares and triangles) and model stars (dots). Circles depict [O/Fe] and [Mg/Fe] ratios of SN II models of the given progenitor mass. In contrast to observations, model stars with subsolar [O/Fe] and [Mg/Fe] ratios are predicted by the applied stellar yields, as visible by the location of the 13 and 15 $M_\odot$ SNe.

In order to reproduce the scatter of observed [O/Fe] and [Mg/Fe] ratios of metal-poor halo stars we assume that the oxygen and magnesium yields represent the true production of those elements well enough and artificially adjust the stellar iron yields $Y_{\mathrm{Fe}}(m)$ as function of progenitor mass m. Since theoretical uncertainties in nucleosynthesis yields are much larger in the case of iron (directly linked to the not fully understood explosion mechanism of core-collapse SNe [3]) than in the case of oxygen and magnesium (produced in hydrostatic burning [2]), this approach seems reasonable. Since it is not known from theory what functional form $Y_{\mathrm{Fe}}(m)$ follows with increasing progenitor mass (increasing, declining or a more complex behaviour), we have the freedom to make some *ad hoc* assumptions. Nevertheless, some important constraints on $Y_{\mathrm{Fe}}(m)$ can be drawn from the scatter, range and mean of observed [O/Fe] and [Mg/Fe] abundances, as visible from Fig. 1:

1. IMF averaged stellar yields (integrated over a complete generation of

stars) should reproduce the mean oxygen and magnesium abundances of metal-poor halo stars, i.e. [O/Fe] ≈ 0.4 and [Mg/Fe] ≈ 0.4.

2. Stellar yields have to reproduce the range and scatter of [el/Fe] ratios observed. Using oxygen and magnesium as reference this requires:

$$\begin{aligned} 0.0 \leq \quad & [\mathrm{O/Fe}] \quad \leq 1.2, \\ -0.1 \leq \quad & [\mathrm{Mg/Fe}] \quad \leq 1.2. \end{aligned}$$

(Note, that the error in abundance determination is of the order 0.1 dex.)

3. There exist a few Type II and Type Ib/c SN observations (1987A, 1993J, 1994I, 1997D, 1997ef and 1998bw) where the ejected ^{56}Ni mass and the mass of the progenitor was derived by analyzing and modelling the light-curve. These observations give important constraints on $Y_{\mathrm{Fe}}(m)$ since they fix the stellar yield for a given progenitor mass. (Note however, that the progenitor masses of SNe 1997D and 1998bw are not unambiguous).

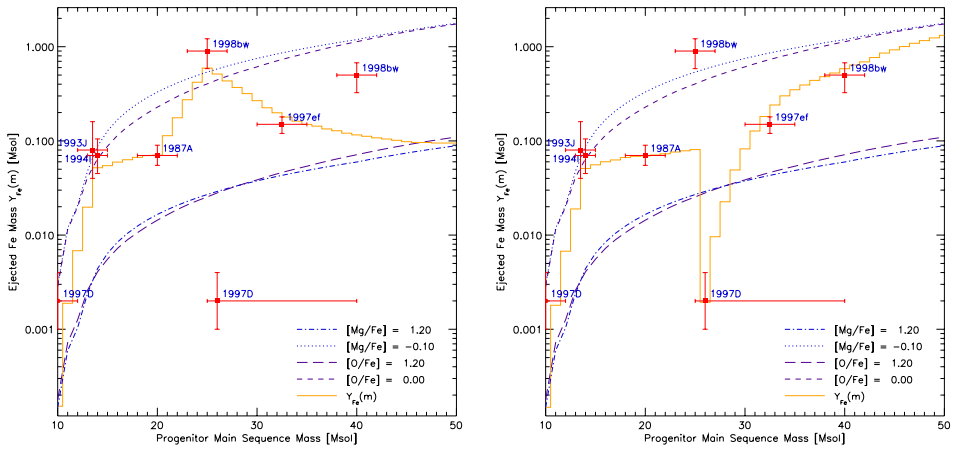

Figure 2: Iron yields $Y_{\mathrm{Fe}}(m)$ respecting the constraints deduced from metal-poor halo stars and SN observations. Model S1 (left panel): The $10\,\mathrm{M}_{\odot}$ model of SN 1997D and $25\,\mathrm{M}_{\odot}$ model of SN 1998bw are assumed to be correct. Model H1 (right panel): The $26\,\mathrm{M}_{\odot}$ model of SN 1997D and $40\,\mathrm{M}_{\odot}$ model of SN 1998bw are assumed to be correct.

With the help of these constraints, it is now possible to derive upper and lower boundaries for $Y_{\mathrm{Fe}}(m)$ under the assumption that oxygen and magnesium yields as function of progenitor mass are known [4]. Fig. 2 shows the upper and lower boundaries (dotted, dashed, long dashed and dotted-dashed lines) derived from observations together with the ^{56}Ni (which decays to ^{56}Fe) yield from observed core-collapse SNe. The solid lines in the left and right panel denote two possible iron yields as function of progenitor mass (see below).

The iron yield of lower-mass SNe (in the range $10 - 20\,\mathrm{M}_{\odot}$) is crucial to the distribution of model stars in [el/Fe] vs. [Fe/H] plots, since progenitors in this mass range compose the bulk (approximately 69%) of SN II events. Thus, the iron yield $Y_{\mathrm{Fe}}(m)$ should start at the lower boundary in Fig. 2 and reach the upper boundary for some progenitor in the mass range $10-20\,\mathrm{M}_{\odot}$. If the observed ^{56}Ni production of SN 1993J, 1994I and 1987A are also taken into account, the observational constraints are stringent enough to fix the iron yield of the low mass SNe apart from small variations: $Y_{\mathrm{Fe}}(m)$ starts at the lower boundary, increases steeply in the range $10 - 15\,\mathrm{M}_{\odot}$ to the values given by SN 1993J and 1994I and remains almost constant in the range $15 - 20\,\mathrm{M}_{\odot}$ (to account for SN 1987A). For the remaining discussion we therefore assume the Fe yield in this range to be $\approx 1.5 \cdot 10^{-4}\,\mathrm{M}_{\odot}$ for a $10\,\mathrm{M}_{\odot}$ progenitor, $\approx 5.5 \cdot 10^{-2}\,\mathrm{M}_{\odot}$ for a $15\,\mathrm{M}_{\odot}$ progenitor and $\approx 7.0 \cdot 10^{-2}\,\mathrm{M}_{\odot}$ for a $20\,\mathrm{M}_{\odot}$ progenitor. The available data for higher-mass SNe is not clear cut enough to present a unique iron yield for $m \geq 20\,\mathrm{M}_{\odot}$, especially since there are two distinct proposed progenitor masses in the case of SN 1997D and 1998bw. We now take a look at two of the four possible iron yield curves of higher mass SNe corresponding to the different models of the progenitor masses of SN 1997D and 1998bw.

The first case (model S1, shown in the left panel of Fig. 2) gives the best fit to abundance observations of metal-poor halo stars. Here, we preferred the lower mass progenitor models of SN1997D and SN 1998bw over the higher mass models. The curve is characterized by a peak of $0.59\,\mathrm{M}_{\odot}$ of iron at $25\,\mathrm{M}_{\odot}$ and a slow decline of the yield down to $9.5 \cdot 10^{-2}\,\mathrm{M}_{\odot}$ for the $50\,\mathrm{M}_{\odot}$ progenitor. The yield has to decline again to meet the mean abundances observed in metal-poor halo stars. Obviously, $Y_{\mathrm{Fe}}(m)$ fulfils all the constraints discussed above. The distribution of model stars in [O/Fe] and [Mg/Fe] is in good agreement with the distribution of observed stars (shown in [4]).

The right panel of Fig. 2 (model H1) shows the iron yield under the assumption that the higher mass models of SN 1997D and SN 1998bw are correct. Here $Y_{\mathrm{Fe}}(m)$ stays almost constant up to $25\,\mathrm{M}_{\odot}$, followed by a sud-

den plunge of the yield down to $1.9 \cdot 10^{-3}\,\mathrm{M}_\odot$ to account for SN 1997D and then a continuous rise to $0.79\,\mathrm{M}_\odot$ of synthesized iron for the $50\,\mathrm{M}_\odot$ progenitor that is necessary to account for the IMF averaged yield. This sudden decrease of the iron yield could indicate a change in the explosion mechanism from supernovae with "canonical" kinetic explosion energies of 10^{51} erg to hypernovae with $10 - 100$ times higher explosion energies. However, as visible in Fig. 2, the very low iron yield of the $26\,\mathrm{M}_\odot$ progenitor violates the [O/Fe] = 1.2 and [Mg/Fe] = 1.2 boundaries derived from observations, so we would expect model stars with much too high [O/Fe] and [Mg/Fe] ratios. A closer examination of the [O/Fe] and [Mg/Fe] distributions (shown in [4]), on the other hand, reveals that these model stars are mainly present at very low metallicities ([Fe/H] ≤ -2.5). The situation for oxygen remains unclear since no oxygen abundances were measured at metallicities where the effect is most pronounced ([Fe/H] ≤ -3.0). However, in the range $-3.0 \leq$ [Fe/H] ≤ -1.5 there are many observations with [O/Fe] ≥ 0.6 whereas the bulk of model stars in this range shows [O/Fe] ≈ 0.4. Furthermore, many observations of Mg abundances in halo stars with [Fe/H] ≤ -3.0 exist, but only one shows a ratio of [Mg/Fe] ≥ 1.0. The remaining stars all have [Mg/Fe] ≤ 0.8, which is in contrast to the predictions of the model.

At present, it is not possible to derive more stringent constraints on $Y_{\mathrm{Fe}}\,(m)$, due to the lack of a large and above all homogeneously analyzed sample of O, Mg and Fe abundances in very metal-poor stars. Even more valuable than a larger sample of abundance determinations would be the observation and analysis of further core-collapse supernovae/hypernovae. Only six core-collapse SNe with known progenitor and ejected ^{56}Ni mass are known to date, and for two of them not even their progenitor masses are clearly determined. Especially the discovery of a SN with a progenitor in the critical mass range from $20 - 30\,\mathrm{M}_\odot$ could provide us with the information needed to discern between the models presented above. This would also be a step towards answering the question whether a change in the explosion mechanism of core-collapse SNe occurs, i.e. the formation of a black hole and significant increase of the explosion energy for SNe with main-sequence mass $m \geq 25\,\mathrm{M}_\odot$.

The method to derive constraints on stellar Fe yields and a discussion of its implications are presented in detail in [4].

References

[1] D. Argast, M. Samland, O. E. Gerhard, and F.-K. Thielemann 2000, A&A, 356, 873

[2] F.-K. Thielemann, K. Nomoto, and M. Hashimoto 1996, ApJ, 460, 408

[3] M. Liebendörfer, A. Mezzacappa, F.-K. Thielemann, et al. 2001, Phys. Rev. D, 6310, 3004

[4] D. Argast, M. Samland, F.-K. Thielemann, and O.E. Gerhard 2002, submitted to A&A, astro-ph/0107153

Chemical evolution of Sr-Y-Zr: the puzzle of the stellar multisource origin

C. Travaglio[1], *R. Gallino*[2], *E. Arnone*[2]

[1] *Max-Planck-Institut für Astrophysik, Garching bei München, Germany*
[2] *Dipartimento di Fisica Generale, Universitá di Torino, Torino, Italy*

At least two major neutron capture mechanisms need to be invoked to build up nuclei heavier than Fe, i.e. the s-process and the r-process. Neutron-capture elements observed in Population II field stars are generally interpreted in a framework developed 'some' years ago: [1] showed from observations of Ba and Eu that low-metallicity stars exibit a typical r-process pattern. Observational support for this view grew with many subsequent works, e.g. the famous halo star CS 22892-052 where a great many elements have been observed (second only to the Sun) by Sneden and collaborators in the last $\sim$10 years combining HST and ground-based facilities. As shown by many studies, solar r-process abundance pattern from Ba to Pb conform to CS 22892-052. Recently similar r-process distributions have been observed in other halo stars with metallicity $-3<$[Fe/H]< -2 (see e.g. [2]; [3]). Theoretically, these observations confirm the idea of a 'primary' origin of r-process, i.e. r-process production is independent of the initial metallicity of the site.

Concerning s-process, the material from which Population II stars formed is not expected to contain significant s-process contributions. Galactic chemical evolution calculations of [4] and [5], showed that s-process products do not feature significantly in newly forming stars until [Fe/H]$\simeq -1.5$ for elements from Ba to Eu, and [Fe/H]$\simeq -2$ for Pb. The stellar s-process yields have been computed through nucleosynthesis calculations in the Asymptotic Giant Branch (AGB) phase of low- and intermediate-mass stars, covering a wide range of metallicities (see [6]; [7]). The physical parameters of the stellar structure are derived with a large series of evolutionary models compuetd with the FRANEC code (see e.g. [8]; [9]). We show in Fig. 1 the elemental (*left panel*) and isotopic (*right panel*) production factor of Sr-Y-Zr versus [Fe/H], obtained for AGB stars of initial 1.5 $M_{\odot}$ and different metallicities. For comparison we also plotted in the *left panel* Ba, Hf and Pb. The complex depedence of the s-process yields on metalliciy is explained more in details by [6], [4],[5]. Here we only notice that starting from AGB stars of nearly

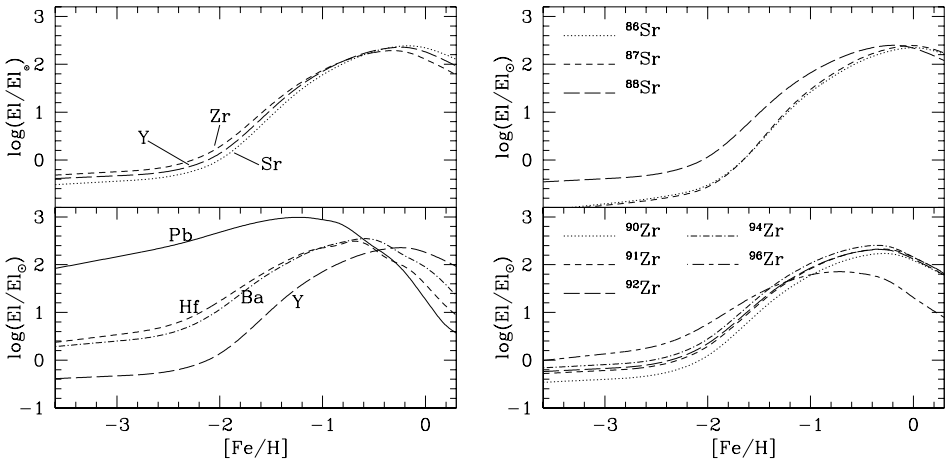

Figure 1: Enhancement factors with respect to solar abundances in the He shell material cumulatively mixed by third dredge-up episodes with the envelope of AGB stars of 1.5 $M_\odot$ and different metallicities.

solar metallicity and going toward more metal-poor stars, the neutron-flux first builds up the *s*-elements belonging to the Zr-peak (at neutron magic N =50). Then the Zr-peak is partly bypassed and the production of the elements at the second *s*-process peak (including Ba, at neutron magic N =82) increases, reaching a maximum at [Fe/H]~ -0.6 ([4]). For lower metal contents, the neutron flux feeds Pb (in particular ^{208}Pb), with a maximum production at [Fe/H]$= -1$ ([5]).

The *s*-process yields discussed above allow us to calculate quantitatively the chemical enrichment of heavy elements at different Galactic ages (considering the Galaxy divided in three zones, halo, thick and thin disk, as described in detail by [10]). Since the astrophysical site of *r*-process is still a debated problem, in order to quantify its contribution we treat the *r*-process in a simplified manner, as a typical primary mechanism occurring in a subset of SNII, those in the mass range 8 - 10 $M_\odot$ (see [4]). Our estimate of *r*-process abundances at $t = t_\odot$ was derived by subtracting from the solar abundances the *s*-fractions (*r*-residual method) for the elements from Ba to Pb. A first result is shown in Fig. 2, where the neutron-capture abundance pattern observed in the CS 22892-052 ([11]) is compared with the scaled *r*-process abundance curve obtained with chemical evolution calculations. The treatment for Sr-Y-Zr is discussed here below.

In Fig. 4 we show the indications for the Galactic evolutionary trend

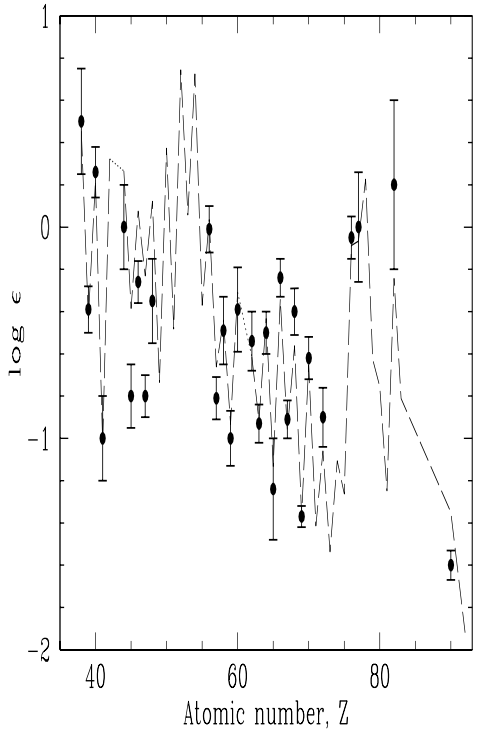

Figure 2: Neutron-capture elements in CS 22892-052 compared to a scaled r-process abundance curves obtained with Galactic chemical evolution calculations described in the text.

of [Zr/Ba],[Y/Ba], [Sr/Ba] from spectroscopic observations of Galactic field stars (mostly F and G dwarfs or chemically unevolved giants) at different metallicities, updated with the most recent data available in literature (different symbols are for different authors). The reason why we point the attention on the ratio of Sr,Y,Zr over Ba is the following. Ba, as discussed before, at low metallicity is mainly produced by r-process nucleosynthesis. *If* Ba and Sr-Y-Zr would have the same stellar source at such low metallicities, we would expect to see a fearly flat ratio (within observational errorbars!), as we see e.e. in the case of [Ba/Eu]. This seems not to be the case, and suggests a different stellar origin. A second point in favour of this is suggested by very low-metallicity stars, and in particular by the CS 22892-052. Since this star has an r-process enrichment of $\sim$40 times with respect to the Solar composition, we can consider the signature of CS 22892-052 as 'pure' r-process (i.e. the contamination by other possible stellar sources is hidden

by the r-process abundance). Under this assumption, and knowing that the Ba r-fraction at the epoch of the Solar System formation is 20% ([4]; [7]), with a simple calculation, one can derive the r-fraction of Sr-Y-Zr from the CS 22892-052 (notice that the same can be done using, e.g. Eu instead of Ba). Therefore we derive that the r-fraction of Sr-Y-Zr is $\sim$10% (and the only-r fraction for Sr-Y-Zr is shown in Fig. 4 as a flat line in the three panels). We also know the contribution at the Solar System composition of s-process to Sr (70%), Y (70%), and Zr (65%) (Travaglio et al. 2002, in preparation), and we consider in addition a small contribution to Sr from the 'secondary' weak component from massive stars ($\sim$8%). This last one, due to the ^{22}Ne(α,n) source, scales as metallicity, giving a significative contribution only at $t = t_{\odot}$ and zero at lower metallicities. As a first approximation, we consider no contribution from the weak-component to Y and Zr. Finally, we find that a fraction of $\sim$20% for Y and Zr and $\sim$20% for Sr is missed to match the Solar composition of Sr, Y, and Zr. We assume this fraction as a 'primary' (i.e. significative also at low metallicities) contribution from massive stars (we need massive stars in order to give a contribution just at early time in the Galaxy, i.e. low metallicity). The result is shown in Fig. 4 (the different lines, solid, long dashed and dotted are for the three Galactic zones, thick disk, thin disk, and halo, respectively). The decreasing trend of [Sr,Y,Zr/Ba] versus [Fe/H] is obtained with the delayed production of Ba (at low metallicity from SNII with masses $\sim$ 10 $M_{\odot}$, [4]) with respect Sr-Y-Zr (from a primary 'n-process', i.e. from a primary neutron source efficient in massive stars, not classical s- nor classical r-process).

References

[1] M. Spite and F. Spite, A&A **67** (1978) 23.

[2] J. Westin, C. Sneden, and J. Truran, ARAA **27** (2001) 279.

[3] J. Cowan, C. Sneden, et al., ApJ in press.

[4] C. Travaglio, D. Galli, R. Gallino, et al., ApJ **521** (1999) 691.

[5] C. Travaglio, R. Gallino, M. Busso, and R. Gratton, ApJ **549** (2001) 346.

[6] R. Gallino, et al., ApJ **497** (1998) 388.

[7] C. Arlandini, et al., ApJ **525** (1999) 886.

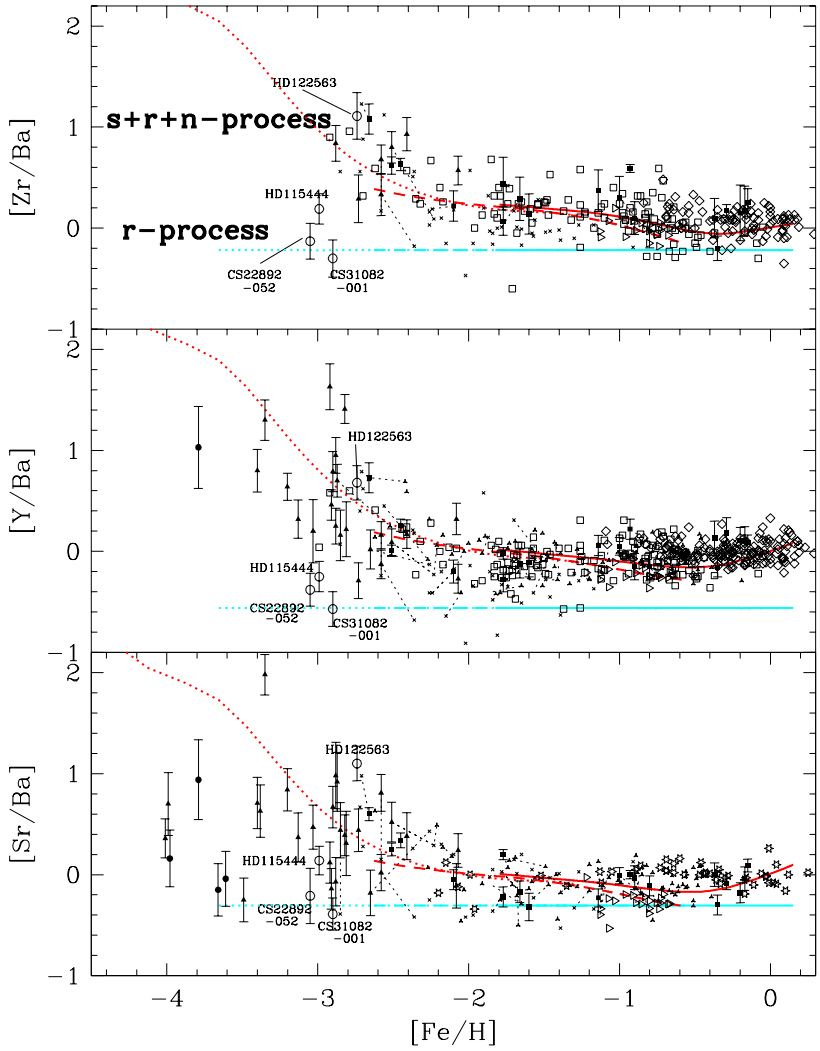

Figure 3: Galactic evolution of [Sr,Y,Zr/Ba] according to our model predictions for the s+r+n process in the halo (*dotted line*), thick disk (*dashed line*), and thin disk (*solid line*). The only-r-process contribution is also shown in the three panels. Different symbols are for observational data available in literature.

[8] A. Chieffi, and O. Straniero, ApJS **71** (1989) 47.

[9] O. Straniero, et al., ApJ **478** (1997) 332.

[10] F. Ferrini, F. Matteucci, C. Pardi, and U. Penco, ApJ **387** (1992) 138.

[11] C. Sneden, et al., APJ **533** (2000) L139.

Inhomogeneous Enrichment of Heavy Elements in the Galaxy

Y. Ishimaru[1], *N. Prantzos*[1], *S. Wanajo*[2]

[1] *Institut d'Astrophysique de Paris, 98bis Boulevard Arago, 75014 Paris, France*
[2] *Department of Physics, Sophia University, 7-1 Kioi-cho, Chiyoda-ku, Tokyo 102-8554, Japan*

Recent spectroscopic studies have shown the existence of intrinsic large dispersions in chemical abundances with respect to iron of metal-poor stars. One of the possible explanations is that the inter-stellar medium was not mixed well at the early epoch of our Galaxy, and metal-poor stars contain heavy elements produced by only one or a few supernovae. Thus, assuming star formation is induced by supernova explosions, we have constructed a chemical evolution model of the Galactic halo. Since stars are formed from the gas mixed with the products of the supernova which induce the star formation, dispersions in chemical abundances are dependent of supernova yields. We take two sets of known supernova yields; the data of a) Nomoto et al. (1997) [1] and that of b) Woosley & Weaver (1995) [2], and compare predicted dispersions in various elements (O–Zn) with observations using statistical method. We have successfully showen clear differences of two sets of yields revealed in the dispersions of relative abundance ratios, even for α-elements, which have been believed as rather robust from the nucleosynthetic point of view (Figure 1). Generally, the width of dispersion is larger in metal-poor stars and diminishs with metallicity (Figure 2). The lower limit of stellar metallicity is around [Fe/H]$\sim$-3.5 for the constant yields independent of metallicity (i.e., yield (a)). On the contrary, considerable number of stars appear from around [Fe/H]~ -5, when the metal dependency is taken into account (i.e., yield (b)), shince lower metallicity stars produce less iron. But even in the case with yield (a), if there are some dispersions in the efficiency of gas mixing (mixing length), a part of stars are formed from more diluted supernova remnants and their metallicty is reduced. Thus, if significant number of extremely metal-poor stars will be found in a future observations, it can constrain either the iron yields of the first stars or the efficiency of dilution at the early epoch. However, since dilutions do not change the relative abundance ratios, the maximum width of dispersions are not affected much by dynamical parameters but is determined mainly

by variety of yields.

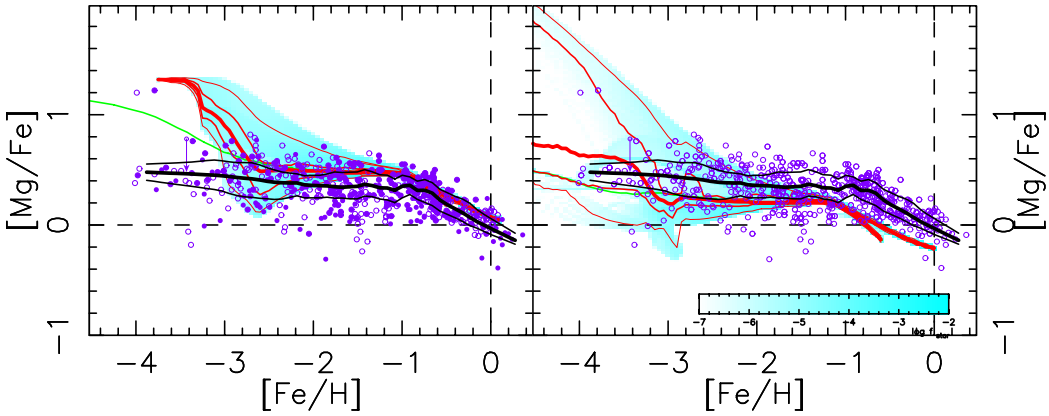

Figure 1: [Mg/Fe] vs [Fe/H] relations predicted from Nomoto et al. (1997, left panel) and Woosley & Weaver (1995, right panel). Predicted stellar fraction (blue shadow) are compared to observational data (circles). The average lines and 50% confidence regions of observations are given by black thick and thin lines, respectively. Those of model predictions are also given by red (gray) thick, thin, and thinner (90%) lines.

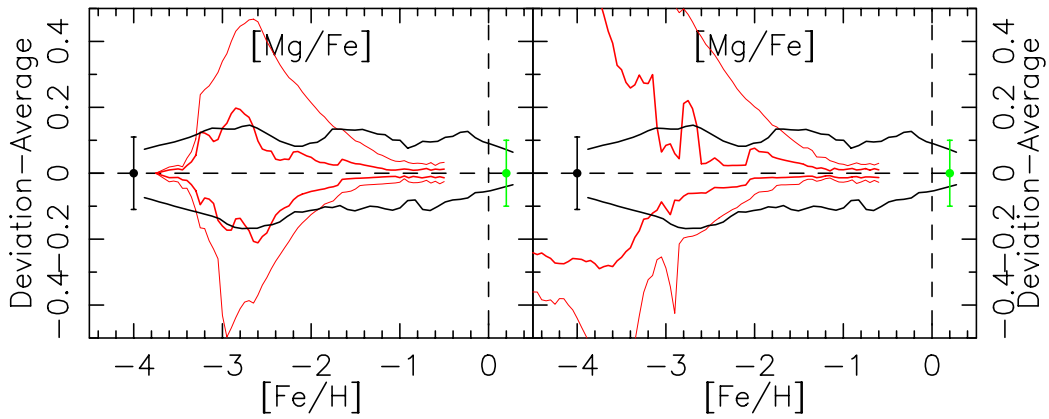

Figure 2: Deviations of 50% and 90% confidece from the average for [Mg/Fe] vs. [Fe/H] ratio. Nucleosynthesis data used in left and right panels are the same with Fig. 1. Observational data is given by black lines, and model predictions are given by red (gray) lines. Typical observational errors for halo stars and disc stars are put in the left and right of figures, repectively.

References

[1] Nomoto, K., Hashimoto, M., Tsujimoto, T., Thielemann, F. -K., Kishimoto, N., Kubo, Y., & Nakasato, N. 1997a, Nucl. Phys. A, 616, 79

[2] Woosley, S. E. & Weaver, T. A. 1995, ApJS, 101, 181

Galactic Global Distribution of ^{22}Na

A.F. Iyudin

MPI für Extraterrestrische Physik, Postfach 1312, D-85741 Garching, Germany

Abstract

Classical novae are believed to be the source of the ISM enrichment with the isotopes of ^{13}C, ^{15}N, ^{22}Na and ^{26}Al. The latter two, especially radioactive ^{22}Na, that decays producing penetrating 1.275 MeV γ-ray photon, could be used as a check probe of the contemporaneous thermonuclear runaway theory (TNR) of classical novae. To tap this problem we have used two-way approach, namely: (1) – by attempting the ^{22}Na line emission detection from old and more recent individual novae; and (2) – by deriving the ^{22}Na line emission global galactic distribution. This makes possible to tap rather uncertain galactic novae rate by comparing observations of the individual Galactic novae with the integrated ^{22}Na line emission from the disk and/or bulge population. The accumulation of ^{22}Na from the frequent novae in the bulge will lead to an observable extended emission.

The COMPTEL telescope on board the Compton Gamma-Ray Observatory (CGRO), due to its combination of imaging and spectroscopic capabilities, is suitable to verify above ideas.

42.1 Results of the 1.275 MeV γ-ray line study from individual novae

It is common belief (e.g. Starrfield 1999) that detectable amounts of ^{22}Na are synthesized almost exclusively in the ONe novae, which have both ingredients for this: *(i)* enough ^{20}Ne seed nuclei (the mass fraction of $X(^{20}\mathrm{Ne}) = 0.313$ in ONe WD model Ritossa, Garcia-Berro & Iben (1996)); and *(ii)* higher peak temperatures necessary for an efficient production of ^{22}Na at the expense of ^{20}Ne. The most recent measurements of the fluxes $F_{1.275}$ from a number of recent ONe novae seems contradict this common belief and can be summarized as follows: *(i)* only upper limits were derived with COMPTEL at the level of down to $\sim 2 \times 10^{-5}$ photons/(cm^{2}s) for the ^{22}Na γ-ray line from the studied ONe novae (V693 CrA, V1370 Aql, QU Vul, V838 Her, NSgr 1991, NSct 1991, NPup 1991, V1974 Cyg, NCir 1995, NAql

1995, and NCen 1995) (Iyudin et al. 1995; Iyudin et al. 2000); *(ii)* upper limits from other γ-ray telescopes are usually less constraining (Leising et al. 1988; Leising et al. 1993; Iyudin et al. 1995; Harris et al. 2000).

Thus, the preliminary attempts to detect the 1.275 MeV γ-ray line emission from ^{22}Na produced in the *fast* ONe novae gave a negative result. The only tentative detection of such emission was found to be related to the *very slow* (presumably CO type) Nova Cas 1995 (Iyudin et al. 2001).

Nova Cas 1995, discovered by Yamamoto (IAUC 6213) on August 24, 1995, was observed by COMPTEL during ∼1470 days time interval. An imaging analysis performed using all the data yields a total significance of the N Cas 1995 detection of ∼4 σ (Iyudin et al. 2001; 2002).

¿From a fit of the 1.275 MeV light curve by the model describing decaying ^{22}Na embedded in the NCas 1995 ejecta that expands with the velocity of ∼150 km/s, the most probable total mass of the ^{22}Na produced in N Cas 1995 TNR was found to be $\sim 5.4{\times}10^{-8} \left(\frac{D}{2.4kpc}\right)^2$ M$_\odot$ (Iyudin et al. 2001).

42.2 Global Galactic Distribution of the 1.275 MeV Line Emission

Usually it is assumed that at least two components (disk and bulge) of the Galactic novae population exist (Higdon and Fowler 1987; Kent, Dame and Fazio 1991; Dawson and Johnson 1994; Hatano et al. 1997).

The full model of the global Galactic distribution of 1.275 MeV line emission have to correspond to the total classical novae space distribution, and depends on the contributions of different types of novae, e.g., CO, and ONe type novae, or, equivalently, slow novae and fast novae. It is likely that disk and bulge novae differ in their composition.

Preliminary COMPTEL results, derived from the distribution of the galactic 1.275 MeV line emissivity, point toward very significant (∼9 σ) detection of the Galactic bulge component of 1.275 MeV line emission.

Assuming that yield of the ^{22}Na in individual nova is between $3{\times}10^{-9}$ $M_\odot$ and $1.2{\times}10^{-8}$ $M_\odot$ (Jose, Coc & Hernanz 1999) we can derive the range for the nova rate in the Galactic bulge as,

$$20.5\ yr^{-1} \leq R_{CN} \leq 82\ yr^{-1}, \tag{18}$$

where the upper bound value is higher than normally quoted (Della Valle et al. 1994; Hatano et al. 1997). Further assuming that all bulge 1.275 MeV emission is due to the massive ONe-type novae, the space density of active classical novae systems in the bulge could be derived under this assumption

as,

$$1.4 \times 10^{-5} pc^{-3} \leq D_{CN} \leq 5.8 \times 10^{-5} pc^{-3}, \quad (19)$$

and appears to be very high, almost equivalent to that of M31, which is in contradiction with the present belief. Could it be that bulge novae are mostly slow, CO-type novae as was suggested by Della Valle and Livio (1998)?

Conclusions

The first detection of 1.275 MeV ^{22}Na γ-ray line emission from the Galactic bulge region, pose a question to the type and space density of the major contributor of the ^{22}Na in the bulge.

Acknowledgements

AFI acknowledges financial support from the German "Ministerium für Bildung und Forschung" through the DLR grant 50 OR 0002.

References

[1] P.C. Dawson and R.G. Johnson, J.R.Astron.Soc.Can. **88** (1994) 369.

[2] M. Della Valle and M. Livio, A&A, **286** (1994) 786.

[3] M. Della Valle and M. Livio, ApJ, **506** (1998) 818.

[4] M.J. Harris, et al., ApJ, **542** (2000) 1057.

[5] K. Hatano, D. Branch, A. Fisher, S. Starrfield, MNRAS, **290** (1997) 113.

[6] J.C. Higdon and W.A. Fowler, ApJ, **317** (1987) 710.

[7] A.F. Iyudin, et al., A&A, **300** (1995) 422.

[8] A.F. Iyudin, in Proc. of the 10th Workshop on "Nuclear Astrophysics", Ringberg Castle, Tegernsee, Germany, March 20-25, 2000, **MPA/P12** (2000) 118.

[9] A.F. Iyudin, et al., in Proc. of the 4th INTEGRAL Workshop, Alicante, Spain, September 04-08, 2000, **ESA-SP459** (2001) 41.

[10] A.F. Iyudin, et al., A&A, (2002) in preparation.

[11] J. Jose, A. Coc, M. Hernanz, ApJ, **520** (1999) 347.

[12] S.M. Kent, T.M. Dame, G. Fazio, ApJS, **127** (1991) 131.

[13] A. Kovetz and D. Prialnik, ApJ, **291** (1985) 812.

[14] M.D. Leising, G.H. Share, E.L. Chupp and G. Kanbach,, ApJ, **328** (1988) 755.

[15] M.D. Leising, et al., in AIP Conf. Proc., **280** (1993) 137.

[16] C. Ritossa, E. Garcia-Berro, I. Iben, ApJ, **460** (1996) 489.

[17] M.M. Shara and D. Prialnik, AJ, **107** (1994) 1542.

[18] S. Starrfield, Phys. Rep., **311** (1999) 371.

[19] J.W. Truran and M. Livio, ApJ, **308** (1986) 721.